MEASUREMENT OF
CHARGED HADRON SPECTRA AT THE Z^0
WITH CHERENKOV RING IMAGING

A DISSERTATION
SUBMITTED TO THE DEPARTMENT OF PHYSICS
AND THE COMMITTEE ON GRADUATE STUDIES
OF STANFORD UNIVERSITY
IN PARTIAL FULFILLMENT OF THE REQUIREMENTS
FOR THE DEGREE OF
DOCTOR OF PHILOSOPHY

By
Tomas Josef Pavel
August 1996

I certify that I have read this dissertation and that in my opinion it is fully adequate, in scope and in quality, as a dissertation for the degree of Doctor of Philosophy.

———————————————————
David W. G. S. Leith
(Principal Adviser)

I certify that I have read this dissertation and that in my opinion it is fully adequate, in scope and in quality, as a dissertation for the degree of Doctor of Philosophy.

———————————————————
John Jaros

I certify that I have read this dissertation and that in my opinion it is fully adequate, in scope and in quality, as a dissertation for the degree of Doctor of Philosophy.

———————————————————
Lance Dixon

Approved for the University Committee on Graduate Studies:

———————————————————

Abstract

This dissertation attempts to probe hadronization, the process by which the fundamental quarks described by quantum chromodynamics produce the jets of hadrons that we observe in experiments. The measurements are made using e^+e^- collisions at the SLAC Linear Collider (SLC), operating at the Z^0 resonance with the SLC Large Detector (SLD), and the unique capabilities of the SLC/SLD facility are exploited. First, the spectra of charged hadrons ($\pi^\pm$, $K^\pm$, and $p/\bar{p}$) are measured. This is accomplished with the SLD Cherenkov Ring Imaging Detector (CRID), one of a first generation of devices that have been developed for efficient particle identification over a wide momentum range. The use of the CRID is central to this dissertation, and its design and performance are described in detail here. The measured spectra agree with other measurements at the Z^0 and extend the momentum coverage. Next, the excellent spatial resolution of the SLD tracking systems, along with the small and stable beam spots of the SLC, is employed to identify jets produced from heavy b or c quarks and to separate them from the remaining light-quark (uds) jets. This removes the effects of heavy quark fragmentation and decays of heavy-quark hadrons from our study of hadronization. The first measurements of particle spectra in light-quark jets are then presented. Finally, the highly-polarized incident electron beam of the SLC, together with the electroweak asymmetries of the quarks, is exploited to separate quark and antiquark jets. Significant differences in quark-antiquark production of protons and of kaons are observed at high momenta. This signal suggests a "leading particle effect," where the particles containing the primary quark of a jet are more likely to populate the high-momentum phase space than are other hadrons.

Acknowledgements

The field of high-energy physics is definately dominated by "large enterprises" nowadays. Although I have heard many people complain about this, I think it has its good points as well. For one thing, it means that graduate students have an almost unlimited supply of people to ask for help. For another, it means that one has the opportunity to meet and work with a large assortment of folks. Most importantly, and of course the reason why we do it, it allows people to pool resources and to solve really challenging problems.

I feel as though I got the most out of all these advantages, as well as getting some of the benefits of a smaller collaboration (SLD is one of the smallest big collaborations around). I was able to work with a lot of different people on a lot of different topics, and I was able to try my hand at a lot of hard problems, but I was also able to see an experiment through from construction to physics results (a feat somewhat unusual these days). For all of these experiences, for giving me the opportunity to work on some challenging problems, and for supporting me over all these years, I would like to thank my adviser, David Leith. I will never forget the first time I came to SLAC and listened to David explain how the CRID works. I immediately appreciated the challenge of the problem . . .

Next, I would like to thank the other members of my thesis and defense committees, not only for putting in the time necessary, but also for putting up with various last-minute problems, changes, and efforts. Many thanks to John Jaros, Lance Dixon, Pat Burchat, Stan Wojcicki (for ducking out at the last minute), and Ed Solomon (for avoiding jury duty just for me).

Now comes my opportunity to test my long-term memory. Please forgive me if that memory inadvertantly fails me. Thanks go to all of the CRID gas-system folks, who got me started on this project and who kept me busy for a long time. This list starts with Greg Hallewell, who first put me to work on the CRID, but includes Hide Kawahara, Youngjoon Kwon, Tom Weber, Bob Reif, Don McShurley, Matt McCulloch, Paschal Coyle, Don Coyne, Michael Snyder, and Gerhard Mueller. Last but not least in this list is Jaroslav Va'vra, who has taken over not only the gas system, but also any other CRID responsibilities that others (such as myself) have passed on. Jerry has done a fine job of keeping me honest, and of reminding me of various projects I never finished.

Thanks also to the online software folks. These include Steve Yellin, Sridhara Dasu, Pierre Antilogus, Alice Bean, Paul Stiles, Gerard Oxoby, Dick Plano, Ian Stockdale, and probably a few other "Endcap-ers." Thanks also to the SLD online folks, Dave Sherden, Tony Waite, Joanne Bogart, Mike Huffer, Jim Russell, Ramon Berger, and particularly to Owen Saxton. Owen had the uncanny ability to solve whatever sort of VMS problem I could manage to find my way into.

Next comes the CRID offline, which are the people with whom I have spent the most time in the past few years. Dave Aston has helped me solve all manner of problems with the SLD and CRID offline tools. He has also been the one-man repository of knowledge about the CRID offline. Analyzing the CRID would be impossible without him. Stephane Willocq was a "recent" convert to the offline (although he was around in Endcap contexts for some time), but he wasted no time in improving things. Stephane also proved to be a meticulous proofreader (even on topics like QCD). Another latecomer is Shinya Narita, who was here "only" a couple years, but never failed to produce results through long hours of toil. Thanks also to Blair Ratcliff, who although he did not have much time to spend on CRID analysis anymore, nevertheless managed to come up with the right questions or insights on many occasions.

Speaking of insights, I cannot forget the eagle-eye of Bill Dunwoodie. Bill would never fail to catch some inconsistency in the CRID analysis minutes and

package which has served me well (and allowed me to never have to learn "that other histogramming package from across the ocean").

A million thanks to Lillian DePorcel, Jennifer Chan, and the other Group B secretaries over the years. Never has there been a problem that could not be solved by just asking Lillian. Thanks also to Marcia Keating and the other Physics Department staff for helping me steer my way through Stanford paperwork and deadlines. And thanks to Sylvia MacBride and the other folks at the SLAC Publications department for helping me put this document together.

Additional help writing this dissertation came from my cat, Hershey (who helped by sleeping on my lap or on my keyboard). I must also give credit to my friends Mike Wall and Alfred Woo for trying to convince me to find time for recreation while working on my thesis (they failed).

Next, my parents deserve special thanks. They have encouraged me on this long trail of higher education without steering me in any direction other than my own. They have made the sacrifices for the futures of myself and my sister, and I cannot express my gratitude in words.

Finally, the greatest thanks go to my wife Elizabeth. She has helped me through this period in many ways, ranging from keeping me from distractions to picking up the slack in the housework. Beyond everything else, she has always been a steady and calming influence. I guess I will have the opportunity to repay you soon enough …

Contents

List of Tables

List of Figures

Chapter 1

Overview

Although our current "Standard Model" of particle physics has had remarkable success in explaining many of the phenomena we observe in experiments, there is one area that has proven resistant to a solid understanding. That area is the process of *hadronization*, whereby the quarks and gluons that are described in the Standard Model become the hadrons that we observe in our experiments. It is the desire to understand more about the hadronization process that provides the motivation for this dissertation. In this overview, we first discuss the Standard Model briefly, then we describe the general features of our measurement, and finally we give an outline of the remainder of the dissertation. The measurement was performed at the Stanford Linear Accelerator Center (SLAC), using data collected in the 1993 and 1994–95 runs of the SLAC Linear Collider (SLC) with the SLC Large Detector (SLD). The SLC/SLD facility has several unique capabilities that make this measurement possible.

1.1   The Standard Model

The current state of understanding in particle physics is that we know of twelve fundamental fermions—three pairs of *leptons* and three pairs of *quarks*—and three interactions (electromagnetism, and the weak and strong nuclear forces)

mediated by gauge bosons (the gluon for the strong force, the photon for elec-
tromagnetism, and the $W^{\pm}$ and Z^0 for the weak force). These elements are
partially unified in a quantum field theory that we call the Standard Model.
The fourth interaction, gravity, has not yet been unified into a common field
theory, although there have been some attempts to do so [1].

The leptons are those particles that do not participate in the strong inter-
action. They are arranged in three pairs, each pair containing one electrically
charged and massive particle (e, μ, τ) and one neutral and massless particle
(ν_e, ν_μ, ν_τ). The charged partners participate in the electromagnetic interac-
tion, while all particles interact via the weak nuclear force. The weak force
is parity-violating. For example, only left-handed particles (and right-handed
antiparticles) participate in the part of the weak interaction mediated by $W^{\pm}$
exchange (charged-current weak interactions).

The quark sector is arranged much like the leptons, except that both part-
ners of each set are charged and massive. The three sets are *down* and *up* $\binom{u}{d}$,
strange and *charm* $\binom{c}{s}$, and *bottom* and *top* $\binom{t}{b}$. The upper partner of each set
has charge $+\frac{2}{3}$, and the lower has charge $-\frac{1}{3}$. The quarks all participate in
the electromagnetic and weak interactions, but in addition, quarks interact via
the strong nuclear force. The properties of all twelve particles are summarized
in Table 1.1 [2]. All of these fermions are accompanied by their antimatter
counterparts.

It is one of the great triumphs of modern particle physics to embed all of
these phenomena into a quantum field theory with one Lagrangian (the Stan-
dard Model). This theory is based on the symmetry of gauge groups, with elec-
tromagnetic and weak interactions unified by the Glashow–Weinberg–Salam
theory ($SU(2)_L \times U(1)_Y$) [3, 4, 5], and the strong interaction described by quan-
tum chromodynamics ($SU(3)$) [6, 7]. Of course, our understanding is not com-
plete. Ideally, one would like a single gauge group to describe both parts of the
Standard Model, one would prefer to have fewer non-fundamental parameters,
such as the particle masses, and one would like to include gravity into the
framework as well. Although the Standard Model has been quite successful at

LEPTONS			
Particle	Mass (GeV/c^2)	Charge	Baryon Num.
e	0.511×10^{-3}	-1	0
ν_e	$< 5 \times 10^{-9}$	0	0
μ	0.106	-1	0
ν_μ	$< 0.3 \times 10^{-3}$	0	0
τ	1.78	-1	0
ν_τ	< 0.03	0	0

QUARKS			
Particle	Mass (GeV/c^2)	Charge	Baryon Num.
u	0.002–0.008	$+\frac{2}{3}$	$\frac{1}{3}$
d	0.005–0.015	$-\frac{1}{3}$	$\frac{1}{3}$
c	1.0–1.6	$+\frac{2}{3}$	$\frac{1}{3}$
s	0.1–0.3	$-\frac{1}{3}$	$\frac{1}{3}$
t	180 ± 12	$+\frac{2}{3}$	$\frac{1}{3}$
b	4.1–4.5	$-\frac{1}{3}$	$\frac{1}{3}$

Table 1.1: Properties of the fundamental particles.

predicting many experimental observations, it has not provided quantitative predictions of hadronization, as will be discussed in the next chapter.

1.2   Measurement of Hadronization

One of the primary ways to probe hadronization is to measure the spectra of various species of hadrons produced in jets in e^+e^- annihilation. Although one can also measure more inclusive observables, such as the momentum spectrum of all charged particles, there is more dynamical information in the spectra of specific particle types because we can learn how the spectra are affected by the mass of the hadron. One might expect the hadron mass to play a dynamical role in the hadronization process (see section 2.4.3, for example). Furthermore, by measuring both mesons ($q\bar{q}$ combinations) and baryons (qqq combinations), we may be able to probe different aspects of the hadronization process.

   Therefore, it is of interest to measure the spectra of the stable[*] charged hadrons (π, K, and p) produced in e^+e^- annihilation. In order to do this, we need a way to determine the identity of the hadrons whose ionization tracks we measure in our detector. The SLD detector has an excellent capability in this regard with its Cherenkov Ring Imaging Detector (CRID), one of a new type of device for delivering excellent identification efficiency over a broad momentum range (see Chapter 4).

   The measurement of identified hadron spectra in e^+e^- annihilation at the Z^0 has been done by other experiments. Although we contribute by covering different momentum ranges and by providing a complementary technique, the basic measurement of spectra is not unique. Moreover, we would like to probe the hadronization process deeper than the basic measurement of hadron spectra allows. The way we approach this is by adding information about the primary quark that initiates the hadronization in a jet.

---

[*]Here "stable" is relative to the time or distance scales at which we can measure. Because our detectors are on the scale of meters in size, with measurement precision on the scale of centimeters or better, the conventional definition of stable hadrons in this context is those with a lifetime $\tau > 3 \times 10^{-10}$ seconds.

In addition to its excellent particle identification capability, the SLD detector has exceptional tracking resolution. The combination of the SLD central drift chamber and silicon-pixel vertex detector can measure the impact parameter of tracks to 11 μm in the plane perpendicular to the beam. Combined with the small and stable beam spots of the SLC and the long decay length of b and c hadrons (several mm), this gives an excellent capability to identify events containing the heavy b and c quarks. Because the masses of these quarks are above the masses of the lighter hadrons and above the scale of the hadronization process, the properties of spectra in heavy-quark jets are expected to be different from those in the light-quark jets (u, d, and s quarks). It is therefore important to disentangle the spectra in heavy-quark jets from those in light-quark jets, which should then represent the "true" hadronization process.

Finally, the combination of SLC and SLD has a unique capability in the operation of a highly-polarized electron beam. Thanks to the electroweak interaction being strongly parity-violating, there is a large forward-backward asymmetry of the production of quarks and antiquarks in e^+e^- interactions at the Z^0 resonance for a particular electron helicity. We exploit this to separate quark jets from antiquark jets on a statistical basis. We can then measure particle and antiparticle spectra in quark jets and the corresponding spectra in antiquark jets. The differences in these spectra should teach us about the propagation of the primary quark quantum numbers through the hadronization process.

In particular, the quark-antiquark separation allows us to search for a *leading particle effect* in e^+e^- annihilation, which is similar to an effect that has been observed for some time in hadron-hadron interactions. In hadron-hadron interactions,[*] one of the particles in the final state may often carry a large fraction of the available energy. This particle is usually one which is identical to one of the incident hadrons, but it can be one which shares many but not all quantum numbers with an incident particle with a lesser degree of enhancement [8]. The effect is also seen in lepton-proton scattering, for example in the

---

[*]with diffractive scattering explicitly excluded

ratio of π^+ to π^- production in νp scattering. This effect has not previously been observed in e^+e^- annihilation; however, previous measurements did not attempt to separate quark-jets from antiquark-jets.

1.3   Outline of Dissertation

The remainder of this dissertation proceeds as follows. We start by reviewing the theory of strong interactions and models of hadronization in Chapter 2. Then we discuss the accelerator and detector apparatus in Chapter 3. Because particle identification is central to our measurement, we focus on the SLD CRID in the following four chapters, starting with an overview of its design in Chapter 4, and a more-detailed description of the gas delivery and monitoring systems in Chapter 5. We continue with a discussion of the reconstruction and particle identification algorithm in Chapter 6, and then we review the performance achieved by the CRID in Chapter 7. Next, we proceed to the details of our measurement with a discussion of event and track selection in Chapter 8 and the analysis technique and results in Chapter 9. Finally, we summarize the main results in Chapter 10.

Chapter 2

The Theory of Strong Interactions

Since our measurement focusses on the strong interaction, we present a brief summary of quantum chromodynamics (QCD), which is the standard theory of strong interactions. After a short description of the background and development of QCD, we describe the QCD Lagrangian, and then go on to discuss the application of QCD to e^+e^- annihilation. Next we turn to the study of hadronization within the framework of QCD and describe several models for hadronization.

2.1   The Development of QCD

The theory of strong interactions has gone through several false starts in explaining the interactions of hadrons (particularly protons and neutrons) before arriving at our current theory, quantum chromodynamics (which describes interactions between quarks and gluons, which compose hadrons). In 1964, Gell-Mann [9] and Zweig [10] independently proposed a trio of particles (*quarks*) whose SU(3) flavor symmetry would be responsible for the array of known hadrons. These quarks (u, d, and s) were intended more as a notational device,

useful for creating a "periodic table" of hadrons, and were not generally considered to be constituent particles of mesons and baryons until later.

Although this SU(3) flavor symmetry was successful at explaining the observed quantum numbers of hadrons, it did have a few difficulties. The existence of symmetric particle states, like the Ω^- (*sss*), the Δ^{++} (*uuu*), and the Δ^- (*ddd*), presented a conflict with the Pauli exclusion principle. Also, there were more available multiplets of the $SU(3)$ group than were observed in hadron species. This led Han and Nambu in 1965 to postulate the existence of an additional dynamical quantum number, *color*, associated with an exact SU(3) symmetry [11]. All hadrons were then assumed to be singlets under the new color quantum number, thus solving the symmetry problems.

Meanwhile, the SLAC–MIT deep inelastic scattering experiments in 1968 discovered scaling in the proton structure functions [12]. Using current algebra techniques, Bjorken [13] was able to explain this scaling in terms of point-like substructure in nucleons. At the same time, Feynman had developed the *parton model* to explain hadronic collisions [14]. This model introduces a probability distribution $f(x)$ for the proton to contain a point-like constituent (a parton) with fraction x of the proton momentum. The important ideas of the parton model were that the distribution $f(x)$ be independent of the particular scattering process and of the proton's total momentum and that the partons behave like quasi-free particles with little interaction among themselves. This latter property required the strong interaction to be *asymptotically free, i.e.,* as the distance scale of interaction becomes smaller (or equivalently as the momentum probing the interaction becomes larger), the interaction becomes weaker. This asymptotic behavior is exactly the opposite to that seen in quantum electrodynamics (QED). It took several years for the connection between partons and Gell-Mann's quarks to become accepted.

In 1973, Gross and Wilczek [6] and Politzer [7] laid the foundations of modern QCD by making the connection with non-commutative Yang–Mills theories [15] and demonstrating the asymptotic freedom of these theories. Yang–Mills theories had been studied earlier in the context of the weak interaction

and shown to be renormalizable[*] [17]. The non-commutative nature of these field theories gives rise to couplings among the gauge fields that make the interaction grow stronger with increasing distance, thus producing the asymptotic freedom that was needed in the strong interaction. In fact, only non-Abelian gauge theories can be both asymptotically free and renormalizable [18, 19]. QCD produced the first coherent model of quark dynamics. In this model quarks exist in the fundamental representation of the SU(3) color group, triplets, and the strong interaction is mediated by gauge fields called *gluons*, which exist in the adjoint representation of SU(3), octets. Only color singlets are allowed as free particles (*i.e.*, qqq or $q\bar{q}$), which can explain why quarks are not observed directly in any experiment.

Further evidence in favor of QCD came in 1975 when the Mark I collaboration at SPEAR observed a tendency for particle collimation ("jets") in e^+e^- annihilation as the center-of-mass energy was increased to 6.7 and 7.4 GeV [20]. Together with the observation that the angular distribution of these jet axes followed that expected for spin-$\frac{1}{2}$ fermions, this was accepted as evidence of underlying quark jets. The lower-energy e^+e^- collisions studied prior to then had produced generally isotropic hadronic events. Hadronic jets are interpreted as the manifestation of a hard interaction producing a high momentum q or $\bar{q}$. The quark dresses itself into a colorless form by producing many new $q\bar{q}$ pairs out of the vacuum. These quarks and antiquarks combine to make a "jet" of hadrons travelling roughly along the direction of the initial hard quark. A few years later, experiments at the 17-GeV PETRA ring reported three-jet events as well as two-jet events [21]. These were believed to represent $e^+e^- \rightarrow q\bar{q}g$ events. By this time, the quark-parton model was able to explain strong-interaction behavior in e^+e^-, lepton-hadron, and hadron-hadron collisions. In the years since then, all available experimental evidence has only served to support QCD as the theory of the strong interactions.

---

[*]In fact, the asymptotic freedom of Yang–Mills theories had been known a year earlier by 't Hooft, but remained unpublished. For an account of this, see [16].

2.2   The QCD Lagrangian

Following the example of QED, but keeping in mind the non-Abelian nature of SU(3), we may write the QCD Lagrangian as:

$$L_{QCD} = -\frac{1}{4}G^a_{\mu\nu}G^{a,\mu\nu} + \sum_k \bar{q}_k \left(i\gamma^\mu D_\mu - m_k\right)q_k, \tag{2.1}$$

where a represents the gluon color indices, k represents the different quark flavors, $G^a_{\mu\nu}$ is the gauge field strength tensor

$$G^a_{\mu\nu} \equiv \partial_\mu A^a_\nu - \partial_\nu A^a_\mu + g_s f^{abc} A^b_\mu A^c_\nu, \tag{2.2}$$

and D_μ is the generalized covariant derivative

$$D_\mu \equiv \partial_\mu - ig_s T^a A^a_\mu. \tag{2.3}$$

In these expressions, the A^a_μ are the gauge fields, q_k are the quark fields, g_s is the quark-gluon vertex coupling, the T^a are the SU(3) group generators, and the f^{abc} are the SU(3) Lie-algebra structure constants. The structure constants embody the non-Abelian aspects of the group and are defined by

$$[T^a, T^b] = i f^{abc} T^c. \tag{2.4}$$

2.3   Perturbative QCD

With the exception of lattice gauge theory [22], the only tool available for calculating observables directly from the QCD Lagrangian is perturbation theory. Fortunately, a consequence of asymptotic freedom is that the strong coupling constant $\alpha_s \equiv g_s^2/4\pi$ decreases with increasing momentum of interaction. Thus, hard processes lend themselves well to perturbation theory. Here "hard" means that the momentum scale Q^2 of the process is large compared to the fundamental scale of the strong interaction, Λ_{QCD}, which has value ~ 0.2 GeV (the precise

definition of Λ_{QCD} will be discussed below). At large scales, $Q^2 \gg \Lambda_{QCD}^2$, the strong coupling constant α_s becomes sufficiently small to allow perturbative expansions in α_s to be reliable, and the collimation of jets is strong enough that hard partons appear as distinct jets in the final state. Hence, we can identify these jets with quarks and gluons and use perturbation theory to describe the properties of events in terms of quark- and gluon-jets. Unfortunately, even at $Q^2 = M_{Z^0}^2$, the coupling constant is not all that small, $\alpha_s(M_{Z^0}^2) \simeq 0.12$, making the higher orders of the perturbative series not necessarily negligible. Furthermore, the non-Abelian nature of QCD leads to a large number of Feynman diagrams, even at low loop order. In addition, higher multiplicities of jets in the final state also complicate the calculations in a similar manner. These factors all make perturbative QCD calculations much more difficult than their QED analogs.

A particularly nice environment in which to study QCD exists in e^+e^- annihilation at high energies. This is because the initial state has only electroweak interactions and can be calculated to high accuracy. The strong interaction is thus involved only in the final state. Furthermore, if the initial-state e^+e^- energy, $\sqrt{s}$, is high enough ($\sqrt{s} \gg 0.2$ GeV), then the interaction is sufficiently asymptotic that we may apply perturbation theory reliably, at least for observables that are insensitive to the infrared structure of the theory.

A conventional view of e^+e^- scattering, for example at the SLC, is shown in Fig. 2.1. The $e^+e^- \rightarrow hadrons$ reaction can be thought of as proceeding via four stages. In the first stage (*i*), we have the *hard scattering* process of $e^+e^- \rightarrow q\bar{q}$. This stage can be calculated from electroweak physics, for which perturbative calculations can be performed to high accuracy. In stage (*ii*), perturbative QCD can be used to calculate modifications to the (tree-level) result of stage (*i*). We call the end result of this stage the *parton level*. Next is stage (*iii*) in which the partons (quarks or gluons) become bound into colorless hadrons. This stage is known as *hadronization* or *fragmentation* and is fundamentally non-perturbative. The boundary between stage (*ii*) and stage (*iii*) must occur at scales around Λ_{QCD}. Finally, we have stage (*iv*), where the hadrons produced
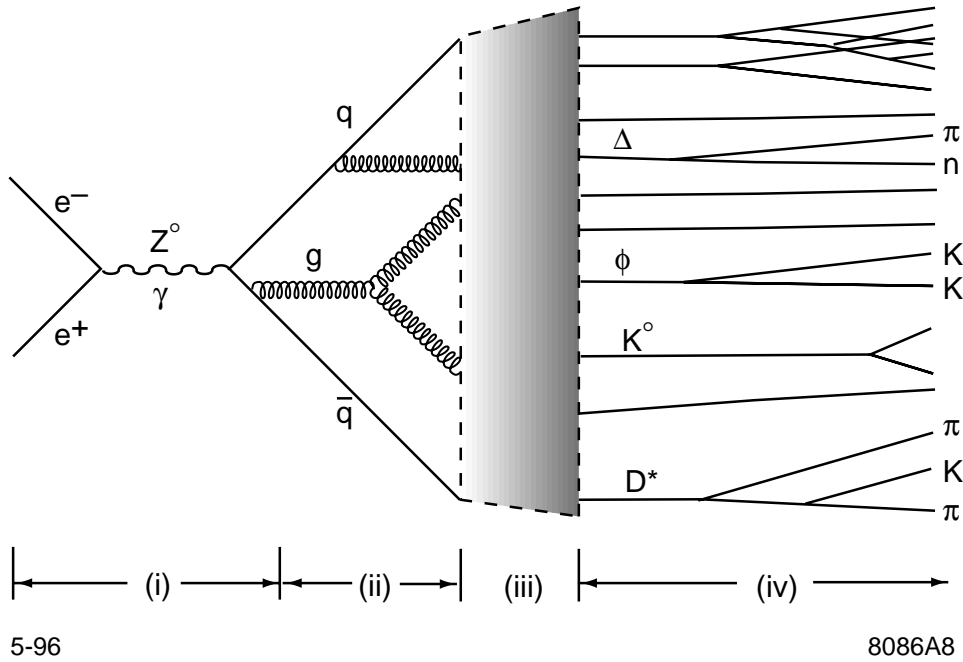
Figure 2.1: The stages of a typical $e^+e^- \to hadrons$ interaction are shown.

in stage (*iii*) may decay to lighter hadrons. The boundary between these two stages depends on which strongly-decaying resonances one wishes to consider part of the hadronization process and which part of the final state. The decay rates of these resonances are generally well-measured, and thus stage (*iv*) can be modelled accurately from purely phenomenological input. Stage (*ii*) will be discussed in the remainder of this section, and stage (*iii*) in the following section. The other two stages are well-understood from the theory of electroweak interaction or from phenomenology, so we omit discussion of their details.

2.3.1   Renormalization

In most perturbative calculations with field theories, there exist divergences that need to be removed in order to obtain physical results. These exist even in quantum electrodynamics. Typically, they arise from the assumption that particles are localized at one point in space-time and have no extent.

The standard technique of removing divergences is known as *renormalization*. In QED, for example, there are divergent self-coupling diagrams for the electron. We renormalize the theory by calling the coupling that appears in the Lagrangian a *bare* coupling, e_0, and noting that this bare coupling is not observable in nature. Only the amplitudes for physical processes are observable, and so we must choose one of these processes to define our physical coupling, e. The Thomson scattering of the electron is usually chosen. If we calculate this process in perturbation theory, we get a divergent answer; however, we can simply absorb divergences into the bare coupling e_0 and into wavefunction renormalization factors Z_ψ and Z_A, and *renormalize* the theory to be finite. Theories for which the bare couplings and wavefunction renormalizations are sufficient to absorb divergences at all orders of perturbation theory are said to be *renormalizable*. Not all theories are renormalizable (for example, the simple scalar $\lambda \phi^6$ theory is not), but 't Hooft showed in 1971 that all Yang–Mills gauge theories are renormalizable [17].

A particular computational technique of renormalization, that of *dimensional regularization* [23], is especially useful for QCD because it preserves the gauge invariance of the theory. This is in contrast to simpler techniques, such as assigning a cutoff to internal loop momenta. The dimensional regularization technique consists of analytically continuing loop integrals from 4 dimensions to $4 - 2\varepsilon$ dimensions. In the limit that $\varepsilon \to 0$, one recovers the original divergences as poles in ε. In order to preserve the units of the interaction terms in the Lagrangian, though, the g_s couplings are replaced with $\mu^\varepsilon g_s$, where μ is an arbitrary scale parameter.

This technique still must be coupled with a particular prescription of how to define the physical coupling g_s, or equivalently $\alpha_s = g_s^2/4\pi$, which now becomes a function of the arbitrary scale μ. The most commonly used prescription is the *modified minimal subtraction* or $\overline{MS}$ scheme [24]. In any perturbative calculation at finite order in α_s, however, there is a residual dependence on μ, which one must address. There are other prescriptions for renormalization which claim advantages for particular situations [25, 23], there are various

prescriptions for choosing the scale μ [26, 27, 28], and there is an extensive literature on this subject (for a summary, see [29]).

All renormalization prescriptions have in common the feature that any physical observable is independent of the scale parameter μ if the calculation could be carried out to all orders of perturbation theory. This can be expressed in the *renormalization group equation* [30]:

$$\left[\mu \frac{\partial}{\partial \mu} + \beta(g_s) \frac{\partial}{\partial g_s} - n\gamma(g_s) \right] \Gamma_R^{(n)} = 0, \tag{2.5}$$

where $\Gamma_R^{(n)}(p_i, g_s, \mu)$ is the Green's function for the n-particle amplitude, the p_i are the four-momenta of the external particles, and the β-*function*, $\beta(g)$, and the *anomalous dimension*, $\gamma(g)$, are defined as:

$$\beta(g_s) \equiv \mu \frac{\partial g_s}{\partial \mu} \tag{2.6}$$

$$\gamma(g_s) \equiv -\frac{\mu}{2Z_\Gamma} \frac{\partial Z_\Gamma}{\partial \mu}. \tag{2.7}$$

Expanding Eq. (2.6) for the scale-dependence of the coupling and switching from g_s to α_s, we get

$$\beta(\alpha_s) \equiv \mu \frac{\partial \alpha_s}{\partial \mu} = -\frac{\beta_0}{2\pi} \alpha_s^2 - \frac{\beta_1}{4\pi^2} \alpha_s^3 - \frac{\beta_2}{64\pi^3} \alpha_s^4 - \ldots \tag{2.8}$$

For the specific case of SU(3) QCD, we have:

$$\beta_0 = 11 - \frac{2}{3} n_f \tag{2.9}$$

$$\beta_1 = 51 - \frac{19}{3} n_f, \tag{2.10}$$

where n_f is the number of active fermions contributing to internal loops. The β_2 and subsequent terms are dependent on the specific renormalization scheme chosen.

The solution to Eq. (2.8) to first order is

$$\alpha_s(\mu^2) = \frac{4\pi}{\beta_0 \log \frac{\mu^2}{\Lambda^2}}, \tag{2.11}$$

where Λ is the fundamental QCD scale Λ_{QCD}, defined as the scale at which α_s ceases to be small ($\lim_{\mu^2 \to \Lambda^2} \alpha_s(\mu^2) = \infty$). If we continue the expansion to next-to-leading (NLO) order in Eq. (2.8), we may write:

$$\alpha_s(\mu^2) = \frac{4\pi}{\beta_0 \log \frac{\mu^2}{\Lambda^2}} \left(1 - \frac{2\beta_1}{\beta_0^2} \frac{\log\left(\log \frac{\mu^2}{\Lambda^2}\right)}{\log \frac{\mu^2}{\Lambda^2}}\right). \tag{2.12}$$

Because the higher order terms of Eq. (2.8) depend on the renormalization scheme, Λ becomes scheme-dependent at higher order, so we generally speak about Λ for a specific scheme, *e.g.* $\Lambda_{\overline{MS}}$. Current experimental measurements put $\Lambda_{\overline{MS}}$ on the order of 200 MeV/c [2].

2.3.2 Fixed Order Matrix Elements

We now consider the perturbative calculation of observables for hadronic jets in e^+e^- annihilation. Although the total cross section has been calculated to $O(\alpha_s^3)$ [31], all other observables are only available to second order in α_s. As described earlier, the tree level cross section for $e^+e^- \to q_k \bar{q}_k$ is given by electroweak physics. The only input from QCD at tree level is the number of colors N_c. The electroweak Born cross section is given by

$$\sigma_0 = \frac{4\pi\alpha^2}{3s} N_c R_{q_k}(s), \tag{2.13}$$

where α is the electromagnetic fine structure constant, s is the square of the CM energy, and $R_{q_k}(s)$ is the ratio to the lowest order QED cross section, which

includes contributions from the γ and Z^0 propagators and their interference:

$$
\begin{aligned}
R_{q_k}(s) = {} & e_{q_k}^2 + 2(v_e - a_e P_e) e_{q_k} v_{q_k} \operatorname{Re} \chi(s) \\
& + (v_e^2 + a_e^2)(v_{q_k}^2 + a_{q_k}^2)(1 - A_e P_e) \, |\chi(s)|^2 \, .
\end{aligned}
\tag{2.14}
$$

Here, $\chi(s)$ is the ratio of the Z^0 and γ propagators

$$
\chi(s) = \frac{1}{4 \sin^2 2\theta_W} \frac{s}{s - M_Z^2 + i\Gamma_Z M_Z} \, .
\tag{2.15}
$$

In these expressions, e_{q_k} is the charge of the quark flavor q_k, θ_W is the Weinberg weak mixing angle, M_Z and Γ_Z are the mass and width of the Z^0, v_i and a_i are the vector and axial-vector electroweak couplings of fermion i, $A_i \equiv 2 v_i a_i / (v_i^2 + a_i^2)$, and P_e is the polarization of the incident electron beam ($P_e = +1$ for right-handed e^-). The polarization of the incident positrons is assumed to be zero. In the Standard Model, $a_e = -1$, $v_e = -1 + 4\sin^2 \theta_W$, $a_{q_k} = +1$ and $v_{q_k} = 1 - \frac{8}{3}\sin^2 \theta_W$ for $q_k = u, c, t$, while $a_{q_k} = -1$ and $v_{q_k} = -1 + \frac{4}{3}\sin^2 \theta_W$ for $q_k = d, s, b$. In the limit where $s \simeq M_Z^2$, we can take

$$
R_{q_k}(s) = \frac{(v_e^2 + a_e^2)(v_{q_k}^2 + a_{q_k}^2)(1 - A_e P_e)}{16 \sin^4 2\theta_W} \frac{s}{(s - M_Z^2)^2 + \Gamma_Z^2 s^2 / M_Z^2} \, .
\tag{2.16}
$$

The angular distribution of the electroweak cross section is given by

$$
\frac{d\sigma}{d\Omega} = \frac{3\sigma_0}{16\pi} \left[1 + \cos^2 \theta + 2 A_{q_k} \frac{A_e - P_e}{1 - A_e P_e} \cos \theta \right] ,
\tag{2.17}
$$

where θ is the angle between q_k and the incoming e^- beam. The $\cos\theta$ term in this expression gives a parity-violating forward-backward asymmetry even when the electron polarization is zero. At the SLC, however, we may produce a larger asymmetry by varying the electron polarization and considering the left-right forward-backward asymmetry

$$
\widetilde{A}_{FB}^{q_k} = \frac{N_{LF} - N_{RF} - N_{LB} + N_{RB}}{N_{LF} + N_{RF} + N_{LB} + N_{RB}} = \frac{3}{4} |P_e| A_{q_k} ,
\tag{2.18}
$$

where N_{LF} is the number of events observed with left-handed electron polarization ($P_e < 0$) and with q_k in the forward hemisphere ($\cos\theta > 0$), and so forth for the other combinations.

If we consider the three-jet process $e^+e^- \rightarrow q\bar{q}g$, we may now see effects proportional to α_s. To leading order, the cross section for three-jet production in the massless quark limit is given by [32]:

$$\frac{d\sigma}{dx_1 dx_2} = \sigma_0 \cdot \frac{\alpha_s}{2\pi} C_F \frac{x_1^2 + x_2^2}{(1-x_1)(1-x_2)}, \qquad (2.19)$$

where σ_0 is the Born cross section above, $C_F = 4/3$ is the quark color factor, and x_1 and x_2 are the scaled quark jet energies ($x_i \equiv 2E_i/\sqrt{s}$). This cross section diverges in the collinear limit where $x_1 \rightarrow 1$ or $x_2 \rightarrow 1$, but in this regime three-jet final states are indistinguishable from two-jet states, and corresponding divergences in the one-loop propagator and vertex corrections cancel the collinear divergences.

One can go on to calculate a higher multiplicity of final-state jets at tree order [33], or to calculate the two-jet or three-jet cross sections at higher order [34, 35, 36, 37]. The calculations involve many Feynman diagrams and the formulas are complex (so we do not reproduce them here). However, the two-jet and three-jet calculations are only available to $O(\alpha_s^2)$ at present. As a result, one should not expect matrix element calculations to describe well the details of e^+e^- reactions where multiple gluon emissions play an important role, such as four-jet or higher final states.

2.3.3 Parton Shower

Another approach to calculating perturbative QCD processes which does a better job of reproducing the soft structure of jets is the method of *parton showers*, which leads to a simple technique of calculation, particularly in iterative computer programs. This method is based on the *leading logarithm approximation* (LLA) to perturbative QCD, where leading logarithmic terms
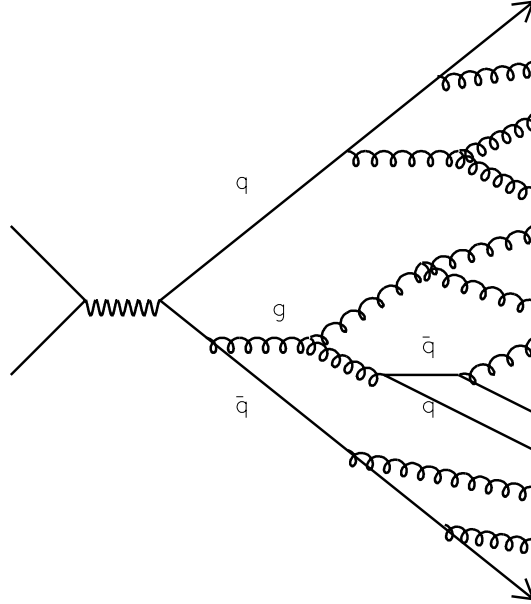
Figure 2.2: A typical diagram of partons produced by a parton shower model.

$\alpha_s^n(Q^2)\log^n(Q^2/\Lambda^2)$ are summed to all orders n. This approximates the calculation of the soft structure of jets down to scales $\sim \Lambda_{QCD}$. Refinements that include sub-leading terms are also possible (we discuss one of these in section 2.3.4).

In the parton shower approach, the production of partons is viewed as a Markov chain of successive branching of off-shell partons: $q \to qg$, $g \to gg$, or $g \to q\bar{q}$, as shown in Fig. 2.2. In the LLA, it is possible to treat these branchings as classical probabilities (*i.e.*, no interference) [38]. In the splitting process $a \to bc$, we let τ represent the virtuality scale of a (*e.g.* $\tau = \log Q^2/\Lambda^2$, with Q^2 the four-momentum squared of a), and we denote by z the fraction of the parent's momentum carried away by daughter b. Then the evolution of the probability $P_{a \to bc}$ that a branching $a \to bc$ will take place during the virtuality interval $(\tau, \tau + d\tau)$ is given by the Dokshitzer–Gribov–Lipatov–Altarelli–Parisi (DGLAP)

equation [38, 39, 40]

$$\frac{dP_{a \to bc}}{d\tau} = \int dz \, \frac{\alpha_s(\tau)}{2\pi} P_{ba}(z), \tag{2.20}$$

where the scale-independent splitting functions P_{ba} are given by:

$$\begin{aligned}
P_{qq}(z) &= \frac{4}{3}\frac{1+z^2}{1-z} \\
P_{gq}(z) &= \frac{4}{3}\frac{1+(1-z)^2}{z} \\
P_{gg}(z) &= 6(\frac{1-z}{z} + \frac{z}{1-z} + z(1-z)) \\
P_{qg}(z) &= \frac{1}{2}(z^2 + (1-z)^2).
\end{aligned} \tag{2.21}$$

The probability that a parton starting with virtuality τ_{max} will reach τ without undergoing any splittings is then given by the Sudakov factor $S_a(\tau)$:

$$P_{\text{no-emission}}(\tau_{max}, \tau) = \exp\left(-\int_\tau^{\tau_{max}} d\tau' \, \frac{dP_{a \to bc}}{d\tau'}\right) = \frac{S_a(\tau_{max})}{S_a(\tau)} \tag{2.22}$$

$$S_a(\tau) = \exp\left(-\int_{\tau_0}^\tau d\tau' \int_{z_{min}(\tau')}^{z_{max}(\tau')} dz \, \frac{\alpha_s(Q^2)}{2\pi} P_{ba}(z)\right), \tag{2.23}$$

where $\tau_0 \equiv \log Q_0^2/\Lambda^2$ and Q_0 is a shower virtuality cutoff, z_{max} and z_{min} are kinematic cutoffs based on the virtuality τ'. This Sudakov factor can be pretabulated in Monte Carlo programs, and the evolution of any individual parton can then be determined by finding τ such that

$$S_a(\tau) = \frac{S_a(\tau_{max})}{R}, \tag{2.24}$$

where R is a random number between 0 and 1.

The main parameters of parton shower models are the virtuality cutoff Q_0 and the scale Λ.* Various parton shower models differ in their choice of the

---

*Because the parton shower calculation is not complete at any order in α_s, however, it is not possible to relate the parton shower Λ to the standard $\Lambda_{\overline{MS}}$ (or any other Λ_{QCD}).

virtuality parameter τ, in their choice of the scale Q^2 for the running of α_s, and in their definition of z (*e.g.* ratio of energy, longitudinal momentum, or light-cone momentum). In general, parton shower calculations give a poor approximation for the hard three-jet rate, but this can be improved by matching the first stages of parton shower branching with a matrix element calculation. In addition, the inclusion of sub-leading logarithms may modify Eq. (2.21) to an extra order in α_s in the case of the *next-to-leading logarithm approximation* (NLLA) [41], or it may impose the additional constraint of angular ordering on the gluon emissions in the case of the *modified leading logarithmic approximation* [42] discussed below.

2.3.4 Modified Leading Logarithmic Approximation

A refinement of the LLA parton shower technique was put forward by Dokshitzer and Troyan [42]. This *modified leading logarithmic approximation* (MLLA) is built upon the *double logarithmic approximation* (DLA) [43], which resums only terms of order $\alpha_s^n(Q^2)\log^{2n}(Q^2/\Lambda^2)$ and is useful for qualitative predictions of spectra but is only useful quantitatively for calculations of the evolution of hadron multiplicities. In the MLLA, single logarithmic terms $\alpha_s^n(Q^2)\log^n(Q^2/\Lambda^2)$ are included in a consistent fashion via angular ordering.

The prediction of MLLA is for the parton (gluon) spectrum in a hard gluon jet. This is given by [42]:

$$x_p\bar{D}_g^g(\xi,Y,\lambda) = \frac{4N_c(Y+\lambda)}{bB(B+1)}\int_{\varepsilon-i\infty}^{\varepsilon+i\infty}\frac{d\omega}{2\pi i}\,x_p^{-\omega}\,K(\omega,\lambda)$$
$$\times\,\Phi(-A+B+1,B+2,-\omega(Y+\lambda)),\quad \text{(2.25)}$$

where $Y=\log(E/Q_0)$, $\lambda=\log(Q_0/\Lambda)$, $\xi=\log(1/x_p)$, $a=(\frac{11}{3}N_c+\frac{2}{3}n_f/N_c^2)$, $b=\frac{11}{3}N_c-\frac{2}{3}n_f$, $A=4N_c/b\omega$, $B=a/b$, $N_c=3$, and

$$K(\omega,\lambda)\equiv\frac{\Gamma(A)}{\Gamma(B)}(\omega\lambda)^B\,\Psi(A,B+1,\omega\lambda).\qquad \text{(2.26)}$$

For three massless quark flavors, $b = 9$, $A = 4/3\omega$, and $B = 101/81$. The functions Φ and Ψ are the two degenerate solutions of the confluent hypergeometric equation. In these expressions, Λ is the QCD scale parameter, and Q_0 is the energy cutoff of the parton evolution ($x_p > Q_0/E$). The integration contour over ω goes parallel and to the right-hand side of the imaginary axis. If we want instead the fragmentation of quarks to gluons $\bar{D}_q^g(x_p, Y, \lambda)$, we can simply multiply by $4/9 = C_F/C_A$.

If our aim is to calculate the spectrum of light hadrons, such as $\pi^{\pm}$, in the context of local parton-hadron duality (see section 2.4.3), we might choose the cutoff Q_0 to approach Λ (since $M_\pi \sim \Lambda$). In this case, $\lambda \to 0$, and we get the *limiting spectrum* [42]:

$$\bar{D}_g^0(\xi, Y) = \frac{4N_c}{b}\Gamma(B)\int_{-\pi/2}^{\pi/2}\frac{d\tau}{\pi}e^{-B\alpha}\left[\frac{\cosh\alpha + (1-2\zeta)\sinh\alpha}{\frac{4N_c}{b}Y\frac{\alpha}{\sinh\alpha}}\right]^{B/2}$$

$$\times I_B\left(\sqrt{\frac{16N_c}{b}Y\frac{\alpha}{\sinh\alpha}[\cosh\alpha + (1-2\zeta)\sinh\alpha]}\right), \quad (2.27)$$

in which $\alpha = \alpha_0 + i\tau$, for $\tanh\alpha_0 = 2\zeta - 1$ and $\zeta = 1 - \xi/Y$, and $I_B(z)$ is the modified Bessel function of order B. This spectrum can be approximated by a distorted Gaussian [44]:

$$x_p\bar{D}_q^0(\xi) \sim \frac{N(Y)}{\sqrt{2\pi}\sigma}\exp\left[\frac{1}{8}k - \frac{1}{2}s\delta - \frac{1}{4}(2+k)\delta^2 + \frac{1}{6}s\delta^3 + \frac{1}{24}k\delta^4\right], \quad (2.28)$$

with $\delta \equiv (\xi - \xi^*)/\sigma$,

$$N(Y) = \Gamma(B)\left[\frac{4N_c}{b}Y\right]^{\frac{-B+1}{2}}I_{B+1}\left(\sqrt{16N_cY/b}\right), \quad (2.29)$$

and

$$\xi^* = \frac{Y}{2}\left(1 + \frac{a}{24}\sqrt{\frac{48}{bY}} + O(Y^{-1})\right) \quad (2.30)$$

$$\sigma = \sqrt{\frac{Y}{3}} \left(\frac{bY}{48}\right)^{1/4} \left(1 - \frac{b}{64}\sqrt{\frac{48}{bY}} + O(Y^{-1})\right) \tag{2.31}$$

$$s = -\frac{a}{16}\sqrt{\frac{3}{Y}} \left(\frac{48}{bY}\right)^{1/4} + O(Y^{-5/4}) = -\frac{a}{16}\frac{1}{\sigma} \tag{2.32}$$

$$k = -\frac{27}{5Y} \left(\sqrt{\frac{bY}{48}} - \frac{b}{24} + O(Y^{-1/2})\right). \tag{2.33}$$

Thus, the parton spectrum in jets (in the limit $Q_0 \simeq \Lambda$) is expected to have an approximate Gaussian shape in $\xi = \log(1/x_p)$, often referred to as a "hump-backed" shape, due to the underlying parton dynamics. The development of the parton shower causes the parton multiplicity to rise with increasing ξ, but this development ceases at some cutoff scale, Q_0, where hadronization takes over, and the spectrum decreases at the soft limit. As the center of mass energy increases, the maximum of this distribution, ξ^*, shifts toward higher ξ, approximately linearly in Y (*i.e.*, $\log E$).

2.4   Hadronization

Since no free quarks have ever been observed directly by experiment [45], any complete theory of strong interactions must explain why quarks exist only in color-singlet hadrons. This characteristic is known as *confinement*. Although the asymptotic freedom of QCD implies that as the distance between two quarks increases, their coupling increases, it has not been rigorously proven that SU(3) QCD implies confinement. In the absence of a theoretical explanation of confinement, we seek experimental constraints on the process of hadronization. One phenomenological framework for these constraints is that of *fragmentation functions*.

2.4.1   Fragmentation Function

The process by which free quarks and gluons become the hadrons that we observe in nature is known as *hadronization* or *fragmentation*. In principle,

this process is determined by the (unknown) dynamics of confinement. Let us define the particle spectrum for a hadronic species h at CM energy $\sqrt{s}$ as $F^h(x,s)$. We can then express this spectrum in terms of *fragmentation functions* $D^h_k(z,\mu^2)$:

$$F^h(x,s) \equiv \frac{1}{\sigma_{tot}} \frac{d\sigma}{dx}(e^+e^- \to hX) = \sum_k \int_x^1 \frac{dy}{y} C_k(s,y,\alpha_s(\mu^2)) D^h_k(\frac{x}{y},\mu^2), \qquad (2.34)$$

where σ_{tot} is the total hadronic cross section ($e^+e^- \to X$), $x = 2E_h/\sqrt{s}$ is the scaled energy of h, k represents primary parton flavor, y is the scaled momentum of the parent k that produces hadron h, and $C_k(s,y,\alpha_s(\mu^2))$ is the production of parton species k with scaled energy $y = 2E_k/\sqrt{s}$. At lowest order,

$$C_k(s,y,\alpha_s) = \frac{\sigma(e^+e^- \to q_k\bar{q}_k)}{\sigma_{tot}}. \qquad (2.35)$$

The fragmentation functions $D^h_k(z,\mu^2)$ can be shown to obey a DGLAP evolution equation [46]:

$$\frac{1}{\mu^2} \frac{\partial}{\partial\mu^2} D^h_k(z,\mu^2) = \frac{\alpha_s(\mu)}{2\pi} \sum_j \int_z^1 \frac{dy}{y} P_{jk}(y) D^h_j\left(\frac{z}{y},\mu^2\right), \qquad (2.36)$$

where j ranges over all parton species. The fragmentation function also obeys certain other relations. First, from energy conservation in the event, we can see that

$$\sum_h \int_0^1 dz\, z D^h_k(z,\mu^2) = 1. \qquad (2.37)$$

Second, if we define $\bar{n}_h$ as the average multiplicity of particle type h per event, we have

$$\sum_k \int_{z_{min}}^1 dz\, D^h_k(z,\mu^2) = \bar{n}_h, \qquad (2.38)$$

where $z_{min} \equiv 2M_h/\sqrt{s}$. Finally, we might expect certain relations from CP

conservation or isospin symmetry. For example

$$D_k^h(z,\mu^2) = D_{\bar{k}}^{\bar{h}}(z,\mu^2) \tag{2.39}$$

$$D_u^{\pi^+}(z,\mu^2) = D_{\bar{d}}^{\pi^+}(z,\mu^2) \tag{2.40}$$

$$D_u^{\pi^+}(z,\mu^2) = D_d^{\pi^-}(z,\mu^2) \tag{2.41}$$

$$\cdots$$

The fragmentation functions $D_k^h(z,\mu^2)$ are the basic features that we would like to probe experimentally. Unfortunately, we cannot identify the individual partons that hadronize and thus cannot measure the $D_k^h(z,\mu^2)$ directly. Traditionally, only the inclusive spectra $F^h(x)$ were experimentally accessible. With heavy-flavor tagging, however, we can separate light-quark (uds) events from the $e^+e^- \to b\bar{b}$ or $c\bar{c}$ events. This is important because it is known experimentally that fragmentation in heavy-quark jets differs from that in light-quark jets [47]. Furthermore, we can use the polarization of the SLC electron beam, together with the electroweak forward-backward asymmetry of quarks (Eq. (2.17)), to separate quark from antiquark jets. This can provide constraints on $D_k^h(z,\mu^2) - D_{\bar{k}}^h(z,\mu^2)$, for $k = u, d, s$.

2.4.2 Hadronization Models

Currently, there is no complete theory of the non-perturbative process of fragmentation that derives from QCD. Therefore, we necessarily rely on models. This is not, however, a failing of QCD so much as it is a failing of our (current) calculational techniques. Furthermore, these models are motivated in many ways by features of QCD, so they are not entirely *ad hoc*. Hadronization models can be tested against a large number of experimental properties, both exclusive and inclusive. Accurately predicting these properties, without an infinite number of adjustable parameters, is the acid test of hadronization models. Moreover, good models of hadronization are important not only because they represent our best understanding of hadronization, but also because

they represent nature well enough to serve as a good simulation of particle physics experiments. In modern collider experiments, such simulation is essential for understanding detector performance. A more detailed overview of hadronization models is available in [48].

Independent Fragmentation

The earliest models of fragmentation were introduced by Field and Feynman in 1978 and were based on the idea that each parton fragments independently via a recursive scheme [49]. In the independent fragmentation (IF) model, a primary quark q_1 may start by combining with an antiquark $\bar{q}_2$ from a pair $q_2\bar{q}_2$ created out of the vacuum. The meson M_1 formed from $q_1\bar{q}_2$ has longitudinal momentum fraction $z_1 = (E + p_\parallel)_{M_1}/(E + p_\parallel)_{q_1}$ distributed according to some *fragmentation function* $f(z_1)$. Next, the remaining q_2 combines with a $\bar{q}_3$, and the resulting meson M_2 has momentum fraction $z_2 = (E + p_\parallel)_{M_2}/(E + p_\parallel)_{q_2}$. The IF *ansatz* is that $z_1, z_2, \ldots$ are distributed according to the same universal function $f(z)$. The process continues until there is insufficient energy to create any more hadrons. If the initial jet is a gluon, one can either convert it to a quark jet of random flavor, or one can split it into two quark jets via a DGLAP splitting kernel, Eq. (2.21).

In addition to the above prescription for longitudinal momentum, one also needs to generate transverse momentum for the produced hadrons. Typically, this is done with a Gaussian distribution $\exp(-p_T^2/2\sigma_T^2)$, where the width σ_T is chosen ~ 300 MeV/c to match experimental data. There is nothing in the IF prescription to specify the hadron species produced, so some sort of *ad hoc* scheme is introduced. One can introduce suppression factors for the various quark flavors to be created from the vacuum:

$$u : d : s : c : b \simeq 1 : 1 : \gamma_s : 0 : 0, \tag{2.42}$$

motivated by the difference in quark masses. One can also introduce similar

factors for pseudoscalar, vector, and tensor mesons:

$$P : V : T \simeq 1 : \gamma_V : \gamma_T. \tag{2.43}$$

The original Field–Feynman model only treated mesons, but one can introduce baryons by adding another suppression factor, γ_B, for the probability of producing a pair of diquarks out of the vacuum instead of a $q\bar{q}$ pair [50]. All of these parameters (γ_s, γ_V, γ_T, γ_B) are to be determined by tuning the model to match experimental data. Typical values used are:

$$\gamma_s \simeq 0.3 \qquad \gamma_B \simeq 0.1 \tag{2.44}$$

$$\gamma_V \simeq 1 \qquad \gamma_T \simeq 0. \tag{2.45}$$

The tensor mesons had not been observed in e^+e^- until recently, and the rates of their production are low; therefore, models generally neglect them. Although one might naively expect $\gamma_V = 3$ from spin-counting, experimental observations support roughly equal production of pseudoscalar and vector mesons [51]. The baryon production fraction of 10% reproduces the multiplicities of baryons reasonably well, but more complex dynamics (such as the *popcorn mechanism* where baryons and antibaryons are separated in the fragmentation chain by one or more mesons [52]) are required to reproduce spectra.

Thus, for any given hadron species h, this model predicts a fragmentation function

$$D_k^h \left(z,\mu^2\right) = \eta\, f(z) + \eta \int_z^1 \frac{dy}{y} f(1-y) D_k^h \left(\frac{z}{y},\mu^2\right), \tag{2.46}$$

where η is a factor that takes into account the *ad hoc* hadron species selection parameters. A typical $f(z)$ is the Field and Feynman function

$$f(z) = 1 - a + 3a(1 - z^2), \tag{2.47}$$

with a a tunable parameter.

Although the IF model is conceptually very simple, it has one important theoretical problem in that it is impossible to conserve both longitudinal momentum and energy in a single independent jet[*]. Therefore, IF models have some additional *ad hoc* prescriptions for rescaling momenta or otherwise fixing up momentum conservation.

Despite these problems, IF does a good job at reproducing global jet properties [53]. However, with more recent measurements of the string effect in e^+e^- annihilation, as discussed below, we can now consider this class of models excluded. Nevertheless, they are still useful, for example in $p\bar{p}$ Monte Carlos, where details of the soft structure of jets are of less interest.

String Models

A refinement of the independent fragmentation technique is the *string model*, originally presented by Artru and Mennessier [54], but extended in the popular JETSET event generator of Andersson, Gustafson, and Sjöstrand at Lund University [55, 56]. This model is motivated by the idea of color flux tubes as a model for confinement. The color flux tube acts like a string with uniform energy density per unit length. Thus, as two quarks separate, they stretch such a string between them, and the potential energy rises linearly with separation distance. Eventually the string energy is sufficient to create a $q\bar{q}$ pair from the vacuum, and thus fragment the string into two pieces. These two pieces are still expanding strings, so the process repeats until all remaining string energy is lower than hadronic masses.

For the case of $q\bar{q}$ pair production ($e^+e^- \rightarrow q\bar{q}$), the string models proceed very much like IF models with similar *ad hoc* parameters for determining hadron flavor. Energy and momentum are conserved, however, at each step of the fragmentation in string models, so there is no rescaling procedure at the end of the fragmentation process. Furthermore all quark quantum numbers are conserved globally.

---

[*]It is also impossible to conserve charge, baryon number, strangeness, *etc.*, but this is perhaps less troublesome since the quark selection is done in an *ad hoc* scheme.

The Lund group initially employed a fragmentation function

$$f(z) = \frac{\alpha + 1}{z}(1 - z)^{\alpha}, \tag{2.48}$$

with α as an adjustable parameter. This function, however, did not reflect the fact that all $q\bar{q}$ production vertices are causally disconnected, and therefore their time-ordering is Lorentz frame-dependent. Thus, all vertices should be treated symmetrically so that it is possible to start from either end of the string and get the same answer. This led to the "left-right symmetric" fragmentation function

$$f(z) = \frac{(1 - z)^{a}}{z} \exp(-bM_T^2/z), \tag{2.49}$$

where $M_T^2 = M^2 + p_T^2$ is the transverse mass of the hadron, and a and b are free parameters. This simplifies the program implementation since the string breakup can be done starting at either end and proceed consistently along the string.

String fragmentation must be combined with some perturbative calculation of the underlying hard process, typically either a second-order matrix element calculation [56] or an LLA parton shower [57]. If the event contains a hard gluon jet, the gluon acts as a "kink" in the string with one half of the string connected to each of the remaining quark/antiquark jets (see Fig. 2.3). The JETSET matrix element model uses the GKS $O(\alpha_s^2)$ calculations [35].

In the case of the JETSET parton shower model, the shower evolution is performed with respect to the mass squared, $\tau = m^2$, and z is interpreted as the energy fraction in the center of mass of frame of the parent parton. The scale of the running α_s is set to $Q^2 = z(1 - z)m^2 \simeq p_T^2$. Angular ordering is imposed as an extra constraint on the mass and z values of each branching. Once the parton shower evolves to its cutoff, the fragmentation string is connected between the partons in the order that they were produced from the parton shower, with each gluon acting as a kink, and $q\bar{q}$ pairs dividing the string. This is not the only possible way to connect the partons with a string, but represents the most
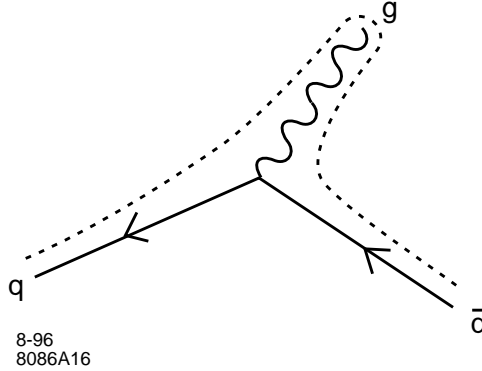
Figure 2.3: String fragmentation in a $q\bar{q}g$ event. The string is stretched between the quark and antiquark, with the gluon acting as a "kink" in the string.

straightforward choice. The JETSET parton shower model has been tuned to reproduce well most experimental observables in e^+e^- data [58], but the large number of parameters necessary lessens our ability to constrain the underlying dynamics of the model.

The connection of the string between the various jets produces a natural effect on the hadron flow in the regions between jets. We might expect, for example, the region between the q and $\bar{q}$ jets in Fig. 2.3 to be less populated than the region between either and the g jet. This so-called "string effect" has been observed at PETRA [59] and also at LEP [60]. However, it has been shown that the "string effect" can be explained on the basis of soft gluon interference in the MLLA framework [61], so it is not really a confirmation of the string model. Nevertheless, the experimental observation requires successful hadronization models to reproduce it.

UCLA Model

The UCLA model of Buchanan and Chun [62] is an extension of the Lund string model with the hadron species parameters determined by phase-space, spin counting, and isospin counting. In the JETSET scheme, M_h and p_T are chosen first, and then z is drawn from $f(z)$, where $\int f(z)dz = 1$ for *each* hadronic species.

In the UCLA model, $f(z)$ is a universal function with $\sum_h \int f^h(z)dz = 1$. Thus a and b remain free parameters, but all of the suppression of vector and strange mesons and baryons is accomplished through the increased masses of those particles and Clebsch–Gordon coefficients for the coupling of spins. This model has had remarkable success in fitting a wide range of data, but agreement is not perfect. In particular, the production of baryons is not entirely well-reproduced and is still an area of development [63].

Color Dipole Models

Another relative of the Lund string model is the color dipole model of Gustafson and Pettersson [64]. The standard implementation of this model is the ARI-ADNE program [65]. In the color dipole model, a parton shower is described in terms of the splittings of color dipoles formed between partons. Instead of the usual angular ordering (as in JETSET PS), this imposes an ordering on the transverse momentum $p_\perp^2$ of the radiated gluons. This shower evolution is cut off at some scale, Q_0, and the resulting partons are hadronized via the standard JETSET string scheme. The general features of ARIADNE are similar to those of the JETSET parton shower model, but the details of the dynamics are different.

Cluster Models

Cluster models represent a very simple model of hadronization where the partons present at the end of the perturbative process are combined into "colorless clusters" [66]. Because second-order matrix elements cannot yield more than four partons, cluster models are invariably combined with parton shower calculations. The most successful of these models has been the HERWIG Monte Carlo of Marchesini and Webber [67], which includes soft gluon interference via a MLLA framework with angular ordering of gluon bremsstrahlung.

In the HERWIG model, the parton shower evolution variable is $\tau = E_a^2 \xi$, where $\xi = p_b \cdot p_c/(E_b E_c) \simeq 1 - \cos\theta_{bc}$, p_b and p_c are the four-momenta of the two

child partons, and θ_{bc} is the angle between b and c. The splitting variable is defined to be the ratio of energies $z = E_b/E_a$, and the scale of α_s used is taken as $Q^2 = 2z^2(1-z^2)\tau \simeq p_T^2$. The shower cutoff in HERWIG is typically $Q_0 \sim 0.65$ GeV. Because τ explicitly involves the angle of emission, angular ordering and gluon coherence effects are automatic. On the other hand, the kinematics of each splitting are not determined until the entire shower is complete, at which point parton masses are propagated backwards and the momenta of each splitting determined.

In cluster models, the parton shower proceeds by successive branching (see Eq. (2.20)) until all partons reach a virtuality cutoff of Q_0^2. After all partons reach this cutoff, the gluons decay to $q\bar{q}$ pairs. Since the color of all partons is tracked throughout the shower, it is straightforward to combine quarks and antiquarks into colorless clusters. The clusters then decay to hadrons via two-body phase-space kinematics. Because the parton shower typically produces a large spread in cluster masses, a parameter M_c can be added which is the maximum cluster mass (*e.g.* $M_c \simeq 5$ GeV in HERWIG). Clusters whose masses are above M_c are decayed to a pair of lighter clusters. Baryon production is generally done purely via phase-space, but an *ad hoc* parameter P_{diqk} can be introduced to give the probability for a gluon to split to a diquark-antidiquark pair rather than $q\bar{q}$.

Besides the pure cluster fragmentation of HERWIG, one can have a combined string-cluster fragmentation, as in the CALTECH-II model of Gottschalk [68]. In this case, the parton shower is cut off at a relatively high Q_0 (~ 1 GeV), and string fragmentation is used to produce colorless clusters (instead of hadrons, as in JETSET PS). These clusters are then decayed by phase-space.

The advantage of cluster fragmentation models is that, like the UCLA model, with all decays controlled by phase-space there are very few arbitrary parameters to tune. The down-side to this is that there are no parameters to control the locality of baryon number or strangeness conservation in rapidity, for example. Furthermore, early versions of HERWIG had no mechanism to produce "leading" baryons in jets, since the baryon number of each cluster is 0. Hence,

there could be no difference in production between q and $\bar{q}$ jets. Later versions of HERWIG (since 5.7) addressed this via the `CLDIR` parameter [69].

2.4.3 Local Parton-Hadron Duality

Going a step further than the cluster-model concept of a simple hadronization stage on top of the parton shower dynamics, is the *ansatz* of *local parton-hadron duality* (LPHD) put forward by Azimov, Dokshitzer, Khoze, and Troyan [70]. This stipulates that the momentum spectra of hadrons are simply proportional to the spectrum of partons produced up to some cutoff scale, Q_0, in the MLLA framework. LPHD is equivalent to the claim that fragmentation is responsible for *none* of the dynamics of hadrons. If $\bar{D}_k^g(\xi, E, Q_0)$ is the distribution of gluons in a jet of energy E, then the fragmentation function for species h is given by

$$D_k^h(\xi, E) = K^h \bar{D}_k^g(\xi, E, Q_0), \tag{2.50}$$

where K^h is a constant that depends only on the hadron species h. Thus, LPHD claims that the duality of parton and hadron properties that is seen globally, *e.g.* in jets at leading order QCD or in the coherence of gluons observed in the "string effect," extends as locally as we care to test it.

This is a remarkable hypothesis, for it would allow the spectra of hadrons to be calculated analytically. It is also somewhat counter-intuitive, because conservation of quantum numbers prohibits a one-to-one correspondence of gluons and hadrons on an event-by-event basis; instead, the proportionality of spectra must hold as a statistical property. Furthermore, the inclusive spectra of hadron species are made up of not only the direct products of fragmentation, but also the hadrons coming from decays of more massive resonances. One might expect these different sources to have very different spectra [71]. It is claimed in [72], however, that somehow the effects of resonance production and decays might be subsumed in the MLLA+LPHD picture, with the sum of all the resonant decay contributions giving the inclusive spectrum predicted

Hadron peak positions at LEP/SLC
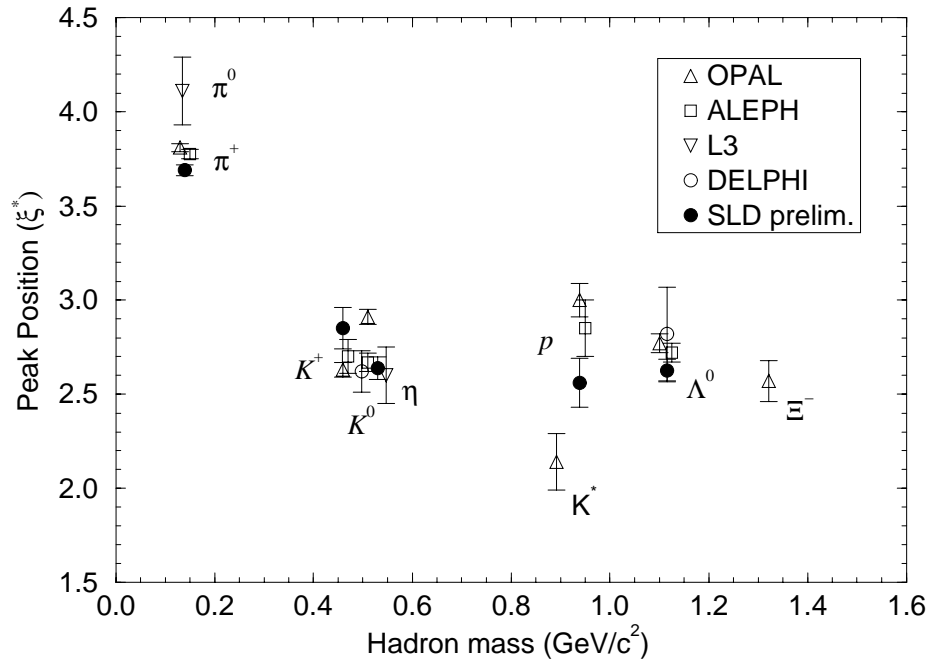
Figure 2.4: The peak positions ξ^* of the Gaussian approximation to the $\xi = \log(1/x_p)$ spectrum of various hadron species are plotted as a function of the mass of the hadron.

by MLLA. An additional problem is the lack of leading particle effects in the LPHD formalism (see [71]). Because u, d, and s jets* should produce the same spectrum of gluons in the MLLA framework, LPHD would therefore predict identical spectra of hadrons in jets of different quark flavor with the same energy. Reference [74] views this as a shortcoming and cautions against trusting the high-momentum part of the LPHD prediction.

Fundamentally, the usefulness of LPHD as a model for hadronization is a matter to be resolved by experimental measurements. The predictions of LPHD are readily testable, and the general features have been shown to hold

---

*Heavy quark jets (c and b), on the other hand, are expected to give different spectra in MLLA because of the heavy quark masses (dead-cone effect) [73]

remarkably well [70, 71]. The spectra of hadrons in e^+e^- are roughly Gaussian in ξ [70]. The peak positions ξ^* have been shown to increase with increasing center of mass energy $\sqrt{s}$ [72]. The observation of leading particle effects would not invalidate LPHD as a model, but simply limit its region of applicability.

It has been speculated that for different hadrons, the mass of the hadron M_h serves as a bound on the cutoff Q_0 (see section 2.3.4). Thus, one might expect that the higher the mass M_h, the lower the peak position ξ^*. This behavior has not yet been so well established. When considering just the meson data alone, or just the baryon data, (see Fig. 2.4) a dependence with mass is observed [71]. Whether this dependence is linear with M_h, as predicted from Eq. (2.30), is still unclear. Furthermore, it would be useful to test the peak positions of the spectra of hadrons produced *directly* from fragmentation. One might expect that LPHD only applies to these spectra (despite the claims of [72]). However, this would require a program of unfolding the production spectra of all sorts of resonances.

Chapter 3

The SLC and SLD

The current chapter discusses briefly the experimental apparatus employed in our measurement. This consists of the Stanford Linear Collider (SLC), which accelerates and collides electrons and positrons at 45.6 GeV/c, and the SLC Large Detector (SLD), which measures many properties of the resulting collisions. A more complete discussion of the SLC can be found in [75], while the details of the SLD are described in [76].

3.1   The Stanford Linear Collider

The SLC is an accelerator project started in 1983. It uses the two-mile SLAC linac for a prototype of a new class of machines, *linear colliders*, which are likely to be the only way to push e^+e^- experiments past their current maximum energies (LEP 2 at about 200 GeV/c). Storage rings lose energy to synchrotron radiation, which is produced in proportion to the centripetal acceleration of the circulating electrons and positrons. The energy lost to synchrotron radiation increases like $E_{loss} \sim E_{CM}^4/R$. Thus, as energies increase, one must build storage rings of increasing radius to reduce the synchrotron losses. For example, the LEP ring has a radius of 4.2 km, which is probably within an order of magnitude of the largest feasible radius. Linear colliders do not suffer
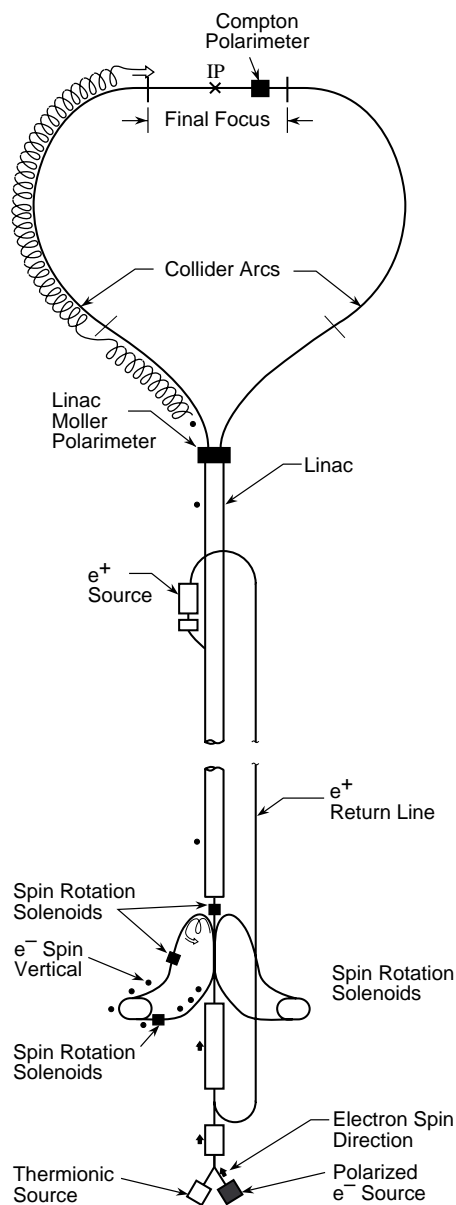
Figure 3.1: The layout of the various components of the SLC is shown, including those needed for spin transport.

from this problem; instead, the challenge is to achieve sufficient luminosity when each pair of particle bunches only gets one chance to collide.

Rather than two linear accelerators facing each other, as would be the case for a true linear collider, the SLC demonstrates the principle using one linac for both electrons and positrons (see Fig. 3.1). Both particle bunches are accelerated down the SLAC linac and separated by a dipole magnet at the end of the linac, where they enter the SLC arcs. The arcs bend the beams around sufficiently slowly that synchrotron radiation does not induce excessive emittance growth. The beams then collide head-on at the SLC Interaction Point (IP), where they are focussed to micron sizes by superconducting quadrupoles. The entire SLC operates at 120 Hz. In contrast to storage rings, operation of the SLC has proved to be difficult and relies on complex feedback systems in order to maintain alignment of the two sub-micron beams stably enough to produce collisions.

3.1.1 Polarized Electron Source

A unique feature of the SLC is its use of a longitudinally polarized electron beam, which is produced by a strained-lattice GaAs photocathode at the linac's electron injector. A circularly polarized laser is used to selectively excite transitions of electrons into longitudinally-polarized states in the conduction band of the photocathode material (see Fig. 3.2). This produces a bunch of approximately 5×10^{10} electrons, which is then accelerated with a 30 kV electric field and injected into the linac.

The 1992 run utilized a photocathode of bulk GaAs. This material has a theoretical maximum polarization of 50% due to a degeneracy in its valence band (see Fig. 3.2). Average polarizations achieved at the SLC IP were $22.4 \pm 0.6\%$ for that run [77]. In the 1993 run, however, the electron gun was upgraded to a strained GaAs lattice. This is composed of a thin layer (300 nm) of GaAs deposited on a substrate of GaAsP. The mismatch in the lattice spacings of these two materials puts a strain on the epitaxial GaAs, which serves to break
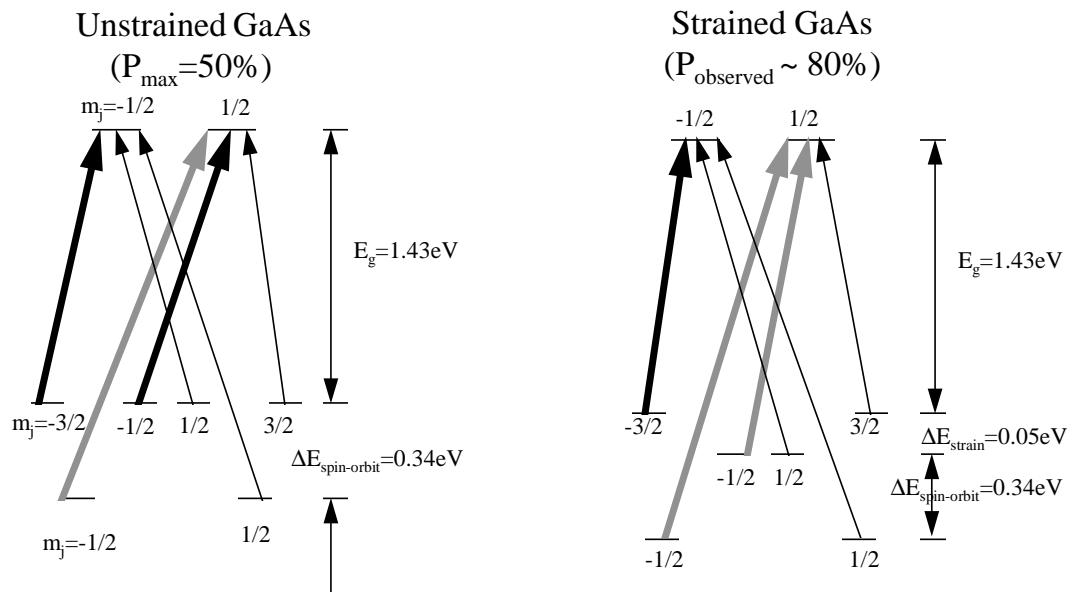
Figure 3.2: The energy state diagram for bulk GaAs (left) and for the strained lattice (right). For the bulk GaAs, the theoretical maximum polarization is 50%. In the strained lattice, however, the degeneracy between the $m_j = \pm\frac{3}{2}$ and the $m_j = \pm\frac{1}{2}$ valence states is broken, allowing, in principle, polarization to reach 100%.

the degeneracy in the valence band spin states. This led to an average polarization of $63.0 \pm 1.1\%$ achieved at the IP [78]. In the 1994–95 run, a thinner epitaxial layer of 100 nm was used, and this boosted the delivered polarization to $77.34 \pm 0.62\%$ [79].

3.1.2 Transport

For each 120 Hz cycle of the SLC, two electron bunches are produced at the electron source. These bunches are accelerated to an energy of 1.19 GeV/c and then diverted into the north damping ring. This ring serves to reduce beam phase-space through emission of synchrotron radiation and application of RF power. Before entering the ring, however, a spin-rotator magnet turns the electron spins from the longitudinal into the vertical direction. This preserves the

spin through the damping process. After a large number of turns (1/120 sec.) in the damping rings, the bunches are kicked out of the ring and go back into the linac.

About two-thirds of the way down the linac, the second pulse is diverted onto a tungsten-rhenium positron target, where positrons are produced, collected, accelerated, and sent back along the linac into the south damping ring. The complete cycle of the SLC includes these three pulses. The bunch coming out of the south damping ring (positrons) leads the two electron pulses down the linac. At the end of the linac, a bending magnet splits the electron and positron pulses and sends them into their respective arcs on the way to the SLC IP. After collision, the beam pulses are steered into beam dumps near the IP.

The steering of the electron polarization from vertical back to longitudinal is accomplished by inducing "spin bumps" in the north arc.* This process works because the SLC arcs (fortuitously) have a betatron oscillation frequency very close to a spin-precession resonance frequency of the electrons. A perturbation in the orbit of the electrons through the arcs is induced, and this bump causes the spin to precess into the desired longitudinal direction. In practice, the orbit perturbation is optimized so as to produce the largest observed polarization at the IP.

3.1.3   Energy Spectrometer

The beam energies of both electrons and positrons are measured on a pulse-by-pulse basis by devices known as the Wire Imaging Synchrotron Radiation Detectors (WISRD) [80]. These detectors are located between the IP and the beam dumps. Their schematic design is shown in Fig. 3.3. The basic principle is that the incoming beam is deflected by two horizontal bend magnets. These magnets each produce a swath of synchrotron radiation which is imaged by a multiwire proportional chamber (MWPC). In between the two horizontal bend

---

*The original design used spin rotating solenoids at the exit of the damping ring (see Fig. 3.1), but controlling the spin orientation through the spin bumps in the arcs has proven more flexible.
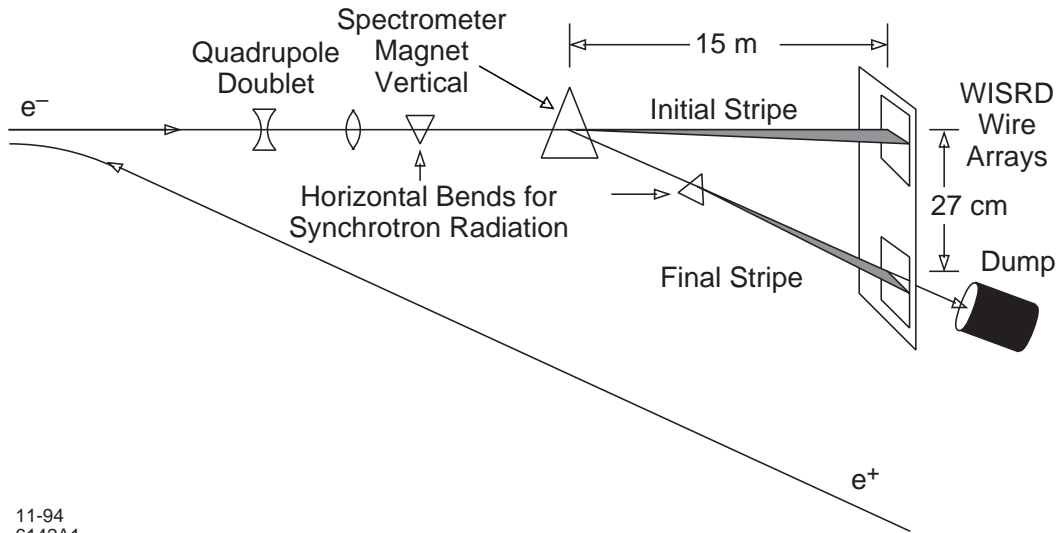
Figure 3.3: A schematic of one of the Wire Imaging Synchrotron Radiation Detectors (WISRD) that is used for determination of the SLC beam energies.

magnets is a precisely calibrated vertical bend magnet. This magnet deflects the beam by an angle inversely proportional to its energy, and that angle can be determined by the distance between the two swaths, as imaged on the MWPC. The average center of mass collision energy measured for the 1993 run was 91.26 ± 0.02 GeV and the energy spread was 110 MeV [78]. The numbers for the 1994–95 run are comparable, except that the energy spread was only 60 MeV.

3.1.4   Compton Polarimeter

In order to make use of the SLC electron polarization for physics measurements, it must be possible to determine precisely the polarization actually delivered to the SLC IP. For example, the SLD measurement of A_{LR} requires a precision of 1% in the electron polarization. This measurement is accomplished by a Compton polarimeter, which is a device that uses the helicity asymmetry
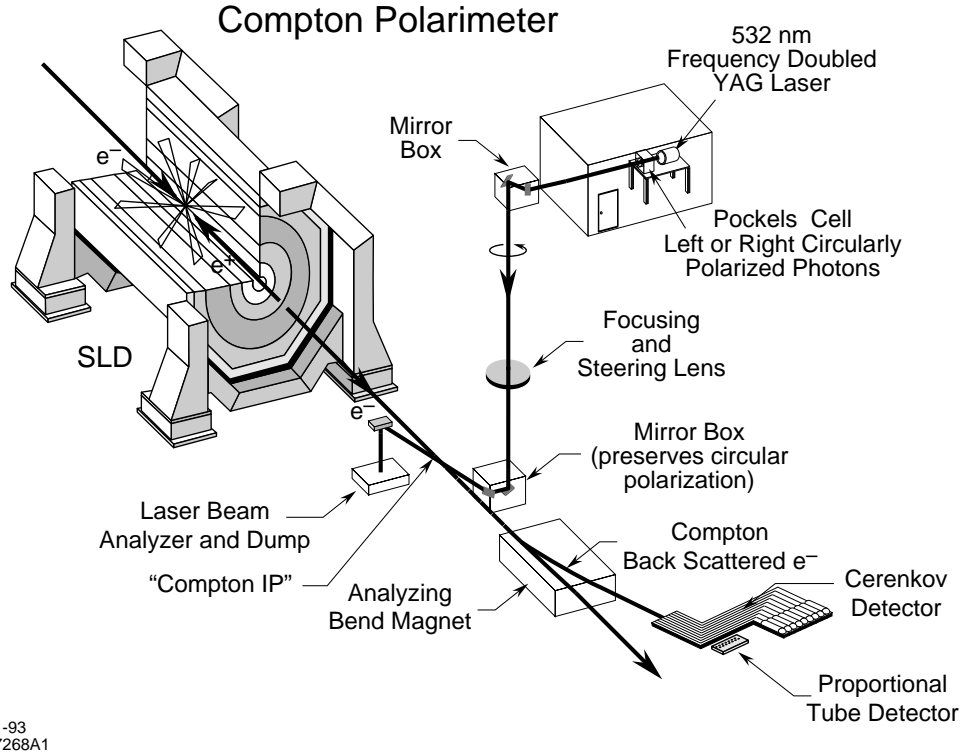
Figure 3.4: A diagram of the SLD Compton polarimeter, showing the positions of various components relative to the SLD detector.

in the Compton scattering cross section (σ_C) to determine the electron beam polarization.

The Compton polarimeter collides 2.33 eV circularly-polarized photons with the 45 GeV electron beam. The scattered electrons lose energy but are not deflected much in angle in the laboratory frame. The Compton cross section can be parametrized as a function of the scattered electron energy, E. Because σ_C depends on the electron and photon spin states, we can define an asymmetry function $A_C(E)$ such that

$$\frac{d\sigma_C}{dE} = \frac{d\sigma_C^u}{dE}\left[1 + P_\gamma P_e A_C(E)\right], \tag{3.1}$$

where $d\sigma_C^u/dE$ is the unpolarized Compton cross section, P_e is the electron beam

polarization, and P_γ is the laser polarization. The shape of this asymmetry $A_C(E)$ does not depend on the incident polarizations P_e or P_γ; it is only a function of the energy in the center-of-mass system and can be calculated from quantum electrodynamics. Thus, the unknown electron beam polarization P_e can be extracted from

$$A_m \equiv \frac{N^{obs}(J_z = \frac{3}{2}) - N^{obs}(J_z = \frac{1}{2})}{N^{obs}(J_z = \frac{3}{2}) + N^{obs}(J_z = \frac{1}{2})} = a_d P_\gamma P_e A_C(E), \tag{3.2}$$

where A_m is the observed asymmetry, N^{obs} represents the number of events observed in the two possible spin configurations, and a_d is the analyzing power of the detector used to measure the scattered electron energy. This analyzing power depends on the transport optics of the electron beam from the Compton IP to the Compton polarimeter detectors.

The polarimeter is shown schematically in Fig. 3.4. Compton photons are produced by a frequency-doubled YAG laser and are circularly-polarized with a series of Pockels cells and quarter-wave plates. After interaction with the electron beam, the laser beam goes to an "analysis box" where its polarization can be measured. Together with polarization measurements of the incident beam, these post-interaction measurements serve to control uncertainty in the photon polarization, which is one of the dominant sources of uncertainty in the measurement of the electron beam polarization.

After interaction with the photon beam, the entire electron beam passes through an analyzing dipole magnet. This bends the off-energy Compton-scattered electrons into the two Compton polarimeter detectors. Two detectors were built for redundancy, but in practice, the proportional tube detector suffers from high backgrounds induced by the main electron beam and is not used for any of the polarimetry analysis. The other detector, a multi-channel Cherenkov device, is positioned farther from the electron beam and shows good signal-to-noise performance.

During normal running, the Compton polarimeter operates asynchronously from the rest of the SLD data acquisition. The Compton laser fires every 11

beam crossings. Data is collected each beam crossing, with the laser-off events used for a background subtraction. The helicities of both the electron and laser beams are selected on every beam crossing in a pseudo-random manner. This information is used to form the measured helicity asymmetry (A_m). Every three minutes or so, the polarimeter delivers a measurement of the current electron beam polarization with a precision of about $\pm 1.5\%$.

One of the difficulties with the polarization measurement is that it occurs at an interaction point that is some 33 m downstream from the SLC IP. Because of the chromatic terms in the SLC final focus optics and the fact that spin-precession in the SLC arcs depends on electron energy, the measured polarization at the Compton IP is systematically different from the luminosity-weighted polarization at the SLC IP. In the 1993 run, this effect was estimated to be less than $1.7 \pm 1.1\%$ [78]. Due to tighter energy collimation on the SLC electron beam and fewer spin precessions in the SLC arcs, the effect was reduced to less than $0.2 \pm 0.2\%$ in the 1994–95 run [79].

3.1.5 SLC Performance History

From its start, the SLC has been a project beset by tight budgetary constraints, which caused many compromises in its design. Together with the fact that there had not been any previous experience in operating a linear collider, this resulted in a lengthy and difficult commissioning period. Even though the SLC was nominally completed in 1987, the first Z^0 events were not observed at the Mark II detector until April 1989. Over the course of the 1989 and 1990 runs, Mark II recorded 826 Z^0 decays, with peak SLC luminosities reaching 4 Z^0/hr or 3.7×10^{28} cm^{-2}s^{-1} [81]. This is compared to a design luminosity of 10^{31} cm^{-2}s^{-1} or 1000 Z^0/hr [75].

In 1991, the SLD started its engineering run. During this run, peak luminosities of 6 Z^0/hr were achieved in 60 Hz operation. The slight improvement over the previous year was due to the new superconducting final focus magnets. A total of 370 Z^0 decays were recorded during this run.
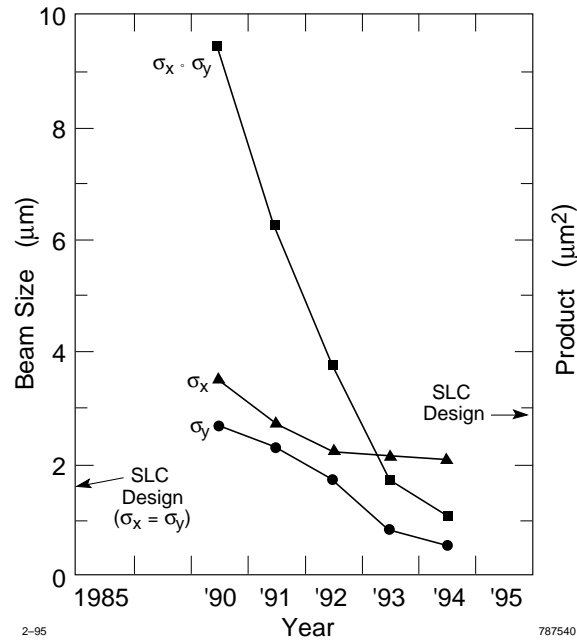
Figure 3.5: The history of the SLC beam spot sizes and area is shown.

The next run in 1992 saw the commissioning of the first polarized source. This first physics run of the SLD produced about 10,000 Z^0 decays with an average polarization of 22%. The peak luminosities reached $30\,Z^0$/hr, due to 120 Hz operation, new feedback systems in the linac, and a sextupole alignment in the SLC arcs. At the end of the 1992 run, during a machine physics program to study final focus systems for the next generation of linear colliders [82], it was realized that the linac was capable of transporting the naturally flat beams from the damping rings without much growth in size. Instead of beam spots of typically $2 \times 2 \; \mu\mathrm{m}^2$, this new mode of operation allowed spots of $2 \times 0.7 \; \mu\mathrm{m}^2$, thus doubling the available luminosity (see Fig. 3.5).

The 1993 run employed this new flat beam configuration. It also employed the new strained-lattice GaAs photocathode, which allowed the average electron polarization at the IP to reach 63%. SLD collected approximately 50,000 Z^0 decays, and peak luminosities reached about $60\,Z^0$/hr.
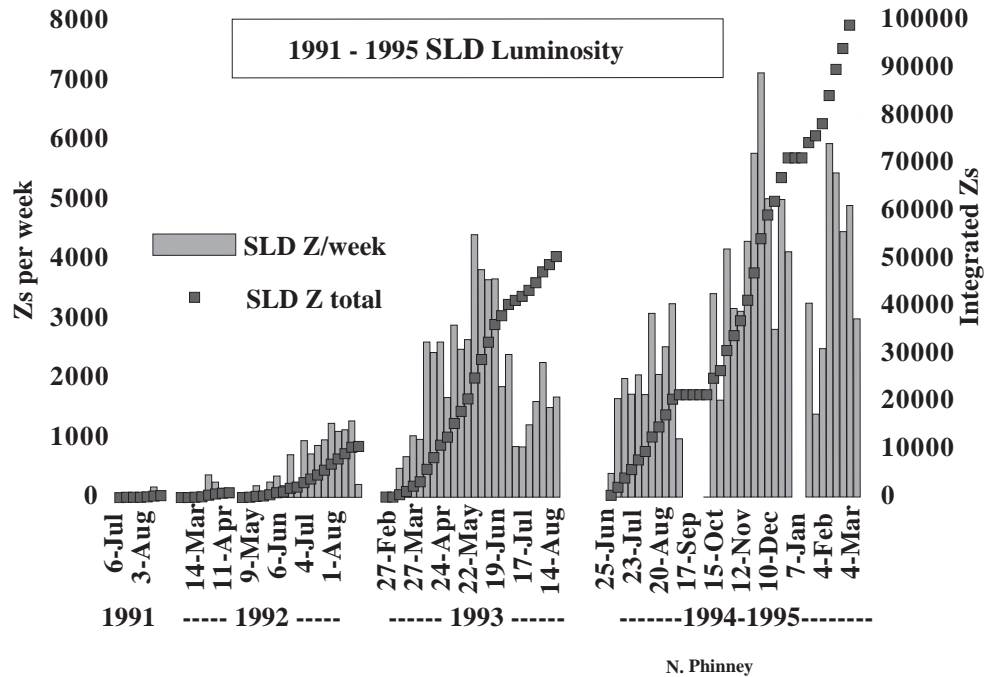
Figure 3.6: SLC Luminosity collected by SLD as a function of time. The four SLD run periods are shown. The histograms show the weekly luminosity, while the points are the integrated totals for each run.

For the 1994–95 run, vacuum elements in the SLC damping rings were upgraded in order to remove instabilities which limited the maximum beam currents. In addition, new final focus elements were installed to cancel chromatic aberrations that limited the vertical spot size. Neither of these upgrades were as successful as hoped, but they did allow peak luminosities to improve to 80 Z^0/hr and, together with good machine uptime, allowed the integrated total to reach 100,000 Z^0 decays. Figure 3.6 summarizes the history of SLC luminosity over the various run periods.

3.2 The SLC Large Detector

The SLD was proposed in 1984 as a state-of-the-art, general-purpose detector to study Z^0 decays at the SLC with 4π-coverage [76]. Its construction was completed in 1990 (except for a few subsystems), and the SLD was moved into position at the interaction point of the SLC, replacing the Mark II detector.

As shown in Fig. 3.7, the SLD has a layout of concentric cylindrical layers, each of which is a separate sub-detector measuring a different aspect of the collision products, as is typical of modern collider detectors. Most subsystem layers are separated into barrel and endcap components. The endcap detectors are mounted on large doors which can be opened during downtimes for access. The general features of the SLD are: a high-precision wire drift chamber and a
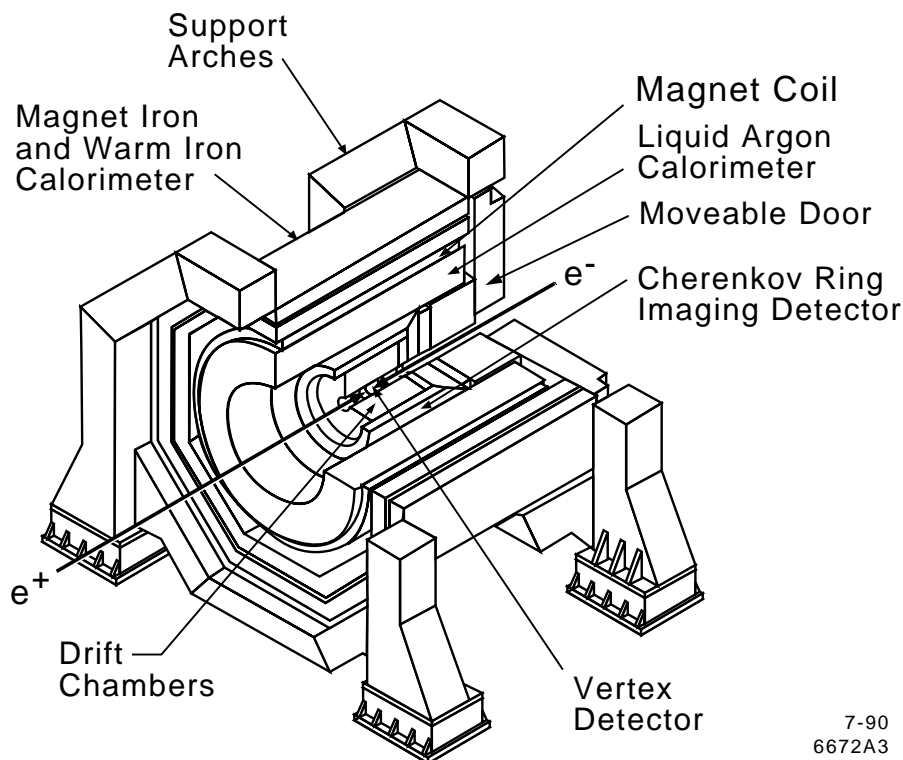
Figure 3.7: An isometric view of the SLD detector, showing the layout of the various component detectors. The Luminosity Monitor is not shown in this diagram.
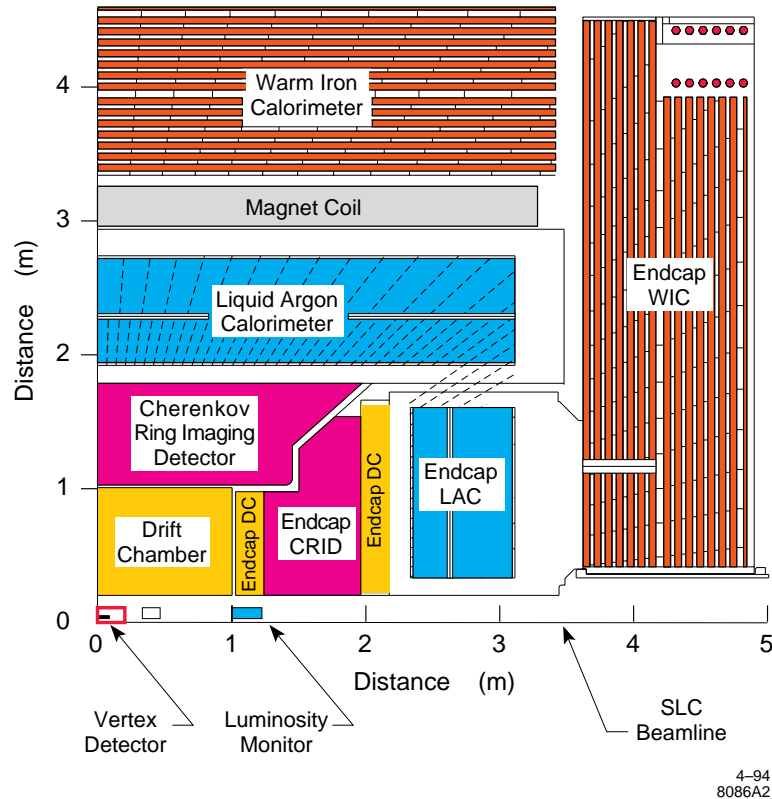
Figure 3.8: A quadrant view of the SLD detector, giving the overall dimensions of the detector components.

silicon-pixel vertex detector for charged particle tracking, a Cherenkov ring imaging detector for particle identification, liquid-argon calorimetry (which gives good e/π discrimination), a 0.6 T conventional solenoid, and an instrumented flux return for muon identification. A summary of SLD performance is given in Table 3.1. All subsystems feature on-detector digitization with fiber optic readout for a minimal cable plant. The various components are described in the following subsections in order from innermost to outermost.

Most of the following discussion will focus on the barrel region, since this is currently understood much better than the endcap regions. As the barrel components cover some $2/3$ of the available solid angle (depending on the subsystem), this is also the majority of the phase space for particle decays. There

solenoidal field	0.6 T
CDC spatial resolution	**80** μm
momentum resolution (CDC-only)	$0.010 \oplus 0.0050 p_t$
VXD spatial resolution	**5.5–9** μm
momentum resolution (CDC+VXD)	$0.0095 \oplus 0.0026 p_t$
impact parameter resolution (xy)	**11** μm
impact parameter resolution (rz)	**38** μm
electromagnetic energy resolution	$15\%/\sqrt{E}$
hadronic energy resolution	$60\%/\sqrt{E}$

Table 3.1: SLD performance summary.

is a standard SLD coordinate system, which will be referred to in the following sections. The SLD z-axis is defined to be along the positron incident direction (North). The x-axis is perpendicular to the incoming beams and lies in the horizontal plane facing West. The y-axis is then in the vertical plane pointing upwards. We will also refer to cylindrical coordinates, in which the radius r is defined in the xy plane, θ is the angle with respect to the positive z-axis, and ϕ is the azimuthal angle with respect to the x-axis.

3.2.1 The Vertex Detector

At the very center of the SLD lies a silicon-pixel vertex detector (VXD), composed of 480 charge-coupled devices (CCDs). These CCDs are the silicon chips commonly used in video cameras. The current vertex detector, which was in place for the 1992 through 1994–95 runs, is the second generation of design and is known as VXD2. There is a third generation design, VXD3, recently installed and being commissioned for the 1996 run.

The SLC beampipe is composed of a thin cylinder of beryllium. Its outer radius is 25 mm, which limits the position of the innermost layer of the VXD2 to 29.5 mm. Including the VXD2 cooling jacket, there is a total of 0.71% radiation

length of material between the IP and the first VXD2 layer. The outer layer of the VXD2 is limited in radius by the relatively large VXD cryostat and is 41.5 mm from the IP.

VXD2 is constructed from sixty 9.2-cm long aluminum-ceramic ladders, arranged in four concentric cylinders. Each ladder contains eight CCDs mounted in an overlapping fashion with half mounted on one side and half on the other. The individual CCDs are approximately 1 cm square, with 375×578 22-μm square pixels. Each pixel has an active depth of 20 μm. A minimum-ionizing track deposits roughly 1000 electrons, about half of which are collected in the CCD pixel. Due to clustering of neighboring pixels, one expects a point resolution of ~ 3.5 μm, which is slightly better than the naive expectation of $22/\sqrt{6}$ μm. Although there are four radial layers, each layer has incomplete coverage in azimuth and overlaps the gaps in its neighboring layers (see Fig. 3.9). The average number of CCD hits per track passing through VXD2 is 2.3, making this effectively a two-layer device.

VXD3 takes advantage of newer fabrication technology, which allows individual CCDs to be made as large as 1.6×8.0 cm. This permits the construction of a three-layer device with only 96 CCDs. VXD3 will have a three-hit acceptance to polar angles $|\cos\theta| < 0.85$ (as compared to VXD2 with $|\cos\theta| < 0.75$ for only two hits). In addition, the larger chips allow simpler ladder construction, which brings the thickness per ladder of VXD3 to 0.4% radiation length at normal incidence from the 1.15% in VXD2 [83].

In order to suppress dark currents, the entire VXD is cooled to -80 °C. This is accomplished with boil-off N_2 gas flowing through a polyurethane-foam cryostat. The biggest disadvantage of CCDs for vertex detection is that they must be readout serially. Each VXD2 CCD has one readout node through which all 240,000 pixels must be clocked. This process takes 160 ms, or about 19 beam crossings. Fortunately, the occupancy of the device is low (0.01%), even when the 19 crossings are overlaid.

All the VXD2 CCDs and ladders were surveyed to 5 μm with optical measurement devices [84]. Nevertheless, the final alignment of the components

VXD3

cos*θ*=0.85 (≧3 Hits)   cos*θ*=0.9 (≧2 Hits)

0   5   10
cm

cos*θ*=0.75 (≧2 Hits)

VXD2

VXD−2 GEOMETRY   VXD−3 GEOMETRY

Y (CM)

4

0

−4

−4   0   4
X (CM)

−4   0   4
X (CM)
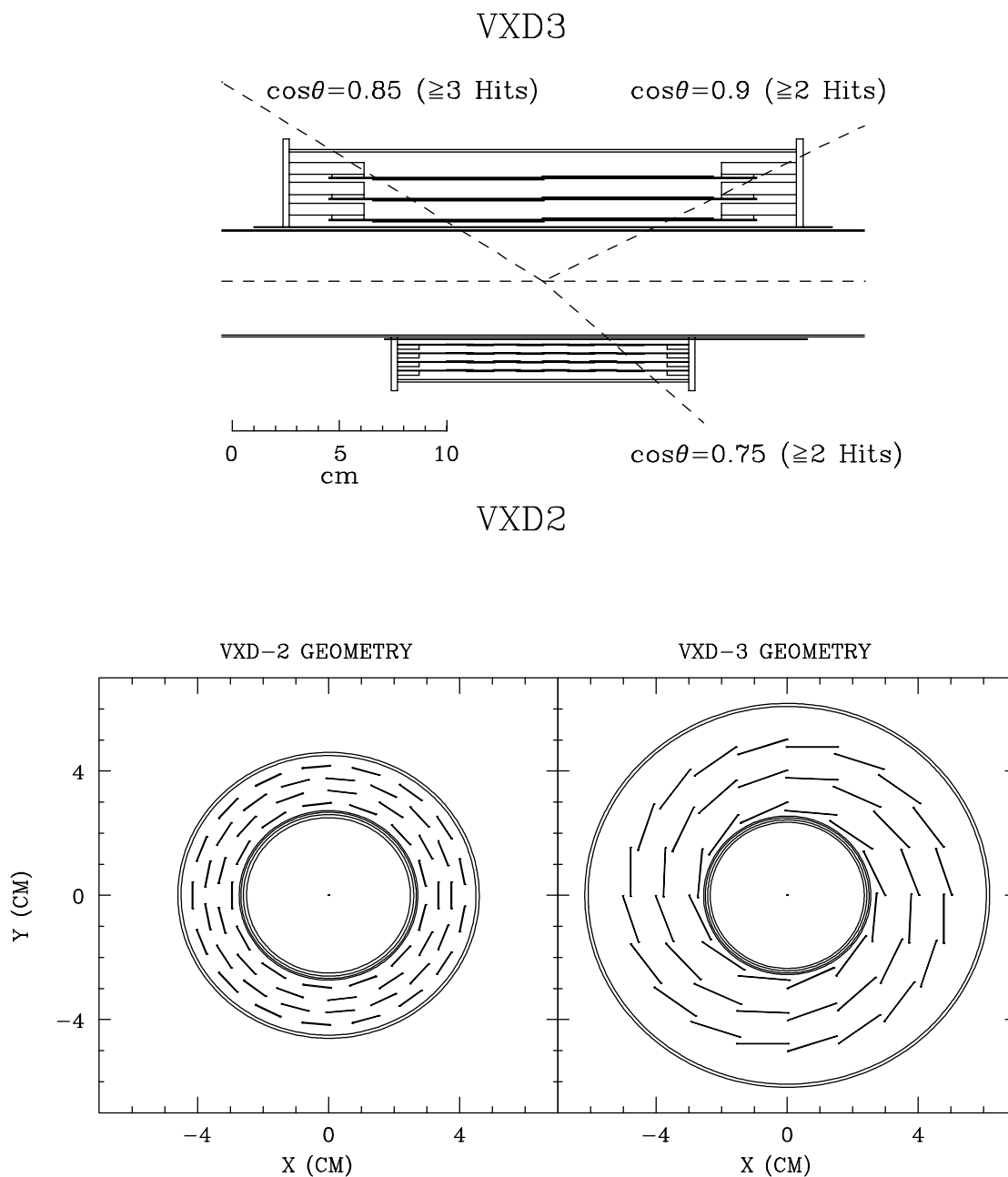
Figure 3.9: An *rz* view (top) and an end view (bottom) of the current SLD Vertex Detector (VXD2) and the planned upgrade (VXD3). Although VXD2 is composed of four layers of CCDs, the gaps between ladders make this effectively a two-layer tracking device. VXD3 has three complete layers which gives it better tracking capability. Also, VXD3 extends farther in polar angle.
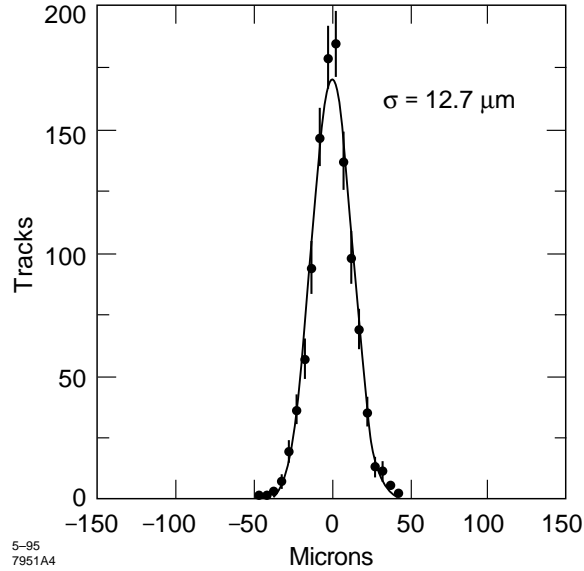
Figure 3.10: Miss distance in xy for $Z^0 \to \mu^+\mu^-$ and $Z^0 \to e^+e^-$ events. The width of this distribution implies an impact parameter resolution $\sigma_b = 11$ μm in xy for tracks with negligible multiple scattering.

was performed using tracks from hadronic Z^0 decays. The result of this alignment is a single-hit resolution (measured using the sagitta from the subset of tracks which have three VXD hits) of 5.5 μm in the xy plane and 5.5–9 μm in z, depending on the dip angle of the track [81]. This slight degradation in resolution at larger dip angles is attributed to radial alignment errors and to bowing of the CCDs.

The overall performance of VXD2 can be evaluated with two-prong $Z^0 \to \mu^+\mu^-$ and $Z^0 \to e^+e^-$ events. Shown in Fig. 3.10 is the xy miss distance between the two tracks in such events. Since these two particles are known to come from a common interaction point, the width of the miss-distance distribution is $\sqrt{2}$ times the xy impact parameter resolution of VXD2 on a single track at the high-momentum limit. The initial beam spot position is known to 7 μm in the transverse plane. Thus, the high-momentum impact parameter resolution of the VXD2 tracking system is 11 μm in xy. A similar analysis yields 38 μm in rz [85].
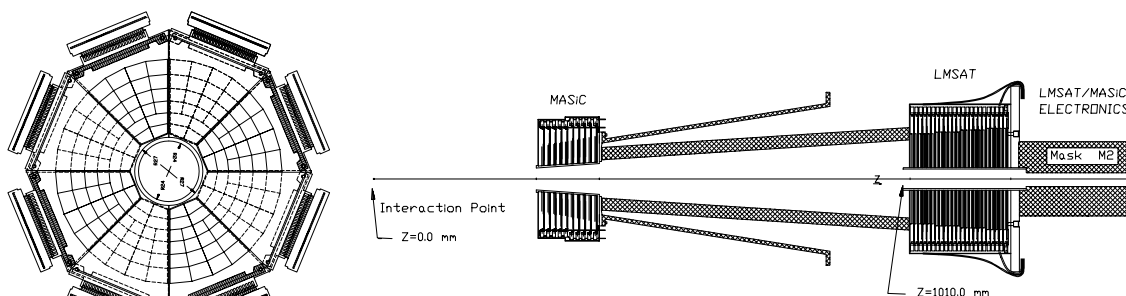
Figure 1. Luminosity Monitors for SLD

Figure 3.11: At left, a face-on view of the SLD Luminosity Monitor (LUM) showing the tower segmentation and readout cards. On the right is an rz view showing the longitudinal segmentation, as well as the SLC beampipe and masking.

3.2.2   The Luminosity Monitor

The SLD Luminosity Monitor (LUM) measures the rate of small-angle Bhabha scattering, which has a well-understood cross section derived purely from QED. The LUM consists of two silicon-tungsten calorimeters arranged in projective towers with a high degree of segmentation and located 1 m downstream from the interaction point in z [86]. Each of the two calorimeters has 160 towers covering the angular region $28 < \theta < 65$ mrad. The LUM towers are further divided into two longitudinal segments, EM1 with a thickness of 5.5 radiation lengths and EM2 with a thickness of 15.6 radiation lengths. The LUM energy resolution has been determined from Bhabha events to be approximately 3% at 50 GeV [87].

3.2.3   The Central Drift Chamber

The Central Drift Chamber (CDC) is the primary tracking device of the SLD. The CDC occupies an annulus of 20 cm to 100 cm in radius and about 180 cm in length. It is composed of 5120 sense wires in a jet-cell arrangement (see Fig. 3.12). Each cell is roughly 6 cm wide by 5 cm high and contains eight active sense wires, two dummy sense wires, 18 guard wires, and 25
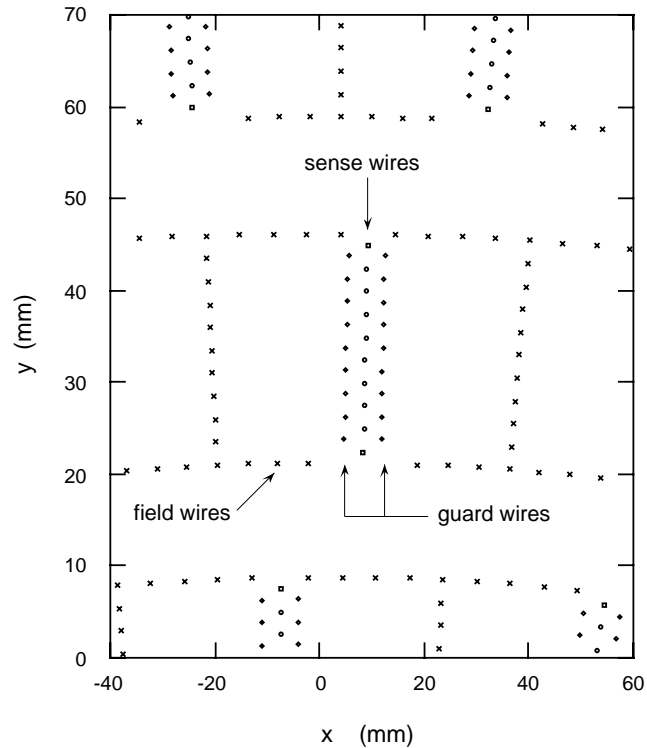
Figure 3.12: A schematic of the CDC cell layout.

field wires. The sense wires are 25-μm gold-coated tungsten, while the guard and field wires are 150-μm gold-coated aluminum. The guard wires serve to keep the gas gain uniform by controlling the field in the vicinity of the sense wires. The sense wires are radially oriented with no stagger. Original designs [76] called for a 5° tilt with respect to the radial direction in order to remove left-right ambiguities, but this was changed to simplify construction. Analysis determined that the ambiguities from radial cells increase processing time somewhat in the pattern recognition, but have a minimal effect on the overall efficiency, since the stagger of cells between superlayers eventually resolves any ambiguities [88]. The sense and guard wires are mounted together in Lexan blocks, which are then precisely positioned and tensioned in the aluminum endplate. The inner and outer walls (in radius) of the CDC are
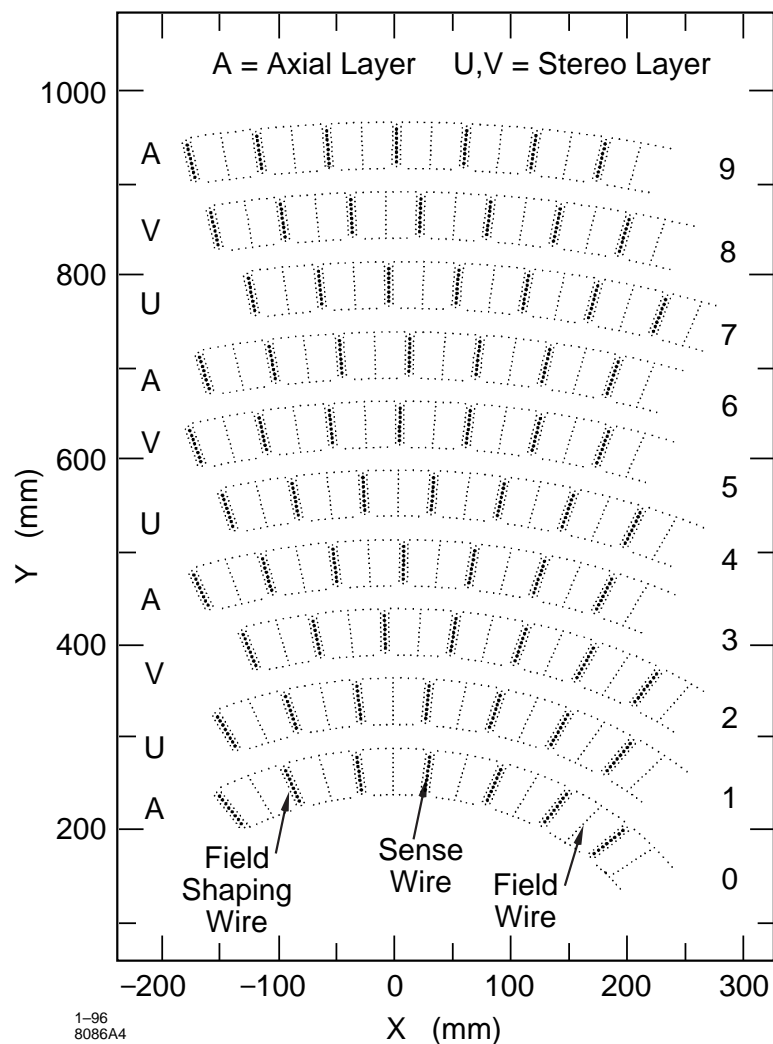
Figure 3.13: A schematic of the CDC endplate, showing the layout of axial (A) and stereo (U, V) layers.

made from an aluminum sheet-Hexcell fiberboard laminate, which comprises only 1.8% and 1.6% radiation length for the inner and outer wall, respectively.

There are 10 layers of cells that make up the CDC (see Fig. 3.13). Six of these superlayers have a stereo angle (on average ±42 mrad) with respect to the beam axis, thus permitting a measurement of the z position of track hits with only 24 times worse resolution than the xy position. In addition, the two ends of

each sense wire are read out into separate amplifiers, allowing reconstruction of the z position to approximately 5 cm by using the ratio of the pulse heights (known as *charge division*). This charge division information is only used in the initial stages of pattern recognition, as the stereo layers give more precise z information once the track has been fit. For details on the track reconstruction algorithms, see [89].

The CDC drift gas is 75% CO_2, 21% Ar, and 4% isobutane, with a 0.3% admixture of H_2O, operated at atmospheric pressure. The CO_2 base gas provides low drift velocity and low diffusion, which aid the spatial resolution. Argon is added to increase the avalanche gain, and isobutane aids quenching. The water is added to suppress the effects of wire aging [90]. The drift velocity of the final gas mixture is 7.9 μm/ns at the mean drift field of 0.9 kV/cm.

The local and global resolution of the CDC are shown in Fig. 3.14 as a function of drift distance from the sense wire plane. The local resolution is calculated from the difference in residuals of hits on a track from adjacent wires in a cell, and this represents the intrinsic performance of the chamber. Factors that limit the local resolution are the diffusion constant of the drift gas, the drift velocity in the chamber, the electrostatics of the drift cell, and the performance of the readout electronics and pulsefinding algorithm. As shown in Fig. 3.14, the local resolution measurements are consistent with a diffusion-dominated model ($\sigma_d \propto \sqrt{d}$), with the exception of the extreme ends of the cell, where the field is varying rapidly or the drift velocity is greater.

The global resolution of the CDC is given by the residuals of all hits on a fitted track. This includes effects from inter-cell alignment errors, variation of the time-to-distance relation between cells, and unaccounted wire sag.[*] The 30–40 μm alignment errors implied by Fig. 3.14 are consistent with the resolution of the cell-to-cell alignment procedure, as described in [91]. The mean resolution of hits between 0.5 and 2.5 cm is 82 μm, making the SLD CDC the most precise large-scale drift chamber ever constructed [92].

---

[*]The gravitational sag of the wires is modelled as 34 μm at the center of the wires and is included in the track fits. The electrostatic sag is unmodelled, but is expected to be small.
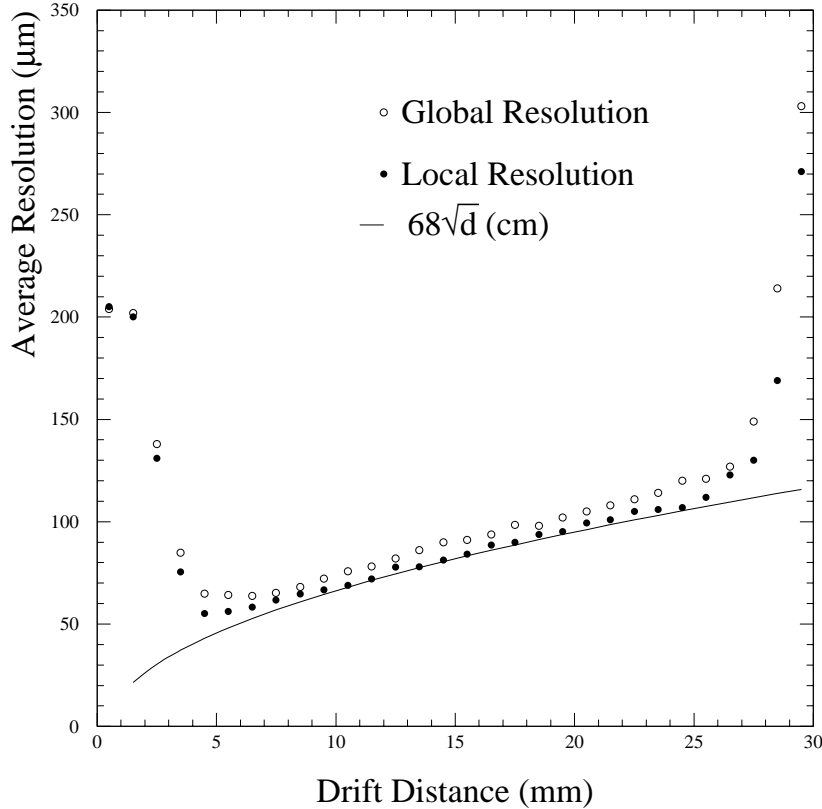
Figure 3.14: The local and global SLD CDC drift distance resolution measured with tracks in hadronic events from the 1994–95 run. Also shown is the resolution expected due to diffusion effects for the CDC gas composition. This diffusion curve has been normalized to the minimum local resolution.

In principle, the spatial resolution and the 0.6 T magnetic field should be sufficient to determine the momentum resolution of the CDC. However, a host of other effects, such as hit inefficiencies, correlated misalignments, and tails on the spatial resolution distribution, can degrade performance from the simplistic expectation. Empirical measures of momentum resolution can be obtained from $Z^0 \rightarrow \mu^+\mu^-$ events, from comparing the two segments of cosmic ray tracks, and from the $K_s^0 \rightarrow \pi^+\pi^-$ invariant mass width. These techniques yield a resolution of $(\sigma_{p_t}/p_t)^2 = (0.010)^2 + (0.0050p_t)^2$, where p_t is the momentum component transverse to the beam axis [92]. This result is consistent

to within a factor of two of the resolution expected from a simplistic model which does not account for correlated misalignments and so forth. When the VXD2 hits are added into the tracking fit, the momentum resolution improves to $(\sigma_{p_t}/p_t)^2 = (0.0095)^2 + (0.0026p_t)^2$ [85].

3.2.4 The Cherenkov Ring Imaging Detector

Situated directly outside of the CDC is the SLD Cherenkov Ring Imaging Detector (CRID). Since it is central to this dissertation, this detector is described in detail in the following chapter. The barrel portion of the CRID provides the SLD with excellent particle identification over the central 70% of its solid angle. A combination of gaseous and liquid Cherenkov radiators, together with momentum measurement from the CDC, allows $\pi/K/p$ separation up to 30 GeV/c and e/π separation up to 6 GeV/c. Cherenkov ring imaging is still a relatively novel technology in particle physics detectors, and successful operation of the SLD CRID has been full of many challenges.

3.2.5 The Liquid Argon Calorimeter

Energy measurement at SLD is provided by the Liquid Argon Calorimeter (LAC) [93]. The LAC is a sampling calorimeter composed of lead plates immersed in liquid argon. The argon is the active medium, being ionized by charged particles passing through it, while the lead serves not only to induce particle showers but also to collect the charge. The advantage of liquid argon over, for example, plastic scintillator is that it is not susceptible to radiation damage, and therefore the energy response should not vary over time. The layers of lead are broken up into alternating grounded plates and tiles held at high voltage (-2 kV), separated by plastic spacers. Each layer of one grounded lead plate and one lead tile is referred to as a single *cell*.

The LAC is segmented into projective towers, roughly 33 mrad in θ and φ. There are 68 towers in polar angle and 192 in azimuth in the barrel section of the LAC. In each LAC endcap there are 17 towers in polar angle and 192,
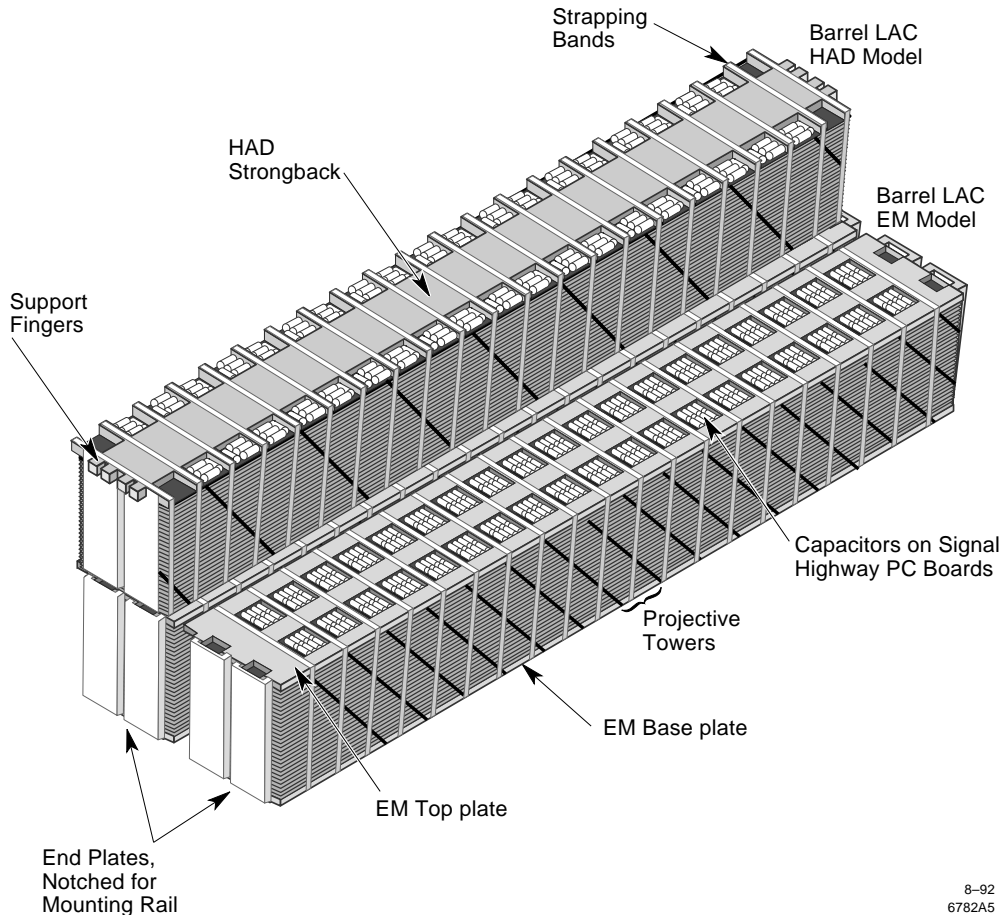
Figure 3.15: Schematic of LAC barrel modules. Two EM modules and one HAD module are shown. There are 48 such modules azimuthally and three longitudinally.

96, or 48 in azimuth (depending on the polar angle). In addition, the LAC is segmented into four longitudinal layers, denoted EM1, EM2, HAD1, and HAD2. The first two sections contain the majority of energy deposited by electromagnetic showers (those induced by electrons or photons), while the outer two sections extend the containment to cover hadronic showers. The EM1 and EM2 sections are formed of 2-mm thick Pb plates separated by 2.75-mm Ar gaps, which yields a sampling fraction of 18.4%. The HAD sections are formed of 6-mm Pb plates and 2.75-mm Ar gaps, for a sampling fraction of 7.0%. In the HAD sections, the angular segmentation is half that of the EM

	EM1	EM2	HAD1	HAD2
φ Segmentation	192	192	96	96
θ Segmentation	102	102	48	48
Depth (num. cells)	8	20	13	13
Pb Thickness (mm)	2.0	2.0	6.0	6.0
Ar Gap (mm)	2.75	2.75	2.75	2.75
Sampling Fraction	0.184	0.184	0.070	0.070
Radiation Lengths (X_0)	6.0	15.0	13.9	13.9
Interaction Lengths (λ_0)	0.24	0.60	1.00	1.00

Table 3.2: Specifications of the SLD LAC.

sections in both dimensions; thus a single HAD tower backs four EM towers. The parameters of the four layers are described in Table 3.2.

The EM sections contain approximately 99% of the energy of a 45 GeV electron, while the entire LAC contains 90–95% of the total energy of a hadronic Z^0 decay [94]. The measured energy resolution of the EM and HAD sections are $15\%/\sqrt{E}$ and $60\%/\sqrt{E}$, respectively [85].

3.2.6   The Warm Iron Calorimeter

The Warm Iron Calorimeter (WIC) [95] is composed of 18 layers of Iarocci tubes [96] sandwiched in 3.2 cm gaps between 5 cm thick steel plates. The total thickness of the WIC is 4.2 interaction lengths. Iarocci tubes are long rectangular plastic (PVC) extrusions lined with slightly conductive carbon paint, fitted with central Cu-Be anode wires, and filled with a gas mixture of 88% CO_2, 9.5% isobutane, and 2.5% Ar. The tubes are instrumented with external Cu cathode readouts, square pads on one side for calorimetric measurements (WIC pads) and long strips on the other side (WIC strips) for muon tracking. Most of the WIC strips in the barrel are oriented parallel to the beam, with two of the 16 layers arranged transverse to the beamline (see Fig. 3.16). In the endcaps, the
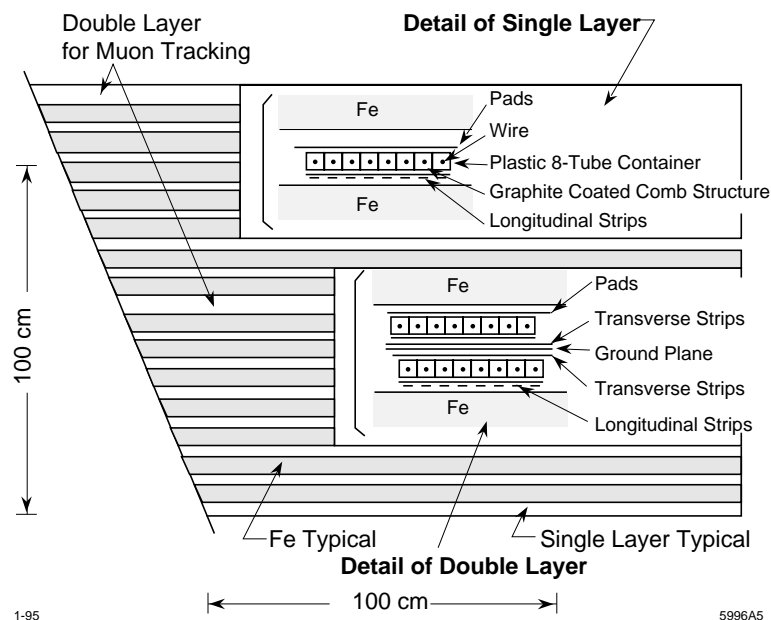
Figure 3.16: Diagram of a section of the WIC, showing the single layers containing longitudinal strips for muon tracking as well as pad tower readout. Also shown are the double layers with crossed strips for tracking in the other plane.

inner half of the WIC has wires running horizontally, and the outer half has wires running vertically.

The WIC serves not only as a flux return for the SLD solenoid, but also as a tracking system for muon identification. In addition, it was intended as a backing calorimeter to catch the 5–10% of hadronic event energy that leaks through the LAC. However, the calibration of and accurate simulation of the WIC calorimetric response have proven difficult. There are several factors that contribute to this. The combination of beam-related backgrounds (primarily SLC muons) and cross talk along the Iarocci tubes serves to produce a high level of noise in the data and to make clustering problematic. The lack of good test-beam data and the fact that the WIC gas gain varies considerably with atmospheric pressure have made calibration of the energy response difficult. Hence, the WIC pads have not been used in the SLD calorimetry reconstruction to date [94].

3.2.7   Data Acquisition

The SLD data acquisition design makes extensive use of the relatively long time (8.3 ms) between SLC beam crossings. For example, little dedicated hardware is required for triggering; instead, the entire calorimeter is read out and energy sums are calculated in software, all within the 8 ms time window. Another example is the readout of the "wire systems" (the drift chambers and CRIDs). In these systems pulses from preamplifiers are fed into Analog Memory Units (AMUs), which are custom VLSI arrays of 256 sample-and-hold circuit elements [97]. These pulses are then digitized in 12-bit 3-μs ADCs on the detector face, and the resulting data are sent on via 32-Mbit/s fiber optics, thus minimizing the required cable plant inside the SLD.

The data acquisition architecture is FASTBUS, and there is a network of 18 FASTBUS crates located on the top deck of the SLD that comprise the system. The work of assembling events is done in ALEPH Event Builder (AEB) modules [98]. These are modules containing Motorola 68020 CPUs and about 5 MB of memory. The AEBs pool data from various slave modules, whose type depends on the subsystem being read out. The calorimetric systems are processed in Calorimeter Data Modules (CDMs), while the drift chamber and CRID systems are processed in Waveform Sampling Modules (WSMs), the vertex detector data are processed in Vertex Data Acquisition (VDA) modules, and the WIC Strip data are processed in WIC Digital Readout Modules (DRMs). All of these slave modules contain some number of 68020 CPUs and are connected to their respective systems via fiber optics.

Triggering is determined by a dedicated trigger AEB. There are several conditions which cause the detector to be read out. For hadronic events, there are three main triggers: an Energy trigger based on a sum of LAC tower response, a Track trigger based on some fast readout of the CDC cells and requiring two tracks at large angles relative to each other, and a "Hadron" trigger which combines the preceding two types of information, but with a lower energy threshold and only one track required. There is also a dedicated

trigger for small-angle Bhabhas in the LUM, and there is a Random trigger which reads out the detector every 20 ± 0.5 seconds.

The control software for the SLD experiment runs on a VMS cluster. The main data acquisition machine is a VAX 8800. There is also a VAX 6420, which is used for monitoring, time histories, and miscellaneous controls. Displays are run via X-windows on VMS workstations or NCD X-terminals. The VAX 8800 writes data to STK 3490 tapes via a fiber optic link to the silo at the SLAC computing center.

An average SLD event is 250–300 kilobytes in size, with about 40% of that volume belonging to the CRID, and another 25% each coming from the drift chamber and VXD subsystems. Event sizes, however, are strongly influenced by background conditions, and those conditions vary rapidly with the tune of the SLC. Typical trigger rates during low background operation are 0.2 Hz, while real Z^0 luminosity is typically 30–70 Z^0/hr, or about one-tenth to one-twentieth of that trigger rate.

3.2.8   Detector Simulation

In order to unfold the detector response from physical quantities of interest, all modern high-energy physics experiments rely on extensive computer simulations of the response of their detectors. The SLD simulation is based on the standard GEANT 3.21 package [99], which tracks particles through a description of the detector material and magnetic field and simulates multiple scattering and energy loss. For showering in the calorimeters, SLD uses a hybrid scheme of a parametrized shower shape for the electromagnetic portion of the showers [100], and the GEANT GHEISHA [101] package for the hadronic interactions.

Once a particle is tracked into a particular detector subsystem, there is code to simulate the response of that detector and to produce data in the same format as the raw data coming from the actual experiment. Details of the simulation of the tracking systems can be found in [89]. A discussion of the

simulation of the calorimetry can be found in [94, 87]. The simulation of response in the CRID is discussed in sections 7.15 and 7.16.

In order to simulate the beam-induced backgrounds, as well as noisy electronics channels, raw data from random triggers is overlaid with the results of the simulation. These random triggers are sampled in a luminosity-weighted fashion, so that they represent the conditions corresponding to actual hadronic events selected for analysis. After the random trigger data is merged with the "data" produced by the simulation, the event is processed with the standard SLD reconstruction package.

The input to all of this simulation is one of several QCD event generators. For the current data set, the JETSET 7.4 parton shower model was used to supply hadronic particles as input to the detector simulation. The parameters of JETSET have been tuned by the SLD collaboration to fit available world data, and the decays of charm and bottom hadrons have been parametrized with the CLEO decay package [102]. These inputs result in good agreement with the charged and neutral multiplicities and spectra observed in the SLD.

Chapter 4

The SLD CRID

This chapter discusses briefly the principles of ring imaging Cherenkov detectors and presents an overview of the design of the SLD Cherenkov Ring Imaging Detector (CRID). Some of the other contemporary ring imaging devices are reviewed briefly. A fuller discussion of the principles of ring imaging detectors can be found in [103]. A more complete discussion of the SLD CRID design can be found in [76], and a thorough survey of ring imaging detectors is available in [104].

4.1   Cherenkov Radiation

The phenomenon of Cherenkov radiation* occurs when a particle traverses a dielectric medium with a velocity exceeding the phase velocity of light in that medium. The particle polarizes molecules in the medium as it passes. When the velocity of the particle is low, this creates no net polarization and no field at large distances; however, if the velocity of the particle is sufficiently high, it can create net polarization and produce coherent radiation, much like a shock wave in fluid mechanics.

---

*In the Russian literature, the effect is known as Vavilov–Cherenkov radiation, recognizing the role of Vavilov, who was Cherenkov's supervisor at the Lebedev Physics Institute, in the interpretation of the phenomenon [105, 106].

The discovery of such radiation is attributed to P. A. Cherenkov [107], who in 1934, while investigating luminescence in uranyl salt solutions excited by gamma rays from radium, observed weak blue light in a nearby crucible of pure sulfuric acid. This radiation was attributed to Compton electrons by S. I. Vavilov [108], and Cherenkov confirmed this by interposing a magnetic field. Cherenkov went on to characterize the angular distribution, intensity, and spectral distribution of this effect, as well as its dependence on the index of refraction and the velocity of the incident particle. The first observations of blue light in solutions of radium, however, were made much earlier by M. Curie in 1910 and refined by L. Mallet in 1926–29 [109], who showed that the spectrum was continuous (*i.e.*, not composed of discrete spectral lines).

Three years after Cherenkov's observations, the effect was explained within classical electromagnetic theory by I. E. Tamm and I. M. Frank [110]. They had to overcome the commonly held assumption at the time that only accelerated charges radiate (this is true only in vacuum) and a general hesitancy to investigate faster than light particles [106]. The quantum theoretical calculation by Ginsberg followed in 1940 [111], but this resulted in only minor modifications to the Tamm–Frank theory. In 1958, Tamm and Frank were awarded the Nobel prize in physics together with Cherenkov. Vavilov had died seven years earlier, and was therefore not recognized by the Nobel committee.

For a charged particle travelling with velocity $v = \beta c$ in a medium with index of refraction n, the polar angle θ_c of Cherenkov radiation with respect to the particle's direction is given by

$$\cos \theta_c = \frac{1}{n\beta}, \tag{4.1}$$

while the azimuthal distribution of the radiation is uniform. The Tamm–Frank relation gives the spectrum of the Cherenkov radiation:

$$\frac{dN}{dE} = \left(\frac{\alpha}{\hbar c}\right) Z^2 L \sin^2 \theta_c, \tag{4.2}$$

where dN is the number of photons with energy between E and $E + dE$, α is the electromagnetic fine structure constant, L is the path length of the particle through the medium, and Ze is the charge of the particle. Note that in the case of a constant index n, this spectrum rises linearly with E. Thus, for most materials (with relatively constant n), Cherenkov photons are usually peaked towards short wavelengths.

In general, optical media have a dispersion $n = n(E)$, so we must integrate Eq. (4.2) over the detectable bandwidth ΔE to get the number of photons produced. Furthermore, what really matters is the number of photons detected in a physical Cherenkov detector, so we must include an efficiency function $\varepsilon(E) = Q(E) \cdot T(E)$, which is the product of detector quantum efficiency and the transmission through any media that are present (as well as factors for other losses, such as mirror reflectivity or readout electronics efficiency), to arrive at:

$$N_{\text{det.}} = \left(\frac{\alpha}{\hbar c}\right) Z^2 L \int_{\Delta E} \varepsilon(E) \left[1 - \frac{1}{\beta^2 n^2(E)}\right] dE. \tag{4.3}$$

In the limit where $n(E)$ is relatively flat (*i.e.*, away from any absorption bands), we may approximate Eq. (4.3) by

$$N_{\text{det.}} = N_0 Z^2 L \sin^2 \theta_c, \tag{4.4}$$

where N_0 is the parameter

$$N_0 = \left(\frac{\alpha}{\hbar c}\right) \int_{\Delta E} \varepsilon(E) \, dE \tag{4.5}$$

which describes the response of a particular Cherenkov detector. Note that the constant $\alpha/\hbar c$ has a value of 370 eV^{-1}cm^{-1} in convenient units. For reference, a typical glass-windowed visible-light photomultiplier tube has a bandwidth from 2.0 to 3.2 eV and an N_0 of 60–70 cm^{-1}, assuming perfect radiator transmission [103]. A typical ring imaging detector achieves N_0 values of 30–80 cm^{-1} in the ultraviolet.

4.2   Principles of Cherenkov Ring Imaging

Traditional threshold Cherenkov counters use the presence or absence of photons to identify particles. The discussion of threshold counters is beyond the scope of this work, but a review can be found in [112]. The idea of using a measurement of the Cherenkov ring radius, rather than presence or absence of photons, in combination with a momentum measurement for particle identification was first put forward by Roberts in 1960 [113]. However, his design had small angular acceptance and utilized optical image intensifiers, which yielded N_0 values of only 2–15 cm^{-1} [103]. These factors made it insufficient for any application in detectors.

The first practical ring imaging detector was proposed by T. Ypsilantis and J. Séguinot in 1977 [115]. This prototype utilized an admixture of benzene in a gas-filled multiwire proportional chamber (MWPC), rather than photomultiplier tubes, for the detection of photons. With this technique, it became
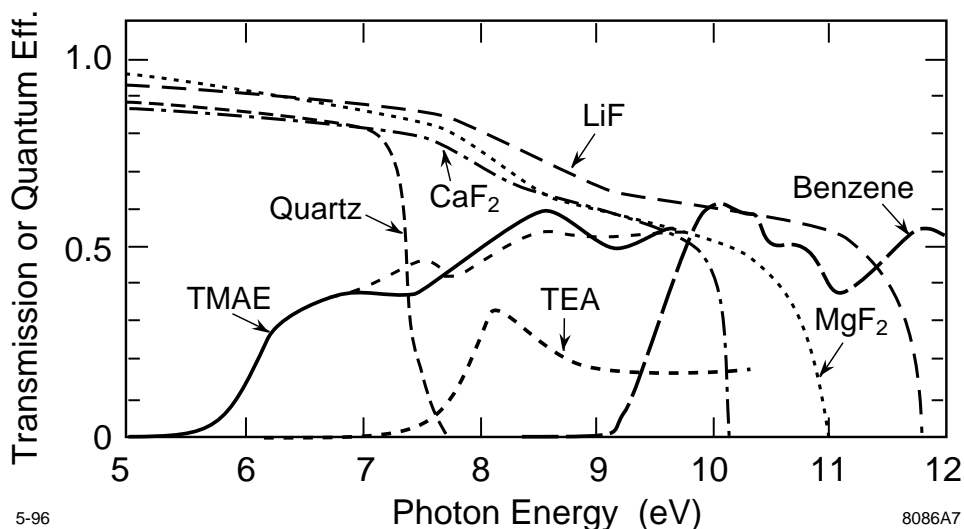
Figure 4.1: Quantum Efficiency $Q(E)$ or Transmission $T(E)$ as a function of photon energy E for various materials. The two curves for TMAE represent the measurements of [114] (solid) and [104] (dashed).
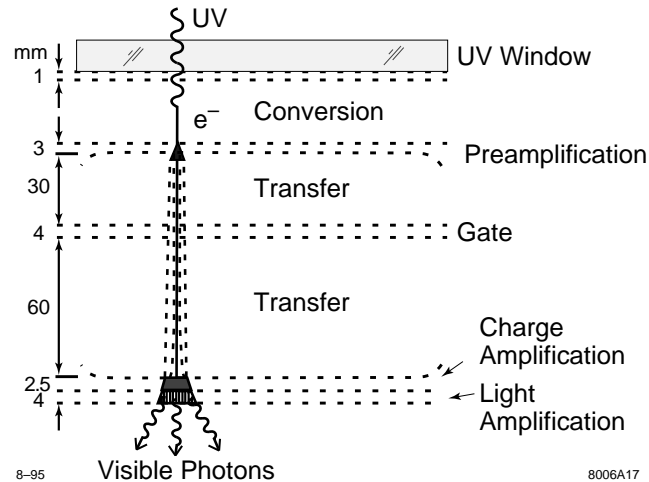
Figure 4.2: Diagram of a typical multistep avalanche chamber (MSAC). Dimensions and details differ from the 1979 detector of Charpak *et al.*, but the fundamental features of conversion, preamplification, and transfer stages are the same. This example uses an optical readout, but the final stage can also be a MWPC with digital readout.

practical to build large-area detectors that could resolve single photons with good spatial resolution.

The next generation of prototype was developed by Charpak, Majewski, Melchart, Sauli, and Ypsilantis in 1979, and utilized a multistep avalanche chamber (MSAC) with triethylamine (TEA) in He gas as the photocathode [116]. TEA has roughly half the quantum efficiency of benzene, but it extends to longer wavelengths (see Fig. 4.1). This makes the task of producing transparent windows much easier; for example, one can use CaF_2 instead of the more costly MgF_2 or LiF. It also increases the requirement for extremely low O_2 and H_2O contamination, since these two compounds are very absorptive in the wavelength region of the TEA quantum efficiency.

A diagram of a typical MSAC is shown in Fig. 4.2. The first visual Cherenkov ring images were seen by viewing the avalanche sparks with a photographic camera. This prototype initially achieved an N_0 of 27 cm^{-1}, but later achieved $N_0 = 56$ cm^{-1} when the mirror was replaced with one having better UV

reflectivity [104]. The Fermilab E605 experiment in 1981–83 went on to refine this design into the first ring imaging detector used successfully for particle identification (see section 4.4).

In 1980, a new photocathode material, tetrakis(dimethylamino)ethylene (TMAE), was explored by Anderson [117]. This compound had previously been used by NASA to track rocket trajectories in the upper atmosphere because it fluoresces green upon reaction with oxygen [103]. TMAE has an ionization potential of 5.4 eV and good quantum efficiency [114], thus permitting the use of fused quartz for windows instead of CaF_2.

The ability to cover large areas with transparent windows favored the use of time projection chambers (TPCs) for the detection of the Cherenkov photons. In this way, relatively few electronics channels could read out a large active area. After a demonstration of the ability to drift single photoelectrons 13-cm in a TPC by Barrelet *et al.* in 1981–82 [118], several groups converged on designs utilizing TMAE in quartz-windowed TPCs with MWPC readout. These designs became the Omega RICH [119], the DELPHI RICH [120], and the SLD CRID [76].

Cherenkov ring imaging is still a novel technology in particle physics detectors, and these ring imaging detectors represent the first large-scale uses of that technology in multipurpose detectors. Ring imaging offers significant advantages, however, over competing particle identification technologies.

Time of flight (TOF) is a relatively straightforward particle identification method that relies on precise timing measurements to compute β, given a known distance L travelled from the interaction point. The best TOF counters have achieved $\sigma_t \simeq 60$ ps in small scale prototypes [121], which would yield $\sigma_\beta/\beta^2 \simeq 2 \times 10^{-2}$ at $L \simeq 1$ m. By comparison, a typical ring imaging detector has resolution of $\sigma_\beta/\beta^2 = 7 \times 10^{-5}$ in the high-momentum gas-radiator region, and even in the proximity-focussed liquid-radiator region has typically a resolution of $\sigma_\beta/\beta^2 = 1 \times 10^{-3}$. This implies that a TOF detector at 1 m radius would require 3 ps timing to perform as well as a typical ring imaging detector, even for low momentum (1 GeV/c) particles [103].

The most common particle identification technology currently in use, for example at the LEP detectors, is ionization energy loss (dE/dx). This relies on the Bethe–Bloch relation [122] for energy loss of a charged particle travelling through a known material as a function of its velocity β. Identification is typically very good in the non-relativistic region up to ~ 1 GeV/c. In the relativistic-rise region (> 3 GeV/c), however, the separation is generally much less significant. In order to achieve 2–3σ of significance, precise corrections must be made for the varying geometric path length of tracks crossing a drift cell, for charge attenuation as a function of drift length, for gain variations due to changing gas pressure or density, for gain variations as a function of the electronics readout, or electrostatics, geometry, and performance of the cells, and for overlapping or partially-overlapping hits and cross talk. An example describing such corrections in detail can be found in [123]. Furthermore, the distribution of energy loss has a Landau tail, so truncated means and other more sophisticated statistical analyses are required. In practice, this technique is not used on a track-by-track basis at high momentum; instead, a purely statistical analysis is performed. In contrast, Cherenkov ring imaging has errors σ_θ that are roughly Gaussian, and separation in a design like the SLD CRID is typically sufficient up to 20 GeV/c or more for individual track identification.

4.3 SLD CRID Design

Although the Omega RICH, DELPHI RICH, and SLD CRID designs are all similar, we describe the SLD CRID design in some detail here. The three systems were developed concurrently and there was much contact and exchange between the two groups [124]. Much of our discussion applies equally to the DELPHI RICH design. The similar environments impose similar design constraints upon the choice of radiators, detector geometry, and so forth. Some of the differences are highlighted in section 4.4.

The environment of hadronic Z^0 decays at the SLC produces charged particles over a wide momentum range. In order to get good particle identification
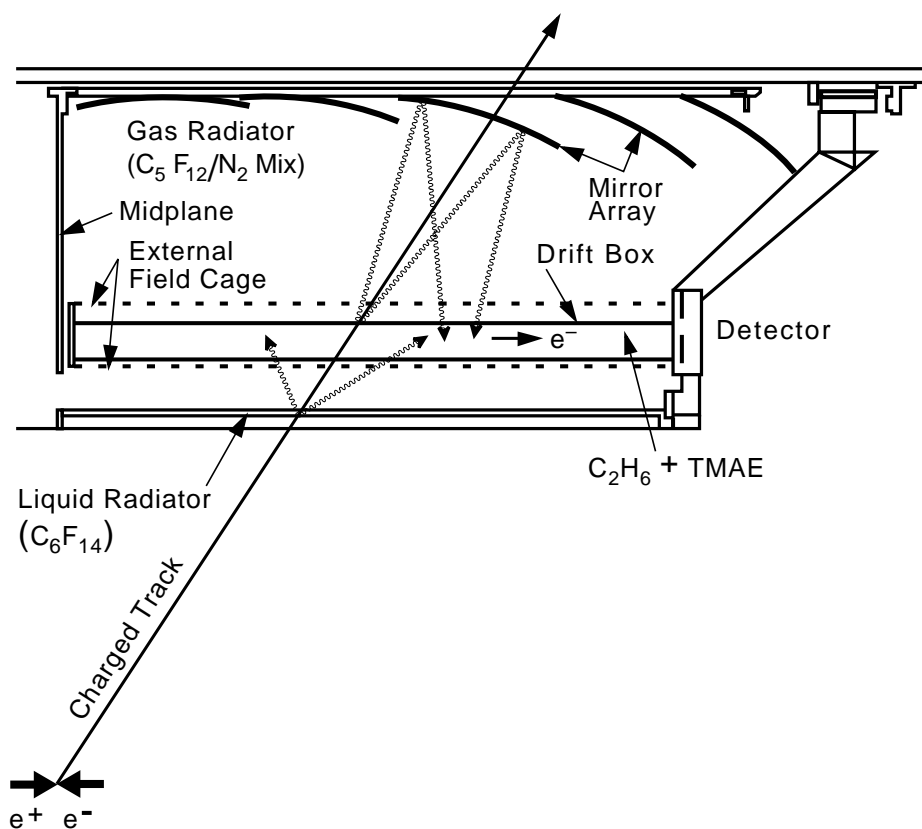
Figure 4.3: Sectional view of the SLD Barrel CRID. One sector is shown in the axial view. The layout is symmetric about the midplane.

performance over this range, two Cherenkov radiators are employed. So as to cover most of the available solid angle, the SLD incorporates both Barrel and Endcap CRIDs. The Barrel CRID was completed two years earlier than the Endcap CRIDs and is the more mature system. In addition, the SLD track finding is better understood in the barrel region. Therefore, we will focus exclusively on the Barrel CRID, which is depicted in Figs. 4.3 and 4.4.

The components of the Barrel CRID can be seen in Fig. 4.3. The liquid Cherenkov radiator (C_6F_{14}) is contained in 40 quartz-windowed trays. The gaseous radiator (C_5F_{12}) fills the vessel and relies on a set of 400 spherical
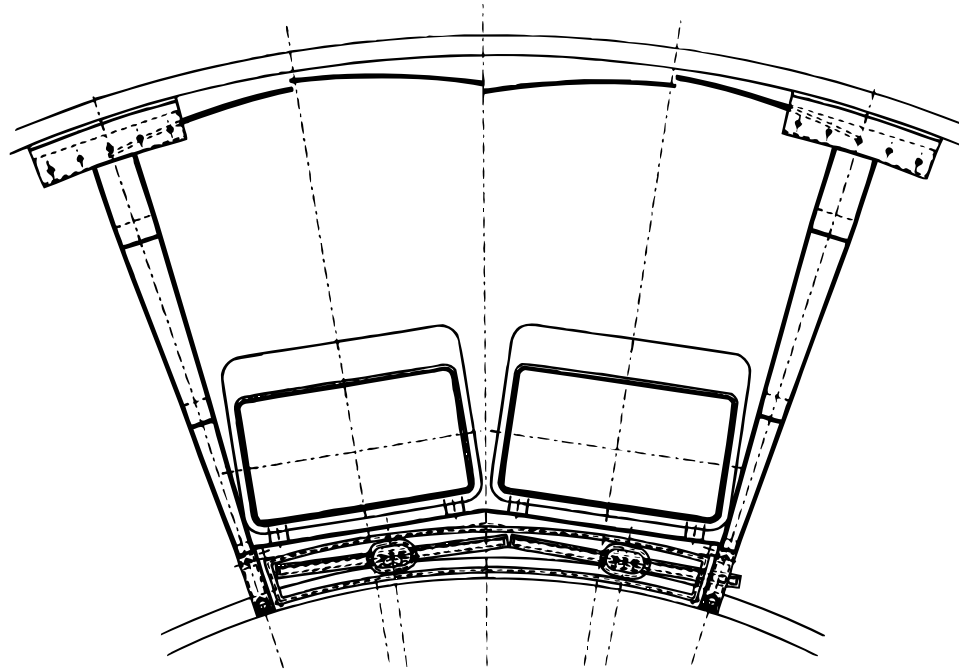
Figure 4.4: End-on view of the SLD Barrel CRID. One sector is shown in the radial view. There are 10 such sectors in each of the two halves (north and south).

mirrors to focus the Cherenkov photons onto the 40 TPCs that make up the active photon detection area of the Barrel CRID. The quartz-windowed TPCs are filled with C_2H_6 and 0.1% TMAE. The Cherenkov photons ionize the TMAE, and the resulting photoelectrons are drifted by an electric field to multi-wire proportional chamber (MWPC) detectors located at the outer end of the TPCs.

An Endcap CRID sector is shown in Fig. 4.5. The design of the Endcaps is similar to that of the Barrel, except that the Endcaps use only a gaseous C_4F_{10} radiator and must drift the photoelectrons perpendicular to the magnetic field. The liquid radiators were omitted for cost reasons, but this is not terribly harmful because the momentum threshold for tracking in the forward angular regions is significantly higher than in the central region. Since there is no liquid radiator, all Cherenkov photons can be focussed by mirrors onto relatively
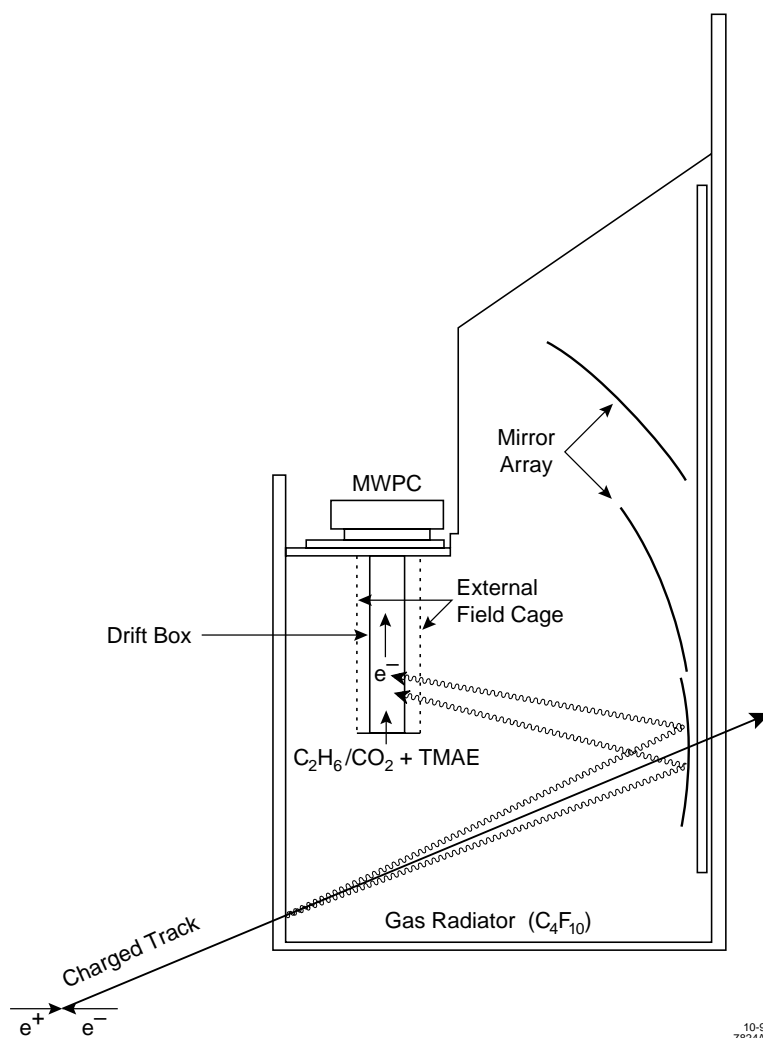
Figure 4.5: View of an SLD Endcap CRID. Each of the two endcaps is composed of five sectors, each containing one TPC and six UV mirrors. One such sector is shown here. The design is similar to the SLD Barrel CRID.

small (28.0 cm $\times$ 43.2 cm $\times$ 5.15–5.60 cm) TPCs. There are five TPCs and 60 mirrors in each of the two Endcaps. The drift gas is a mixture of 85% C_2H_6 and 15% CO_2, which is selected to minimize the Lorentz angle. A summary of the hardware performance to date of the Endcap CRIDs can be found in [125].

CRID Cherenkov Angle Curves
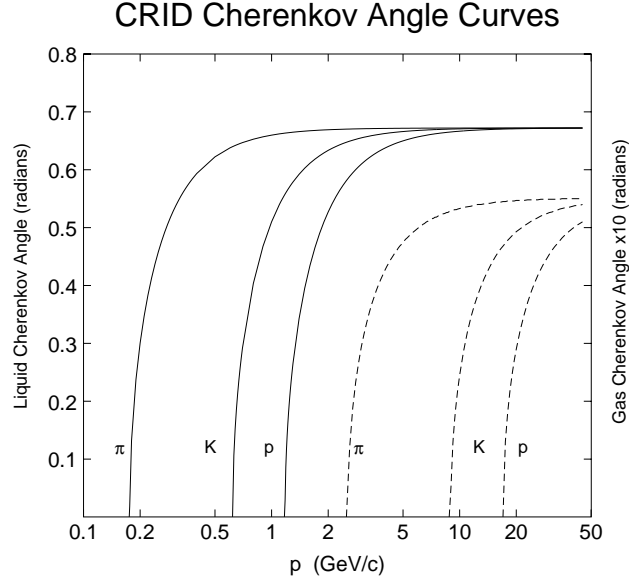
Figure 4.6: The Cherenkov angle as a function of momentum is shown for the two CRID radiators and for the three hadronic particle hypotheses.

4.3.1 Radiators

The SLD Barrel CRID is designed to provide particle identification over 70% of the available solid angle and for momenta up to 6 GeV/c (e/π) or 30 GeV/c (π/K/p). This is accomplished by a combination of liquid C_6F_{14} and gaseous C_5F_{12} radiators. Cherenkov angle curves for these two radiators are shown in Fig. 4.6. The two fluorocarbon radiators used in the SLD CRID were chosen for their refractive indices, so as to provide particle identification coverage with a minimal gap in momentum. They were also chosen for their transmission at relevant UV wavelengths, for their relatively low chromatic dispersion, and for their compatibility with other materials used in the CRID. Furthermore, fluorocarbons are non-flammable, unlike isobutane (C_4H_{10}), for example, which was also considered at one time for use as a gaseous radiator.

The liquid C_6F_{14} is contained in quartz-windowed trays of thickness 1 cm (see Fig. 4.3) and has an index of refraction $n = 1.2723$ at $\lambda = 190$ nm [103].
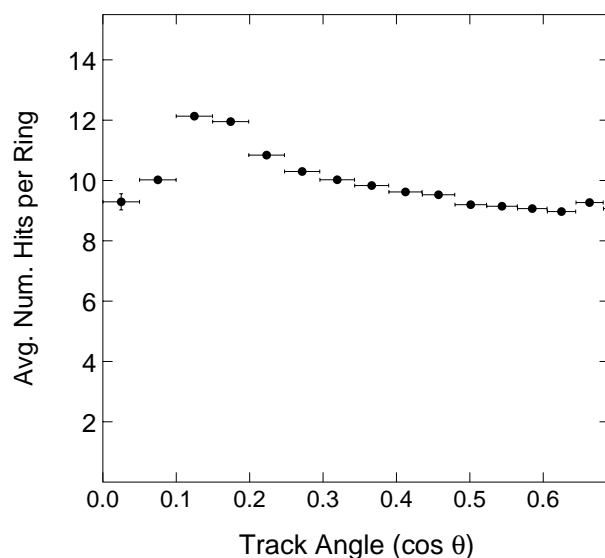
Figure 4.7: The average number of photons per liquid Cherenkov ring observed in hadronic events in the SLD CRID as a function of the track dip angle.

The Cherenkov light from the liquid radiator trays is imaged directly onto the TPCs. This situation, in which no optical elements are involved between the Cherenkov radiator and the photon detector, is known as *proximity focussing*. In this case, resolution on the Cherenkov angle relies on the relative thinness of the radiator compared to the distance from the radiator to the detection plane. The images of the Cherenkov rings start out as conic sections, but are distorted by refraction at the radiator window. In addition, total internal reflection can cause a loss of photons, but in practice this loss is at most 50% for track dip angles less than $45°$ and part of that loss is offset by the longer path lengths seen by tracks entering at large angles to the radiator plane (see Fig. 4.7).

The gaseous C_5F_{12} radiator is contained within the volume of the CRID vessel, most of which lies outside the radius of the TPCs. A set of 400 UV-reflective spherical mirrors [126] installed on the outer cylinder of the CRID vessel is used to reflect the Cherenkov photons onto the 40 TPCs. A spherical mirror

focusses parallel rays emitted at different points along a track's trajectory into a single point at a focal distance equal to half of the mirror's spherical radius [115]. This is important because otherwise the 45-cm average path length would completely obscure the necessary precision in Cherenkov angle.

The C_5F_{12} radiator gas has a condensation point of 30 °C. In order to keep it gaseous with some safety margin, the entire Barrel CRID is designed to operate at 40 °C. To date, however, this high-temperature operating point has not been achieved because of safety concerns for the SLD drift chamber. Instead, the CRID is operated at 35 °C, and the gaseous radiator is mixed with nitrogen in a ratio of roughly 85% C_5F_{12} to 15% N_2. This yields an index of refraction of about $n = 1.0017$ at $\lambda = 190$ nm [127].

4.3.2 TPCs

The Cherenkov photons from the two radiators are imaged onto 40 quartz-windowed TPCs, where they photoionize the C_2H_6 drift gas with TMAE dopant. The resulting single photoelectrons are drifted parallel to the SLD magnetic field by an electric field of 400 V/cm to proportional wire planes (MWPCs) at the outer edge of the CRID (see Fig. 4.8). The volume inside the TPCs is 126.8 cm long by 30.7 cm wide, with a thickness that tapers from 5.6 cm at the high voltage end to 9.2 cm at the detector end. This taper prevents transverse diffusion from causing electron losses near the faces of the TPC. The taper is not symmetric; instead, there is more taper on the outer side of the TPC (the gas radiator side) to compensate for the small radial component of the SLD magnetic field, which imparts a Lorentz force on the drifting photoelectrons (see section 7.4).

The two large-area surfaces of the TPCs are composed of fused quartz, while the other surfaces are G-10.[*] All the pieces are held together by DP-190 epoxy.[†] In addition, the side surfaces are double-walled as seen in Fig. 4.9. This provides a small gas volume (referred to as the "DMZ") that can be purged with

---

[*] G-10 fiberglass epoxy, NVF Technical Products, Kennet Square, PA.
[†] DP-190 epoxy, 3M Inc., St. Paul, MN.
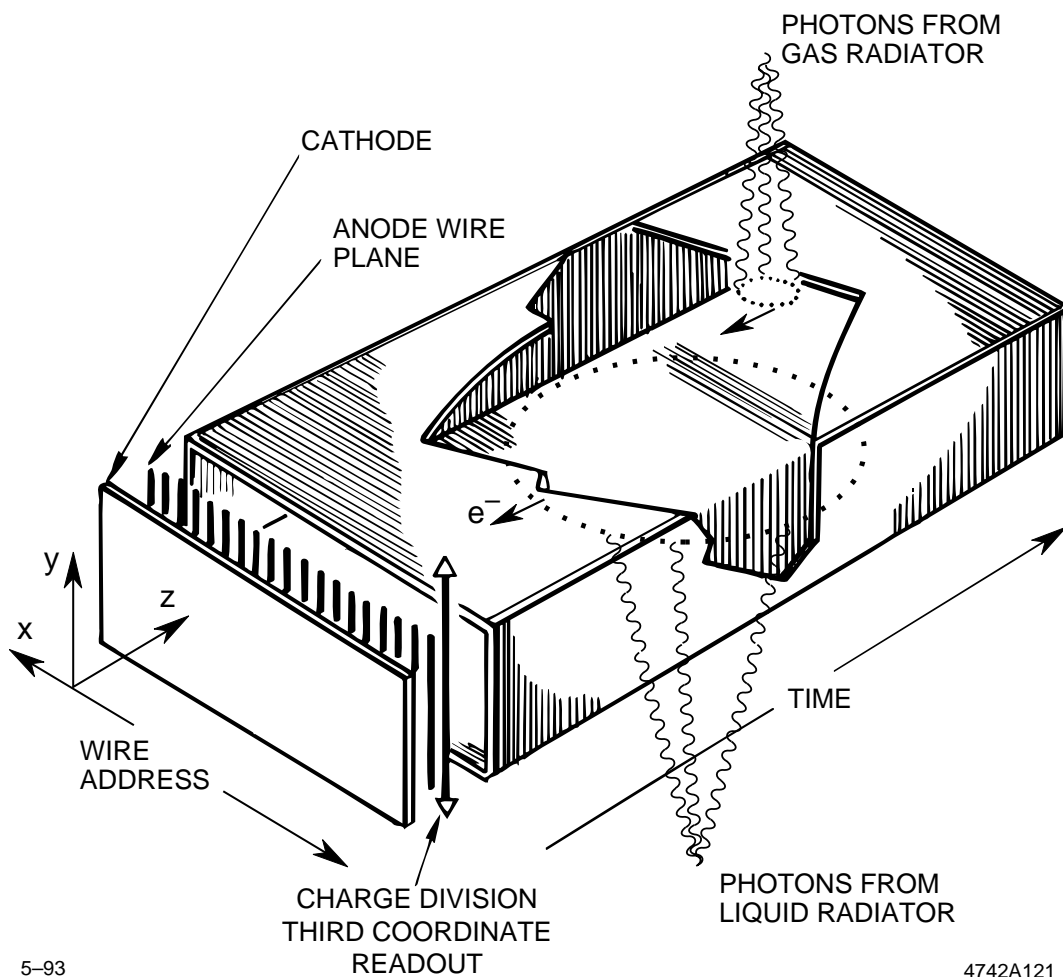
Figure 4.8: Schematic view of a TPC and MWPC detector for the SLD Barrel CRID. Also shown is the standard TPC coordinate system employed in the CRID reconstruction.

N_2 in order to prevent any of the C_5F_{12}, which has a large electron absorption cross section, from leaking into the drift volume through the glue joints.

The inner and outer surfaces of both the quartz and G-10 sides of the TPCs are covered with metal traces, placed on a 3.175 mm pitch. The quartz surfaces have large Cu-Be etched arrays to provide the traces, while the G-10 walls use copper strips. The potentials of all these traces are set via a resistor ladder

Resistor
chain

Sidewall purge
space

G10 Circuit boards with
1/8" pitch copper traces
on each side

Solder
Connection

Epoxy
Glue
Joints

Plated-Through
Holes

Conductor tabs
bent & soldered
to inner & outer
walls

Quartz
Windows

Field
cage
wires

Individual conductors of
etched arrays, tensioned
and glued to windows

4-90
6560A24
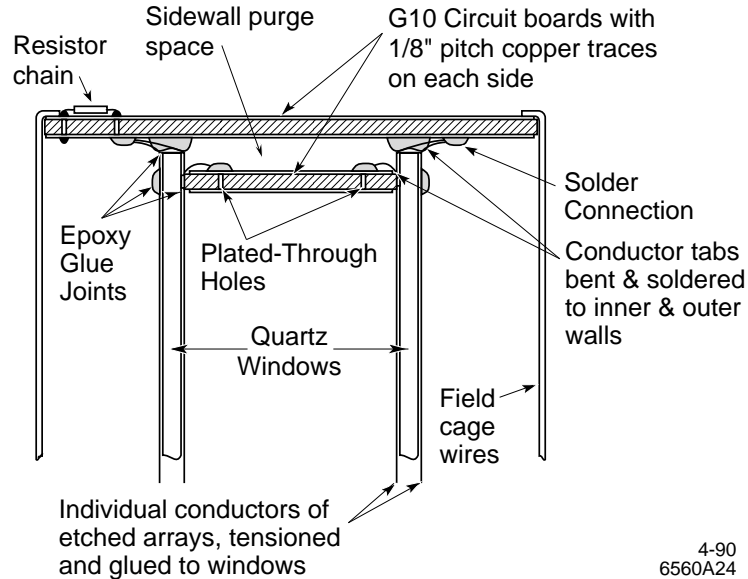
Figure 4.9: Cross-section of an SLD CRID TPC showing construction materials and the interconnection of various electrostatic traces.

connecting the 55 kV high voltage end of the TPC with the 1.5 kV detector end. In addition, there are spark gaps across every four resistors in order to protect the resistors from possible spark damage. The potentials of these traces shape the field inside the TPC, together with an additional Cu-Be wire field cage that serves to reduce the danger of corona discharge from the sharp edges of the TPC traces [128, 129]. The field cage wires can be seen in Fig. 4.10.

4.3.3 Drift Gas

The selection of the drift gas is governed by concerns for UV transparency and long electron lifetime. In addition, a high gas gain and good quenching properties are required, and electron diffusion should be minimized. Early tests employed a mixture of CH_4 and C_2H_6, but later tests showed that pure C_2H_6 was sufficient [130]. Clearly, a single-component gas simplifies the gas delivery
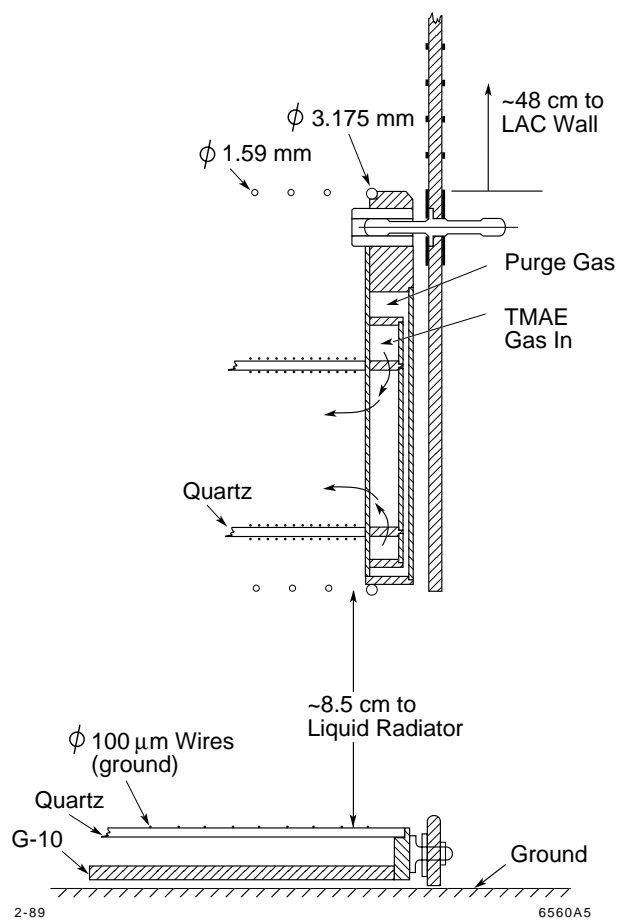
Figure 4.10: Schematic of the high voltage end of SLD CRID TPCs.

system. Furthermore, gas mixtures have the difficulty that drift velocity varies with the precise mixture and is therefore less stable.

The TMAE is introduced into the drift gas by bubbling the gas through liquid TMAE in a constant temperature bath. The concentration is thus determined by the vapor pressure of TMAE. For the 1994–95 run, the TMAE bubbler was operated at 27 °C. This corresponds to a TMAE concentration of $\sim 0.1\%$, which yields an absorption length of 1.9 cm. The drift gas delivery system is described in more detail in Chapter 5.
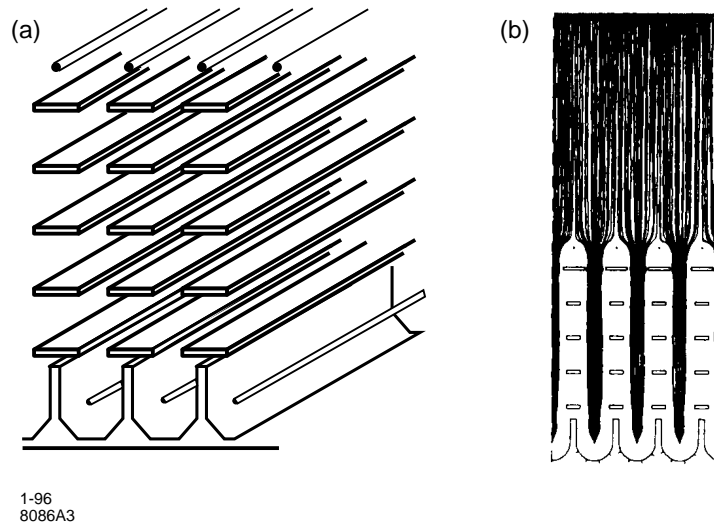
Figure 4.11: A schematic of the SLD CRID MWPC detector is shown in (a), and the field lines from an electrostatic simulation of the detectors is shown in (b).

4.3.4 Detectors

Detection of the photoelectrons is accomplished by a proportional wire plane composed of 93 7-μm carbon filaments on a 3.175 mm pitch. The wires are 10.35 cm long and oriented along the radial direction of the CRID. The radial coordinate of the photoelectrons is determined by reading out both ends of the resistive wire with separate amplifiers and comparing the amplitudes obtained. This process of charge division is the same as that used in the SLD CDC, and is unique among ring imaging devices. The DELPHI RICH detectors use cathode strips for readout of the third coordinate [120], and the Omega RICH uses only two-coordinate readout [119]. A more complete description of the CRID detectors can be found in [131].

The choice of 7-μm wires was made in order to obtain the best charge division performance and in order to minimize electronic noise in the system. Early tests showed that the 7-μm wires gave a charge-division performance

of $\sigma_y/l = 0.7\%$, while 33-μm wires had $\sigma_y/l = 1.4\%$. Performance of the 7-μm wires in the actual SLD detectors, however, is $\sigma_y/l = 2.5\%$ [132]. This is due partly to increased noise in the production CRID amplifiers, but mostly to the choice of lower operating gain (1.5 kV v. 1.55 kV) made because of aging concerns [133]. However, this charge division resolution of $\sim 2\%$ has been shown to have minimal effect on the Cherenkov angle resolution σ_θ (see section 7.5). In practice, the 7-μm wires have proven difficult to work with and are very fragile in operation. The breakage rate has been some 0.2–0.3% per run, which may seem small but is actually substantial since each broken wire removes one TPC from operation until the detector can be extracted.

One difficulty that was realized in the course of development for the three large-scale ring imaging detectors is the effect of photon feedback. During the avalanche that occurs at the anode wire, the atomic levels of carbon (in the CH_4 or C_2H_6 drift gas) can be excited, and UV photons of wavelength 156, 166, and 193 nm are emitted [134]. If the drift gas is sufficiently transparent to these photons, they can travel back into the drift volume and photoionize just like the Cherenkov signal photons. The solution that was adopted by all three groups was to build "blinds" into their MWPC detectors. These blinds are opaque structures designed to absorb the majority of these feedback photons. In the SLD CRID, a stack of five Cu-Be etched arrays separated with G-10 spacers is used for this blinding structure. These, along with the U-shaped cathode structure are depicted in Fig. 4.11. The 93 openings in the etched arrays are 2 mm wide and limit the angle in which avalanche photons can reach the drift volume to 6.6°. Feedback rates were measured to be less than 1% at nominal gain with blinding, compared to about 6–8% with no blinding [128]. The feedback rate has been measured to be $< 1\%$ in the production detectors.

The Barrel CRID detectors are operated at a total gas gain of 2–3×10^5, which corresponds to a cathode voltage of 1500 V. This operating point is a compromise between a sufficiently high gain to maximize the number of pulses above noise threshold and to improve charge-division resolution on the one hand, and a sufficiently low gain to minimize photon feedback and to minimize

aging of the wires [135] on the other hand.* Operating experience has shown that this compromise is difficult to reach.

4.3.5 Detector Readout

A description of the CRID readout electronics and data processing can be found in [136], and the general SLD data acquisition features are described in section 3.2.7. Briefly, the amplifiers on both ends of the CRID wire planes are read out in 67.2 ns buckets into a hybridized 512-channel switched capacitor array, known as the Analog Memory Unit (AMU) [97, 137], and then serially digitized in 12-bit ADCs. These amplitudes are zero-suppressed and corrected for pedestals in the Data Correction Units (DCUs) [138]. Minimal processing is done in the FASTBUS Waveform Sampling Module (WSM) CPUs, and this "snipped" (*i.e.*, sparsified) amplitude information is sent to FASTBUS ALEPH Event Builders (AEBs) [98] and then to a VAX 8800 and onto tape. All pulsefinding is currently done offline, which allows for tuning and debugging of the pulsefinding algorithm. The pulsefinding is discussed further in section 6.1.

4.3.6 Required resolution

The performance of a Cherenkov ring imaging detector is summarized by the resolution on the measured particle velocity, σ_β, which can be parametrized in terms of two basic quantities: the number of photons observed per Cherenkov ring $N = N_0 L \sin^2 \theta_c$ and the resolution in Cherenkov angle on an individual photoelectron σ_θ,

$$\sigma_\beta = \beta \tan \theta_c \frac{\sigma_\theta}{\sqrt{N}} = \frac{n\beta^2 \sigma_\theta}{\sqrt{N_0 L}}. \tag{4.6}$$

Thus, we see for example, that in order to achieve the SLD CRID design of 3σ π/K separation at $30\ \mathrm{GeV}/c$, $\sigma_\beta/\beta^2 = 4.2 \times 10^{-5}$ is required. The SLD design

---

*There is a system to heat the wires via a DC current [129], but this system has not been tried on the CRID detectors because of concerns about the heat breaking wires.

parameters for achieving this precision are $N_0 = 100$ cm^{-1}, $L = 45$ cm, and an angular precision of $\sigma_\theta = 3$ mrad. In practice, the achieved performance is somewhat short of the design, with $\sigma_\beta/\beta^2 \simeq 7 \times 10^{-5}$ (see sections 7.12 and 7.13).

The Cherenkov angle resolution has obvious contributions from the measurement precision $\sigma_x/\sigma_y/\sigma_z$ of photoelectrons, related by the geometry of the Cherenkov angle reconstruction (see sections 6.2 and 6.3). However, there are other irreducible contributions to angle resolution from chromatic errors, thickness of the proximity-focussed liquid radiator, multiple scattering of the incident particle, and bending of the particle in the magnetic field. The magnetic bending error in the SLD CRID gas radiator, for example, is $15/p$ mrad (with p expressed in GeV/c) averaged over the Cherenkov azimuthal angle. This becomes the dominant contribution to resolution for tracks below about 4 GeV/c. The chromatic errors are caused by optical dispersion ($n(E) \neq$ constant) over the detector bandwidth. This is discussed in detail in [103]. For the SLD CRID design, the chromatic errors are about 5 mrad in the liquid and about 0.3 mrad in the gas. The liquid radiator thickness contributes an average of ~ 7 mrad resolution, which is roughly comparable to the contribution from spatial precision. The spatial precision on individual hits, however, dominates the Cherenkov angle resolution in the gas region. The SLD design of ~ 1 mm precision yields ~ 3 mrad resolution.

4.4 Other Ring Imaging Detectors

There are several other large-scale Cherenkov ring imaging detectors that were developed contemporarily with the SLD CRID, and there are several more that were developed later as a "second generation" of detectors. For a discussion of some of these second-generation detectors, see for example [139]. The various early ring imaging detectors fall into two general classes: those installed in fixed-target experiments (E605 and Omega) and those in collider experiments (SLD and DELPHI). The fixed target detectors were generally quicker in development and produced physics results sooner. The collider detectors had more

difficult engineering and operational constraints (*e.g.* limited access for long runs, requiring greater reliability). Consequently, it is not so surprising that it took longer for the DELPHI and SLD detectors to reach reliable operation and to produce useful physics results.

The first ring imaging detector to operate successfully in a physics experiment is the Fermilab E605 CRID. This was a MSAC detector with a He radiator, CaF_2 windows, and He-TEA drift gas. Readout was digital with two planes of crossed cathode wires in addition to the 20-μm anode wires. This allowed for fairly straightforward reconstruction of two-dimensional space points, provided that the multiplicity remained below about 4 hits or so. The observed performance was an average of 2.8 hits per ring, but the point resolution was $\sigma_\theta = 0.059$ mrad, which was dominated by the chromatic dispersion. E605 achieved π/K separation from 50 to 120 GeV/c [140].

Though its development started at about the same time as the DELPHI and SLD devices, the Omega RICH was completed in 1984 and ran in the CERN WA69 experiment. It uses only a 5-m long N_2 radiator with mirrors to focus rings onto 16 short-drift (20-cm) TPCs. The Omega detectors use 20-μm gold-plated tungsten wires with 4-mm fiberglass blinds. Since the TPCs are sufficiently thin and the photons are focussed at near-normal incidence, there is no attempt to read out three dimensions. Due to various problems in the design of the TPCs and detectors, the photon detection efficiency was only $\sim 30\%$, resulting in an N_0 of 35 cm^{-1}, for an average of 10.5 photoelectrons per ring [119]. This was adequate, however, for good identification performance, and 3σ π/K separation from 5 to 100 GeV/c was achieved. The central TPCs and gas system were upgraded for the WA89 experiment in 1990, and the N_0 was improved to 49 cm^{-1} [141].

In the autumn of 1985, a RICH detector was installed in one of 12 azimuthal sectors of the UA2 endcap in order to measure the e/π ratio in $p\bar{p}$ events. The detector consisted of a 60-cm long vessel filled with C_2F_6 and a mirror to focus Cherenkov photons onto a 20-cm TPC with MWPC readout. The N_0 achieved was 47 cm^{-1}, and the e/π rejection factor was 10^{-4} over the range

of 2–4 GeV/c [142]. This was the first ring imaging device used in a collider detector, but its limited coverage and duration of operation did not present the engineering problems faced by SLD and DELPHI.

The DELPHI RICH detector is very similar to the SLD CRID. The choice of radiators is identical, except that the DELPHI RICH does operate at 40 °C with 100% C_5F_{12}. In 1992, the gas radiator pressure was increased to 1.3 bar from atmospheric pressure. The TPC designs are similar as well. The DELPHI RICH employs a volume degrader on its inner cylinder and vacuum-deposited traces on its TPC windows to define the electric field. The SLD CRID uses etched arrays on the TPC windows and holds the inner cylinder at ground, transferring the design problem to that of controlling corona discharge from the TPC traces and field cage.

As discussed above, the SLD detectors use 7-μm carbon wires and charge division, while the DELPHI RICH uses more conventional 20-μm gold-plated tungsten wires with cathode strip readout. The blinding structure is similar, but DELPHI uses 10-mm alumina blinds instead of the etched arrays used in SLD. Minimum ionizing pulses cause a large cross-talk signal in the cathode strips, blinding a region of the TPC around the MIP hit. This is estimated to cause a 20% loss of photoelectron signal in hadron jets [143].

The DELPHI RICH performance in $e^+e^- \rightarrow \mu^+\mu^-$ events has been reported as $N_0 = 32$ cm^{-1} and $\sigma_\theta = 13.9$ mrad in the liquid, and $N_0 = 50$ cm^{-1} and $\sigma_\theta = 4.5$ mrad in the gas [143]. The performance in hadronic events degrades slightly, particularly in the liquid, to $\sigma_\theta = 17$ mrad. This effect is attributed to higher backgrounds due to very low energy electrons and δ-rays which produce Cherenkov light in the quartz windows of the TPCs [104].

The SLD CRID performance will be described in some detail in Chapter 7, but it is roughly comparable to that of the DELPHI RICH, with perhaps slightly better N_0 values. The details of the CRID reconstruction process and particle identification algorithm are described in Chapter 6. The next chapter describes some more about the CRID fluid systems, which play a vital role in achieving good performance.

Chapter 5

CRID Fluid Delivery and Monitoring Systems

One of the largest engineering challenges of developing a successful Cherenkov ring imaging detector is that of maintaining the quality of the various materials involved in the detector. In the case of systems like the SLD CRID, the materials of most concern are the C_5F_{12} and C_6F_{14} radiators and the TPC drift gas, although the transparency of quartz windows, the reflectivity of the UV mirrors, and the integrity of construction materials like G-10 sidewalls, plumbing seals, and various gaskets are also significant concerns.* Some second-generation ring imaging designs employ solid Cherenkov radiators [145, 146] to avoid the complexity of radiator fluid systems. Nevertheless, fluid radiators do have the advantage that purity and UV transparency are maintained in a system external to the detector, which is accessible at all times during running.

The challenge of the gas and liquid radiator systems is to ensure good UV transparency and stable refractive index for those materials. As discussed in section 4.3.6, particle identification performance depends on the square root of the number of photoelectrons detected. With operating points of 10–15 photoelectrons per ring, there is not an excess of hits to spare, and so optimal

---

*See [144] for a summary of the extensive material-testing program undertaken by the CRID group to ensure integrity of construction materials under prolonged exposure to TMAE and fluorocarbons.

UV transparency of the Cherenkov radiators is vital to successful operation. Because of the expense of both fluorocarbons, these systems for the SLD CRID are necessarily of the recirculating type. This adds an additional level of complexity, as trace quantities of contaminants can be accumulated during each circulation and gradually build up to cause significant problems. Therefore, sophisticated filtering must be built into the systems to ensure that such contaminants are removed.

The challenge of the drift gas delivery system is even more severe. Although it has wonderful photoionization properties, TMAE is highly reactive with oxygen and with many plastics. The oxides of TMAE, primarily tetramethyloxamide (TMO), are highly electronegative and would destroy the ability to drift single photoelectrons over the 1.2-m TPC, even in trace concentrations. Therefore, the drift gas system must be free of O_2 to better than 1 ppm. In order to meet this requirement, the entire system is built from electropolished stainless-steel tubing, with all joints either orbital welded or made using silver-plated metallic gaskets.[*]

A further challenge of all three fluid systems is to maintain pressures such that there is never a pressure differential large enough to crack the quartz windows in the TPCs or liquid trays. This pressure difference is estimated to be ~ 10 torr, which compels one to an operating region of ± 1–2 torr. This pressure limit must be enforced at all times, requiring fail-safe control systems, which are provided by a system of passive bubblers and active electronic control in the case of the two gas systems, and by a gravity-fed, passive design in the case of the liquid C_6F_{14} system.

In order to meet the purity requirements, all three fluid systems have the capability for routine monitoring of fluid quality built into them. These monitors are essential for the timely discovery of problems, for locating the source of problems, and for the commissioning of the systems at the beginning of each run. Much of these monitoring systems is automated. Measurements are made

---

[*]VCR fitting, Cajon Inc., Macedonia, OH

continuously and an alert is raised if any value is out of tolerance. This is controlled by software running on a dedicated microvax (VaxStation II) computer.

The CRID is operated at elevated temperature in order to achieve sufficient concentration of TMAE in the drift gas and to prevent condensation of the C_5F_{12} gas radiator.[*] As discussed in section 4.3.1, the CRID design was to operate at $40\,°C$, but concerns about the reliability of the CRID–CDC cooling shield and the danger to the CDC wires from an elevated temperature have limited CRID operation to $35\,°C$. Nevertheless, this temperature must be maintained uniformly within the CRID and stably in time. This is accomplished by a system of 200 Kapton-encapsulated heater pads and 1000 solid-state temperature probes, operating under software control on the CRID microvax.

Each of the above elements is briefly surveyed in the remainder of this chapter. Details of the overall design are available in [147, 148]. A summary of operating experience with these systems can be found in [149].

5.1   Liquid Radiator Recirculation

The liquid C_6F_{14} recirculation system is shown schematically in Fig. 5.1. More detailed descriptions of the system can be found in [147, 150, 76]. The system is gravity-fed, with a set of spill tanks providing pressure limits for each liquid tray. Gear pumps[†] are used in the system only to pump the C_6F_{14} through filters and up from the sump reservoir into the feed reservoirs. Purification consists of bubbling pure N_2 through the liquid reservoir to remove O_2 and pumping approximately half of the recirculating flow of C_6F_{14} through Oxisorb[‡] filters. The need for this continuous cleaning is demonstrated in Fig. 5.2. To maintain good purity, the Oxisorb cartridges are changed every four months or so. The loss rate of C_6F_{14} in the system has been measured to be about 180 cc/day and is consistent with evaporative losses.

---

[*]The boiling point of C_5F_{12} is $28\,°C$.

[†]Micropump, Concord, CA

[‡]Messer Griesheim GmbH, D-4000 Düsseldorf 30, Germany

CRID Liquid Radiator
Circulation System

Oct. 25, 1992

to All Buffer Volumes

to Atm.

N2

Distribution Tank South

Distribution Tank North

Pressure Defining Bubbler

for de-oxygenation

C6F14

Cooling Loop

to Spill Tanks

High Flow Bubbler

Condenser

Oxisorb

Spill Tank

Pump

Pump

C6F14 Liquid Reservoir

Liquid Tray

N2

for de-oxygenation

from Liquid Trays

to Monitor

from Spill Tanks

Safety Bubbler

to Atm.

Main System Sump

Pump

———— : C6F14 liquid;   ▬▬▬ : C6F14 liquid drain;   ▬▬▬ : N2/C6F14 vapor;

Figure 5.1: A schematic of the CRID C_6F_{14} liquid radiator recirculation system.
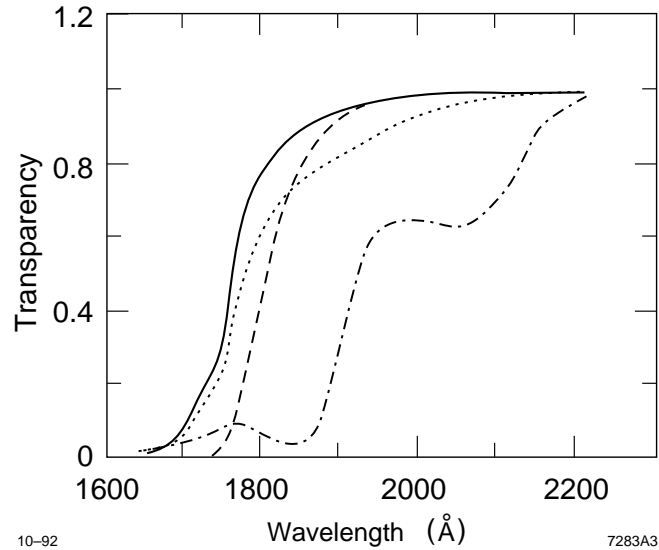
Figure 5.2: The transparency of 1 cm of clean C_6F_{14} liquid (solid), fully-oxygenated liquid (dashed), liquid exposed to G-10 for 107 days (dotted), and liquid exposed to DP-190 for 128 days (dot-dashed) are shown.

5.2 Gas Radiator Recirculation

The CRID vessel is operated at 30–35 °C. Since this is not sufficiently above the condensation point of pure C_5F_{12} (28–30 °C) for safe operation, the CRID vessel is filled with a mixture of 87% C_5F_{12} and 13% N_2. The condensation point of this mixture is ~ 22 ° C [127].

The recirculation system operates in a distillation mode, as shown in Fig. 5.3. The return gas from the vessel enters a large -80 °C tank, where the C_5F_{12} liquefies and the N_2 gas is vented (this requires about 1 kW of cooling power). The liquid C_5F_{12} is extracted from the bottom of the tank and vaporized in an electrically-heated evaporator, where it acquires enough pressure to reach the vessel. This gas is then mixed with purified nitrogen to achieve our desired C_5F_{12}/N_2 ratio. The gas mixture is measured with a sonar mixture detector [151]. The gas composition measurement is digitized and fed back electrically to the N_2 flow controller to adjust the mixture automatically. The overall

CRID Radiator Gas Circulation System
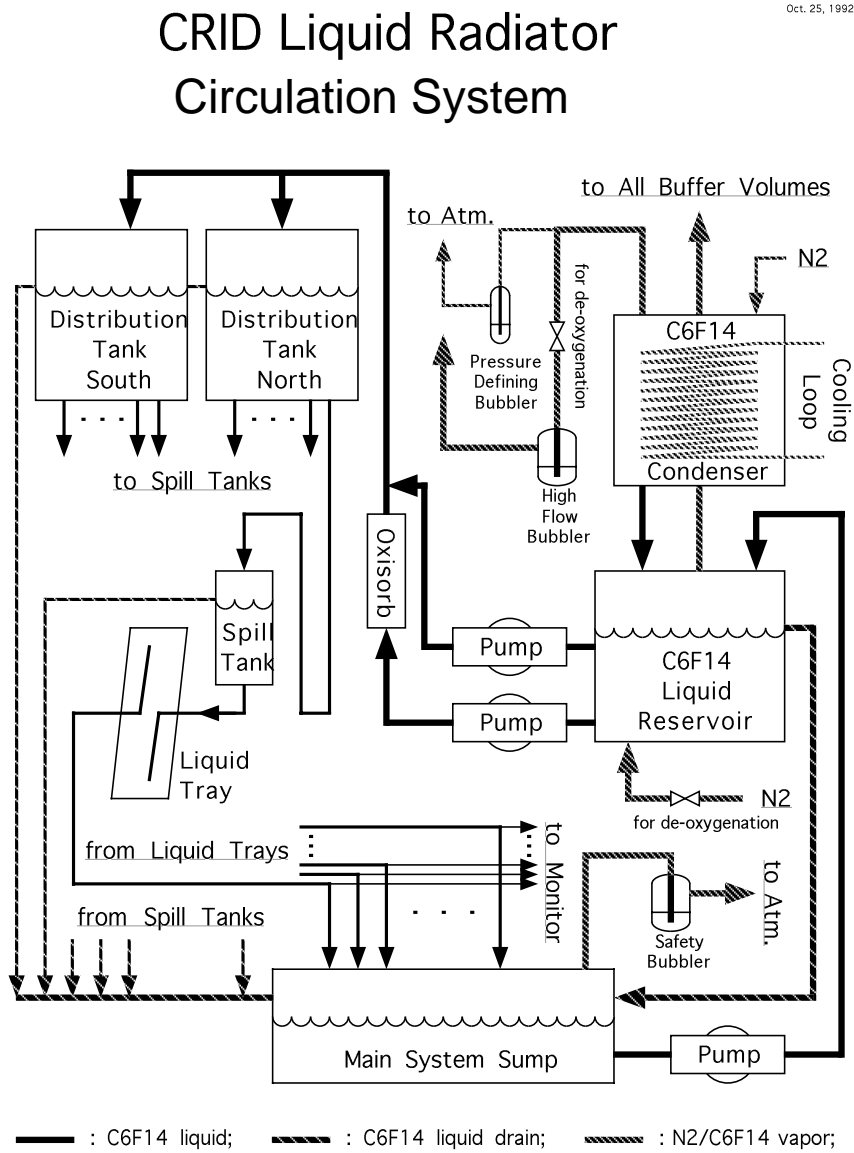
Sep. 25, 1992

Figure 5.3: A schematic of the CRID C_5F_{12} gas radiator recirculation system is shown.
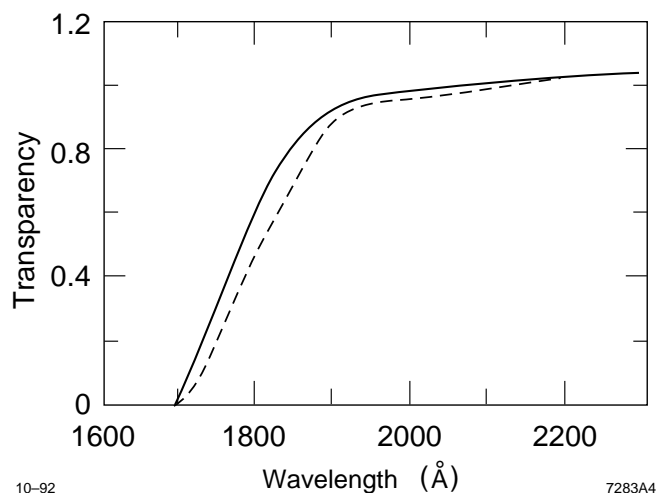
Figure 5.4: The transparency of 1 cm of clean C_5F_{12} in the liquid phase (solid curve) is shown. Also shown is the 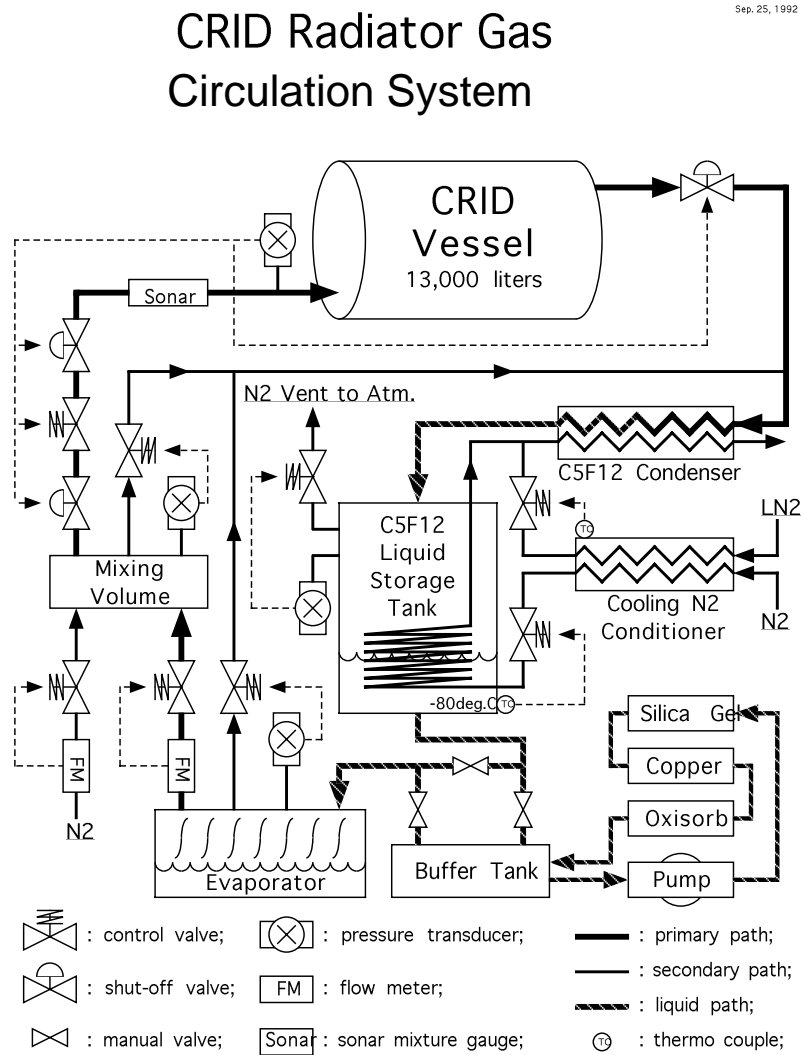transparency of 1 cm of C_5F_{12} liquid after it has been circulated through the CRID vessel for 11 days without any filtration (dashed curve). With normal filtration, the dashed curve returns to the transparency of the solid curve.

flow is 15–20 l/min., or about one volume change every 11 hours. The design of the gas recirculation system is described in more detail in [149, 147].

Along with the sonar detector on the inlet flow, there is a set of six ultrasonic transmitters and receivers mounted at three levels in the CRID vessel (three on the North side and three on the South). The operation of these "sonar" sensors is described in detail in [151]. By measuring the sound velocity in the CRID vessel, the relative concentration of C_5F_{12} and N_2 can be determined, and from this the index of refraction of the gas radiator. Stratification of the C_5F_{12}/N_2 mixture can be checked for by comparing the sonar meters at the three heights.

In addition to the distillation process itself, the C_5F_{12} is purified in the liquid phase by filtration. A sliding-vane pump[*] circulates the C_5F_{12} liquid from the -80 °C reservoir through a set of silica gel,[†] elemental copper,[‡] and Oxisorb

---

[*]Caster MPA-114, R. E. MacDonald Co., Foster City, CA
[†]Silica Gel Sorbead R, purchased from Adcoa Co., Gardena, CA
[‡]Ridox, made by Engelhard Co., Elyria, OH

filters back into the reservoir. One set of these cartridges is typically sufficient for one year's running. The effect of the filtration is shown in Fig. 5.4.

5.3   Drift Gas Delivery

Figure 5.5 depicts the CRID drift gas delivery system. High purity C_2H_6 gas is delivered in tube trailers and filtered through 13X molecular sieve and Oxisorb. During certain periods of running, there was a problem with sulfur contamination in the C_2H_6 gas. During this time, a nickel-catalyst filter was added. However, the filter outgassed O_2 and CO_2 when heated as it absorbs sulfur (exothermally). The O_2 is trapped in the standard Oxisorb filters, but the CO_2 remains in the drift gas, causing temperature-dependent variations in drift velocity (see section 7.1). Therefore, the Ni filter was removed when a more pure supply of C_2H_6 gas was obtained.

After filtration, the C_2H_6 drift gas is delivered through a mass flow controller (MFC) to a high-flow bubbler [152] filled with liquid TMAE and held in a constant-temperature bath. The concentration of TMAE induced into the drift gas is determined by the bath temperature (and must therefore be held stable to ± 0.5 °C). This bubbler holds about 8–10 l of TMAE and is capable of supporting flows of up to 10 $l/$min. The purification procedure for the TMAE is described in [147]. A safety system operates a triplet of valves around the bubbler and allows the bubbler to be automatically bypassed should any hazard alarm be raised.

A typical flow rate is 6 $l/$min for all 40 TPCs. Each TPC has a capacity of approximately 37 l, giving a time per volume change of about 4–5 hours. The flow through each drift box is determined by the relative heights of oil in each of the 40 TPC exit bubblers. The output of these bubblers flows into a common vent. The pressure in each TPC is determined from the vent pressure, the bubbler height, and the flow rate through the bubbler. This pressure is typically 1 torr above atmospheric pressure.

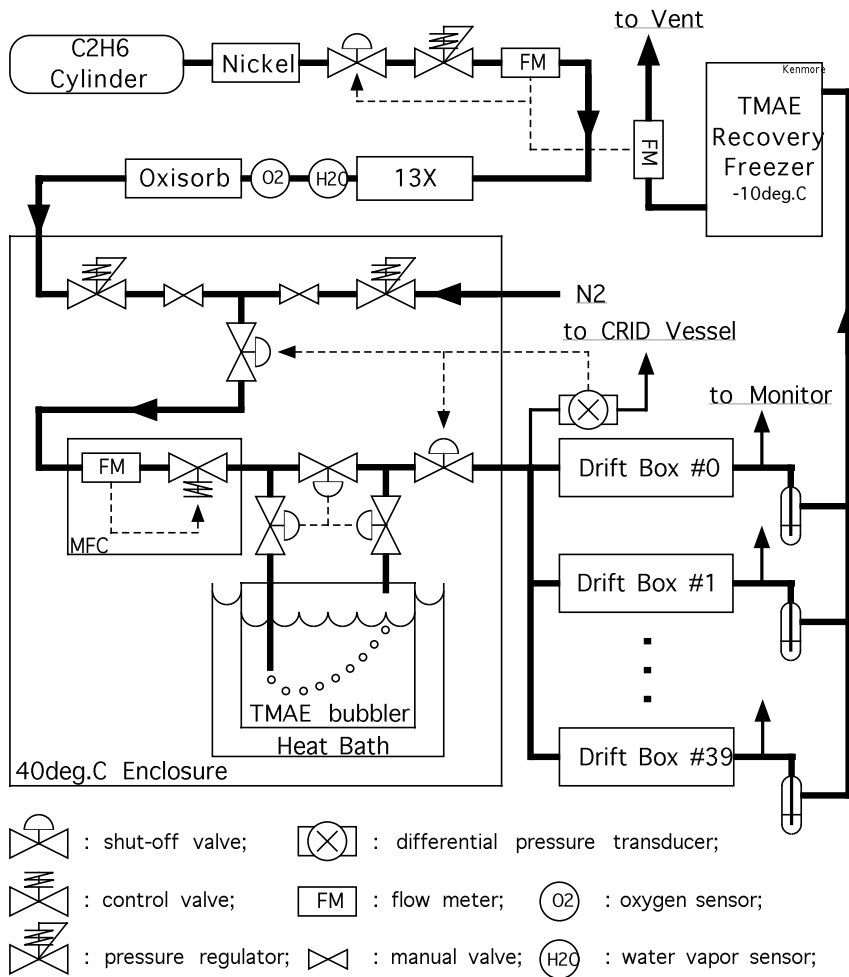# CRID Drift Gas
Delivery System

Oct. 22, 1992

Figure 5.5: The CRID drift gas delivery system is represented schematically.

The drift gas output vent flows through a TMAE recovery freezer, which operates at ~ 0 °C. This recovers $> 95\%$ of the TMAE in the drift gas. After the freezer is an output flowmeter, whose measurements are combined with an input flowmeter, located upstream of the input filters, to produce a flow-balance signal. This signal is used in a safety system that shuts off C_2H_6 flow in the event of a major leak anywhere in the system. Because the filter cartridges are located on the CRID gas rack and have a significant volume capacity, the time constant of this safety system is necessarily some 15–30 minutes.

5.4   Pressure Control

As discussed above, the pressures of all of the fluid systems must be maintained to several torr, and the control systems for this pressure control must be failsafe. The scheme for this in the liquid radiator system is described above. The gas radiator and drift gas systems have a common pressure control system, which is based on a custom digital controller [148, 153]. The controller is built around a programmable logic array,[*] which functions as a finite state machine. The input to this controller comes from ten capacitance manometers,[†] arranged in five pairs for redundancy. The readouts of each pair are compared and discrepancies cause the system to close valves and remain in a suspended state for operator intervention. If the TPC pressure relative to the vessel or the vessel pressure relative to atmosphere exceeds a threshold (~ 2 torr), the controller closes upstream valves in the delivery system until the pressure returns to a safe range. Larger excursions in pressure may activate an emergency venting of the CRID vessel, in the event of overpressure, or activate an emergency flow of N_2 into the vessel, in the event of underpressure.

In order to keep pressure control in the event of a power outage, the pressure controller and associated control valves are operated from a battery-backed

---

[*]EP1800, Alterra Inc., Santa Clara, CA
[†]Model 221AD, MKS Inc., Burlington, MA

uninterruptible power supply (UPS).* The UPS is capable of supplying 1 kW for up to 2 hours.

The last fallback in this system is a passive high-flow bubbler. The oil level in this bubbler is set to 5 torr, which is several torr above the thresholds for all of the active parts of the system. The bubbler is designed to handle a flow of 200 l/min., which would be required in the event of a sudden condensation in the CRID vessel. This bubbler has not yet engaged during the life of the CRID.

The original designs for the gas delivery system [148] had the pressure signals feeding back into the MFCs, thus varying the flow in order to maintain a constant pressure. The system has proved sufficiently stable, however, that it is operated in the constant-flow mode. This avoids the problem of maintaining sufficient flow at all times, which one might have in the pressure-feedback mode. The most significant pressure problems observed, apart from hardware failures, have been large pressure variations in the drift gas vent due to storms and high-wind conditions.

5.5   Gas Monitoring

As described above, there is an extensive system for online monitoring of gas quality. This system is depicted in Fig. 5.6. The system is split into gas sources which may contain TMAE (the TPC returns, the DMZ side spaces, and the lines sampling the two TMAE bubblers), and those sources which cannot (the base C_2H_6 drift gas and the C_5F_{12} radiator inlet and outlet streams). One difference between the two subsystems is that the TMAE-capable part must contain all metal valves with a stainless-steel seat and bellows construction, while the non-TMAE portion contains valves with ordinary elastomeric seals. Any gas in either of the two sample manifolds can be monitored for UV transparency, or for O_2 and H_2O content. In addition, the gases in the TMAE-capable subsystem can be monitored for electron lifetime. These monitors are described in turn below, followed by a summary of the control software for the system.

---

*Model 982-4M2, Abacus Controls Inc., Somerville, NJ

CRID Gas Monitor System
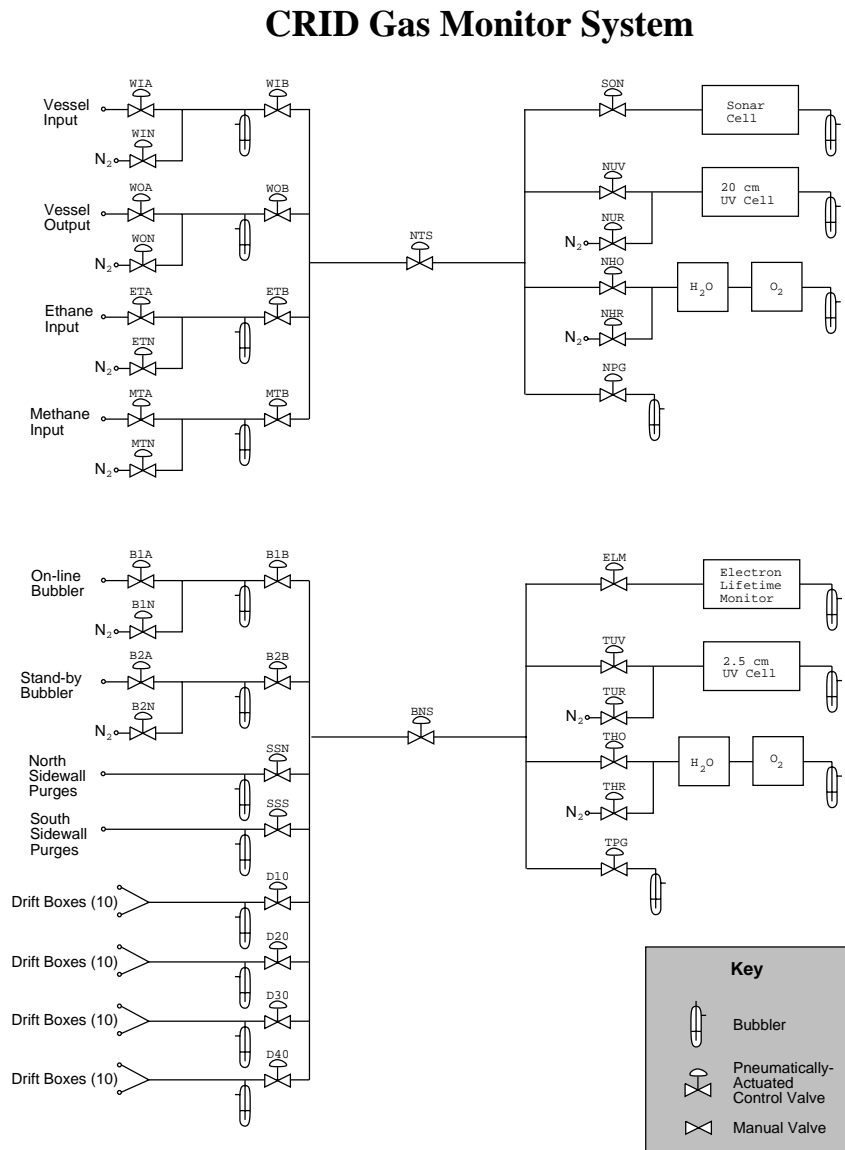
Figure 5.6: A schematic of the CRID gas monitoring system is shown.
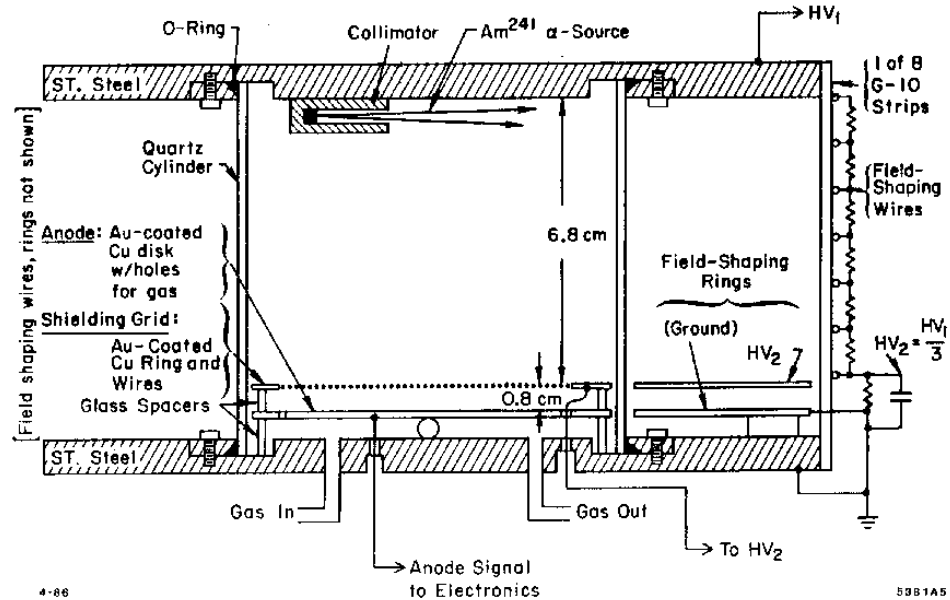
Figure 5.7: A diagram of the CRID Electron Lifetime Monitor (ELM) is shown.

5.5.1 Electron Lifetime Monitor

In a sense, the attachment lifetime of photoelectrons in the drift gas is the ultimate test of drift gas purity, since the purity requirements are driven by the need to drift photoelectrons along the 1.2-m length of the TPCs with minimal loss at long drift. The electron lifetime monitor (ELM) [154] is a device to measure this attachment lifetime as directly as possible. The ELM is miniature ion chamber containing an ^{241}Am source. The charge collected in the chamber is measured as the drift field, and hence the drift time, is varied. Four or five different voltage settings are fit to an exponential, and an electron lifetime is extracted.

In practice, the ELM is not quite long enough (it is 7 cm) to measure very long electron lifetimes accurately. Furthermore, the correspondence between lifetimes measured in the ELM and lifetimes seen in the TPCs is not clear, due to the difference in drift fields and other possible systematics. However, the
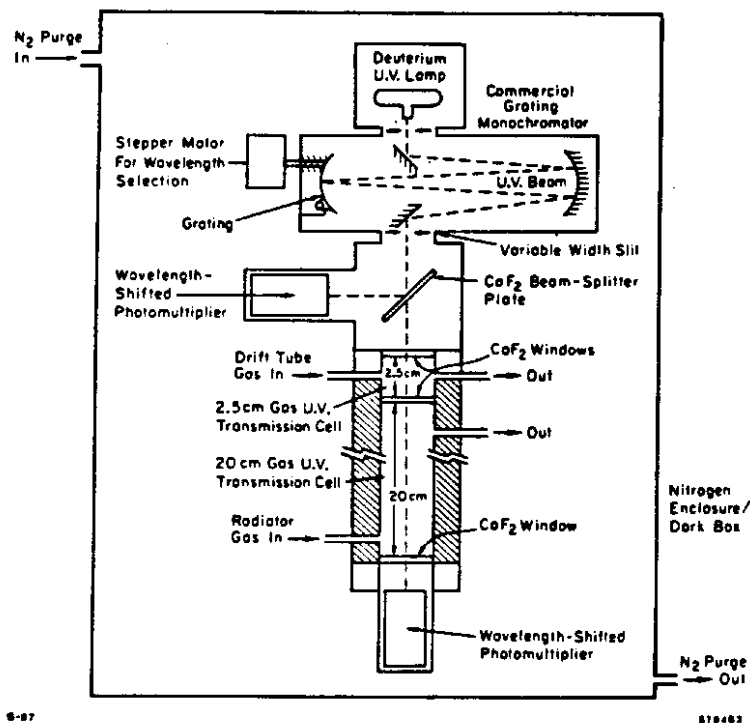
Figure 5.8: A diagram of the CRID UV transparency monitor is shown.

ELM serves well as a relative gas-quality device. Problems in gas purity show up clearly as a reduced ELM lifetime. The ELM has the advantage of being able to operate continuously during running in the presence of TMAE. Operating experience has shown a correspondence between low O_2 contamination (< 1 ppm) and good electron lifetime.

5.5.2   Ultraviolet Transparency

Another important measure of gas purity is UV transparency. This is the essential test for the two radiator fluids, but it is also useful for the drift gas. The gas monitor system contains a UV transparency monitor depicted in Fig. 5.8, which consists of a deuterium lamp with MgF_2 window,* a diffractive

---

*L879-01, Hamamatsu Photonics, Hamamatsu 430, Japan

monochromator,[†] and photomultipliers with wavelength shifters.[‡] A similar system exists for monitoring C_6F_{14} or C_5F_{12} in the liquid phase.

The gas UV monitor consists of two cells with MgF_2 windows. The 2.5 cm cell is connected to the TMAE-capable monitor subsystem, and the 20 cm cell is connected to the non-TMAE subsystem. The longer cell is useful for monitoring the C_5F_{12} radiator gas, while the shorter cell is adequate for the TMAE-laden drift gas, which has a UV absorption length of 1.9 cm.

The UV monitor employs a CaF_2 beam splitter and two photomultiplier tubes to monitor simultaneously the D_2 lamp intensity and the transmission through the sample. This is done because the intensity of the D_2 lamps has been found to be unstable over time. Transmission measurements are made by comparing to a reference gas of pure N_2, which is UV transparent. The double ratio of $(I_{samp}/I_{src})/(I_{N_2}/I_{src})$ at each wavelength gives the transmission of the sample gas.

5.5.3 Other Monitors

In addition to the ELM and UV monitors, trace contamination of O_2 and H_2O in the drift and radiator gases can be measured at various points in the system. These measurements are based on commercial devices. The oxygen content is measured by a lead-based fuel cell[§] to an accuracy of $\lesssim 1$ ppm. The H_2O concentration is measured via capacitive sampling of a Al_2O_3 mesh structure.[¶] The precision of the H_2O measurements is several ppm. Neither of these monitors are compatible with TMAE, so they must only be used when TMAE is not present in the system or in the upstream portions of the drift gas system (ahead of the TMAE bubbler).

[†]77250 Monochromator, Oriel Corp., Stratford, CT
[‡]RCA Quanticon C31000N
[§]Trace Oxygen Analyzer, Teledyne Analytical Instruments, City of Industry, CA
[¶]System 5 Hygrometer, Panametrics Inc., Waltham, MA

5.5.4   Software Control

Gas flow to all of the monitors depicted in Fig. 5.6 is regulated by pneumatically-actuated shutoff valves. Compressed air to operate these valves is switched by miniature solenoid valves,* which are operated by 5-V TTL signals. Each valve contains a micro-switch to sense the valve stem position. This micro-switch is used as an independent check of valve operation. Any discrepancy between the requested valve state and the micro-switch readback is flagged as a fault in the valve driver boards.

Rather than being operated directly by software, the monitoring valves are operated by a custom controller, which is based on a programmable logic array finite-state machine, like the pressure control processor. This controller communicates with the software control program via CAMAC input and output registers. The benefit of a hardware controller is that it ensures that valves are operated in the right order and in the right combinations. The controller also alleviates synchronization problems, as the valves have long time constants (up to 10 sec.) for activation.

The software control program for the gas monitoring runs as a batch process on the CRID microvax. It is a multi-threaded program, using VMS asynchronous traps (ASTs) to implement (non-preemptable) threads. There is one thread per monitor manifold task. All data is stored in a memory-resident SLD Monitor Database (MDB). A separate process samples the MDB database and records time histories. Both the current values and the histories can be viewed with the SLD Solo Control Program (SCP) from any VMS workstation or X-terminal in the cluster. Limited control functions are also available from the SCP, but these communicate to the monitor process solely through the MDB database.

---

*K3P02LO, Honeywell, Skinner Valve Division, New Britain, CT

5.6 Temperature Control

The vessel and internal components are heated by a system of approximately 200 Kapton–encapsulated heaters mounted on all of the CRID internal surfaces [148]. Current to each heater pad is switched using individual AC "zero-crossing" solid-state relays.[*] The relay is followed by a rectifier and a large 1 mF smoothing capacitor to provide a slowly-varying DC current to the pads inside the SLD magnetic field.

Input for the temperature control system is provided by a set of 1024 solid-state temperature sensors.[†] The control system runs on the CRID microvax via a CAMAC interface. There is also an analog-hardware control system that serves as a backup during failure of the software control system. The back-up controller uses a set of 52 platinum-resistor temperature sensors.[‡] The hardware control is activated via a CAMAC "watchdog timer."[§] If the software control program fails to probe the watchdog module for longer than 15 seconds, a digital signal activates the hardware control. For this reason, the temperature control process runs at an elevated priority on the microvax.

The heaters are controlled in groups, with each group being linked to a particular temperature sensor average. If the sensor average is below the target temperature, then all pads in the heater group are activated. Different groups have different maximum duty cycles, ranging from 15 seconds per 2 minutes to continuous operation, for activation until the temperature average reaches the target value. Temperature sensors with readings outside of certain extreme limits are discarded before constructing the sensor averages. This is to prevent failed sensors from unduly influencing the temperature averages. In practice, the temperature of most CRID surfaces is maintained to within $\pm 0.5\,^\circ$C, although local fluctuations in the vicinity of the heater may be higher.

---

[*]70 OAC5, Grayhill Inc., LaGrange, IL

[†]AD590JF, Analog Devices, Norwood, MA

[‡]F3103, Omega Engineering Inc., Stamford CT

[§]Model 3792, Kinetic Systems Corp., Lockport, IL

Half of the heaters are operated from a diesel-generated emergency power supply in the event of a failure of the standard AC power delivery. The hardware temperature controller is run from the CRID uninterruptible power supply described above.

In addition to the electrical heaters inside the CRID vessel, there is a separate system to heat the plumbing that carries fluids to and from the CRID. This system heats water ($35\,^\circ$C) and circulates that water in copper tubes that are attached to the main stainless-steel tubing bundles with copper foil and brazing. There are some 64 of the solid-state temperature probes that monitor the various tubing bundles.

5.7   Slow Protection System

Another important monitor system is an array of eight SLD Smart Interface Alarm Modules (SIAMs). These are custom CAMAC modules that sample a digital or analog input and raise an alarm flag if the input is out of tolerance. In the CRID fluid systems, SIAMs are used to sample critical operating parameters and to catch hardware failures. When one of the alarm flags is raised, an audible alarm alerts SLD technicians, who contact CRID experts. Several critical alarm trigger an automatic dialing system which pages CRID personnel directly.

In many cases, the inputs to the SIAM alarm system come from simple hardware signals (*e.g.* pressures in the drift gas supply, or flow rates falling out of tolerance). In some cases, however, more complex quantities need to be monitored, such as temperature averages over large sets of sensors. These could be sampled with one analog signal, but an average is preferable to ensure integrity of the whole system. Therefore, a separate software process is run to sample these "complex" quantities, check them against current tolerances, and to set a CAMAC output register if the value is out of tolerance for longer than a certain transient time (6 minutes).

This system of automatic alarms has proved vital to the success of the SLD CRID. Over the course of several years of operation of the CRID fluid systems, a variety of strange and unexpected problems have occurred, and many times these problems were initially detected by the automatic alarm system. In the absence of a large crew of people to watch over the fluid systems at all times, such an automated protection system is a necessity.

Chapter 6

CRID Reconstruction and Particle Identification Analysis

This chapter describes the reconstruction process and the algorithm used to extract particle identification information from the SLD CRID. The entire chain from raw data to particle hypothesis likelihoods is outlined in an attempt to provide a reference for the main features of the CRID reconstruction code. To this end, references to specific PREPMORT routines are given, and the important parameters are referred to by their JAZELLE bank names. Generally, more detail on the reconstruction can only be found in the reconstruction code itself.

6.1   Pulsefinding and Hit Cuts

Hits in the CRID start with Cherenkov photons ionizing TMAE molecules and the resulting electrons drifting toward the MWPC detectors and inducing avalanches on the anode wires. These pulses are fed into shaping amplifiers with an exponential decay time. The output signal is sampled and stored in the AMU, where it can then be serially digitized and read out over a fiber optic connection. The amplifiers are trimmed so as to match their decay time τ to the AMU sampling interval of 67.2 ns.

The SLD data acquisition contains an array of 80 WSM CPUs (Motorola 68020s) for use in processing CRID raw data. Originally, it was conceived that the reduction of digitized amplitude information ("snips") into 7-parameter pulse information would be done in the WSM CPUs. The algorithm of deconvolving the $te^{-t/\tau}$ pulse shape from the amplifier response was selected as a computationally efficient way to get maximal precision ($\lesssim 0.1$ bucket) on the pulse arrival time and good double-pulse resolution (~ 1.5 buckets) [136, 131]. In practice, however, the control parameters to the pulsefinding needed to be tuned from real data and there was a great deal of concern about unrecoverable loss of information. Therefore, instead of running the pulsefinding in the WSM CPUs, it was decided to write the snipped data to tape and to run the pulsefinding in the offline reconstruction. It also turns out that the time required to move this ~ 100 kB of data per event through the SLD FASTBUS data acquisition is 2–3 times less than the time it would take to run the pulsefinding in the WSMs. Therefore, writing the snipped data has actually proven better for SLD dead-time, so long as the bandwidth to tape is not saturated by the extra data volume.

Because of its origins (*i.e.*, being designed to run in the WSMs), the pulsefinding code is written in C and interfaced to the rest of the reconstruction PREPMORT code via a single well-defined interface. The `CDOWSM` processor sets up the parameters (via `CRunWSM`) and then calls `CDecRun` with the snips passed as an array of shorts. There are four basic parameters to the pulsefinding:

- `CDOWSMP%(TAU)` - the amplifier shaping time constant. In principle, each amplifier has a different shaping time. We have not calibrated the `TAU` for each amplifier, so all of them are set to a common value of 67.2 ns. Although unused, there is some capability to adjust the `TAU` for different amplifiers [131].

- `CDOWSMP%(SAMPINT)` - HAMU sampling interval (fixed at 67.2 ns).

- `CDOWSMP%(CUTOFF)` - the minimum accepted pulse amplitude (in deconvolved space). This is currently set at 100 counts, which is sufficiently above the noise amplitude seen in data. The minimum amplitude of signal pulses is determined by the snip threshold passed to the DCU in the readout electronics.

- `CDOWSMP%(HAMUPED)` - the nominal pedestal. This is set to the pedestal value to which the HAMUs are calibrated (300 counts).

The output of the pulsefinding becomes the `CRDAEB` data structures, which are a series of pulses for each WSM CPU. Each pulse contains seven 2-byte words of information: wire number, inner and outer pulse time, inner and outer amplitudes, number of buckets above threshold, and a quality word where various bit-fields can be set.

These pulses are then turned into three-dimensional hit points in TPC coordinates by the `CAEB2RE` routine, which outputs `CREHIT` banks. All of the `CRDAEB` quality codes are carried forward, and several more bits are potentially added (in the pulsefinding, only 16 bits are used). For each hit, the TPC (x, y, z) coordinates are stored, as well as the combined pulse amplitude, three spatial errors, and the number of deconvolved buckets above threshold on each end of the wire.

Several corrections, such as the measured drift velocity for the event, the gain calibration (for charge division), and the magnetic field distortion correction, are also applied at this stage. In addition, hits are tagged for post-pulsefinding quality cuts (*e.g.* cross talk, calibration strobe, fiber fiducial), and TPCs that are off due to high voltage, broken wires, or electronic problems are flagged.

The quality word of the `CRDAEB`/`CREHIT` hits is used to tag certain categories of hits which are unlikely to be good signal hits. For example, single photoelectrons should almost never saturate the amplifiers; therefore, we improve signal-to-noise by removing hits with the `SATURATE` bit set. Another important category of hits are those caused by cross talk from nearby MIP
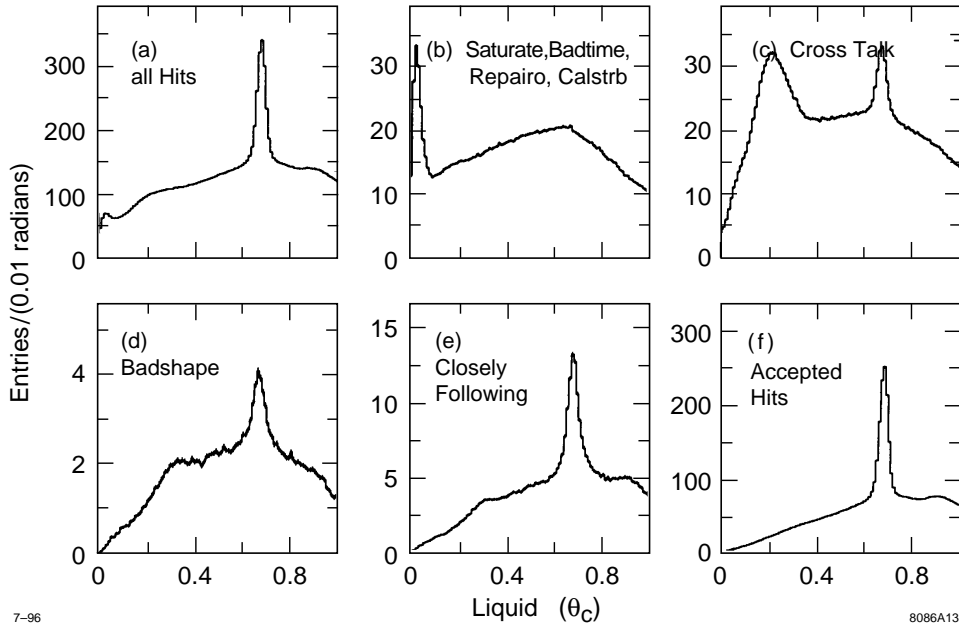
Figure 6.1: Liquid Cherenkov angles for tracks above 3 GeV/c are shown for various categories of hit quality flags. The starting sample containing all recorded hits is shown in (a). Various categories of hits that are cut away are shown in (b)–(e). The final accepted hits is the distribution in (f). The loss of signal is $\sim 15\%$, but the signal-to-noise is improved considerably.

hits. The cross-talk effect is described in [133, 155], and the algorithm to tag cross-talk hits is described in [156]. Basically, the procedure consists of removing all hits in a window in drift time and wire number around the leading and trailing edges of saturated pulses. The effectiveness of this and other hit quality codes at improving signal-to-noise is shown in Fig. 6.1. The set of hit categories that are removed is determined by the `CRDRECP%(LIQKLMSK)` and `CRDRECP%(GASQKLMSK)` parameters described below.

6.2 Liquid Angle Reconstruction

For each drift chamber track (`PHTRK`), there is a `CANGLE` bank produced that contains the Cherenkov angle information from any relevant `CREHIT`s. A

`CANGLE` bank stores both liquid and gas angles, as well as angles for Cherenkov photons produced in the quartz windows of liquid radiator trays. Each angle is tagged by type (`CANGLE%(CHIT(`i`),TYPE)`) and contains indexes which point to the `CREHIT` entry that generated it (`CANGLE%(CHIT(`i`),TPC)` and `CANGLE%(CHIT(`i`),NCREH)`).

In order to produce a liquid `CANGLE` entry, a given `CREHIT` hit must not have any of the bits from the liquid kill mask (`CRDRECP%(LIQKLMSK)`) set in its quality word (`CREHIT%(CHIT(`i`),QUALITY)`), and it must have a TMAE depth of less than 5 cm (`CRDRECP%(LIQTCUT)`). In order to suppress the increased background coming from phase-space effects as the photon trajectory approaches total internal reflection in the liquid radiator window, there is a cut on the angle θ_2, defined in Fig. 6.2, such that $\sin\theta_2 < 0.940$ (`CRDRECP%(TIRCUT)`). In addition, the incident track must have momentum greater than `CRDRECP%(PEXTLOW)` at the end of its extrapolation into the CRID (from `PHEXTR`).

The liquid Cherenkov angles are calculated by the `CLIQUR` routine. Figure 6.2 shows the relevant geometry. The point H is known from the `CREHIT` bank, and the points O and A come from the extrapolated track (`PHTRK` to `PHEXTR` to `CCHGTK`). Point A is where the track intersects the liquid radiator window, and O is the Cherenkov photon origin point. The point O is unknown up to the thickness of the liquid radiator, but the point halfway along particle trajectory inside the liquid radiator is used as a nominal origin. The contribution to the Cherenkov angle error from the thickness of the radiator is taken into account in the uncertainty σ_θ, as described below. Given points O and H, let us define point Q so as to form a right triangle OQH with $\overrightarrow{OQ}$ parallel to the liquid radiator normal $\hat{n}$. Denote by P the point where $\overrightarrow{OQ}$ intersects the liquid radiator window.

The problem is now reduced to finding the point B, where the Cherenkov photon intersects the liquid radiator window and refracts on its way to the TPC. For this derivation, we ignore the refraction in the liquid radiator and TPC quartz windows, which creates small displacements in the photon trajectory,
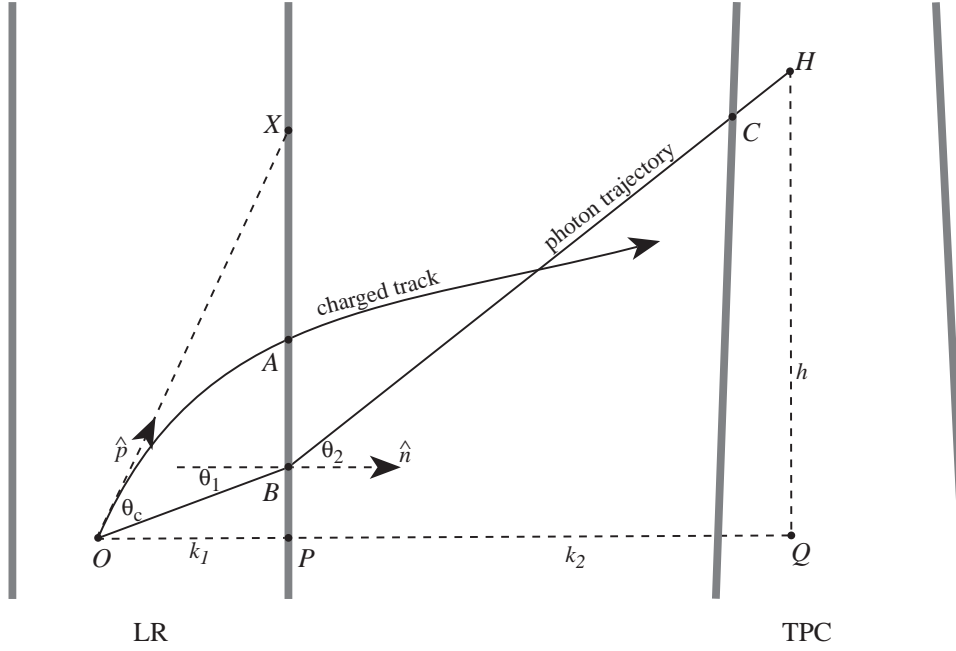
Figure 6.2: Diagram of the geometry of the liquid angle reconstruction. Distances are not drawn to scale.

but does not change the angles appreciably. The `CLIQUR` reconstruction, however, does take this refraction displacement properly into account. A simplification that the `CLIQUR` code does make is to ignore the difference in refractive index between the C_2H_6 drift gas and the C_5F_{12} gas radiator, which would cause the photon ray to refract at point C. Because these indexes are relatively similar and because the absorption depth in TMAE (distance $|\overrightarrow{CH}|$) is relatively small, this approximation is safe to make.

Given B, we can find the Cherenkov angle by

$$\cos\theta_c = \hat{p} \cdot \frac{\overrightarrow{OB}}{|\overrightarrow{OB}|}$$

$$\tan\phi_c = \frac{\overrightarrow{OB}\cdot\hat{y}}{\overrightarrow{OB}\cdot\hat{x}},$$

(6.1)

where $\hat{p}$ is the track direction at O and $\hat{x}, \hat{y}$ are the unit vectors used to define the angle ϕ_c. The standard CRID reconstruction takes $\hat{x}$ in the plane of $\hat{p}$ and $\hat{n}$. Optionally, $\hat{x}$ can be taken along the SLD z-axis (magnetic field direction). The constraints that determine B are:

$$n_g \sin\theta_2 = n_l \sin\theta_1 \tag{6.2}$$

$$h = k_1 \tan\theta_1 + k_2 \tan\theta_2. \tag{6.3}$$

Equation (6.2) is Snell's law for the refraction at the liquid radiator window, with n_g the index of refraction of the C_5F_{12} gas radiator (which sits outside the liquid radiator tray) and n_l the index of the C_6F_{14} liquid radiator. In Eq. (6.3), the distances h, k_1, and k_2 are defined as in Fig. 6.2. The relation follows from the geometry of these points.

These two equations have two unknowns, θ_1 and θ_2, but the solution is a difficult transcendental equation. Instead, the CRID reconstruction solves them via an iterative procedure. A function $f(\theta_1)$ is defined by

$$
\begin{aligned}
f(\theta_1) &= k_1 \tan\theta_1 + k_2 \tan\theta_2 - h \\
&= k_1 \tan\theta_1 + k_2 \frac{\mu \sin\theta_1}{\sqrt{1 - \mu^2 \sin^2\theta_1}} - h,
\end{aligned}
\tag{6.4}
$$

where μ is defined to be the ratio of the refractive indices, $\mu \equiv n_l/n_g$, and the root of Eq. (6.4), $f(\theta_1) = 0$, is computed by Newton's method

$$\theta_1^{(i+1)} = \theta_1^{(i)} - \frac{f(\theta_1^{(i)})}{f'(\theta_1^{(i)})}, \tag{6.5}$$

where $\theta_1^{(i)}$ denotes the value for θ_1 at the ith iteration. The derivative,

$$
\begin{aligned}
f'(\theta_1) &= k_1 \sec^2\theta_1 + k_2 \sec^2\theta_2 \frac{d\theta_2}{d\theta_1} \\
&= k_1 \sec^2\theta_1 + k_2 \sec^2\theta_2 \, \mu \frac{\cos\theta_1}{\cos\theta_2},
\end{aligned}
\tag{6.6}
$$

can be computed from Eqs. (6.2) and (6.3). We start with the point B where it would be if OBH were a straight line, and then iterate. The computation of quartz angles is very similar, with the quartz index n_q replacing n_l and with k_1 much smaller. Also, there is no refraction displacement at point B in this case, since the photon starts out in the quartz medium.

This procedure gives us the values of θ_c and ϕ_c, but we still require the contributions to the uncertainty σ_θ from various sources, and the Jacobian of transformation between the TPC coordinates and θ_c, ϕ_c. For this, we follow the derivation in [157].

Let us define another coordinate system with origin at the point X where the track's momentum direction $\hat{p}$ intersects the quartz plane of the liquid radiator. Note that this is not quite point A in Fig. 6.2, due to the curvature of the track. Define the z-axis to be along the liquid radiator normal $\hat{n}$, and the x-axis to be such that the track direction $\hat{p}$ lies entirely in the xz plane. Let $\vec{x}_0 = (x_0, 0, -k_1)$ be the coordinates of the emission point O, and α be the polar angle of $\hat{p}$ in this frame. Then,

$$x_0 = -k_1 \tan\alpha. \tag{6.7}$$

Let $\vec{x}_1 = (x_1, y_1, 0)$ be the coordinates of the point B where the photon ray exits the liquid radiator, and let θ_1, ϕ_1 be the photon ray direction, as before. Define a vector $\vec{R} \equiv \vec{x}_1 - \vec{x}_0$. Then, by equating the Cartesian and spherical coordinates of $\vec{R}$, we have three equations

$$k_1 = R\cos\theta_1 \tag{6.8}$$

$$y_1 = R\sin\theta_1 \sin\phi_1 \tag{6.9}$$

$$x_1 - x_0 = R\sin\theta_1 \cos\phi_1, \tag{6.10}$$

which we can solve for x_1 and y_1:

$$y_1 = k_1 \tan\theta_1 \sin\phi_1$$
$$x_1 = k_1 (\tan\theta_1 \cos\phi_1 - \tan\alpha).$$

(6.11)

Next, let us define $\vec{x}_2$ to be the vector along the photon trajectory from the liquid radiator (point B) to where it enters the TPC (point C). Call the coordinates of this vector $\vec{x}_2 = (x_2, y_2, D)$, with its direction being given by θ_2, ϕ_2. Here, D denotes the distance between the liquid radiator and the TPC. We then have

$$|\vec{x}_2| = \frac{D}{\cos\theta_2}$$
$$x_2 = |\vec{x}_2| \sin\theta_2 \cos\phi_2 = D\tan\theta_2 \cos\phi_2$$
$$y_2 = |\vec{x}_2| \sin\theta_2 \sin\phi_2 = D\tan\theta_2 \sin\phi_2.$$

(6.12)

Relating the two sets of angles, we have

$$\sin\theta_2 = \mu \sin\theta_1 \qquad (6.13)$$

$$\phi_2 = \phi_1, \qquad (6.14)$$

where we have rewritten Eq. (6.2) with $\mu \equiv n_l/n_g$. Equation (6.14) follows from the definition of our coordinate system.

The remaining piece of information is the vector from the TPC window (C) to the actual conversion point (H). Let us call this vector $\vec{x}_3 = (x_3, y_3, d)$, with d denoting the conversion depth within the TPC (in our earlier notation, $k_2 = D + d$). Since the index of C_5F_{12} is close to that of C_2H_6, we make the approximation

$$\sin\theta_3 \simeq \sin\theta_2 \qquad (6.15)$$

$$\phi_2 \simeq \phi_3. \qquad (6.16)$$

Then, we have:

$$|\vec{x}_3| = \frac{d}{\cos\theta_2}$$

$$x_3 = |\vec{x}_3|\sin\theta_2\cos\phi_2 = d\tan\theta_2\cos\phi_2 \tag{6.17}$$

$$y_3 = |\vec{x}_3|\sin\theta_2\sin\phi_2 = d\tan\theta_2\sin\phi_2.$$

Now, we can consider the reconstruction process as the task of finding the two points O and H in this coordinate system. Since we assume the emission depth k_1 to be half of the thickness of the liquid radiator and since the track position is fixed, point O has no dependence on the measurement of photoelectron hits. The point H has coordinates given by

$$\vec{x} = \vec{x}_1 + \vec{x}_2 + \vec{x}_3 = (x_1 + x_2 + x_3,\ y_1 + y_2 + y_3,\ D + d) \tag{6.18}$$

in our notation. We may choose three independent variables, say (x_2, y_2, d), and compute the Jacobian of transformation from these variables to (θ_c, ϕ_c, l). Because the absorption depth l only affects $\vec{x}_3$, we may write the Jacobian J as follows:

$$J = \frac{\partial(x,y,z)}{\partial(\theta_c,\phi_c,l)} = \begin{vmatrix} \dfrac{\partial(x,y)}{\partial(\theta_c,\phi_c)} & \dfrac{\partial d}{\partial\theta_c} \\[2ex] & \dfrac{\partial d}{\partial\phi_c} \\[2ex] \dfrac{\partial x}{\partial l} \quad \dfrac{\partial y}{\partial l} & \dfrac{\partial d}{\partial l} \end{vmatrix} = \begin{vmatrix} \dfrac{\partial(x,y)}{\partial(\theta_c,\phi_c)} & -l\sin\theta_2\dfrac{\partial\theta_2}{\partial\theta_c} \\[2ex] & -l\sin\theta_2\dfrac{\partial\theta_2}{\partial\phi_c} \\[2ex] \dfrac{\partial x}{\partial l} \quad \dfrac{\partial y}{\partial l} & \cos\theta_2 \end{vmatrix}. \tag{6.19}$$

In the approximation that $l \ll D$, we can ignore the terms proportional to l, and derive

$$J \simeq \cos\theta_2\left|\frac{\partial(x,y)}{\partial(\theta_c,\phi_c)}\right|. \tag{6.20}$$

A similar argument, based on the approximation $k_1 \ll D$ gives us

$$J \simeq \cos\theta_2 \left| \frac{\partial(x_2, y_2)}{\partial(\theta_c, \phi_c)} \right|. \tag{6.21}$$

We then decompose the remainder of the Jacobian as follows

$$J = \cos\theta_2 \begin{vmatrix} \dfrac{\partial x_2}{\partial \theta_2} & \dfrac{\partial y_2}{\partial \theta_2} \\[2mm] \dfrac{\partial x_2}{\partial \phi_2} & \dfrac{\partial y_2}{\partial \phi_2} \end{vmatrix} \cdot \begin{vmatrix} \dfrac{\partial \theta_2}{\partial \theta_1} & \dfrac{\partial \phi_2}{\partial \theta_1} \\[2mm] \dfrac{\partial \theta_2}{\partial \phi_1} & \dfrac{\partial \phi_2}{\partial \phi_1} \end{vmatrix} \cdot \begin{vmatrix} \dfrac{\partial \theta_1}{\partial \theta_c} & \dfrac{\partial \phi_1}{\partial \theta_c} \\[2mm] \dfrac{\partial \theta_1}{\partial \phi_c} & \dfrac{\partial \phi_1}{\partial \phi_c} \end{vmatrix}$$

$$= \cos\theta_2 \begin{vmatrix} D\dfrac{\cos\phi_2}{\cos^2\theta_2} & D\dfrac{\sin\phi_2}{\cos^2\theta_2} \\[3mm] -D\tan\theta_2\sin\phi_2 & D\tan\theta_2\cos\phi_2 \end{vmatrix} \cdot \begin{vmatrix} \mu\dfrac{\cos\theta_1}{\cos\theta_2} & 0 \\[3mm] 0 & 1 \end{vmatrix} \cdot \begin{vmatrix} \dfrac{\partial \theta_1}{\partial \theta_c} & \dfrac{\partial \phi_1}{\partial \theta_c} \\[2mm] \dfrac{\partial \theta_1}{\partial \phi_c} & \dfrac{\partial \phi_1}{\partial \phi_c} \end{vmatrix} \tag{6.22}$$

$$= D^2 \frac{\sin\theta_2}{\cos^2\theta_2} \cdot \mu\frac{\cos\theta_1}{\cos\theta_2} \cdot \left[\frac{\partial \theta_1}{\partial \theta_c}\frac{\partial \phi_1}{\partial \phi_c} - \frac{\partial \theta_1}{\partial \phi_c}\frac{\partial \phi_1}{\partial \theta_c} \right].$$

It remains now to relate (θ_1, ϕ_1) to (θ_c, ϕ_c). If we consider the photon direction in a coordinate system defined along $\hat{p}$, it is clear that

$$\hat{R}' = \begin{pmatrix} \sin\theta_c \cos\phi_c \\ \sin\theta_c \sin\phi_c \\ \cos\theta_c \end{pmatrix}. \tag{6.23}$$

Because the track direction $\hat{p}$ is defined to be in the xz plane, it follows that the transformation from $\hat{R}'$ to $\hat{R}$ is a simple rotation

$$\hat{R} = \begin{bmatrix} \cos\alpha & 0 & \sin\alpha \\ 0 & 1 & 0 \\ -\sin\alpha & 0 & \cos\alpha \end{bmatrix} \hat{R}'$$

$$= \begin{pmatrix} \sin\theta_c \cos\phi_c \cos\alpha + \cos\theta_c \sin\alpha \\ \sin\theta_c \sin\phi_c \\ -\sin\theta_c \cos\phi_c \sin\alpha + \cos\theta_c \cos\alpha \end{pmatrix} \tag{6.24}$$

$$= \begin{pmatrix} \sin\theta_1 \cos\phi_1 \\ \sin\theta_1 \sin\phi_1 \\ \cos\theta_1 \end{pmatrix}.$$

By equating the two expressions for $\hat{R}$, we get the following relations:

$$\sin\theta_1 \sin\phi_1 = \sin\theta_c \sin\phi_c. \tag{6.25}$$

$$\cos\theta_1 = \cos\theta_c \cos\alpha - \sin\theta_c \cos\phi_c \sin\alpha. \tag{6.26}$$

We can derive a similar relation by considering the dot product of $\hat{R}$ with the direction $\hat{p} = -\vec{x}_0/|\vec{x}_0|$

$$\begin{aligned} \cos\theta_c &= \hat{R} \cdot \hat{p} \\ &= \begin{pmatrix} \sin\theta_1 \cos\phi_1 \\ \sin\theta_1 \sin\phi_1 \\ \cos\theta_1 \end{pmatrix} \cdot \begin{pmatrix} \sin\alpha \\ 0 \\ \cos\alpha \end{pmatrix} \\ &= \sin\theta_1 \cos\phi_1 \sin\alpha + \cos\theta_1 \cos\alpha. \end{aligned} \tag{6.27}$$

Differentiating Eq. (6.25) and Eq. (6.26), we find

$$\frac{\partial\phi_1}{\partial\theta_c} = \frac{1}{\sin\theta_1 \cos\phi_1} \left(\cos\theta_c \sin\phi_c - \cos\theta_1 \sin\phi_1 \frac{\partial\theta_1}{\partial\theta_c} \right) \tag{6.28}$$

$$\frac{\partial\phi_1}{\partial\phi_c} = \frac{1}{\sin\theta_1 \cos\phi_1} \left(\sin\theta_c \cos\phi_c - \cos\theta_1 \sin\phi_1 \frac{\partial\theta_1}{\partial\phi_c} \right) \tag{6.29}$$

$$\frac{\partial\theta_1}{\partial\theta_c} = \frac{\sin\theta_c}{\sin\theta_1} \cos\alpha + \frac{\cos\theta_c}{\sin\theta_1} \cos\phi_c \sin\alpha \tag{6.30}$$

$$\frac{\partial\theta_1}{\partial\phi_c} = -\frac{\sin\theta_c \sin\phi_c \sin\alpha}{\sin\theta_1}. \tag{6.31}$$

After a bit of algebra, this reduces to:

$$\begin{vmatrix} \dfrac{\partial \theta_1}{\partial \theta_c} & \dfrac{\partial \phi_1}{\partial \theta_c} \\[2ex] \dfrac{\partial \theta_1}{\partial \phi_c} & \dfrac{\partial \phi_1}{\partial \phi_c} \end{vmatrix} = \frac{\sin \theta_c}{\sin^2 \theta_1 \cos \phi_1} \left[\sin \theta_c \cos \phi_c \cos \alpha + \cos \theta_c \sin \alpha \right]$$

$$= \frac{\sin \theta_c}{\sin \theta_1},$$

(6.32)

using Eq. (6.26) and Eq. (6.27). This results in a Jacobian of

$$J = \mu^2 \frac{D^2}{\cos^2 \theta_2} \frac{\cos \theta_1}{\cos \theta_2} \sin \theta_1 \cdot \begin{vmatrix} \dfrac{\partial \theta_1}{\partial \theta_c} & \dfrac{\partial \phi_1}{\partial \theta_c} \\[2ex] \dfrac{\partial \theta_1}{\partial \phi_c} & \dfrac{\partial \phi_1}{\partial \phi_c} \end{vmatrix}$$

$$= \mu^2 \frac{D^2}{\cos^2 \theta_2} \frac{\cos \theta_1}{\cos \theta_2} \sin \theta_c.$$

(6.33)

Besides the Jacobian, we need also to know the uncertainty in θ_c due to our ignorance of the true emission depth k_1. For this, it suffices to compute $\partial(\vec{x}_1 + \vec{x}_2 + \vec{x}_3)/\partial k_1$ and use the Jacobian to transform to (θ_c, ϕ_c). From our definitions, it is clear that only x_1, y_1 are affected by k_1. Differentiating Eq. (6.11), we have

$$\frac{\partial x_1}{\partial k_1} = \tan \theta_1 \cos \phi_1 - \tan \alpha$$

$$\frac{\partial y_1}{\partial k_1} = \tan \theta_1 \sin \phi_1,$$

(6.34)

and

$$\frac{\partial \theta_c}{\partial k_1} = \left| \frac{\partial(\theta_c, \phi_c)}{\partial(x, y)} \right| \cdot \begin{pmatrix} \dfrac{\partial x}{\partial k_1} \\[2ex] \dfrac{\partial y}{\partial k_1} \end{pmatrix}.$$

(6.35)

Combining all the contributions to σ_θ, we have

$$
\begin{aligned}
\sigma_\theta &= \left| \frac{\partial(\theta_c, \phi_c, l)}{\partial(x, y, z)} \right| \begin{pmatrix} \sigma_x \\ \sigma_y \\ \sigma_z \end{pmatrix} \oplus \left| \frac{\partial(\theta_c, \phi_c, l)}{\partial(x, y, z)} \right| \begin{pmatrix} \dfrac{\partial x}{\partial k_1} \\ \dfrac{\partial y}{\partial k_1} \\ 0 \end{pmatrix} \sigma_{k_1} \\[2em]
&= \left| \begin{matrix} \dfrac{\partial x}{\partial \theta_c} & \dfrac{\partial y}{\partial \theta_c} \\ \dfrac{\partial x}{\partial \phi_c} & \dfrac{\partial y}{\partial \phi_c} \end{matrix} \right|^{-1} \begin{pmatrix} \sigma_x \oplus \left(\dfrac{\partial x}{\partial k_1} \right) \sigma_{k_1} \\ \sigma_y \oplus \left(\dfrac{\partial y}{\partial k_1} \right) \sigma_{k_1} \end{pmatrix},
\end{aligned}
\tag{6.36}
$$

where σ_x and σ_y are the drift distance and wire number position errors (including diffusion), and σ_{k_1} is the the liquid radiator thickness error ($= 1/\sqrt{12} \times 1$ cm).[*]

6.3 Gas Angle Reconstruction

The gas angle reconstruction proceeds very similarly to that of the liquid angles. There is a corresponding set of criteria for producing a gas `CANGLE` entry: the `CREHIT%(CHIT(`*i*`),QUALITY)` quality word must survive the `CRDRECP%(GASKLMSK)`, the resulting angle must be less than 250 mrad (`CRDRECP%(GASREGN)`), and the TMAE depth of each gas hit must be less than 6 cm (`CRDRECP%(GASTCUT)`). Additionally, there is a cut on isolation of the gas Cherenkov ring from saturated hits due to MIPs. This is because the saturated hits "blind" a region of the TPC, which should properly be accounted for in the expected number of hits. In lieu of such an accounting, we merely cut all tracks for which more than half of their gas ring is expected to be obscured by these MIP regions. In fact, there are two cut criteria, `P%(PHCRID,GASMESS)`, which sets `P%(PHCRID,BADID)` by default and cuts the track from particle identification consideration, and `P%(PHCRID,GASXISO)`, which is a stronger

---

[*]In this derivation, parallax errors due to uncertainty in the charge-division coordinate are ignored (*i.e.*, $l \ll D$ is assumed).

cut requiring no overlap of MIP hits with the gas ring, and which must be checked explicitly.

The gas angle reconstruction is performed by the routine CGFNAN. We outline the algorithm here, but it is described in more detail in [157]. The positions of the 400 mirrors are assumed to be known exactly, and the problem is then to find a set of emission coordinates $(\theta_c, \phi_c, \beta, l)$ that produce a photoelectron hit at the position observed (x_h, y_h, z_h). Here, θ_c and ϕ_c are the two Cherenkov angles, l is the conversion depth in the TPC along the photon trajectory, and β is a parameter which denotes the emission point of the photon along the trajectory of the incident particle. We define β such that it is -1 where the track leaves the outside of the TPC and $+1$ at the mirror. Let us define a vector $\vec{\alpha}$ from the Cherenkov angles

$$\vec{\alpha} \equiv \begin{pmatrix} \theta_c \cos \phi_c \\ \theta_c \sin \phi_c \end{pmatrix}. \tag{6.37}$$

If we denote the photoelectron (x, z) position that is produced from a given set of emission parameters as the function $\vec{r}(\vec{\alpha}, \beta, l)$, and the corresponding conversion depth as $y(\vec{\alpha}, \beta, l)$, then our task is to solve the equations:[*]

$$\vec{r}(\vec{\alpha}, \beta, l) = \vec{r}_h = (x_h, z_h) \tag{6.38}$$

$$y(\vec{\alpha}, \beta, l) = y_h. \tag{6.39}$$

We make use of the fact that gas Cherenkov angles are small, $\theta_c \ll 1$, and the fact that the spherical mirrors are, by design, insensitive to the emission point β. Thus, we approximate $\vec{r}(\vec{\alpha}, \beta, l)$ by

$$\begin{aligned} r_i(\vec{\alpha}, \beta, l) &\simeq r_i(\vec{0}, \beta, l) + A_{ij}(\beta, l)\,\alpha_j + B_{ijk}(\beta, l)\,\alpha_j \alpha_k + \ldots \\ r_i(\vec{0}, \beta, l) &\simeq r_i(\vec{0}, \beta_0, 0) + (\beta - \beta_0)b_i + l s_i + \ldots, \end{aligned} \tag{6.40}$$

---

[*]Note that in [157], the TPC coordinates are defined differently from the standard CRID convention. The y_h and z_h are interchanged in [157], with z_h being the coordinate determined from charge division and y_h being the drift distance.

where we expand in terms of the small parameters $\vec{\alpha}$, l, and $(\beta - \beta_0)$,[*] and neglect terms of higher orders. The matrices A, B, and the vectors $\vec{b}$, $\vec{s}$ are just the Taylor coefficients of this expansion. The expansion point β_0 is chosen to be the best guess for the emission point β. Typically, this is $\beta_0 = 0$, unless segments of the track point at different mirrors. Since there is no way of determining β given only the CRID hit information, let us approximate A and B by their values at β_0

$$
\begin{aligned}
A_{ij}(\beta, l) &\simeq A_{ij}(\beta_0, l) = C_{ij} + l D_{ij} \\
B_{ijk}(\beta, l) &\simeq B_{ijk}(\beta_0, l) = B^0_{ijk},
\end{aligned}
\tag{6.41}
$$

where the matrices on the right hand side are constants (independent of β or l). We keep the $(\beta - \beta_0)\vec{b}$ term in Eq. (6.40) only to calculate the uncertainty σ_θ due to our lack of knowledge of β.

Thus, we can now fix $\beta = \beta_0$, set $l = z/\sqrt{|\vec{s}|^2 + 1}$, and solve iteratively for $\vec{\alpha}$. Let $\vec{\alpha}^{(i)}$ be the value of $\vec{\alpha}$ at iteration i, and let $\vec{w}(\vec{\alpha}^{(i)})$ be the difference between the photoelectron hit and the position associated with $\vec{\alpha}^{(i)}$. At this point we introduce the more compact notation $B\vec{a}\vec{b} = \vec{c}$ to denote the matrix product where $c_i = B_{ijk} a_j b_k$.

$$
\begin{aligned}
\vec{w}(\vec{\alpha}^{(i)}) &\equiv \vec{r}_h - \vec{r}(\vec{\alpha}^{(i)}, \beta_0, l) \\
&= \vec{r}(\vec{\alpha}, \beta, l) - \vec{r}(\vec{\alpha}^{(i)}, \beta_0, l) \\
&\simeq A(\vec{\alpha} - \vec{\alpha}^{(i)}) + B(\vec{\alpha}\vec{\alpha} - \vec{\alpha}^{(i)}\vec{\alpha}^{(i)}) + \ldots
\end{aligned}
\tag{6.42}
$$

If we define $\vec{\delta}^{(i)} \equiv \vec{\alpha} - \vec{\alpha}^{(i)}$, then

$$
\vec{w}(\vec{\alpha}^{(i)}) \simeq A\vec{\delta}^{(i)} + 2B\vec{\alpha}^{(i)}\vec{\delta}^{(i)} + B\vec{\delta}^{(i)}\vec{\delta}^{(i)} = A\left[I + A^{-1}B(2\vec{\alpha}^{(i)} + \vec{\delta}^{(i)})\right]\vec{\delta}^{(i)}.
\tag{6.43}
$$

---

[*]Actually, $(\beta - \beta_0)$ is not necessarily small, but the coefficient $\vec{b}$ is small, so we may nevertheless ignore higher order terms in this expansion variable.

Solving this for $\vec{\delta}^{(i)}$, we have

$$
\begin{aligned}
\vec{\delta}^{(i)} &= \left[I - A^{-1}B(2\vec{\alpha}^{(i)} + \vec{\delta}^{(i)}) \right] A^{-1}\vec{w} \\
&= \left(A^{-1} - 2E\vec{\alpha}^{(i)} \right) \vec{w} - E\vec{\delta}^{(i)}\vec{w},
\end{aligned}
\tag{6.44}
$$

where we define the matrix $E_{ijk} \equiv A_{il}^{-1} B_{ljm} A_{mk}^{-1}$. We can solve Eq. (6.44) by first neglecting the term proportional to $\vec{\delta}^{(i)}$ on the right, calculating the value for $\vec{\delta}^{(i)}$ in this approximation, and then substituting that value into the term on the right. This single iteration for $\vec{\delta}^{(i)}$ is sufficient because the right-hand term will be small. The result can now be used to calculate the new estimate for $\vec{\alpha}$

$$
\vec{\alpha}^{(i+1)} = \vec{\alpha}^{(i)} + \vec{\delta}^{(i)}.
\tag{6.45}
$$

We then continue the iteration process until $|\vec{\delta}^{(i)}| < 0.03$ mrad.

In Eq. (6.44), we make use of A^{-1}. For the computation of E, we can simply approximate A^{-1} by C^{-1}, but for terms like $A^{-1}\vec{w}$, we should retain terms linear in l. Since

$$
A = C + lD = C \left(I + lC^{-1}D \right),
\tag{6.46}
$$

we have

$$
A^{-1} = \left(I + lC^{-1}D \right)^{-1} C^{-1} \simeq \left(I - lC^{-1}D \right) C^{-1} = C^{-1} - lF,
\tag{6.47}
$$

where $F \equiv C^{-1}DC^{-1}$. The values of C^{-1}, F, E, $\vec{b}$, and $\vec{s}$ all depend only on the parameters of the incident track and are independent of the coordinates of the individual hits. They are calculated from the geometry of the mirrors and the parameters of the track (see [157]), and are reused in the loop over all hits to form CANGLEs for the incident track.

Another quantity that is required from the reconstruction is the Jacobian of transformation from TPC coordinates to $(\theta_c, \phi_c, l)^*$

$$J = \frac{\partial(x_h, y_h, z_h)}{\partial(\theta_c, \phi_c, l)} = \frac{\partial(x_h, y_h, z_h)}{\partial(\alpha_1, \alpha_2, l)} \frac{\partial(\alpha_1, \alpha_2)}{\partial(\theta_c, \phi_c)}$$

$$\simeq \begin{vmatrix} A_{11} & A_{12} & 0 \\ A_{21} & A_{22} & 0 \\ s_1 & s_2 & \sqrt{1 - \vec{s}^2} \end{vmatrix} \cdot \begin{vmatrix} \cos\phi_c & \sin\phi_c \\ -\theta_c \sin\phi_c & \theta_c \cos\phi_c \end{vmatrix} \tag{6.48}$$

$$= \det(A)\sqrt{1 - |\vec{s}|^2} \cdot \theta_c$$

Finally, we need to calculate the uncertainty in Cherenkov angle coming from measurement errors. Let $\vec{\sigma}_r = (\sigma_x, \sigma_z)$ be the measurement error in TPC (x, z), and let σ_y be the error in TPC-y. Since β is undetermined, it can take on any value from -1 to 1; this implies $\sigma_\beta^2 = 1/3$. If we keep only terms linear in the errors $\vec{\sigma}_\alpha, \sigma_l, \sigma_\beta$, we can calculate from Eq. (6.40):

$$\vec{\sigma}_r = A\vec{\sigma}_\alpha \oplus \sigma_\beta \vec{b} \oplus \sigma_l \vec{s}$$
$$\vec{\sigma}_\alpha = A^{-1}\left[\vec{\sigma}_r \oplus \sigma_\beta \vec{b} \oplus \sigma_l \vec{s}\right]. \tag{6.49}$$

From the definition of $\vec{\alpha}$ (6.37), we have

$$\theta_c^2 \sigma_\theta^2 = \left\langle (\theta_c \sigma_\theta)^2 \right\rangle = \left\langle (\vec{\alpha} \cdot \vec{\sigma}_\alpha)^2 \right\rangle = \left\langle \left(\vec{\alpha} \cdot A^{-1}\left[\vec{\sigma}_r \oplus \sigma_\beta \vec{b} \oplus \sigma_l \vec{s}\right] \right)^2 \right\rangle. \tag{6.50}$$

Let $\vec{t} \equiv \vec{\alpha} A^{-1}/\theta_c$. Then,

$$\sigma_\theta^2 = (\vec{t} \cdot \vec{\sigma}_r)^2 + \sigma_\beta^2 (\vec{t} \cdot \vec{b})^2 + \sigma_l^2 (\vec{t} \cdot \vec{s})^2. \tag{6.51}$$

This is, of course, only the uncertainty due to measurement error and to the

---

*Reference [157] parametrizes Eq. (6.40) in terms of z ($= y_h$) instead of l. With this alternate notation, our factor of $\sqrt{1 - |\vec{s}|^2}$ would become $1/\sqrt{1 + |\vec{s}|^2}$.

bending of the track in the magnetic field. We also need to add to this the chromatic error and the track momentum uncertainty.

6.4 The Likelihood Method

The final step of the CRID reconstruction involves using the `CANGLE` information to produce a set of particle identification likelihoods for each `PHTRK`. This is done by the `CFNHYP` routine. There are five possible particle hypotheses considered, $e/\mu/\pi/K/p$, and these are hard-wired into the reconstruction. A maximum-likelihood method is used, which has the advantages that it makes the best use of available information, gives smooth behavior as a particle's momentum crosses the Cherenkov threshold for a particular hypothesis, and provides a simple framework for combining liquid and gas Cherenkov information. Early on, it was decided not to attempt to produce absolute likelihoods or confidence probabilities on individual particle hypotheses, because particle identification requirements are strongly dependent on particular analyses and the physics backgrounds expected for those analyses. Therefore, only the ratios of the reported particle likelihoods are meaningful. The likelihoods are normalized to sum to 1, and the logarithms of the likelihoods are stored in the `PHCRID` bank (`PHCRID%(LIQ,LLIK,`h_k`)`, and `PHCRID%(GAS,LLIK,`h_k`)`) for hypothesis h_k.

The CRID likelihood algorithm is described in [158] and in [157]. The technique is somewhat similar to the Omega RICH analysis [159], but extends the idea from fixed-size pixels to arbitrary hits in space with finite resolution. The DELPHI RICH group uses a similar analysis, but computes each track's likelihoods independently and does not explicitly model the background due to Cherenkov photons from other tracks [160].

The statistical technique of *maximum likelihood* tests a hypothesis for the distribution of observed data by considering a likelihood function L, which is the probability of producing the observed data given a particular hypothesis. In our case, a hypothesis consists of a set of particle assignments $\{h_k\}$ for each

track k and a background model $B(\vec{x})$. Let $\bar{n}$ be the expected number of photons for the hypothesis $\{h_k\}$. If n is the observed number of photoelectrons in the CRID, then the probability of n given $\bar{n}$ is just the Poisson term

$$P(n|\bar{n}) = \frac{\bar{n}^n}{n!}e^{-\bar{n}}. \tag{6.52}$$

In addition to the number of photons, we also have information from the spatial distribution of the photons. Let $P(\vec{x})$ be the probability of a given photo-electron being in a differential volume $d^3\vec{x}$. Then $\bar{n}P(\vec{x})$ is the expected number of photoelectrons in $d^3\vec{x}$. Define this to be $\rho(\vec{x})$. Taking into account the permutations of the n photoelectrons, the overall likelihood is given by

$$\begin{aligned} L &= P(n|\bar{n})P\left(\{\vec{x}_i\}\right) \\ &= \bar{n}^n e^{-\bar{n}} \prod_{i=1}^{n} P(\vec{x}_i) \\ &= e^{-\bar{n}} \prod_{i=1}^{n} \rho(\vec{x}_i), \end{aligned} \tag{6.53}$$

where the index i runs over all observed photoelectrons.

It is convenient to split up $\rho(\vec{x})$ into a background term independent of tracks and a term representing the Cherenkov rings produced by each track,

$$\rho(\vec{x}) = B(\vec{x}) + \sum_k \rho_{k,h_k}(\vec{x}), \tag{6.54}$$

where $\rho_{k,h_k}(\vec{x})$ represents the density due to track k, given particle hypothesis h_k for that track. Furthermore, it is simpler to describe ρ_{k,h_k} in terms of a different set of coordinates, (θ_c, ϕ_c, l), in which θ_c is the Cherenkov polar angle, ϕ_c is the Cherenkov azimuthal angle, and l is the conversion depth of the photoelectron along the photon's trajectory. In this new set of coordinates, we can write the

density as

$$\rho_{k,h_k}(\vec{x}) = \frac{N_{k,h_k}}{2\pi} \frac{e^{-l/\lambda}}{\lambda} \frac{e^{-(\theta_c-\theta_0)^2/2\sigma_\theta^2}}{\sqrt{2\pi}\sigma_\theta} \frac{1}{J}, \tag{6.55}$$

where J is the Jacobian $\partial(x,y,z)/\partial(\theta_c,\phi_c,l)$, λ is the photon absorption length in the TPC gas, θ_0 is the expected Cherenkov angle for track k and hypothesis h_k, and σ_θ is the resolution on the Cherenkov angle measurement at position $\vec{x}$. The factor N_{k,h_k} is the number of photoelectrons expected per full ring for track k and hypothesis h_k (which may be zero if h_k is below threshold, for example). Because of total internal reflection, the allowable ϕ_c range for a liquid ring may be less than the full $[-\pi,\pi]$. This effect is included into the Jacobian J, which will go to 0 where no space point (x,y,z) can produce a hit at the given (θ_c,ϕ_c,l). Alternatively, one can define M_{k,h_k} to be the number of photoelectrons expected after accounting for total internal reflection. Then $N_{k,h_k}/2\pi = M_{k,h_k}/\Delta\Phi$, where $\Delta\Phi$ is the allowed ϕ range. This latter form is more convenient in the reconstruction program since the NHEXP calculated already includes the total internal reflection effect.

In principle, the likelihood L is now straightforward to compute for all 5 hypotheses of each track, and the set $\{h_k\}$ which maximizes L is our best answer. In practice, however, we cannot compute such an exponentially-large number of combinations. Instead, we make the simplifying assumption that the most likely hypothesis h_k for track k is largely independent of the hypotheses for other tracks $\{h_j\}_{j\neq k}$. We then iterate through the set of tracks, choosing each h_k to be the current best hypothesis for track k (favoring the π hypothesis when information is absent or ambiguous), and continue until the set $\{h_k\}$ is stable.

Let us define the likelihood for a hypothesis h_k to be

$$L_{k,h_k} \equiv e^{-M_{k,h_k}} \prod_i \left(B_k + \rho_{k,h_k}(\vec{x}_i) \right), \tag{6.56}$$

where B_k is the background that is independent of track k,

$$B_k(\vec{x}) \equiv B(\vec{x}) + \sum_{j \neq k} \rho_{j,h_j}(\vec{x}). \tag{6.57}$$

Then our independence assumption is equivalent to the difference in overall likelihood between hypothesis h_k and h_k' being given by

$$\frac{L(h_k, \{h_j\}_{j \neq k})}{L(h_k', \{h_j\}_{j \neq k})} = \frac{L_{k,h_k}}{L_{k,h_k'}}. \tag{6.58}$$

Hence, we need only maximize each L_{k,h_k} for the five hypotheses h_k (and then iterate).

Since we are only concerned with relative likelihoods, we can divide through by a factor to get

$$L_{k,h_k}' = e^{-M_{k,h_k}} \prod_i \left(1 + \frac{\rho_{k,h_k}(\vec{x}_i)}{B_k(\vec{x}_i)} \right), \tag{6.59}$$

or

$$\log L_{k,h_k}' = -M_{k,h_k} + \sum_i \log \left(1 + \frac{\rho_{k,h_k}(\vec{x}_i)}{B_k(\vec{x}_i)} \right), \tag{6.60}$$

which is what is reported in the PHCRID banks. Hence, the important criteria for particle identification are the ratios of Cherenkov angle weights $\rho_{k,h_k}(\vec{x}_i)$ to backgrounds $B_k(\vec{x}_i)$. Hits with signal weight significantly below the background weight are automatically ignored. Thus, a particle with hits nowhere near expected rings for any hypotheses is classified as ambiguous. For particles which are below threshold, the likelihoods of their above-threshold assignments are controlled by the expected number of hits $\log L_{k,h_k}' = -M_{k,h_k}$.

In practice, the iterative procedure is found to converge rapidly. The $\{h_k\}$ all start at the π hypothesis and converge for most events in only two iterations. One weakness of the method lies in the need to know the correct background

model $B(\vec{x})$. We currently use a uniform density per TPC, with the normalization computed from counting photoelectrons which have negligible weight ($< 10^{-4}$) for any hypothesis for any track. This normalization is bounded below by the parameters CRDRECP%(BKMINLIQ) and CRDRECP%(BKMINGAS) (which are set to 10 hits per TPC). Separate backgrounds are used for the liquid and gas sides of the TPCs, and quartz Cherenkov photons are properly included in the background (*i.e.*, they are treated in the category of signal hits from other tracks). There is some evidence that real backgrounds are non-uniform and concentrated towards the two windows of the TPC. Tuning of the background model could be an area for future improvement of the CRID particle identification performance (see section 7.16).

Chapter 7

CRID Performance

In order to achieve the design angular resolution of the SLD Barrel CRID, spatial resolutions on individual photoelectrons of 1–2 mm are required (see section 4.3.6). This requires a thorough understanding of both the drift of photoelectrons within the TPCs and of the positions of the TPCs, liquid radiator trays, and mirrors within the SLD. In this chapter, we describe the derivation of various corrections and alignments that are required to achieve this precision.

The end result is that we achieve good performance, very close to the design values. In general, the performance within the frame of reference of individual components of the CRID ("local resolution") meets the design. The alignment of the components to one another and to the rest of the SLD is believed to be responsible for the slightly degraded overall resolution that is observed. A few changes in operating parameters (*e.g.* use of a C_5F_{12}/N_2 mixture instead of pure C_5F_{12}, and lower detector gain) have decreased our identification performance compared to the original design, but not tremendously.

Many of these measurements and calibrations rely on a system of fibers for injecting UV light from a xenon flashlamp at 19 fiducial positions on each TPC. This hardware is discussed in detail in [161, 162]. The fiber fiducials serve to calibrate various aspects of the electron drift within the TPCs. A diagram of the fiber system is shown in Fig. 7.1. Four vertical fibers along the centerline of the TPC are used for drift velocity measurements. The $45°$ angled fibers
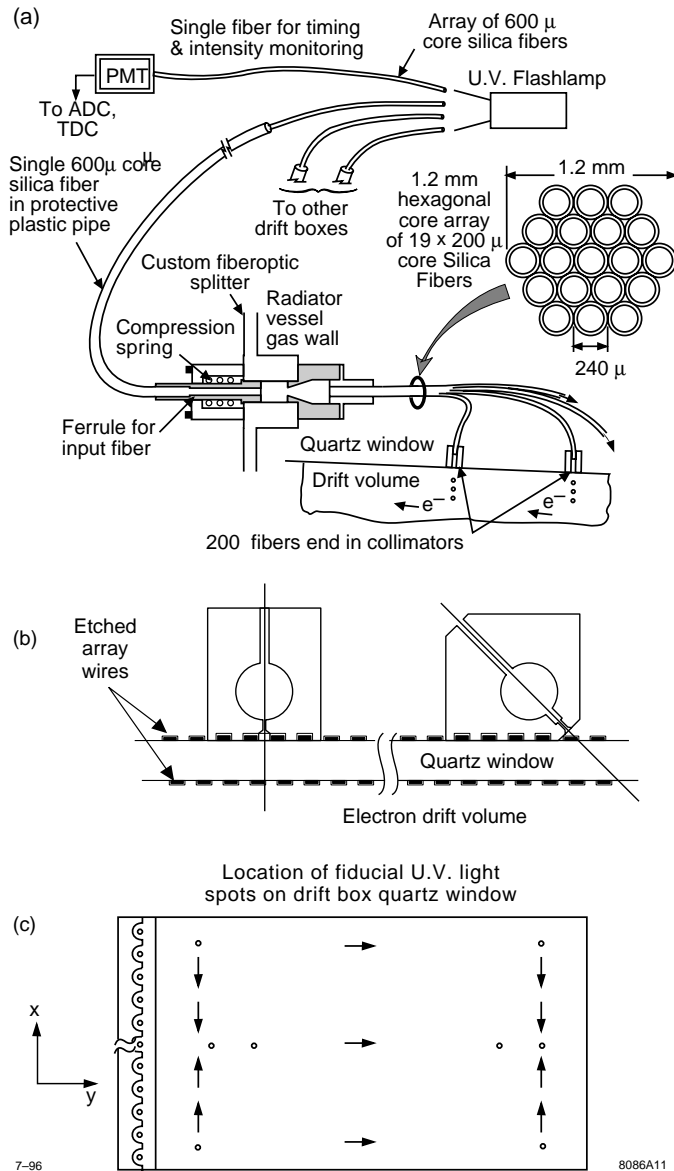
Figure 7.1: Diagram of the CRID fiber fiducial system. A xenon flashlamp provides UV light pulses, which are transmitted by optical fiber to known positions on the surface of the CRID TPCs. The collimators which mount the fibers onto the TPC surfaces are shown in (b). The positions of the 19 fiducials are shown in (c).

near the detector plane are used for charge-division calibration. The vertical and angled fibers at the far (high-voltage) end of the TPCs are used to study transverse drift distortions and drift velocity variations, along with the angled fibers along the centerline and edges.

In the 1992 and 1993 runs, the fibers were flashed at 120 Hz, with every beam crossing. Starting in the fall of 1994, this was changed to flash at 0.05 Hz and read out with a special trigger. In addition to the primary advantage of depositing less charge on specific wires (see [163] for a discussion of the dangers of this), the new arrangement has the added advantage that fiber hits do not get confused with data hits and *vice versa*.

7.1 Drift Velocity

Knowledge of the electron drift velocity v_d in the C_2H_6 drift gas is essential in order to determine the position of the photoelectron hits from the arrival time of their avalanche pulses. A precision of 0.1% on v_d is required in order to achieve the 1-mm target resolution in TPC-z. However, the drift velocity is very sensitive to gas composition and purity, as well as to the electric field, gas pressure, and temperature. Although the electric field is very stable ($< 10^{-4}$ variation in the high-voltage power supply) and the temperature is reasonably stable (controlled to $\lesssim 0.5\,°C$), the drift gas pressure varies directly with atmospheric pressure, and there have been some difficulties with gas purity.

Therefore, we determine the drift velocity from fiber data on a continuous basis [162]. Fiber data is accumulated for every 1-hour block of data taking. A fit is performed to determine the positions in time of photoelectrons from the four vertical fibers located along the centerline of the TPC. These individual (hourly) drift velocity measurements are then parametrized in time using cubic splines. In the CRID reconstruction, the drift velocity of each event is then determined from its event time using this parametrization.

The procedure of determining and parametrizing drift velocities is now well-understood and automated. A filter job runs automatically as part of the
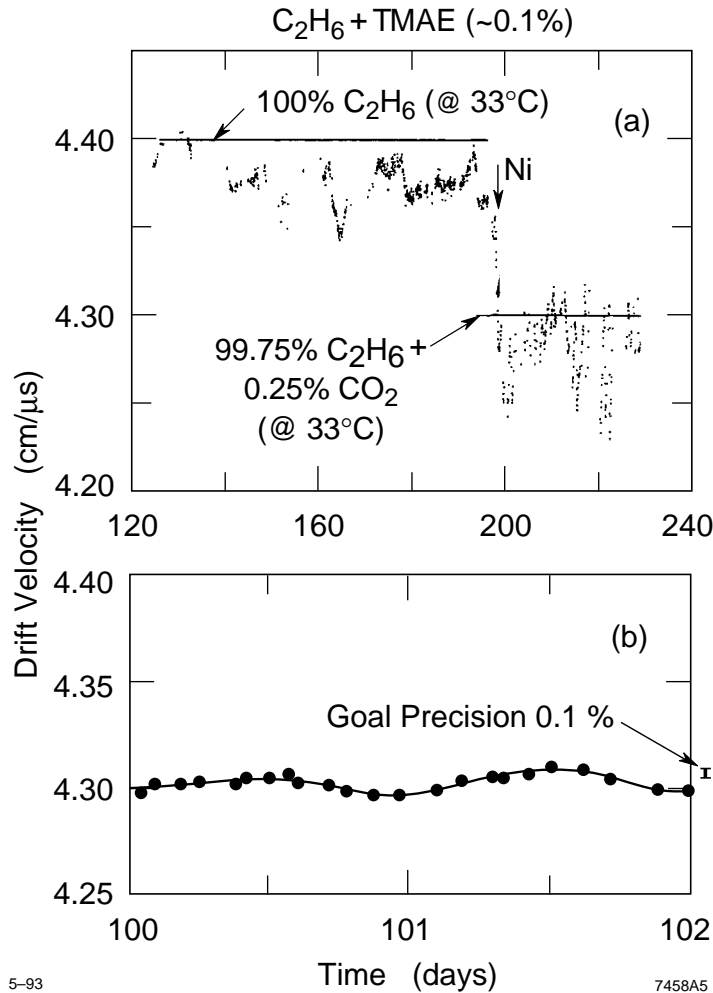
Figure 7.2: Measurements of the time-dependence of the CRID drift velocity in the 1992 data. The variation on long time scales (a) shows effects due to gas composition, while the variation on shorter time scales (b) shows individual (1-hour) measurements and the (cubic-spline) interpolation curves used for extracting drift velocities in the CRID reconstruction. The accuracy of individual measurements is typically 0.05%.

first-pass SLD reconstruction. The precision on individual measurements is typically 0.05%, which is well within the goal of 0.1% precision. Variations from TPC to TPC and within the TPCs have been found to be small ($< 0.1\%$) [162]. A sample of the drift velocity measurements for 1993 data is shown in Fig. 7.2.
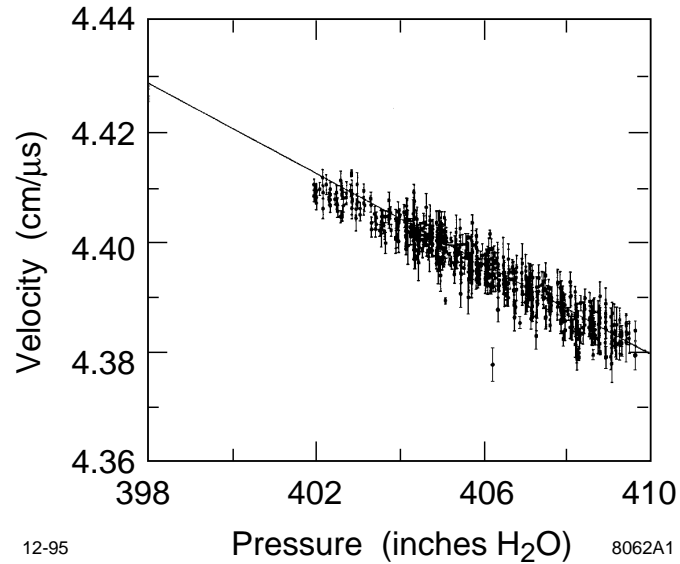
Figure 7.3: Correlation of CRID drift velocity with atmospheric pressure in the 1994–95 run. No correction for temperature is made, indicating that the temperature of the drift gas is sufficiently stable.

Although there is a large amount of fluctuation in the drift velocity (a), one can see that the individual measurements are taken on a short time scale compared to the drift velocity variation (b). The large fluctuations in v_d were understood to be the result of gas impurities and a (temperature-dependent) reaction of the C_2H_6 drift gas with a Ni filter installed to remove sulfur impurities in the gas [133].

In the 1994–95 run, a more pure source of C_2H_6 was found, and the Ni filter was no longer required. As a result, the main systematic influence in the 1994–95 drift velocities is now atmospheric pressure, which is measured and recorded to tape. The correlation of drift velocity with atmospheric pressure is shown in Fig. 7.3, where one can see that the spread of velocities due to pressure variations is much larger than the spread about the correlation. The recorded pressure is now used to determine the CRID drift velocity if a fiber-fiducial v_d measurement is unavailable for a particular run.
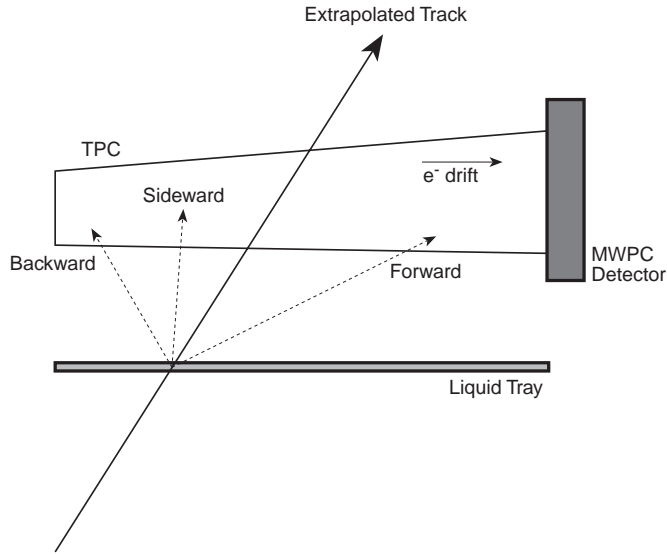
Figure 7.4: Diagram of the analysis technique used for determining t_0 and for the radial positions and tilts of the liquid radiator trays. The average Cherenkov angle of forward, backward, and sideward quadrants of the ring in ϕ_c is considered. See text for more description.

7.2   Time Zero

In addition to the drift velocity v_d, there is another parameter required for determination of the z-position of photoelectrons, namely the time offset of the arrival of electron and positron beams at the SLC interaction point from the time at which the CRID data acquisition clocks start, denoted t_0. The CRID acquisition timing is run relative to the SLC timing reference, so the t_0 should be constant throughout a run period. On the other hand, it is difficult to determine *a priori* what this should be, because it includes delay times in all of the cabling and electronics on the way to the CRID AMUs.

   Therefore, we determine the t_0 empirically by looking at the first arrival of hits at the CRID detectors. However, there is another degree of freedom because the drift field inside the CRID detector volume is not the same as that in the TPC volume, and this difference is equivalent to a time shift in the arrival of photoelectrons from the TPC. In principle, this shift due to the
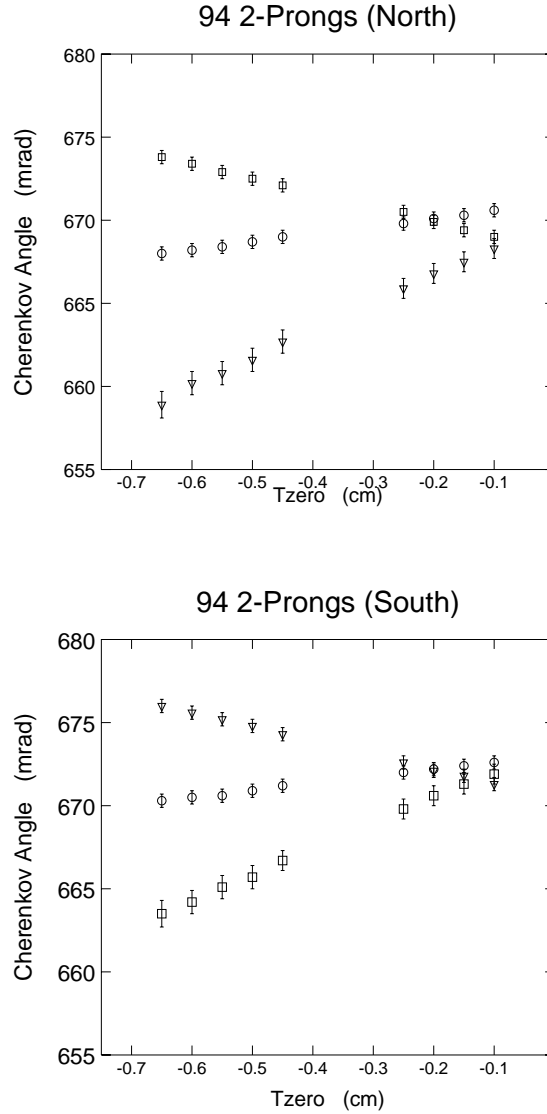
Figure 7.5: The Cherenkov angle θ_c for three different quadrants in ϕ_c (defined along the SLD-z direction) for liquid rings from $e^+e^- \to \mu^+\mu^-$ and $e^+e^- \to e^+e^-$ events is plotted versus the t_0 parameter. The squares are the quadrant $|\phi_c| < 45°$, the triangles are the quadrant $|\phi_c| > 135°$, and the circles are the remaining range in ϕ_c. The point where these three curves intersect is the (measured) correct value of t_0.

different drift velocity over the last 15 mm of drift is calculable, but in practice it is difficult to do so reliably. Therefore, we measure it by using liquid rings from $e^+e^- \to \mu^+\mu^-$ and $e^+e^- \to e^+e^-$ events. A shift in t_0 is equivalent to shifting all hits uniformly in TPC-z. We consider the forward and backward portions (along z) of liquid rings (see Fig. 7.4), and tune t_0 until the ring radii agree for the two. This process is demonstrated in Fig. 7.5.

The two parameters in the CRID reconstruction are represented by `CDOWSMP%(T0RUNDEP)`, which denotes the time of the arrival of the first hits (current value is 24.0 buckets), and `CTPCDIS%(ZBTPCT0N)`/`CTPCDIS%(ZBTPCT0S)`, which are the corrections for nonlinear drifts within the volume of the MWPC detector. As seen in Fig. 7.5, we determine `ZBTPCT0` to be consistent with -0.15 cm in both the north and south TPCs. This is a small correction and is consistent with expectations from electrostatics.

7.3 Electrostatic Distortions

Deviations from the expected direction of photoelectron drift in the TPCs can be caused by a variety of factors. We classify them into two broad categories, electrostatic distortions, which are shifts that occur even with the SLD solenoid magnet off, and magnetic distortions, which are those shifts caused by the $\vec{E}$ and $\vec{B}$ fields within the TPCs not being perfectly aligned. The magnetic distortions are discussed in the next section.

Distortions in the drift due to electrostatics can arise from several causes. If the electric potential gradient along the TPC is not uniform, a non-linear time-to-distance relationship would result. Another source of distortions is the perturbations in the drift field caused by a buildup of positive ions on the walls of the chambers or in the gas volume. This was studied at length in the CRID prototype tests, and the former found to be minimal [150]. A gating system was demonstrated to be effective for the latter [144], but there has not been evidence in the data of a need to use the gating [133].
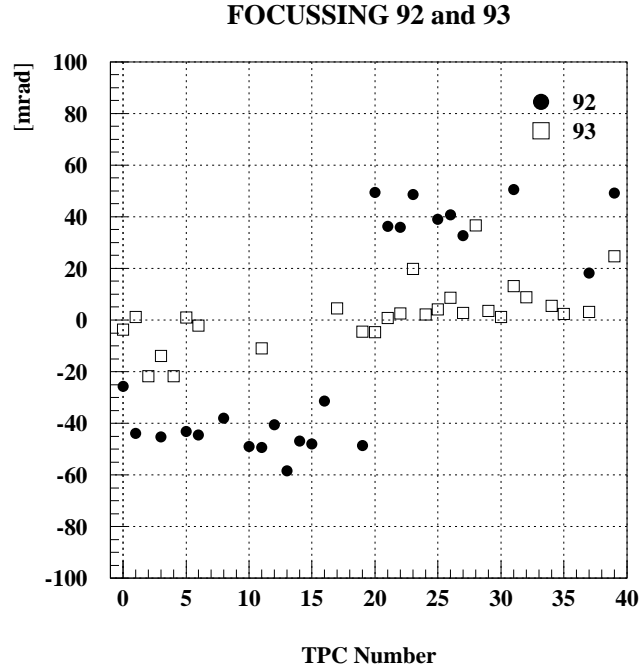
FOCUSSING 92 and 93

Figure 7.6: The electrostatic focussing $\delta x/(y-y_c)$ (see Eq. (7.4)) measured in fiber fiducial data as a function of the TPC number for the 1992 (dots) and 1993 (squares) data [164]. The effects of the adjustment of the voltage V_B are clearly visible.

The major distortion effect seen in the CRID TPCs is the "focussing" caused by nonuniform fields in the transition between the TPC active volume and the MWPC detector region. Early studies showed that this focussing could be minimized in either the TPC-x or the TPC-y direction through careful tuning of the voltage V_B that defines the end of the TPC potential gradient [150]. Since gas rings are focussed by the mirrors near the centers of the TPCs in x, the voltages were tuned to yield good axial drift over the entire depth of the TPC in y and the central part in x. The outermost 1–2 cm in x still suffer from uncorrected focussing effects at the level of ~ 2 mm [150, 144].

The focussing distortions are measured using dedicated UV fiber runs. Although significant effects were found in 1992, an adjustment of the operating

voltages (V_B) reduced these effects to < 0.5 mm for the 1993 and 1994–95 runs [164]. This is demonstrated in Fig. 7.6.

7.4 Magnetic Field Distortions

Because the SLD solenoidal field is not perfectly axial, distortions in the drift of photoelectrons are induced from the small radial component of the magnetic field, B_r. In addition, any misalignments of the TPCs with respect to the SLD z-axis cause a similar effect. These distortions are measured from dedicated UV fiber runs taken with low TMAE concentration, thus allowing fiber hits along the entire depth of the TPC. By comparing fiducial positions with the SLD solenoid on against those with the magnet off, we can measure the shifts as a function of drift distance.

The basic relationship is described in [133]. The drift velocity of an electron is given by

$$\vec{v}_d = \frac{\mu}{1+(\omega\tau)^2}\left[\vec{E} + \frac{\omega\tau}{B}(\vec{E}\times\vec{B}) + (\omega\tau)^2\frac{\vec{E}\cdot\vec{B}}{B^2}\vec{B}\right], \tag{7.1}$$

where μ is the electron mobility, ω is the Larmor frequency, and τ is the mean time between collisions. Working in the SLD coordinate system, the electric field is assumed to be along z, pointing towards the midplane, $\vec{E}\cdot\hat{z} = \mp E_z$. The magnetic field lies approximately along the z-axis $\vec{B} \simeq B_z\hat{z}$, but with a small radial component

$$\vec{B}\cdot\hat{r} = B_r(r,z) = B_r^0\frac{rz}{r_0 z_0}, \tag{7.2}$$

where the parametrization of $B_r(r,z)$ is based on a simple finite solenoid model, which has been confirmed by measurements of the actual field [76]. Integrating
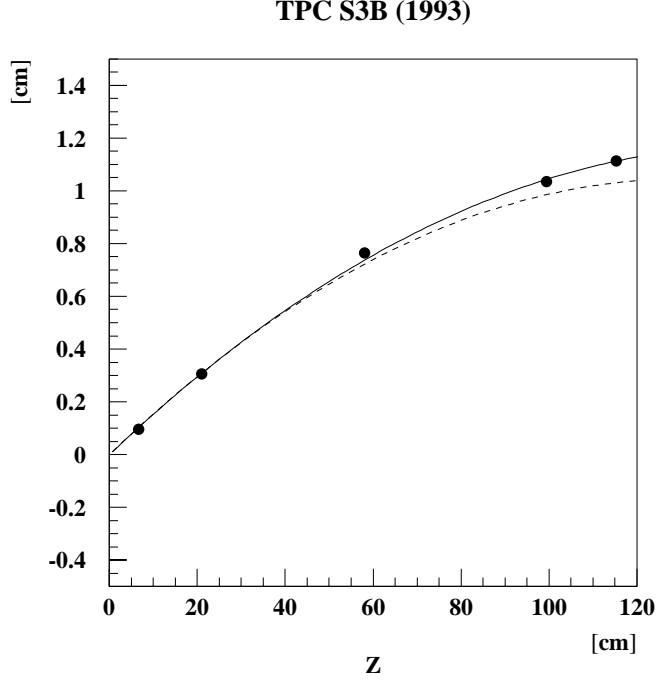
Figure 7.7: The δx shift in positions of fiber fiducials with the SLD magnetic field as a function of TPC-z for one TPC on the south barrel [164]. The dashed curve is the quadratic shift expected from the radial magnetic field B_r in Eq. (7.3). The solid curve includes a linear term for misalignments of the TPC drift direction with respect to the axis of the SLD $\vec{B}$ field (see Eq. (7.4)).

Eq. (7.1) over z, we get

$$
\begin{aligned}
\delta r &= \frac{(\omega\tau)^2}{1+(\omega\tau)^2} K \left(z_1^2 - z_2^2\right) \\
r\,\delta\phi &= \frac{\omega\tau}{1+(\omega\tau)^2} K \left(z_1^2 - z_2^2\right),
\end{aligned}
\tag{7.3}
$$

where z_1 and z_2 are the start and end of drift considered, and $K = r_c B_r^0 / (2 r_0 z_0 B_z)$ with r_c the radius at the CRID TPCs.

For each TPC, the shifts in fiber positions with magnetic field are measured at various drift distances. An example of these measurements is shown in Fig. 7.7, where one can see that the effect is quite large (11 mm at long drift).

If we include the effects of electrostatic focussing and of small misalignments of the TPCs, these shifts can be parametrized by a quadratic function of drift distance (in TPC coordinates) [164]:

$$\delta x = (\sin^2\alpha\,\varepsilon_x \pm \sin\alpha\cos\alpha\,\varepsilon_y)z \,\pm\, \sin\alpha\cos\alpha\,f(y-y_c) \,\pm\, \sin\alpha\cos\alpha\,Kz(2z_0-z)$$
$$\delta y = (\sin^2\alpha\,\varepsilon_y \mp \sin\alpha\cos\alpha\,\varepsilon_x)z \,-\, \cos^2\alpha\,f(y-y_c) \,+\, \sin^2\alpha\,Kz(2z_0-z),$$

(7.4)

where the upper (lower) signs hold for south (north) TPCs, α is the Lorentz angle, $\tan\alpha = \omega\tau$ (41° for C_2H_6), f is a focussing strength, and ε_x, ε_y are angular misalignments of the TPCs. The center of the anode wires is y_c, the distance from the SLD midplane to the anode plane in the CRID detectors is z_0, and $r \simeq (y-y_c)+r_c$ is the SLD radial coordinate. These parameters $(\varepsilon_x, \varepsilon_y, f, K)$ have been determined for each TPC, and are found to be in good agreement between the 1992, 1993, and 1994–95 run periods [164].

7.5   Charge Division Resolution

The third coordinate (TPC-y) of each photoelectron hit is measured by the ratio of the amplitudes of the pulses on either end of the anode wire. Therefore, an important element of accurate reconstruction of TPC-y is the calibration of the gain of each amplifier so as to achieve a uniform response. This is done via a special calibration run where pulses are injected into each amplifier from a calibration DAC and the resulting waveforms written to tape [132]. Due to electronics and detector replacements, this process must be repeated for every run. The gain calibration has been shown to improve charge division performance by some 0.8%, subtracted in quadrature [132].

The charge division resolution has been measured from the front row of angled fiber fiducials [133, 132], as shown in Fig. 7.8. The residuals have a component from the width of the UV fiber (0.91 mm), which must be subtracted in quadrature to obtain the charge division resolution of $\sigma_y = 2.3$ mm in 1992 and $\sigma_y = 2.6$ mm in 1993 [132].
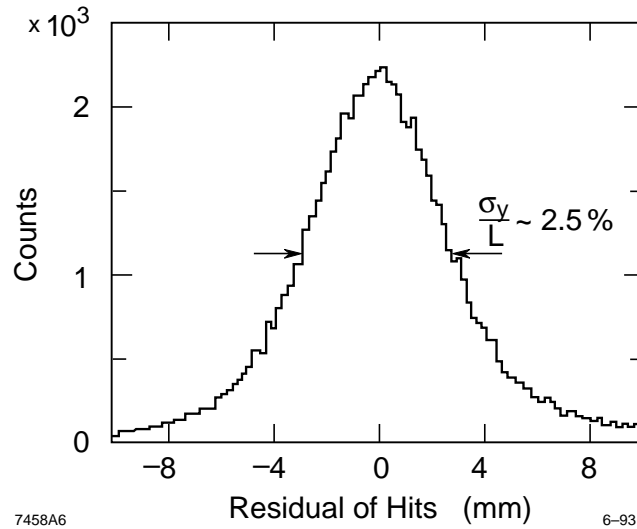
Figure 7.8: The residuals in depth (TPC-*y*) of hits from the front row of angled fibers. This width of 2.7 mm includes a contribution of 0.91 mm from the width of fiber beam, giving a charge-division resolution of $\sigma_y/l = 2.6$ mm or 2.5% [132].

As discussed in section 4.3.4, the charge division performance of the SLD detectors was degraded from the original design of 0.7% to $\sim 2\%$ by the choice of a lower operating gain. In retrospect, this 2-mm performance is adequate, as evidenced by the local resolution achieved in the gas (see section 7.12), and also by analytical calculation [165]. Furthermore, the contribution to σ_x, σ_y from diffusion has been measured in the production TPCs to be $165 \ \mu m \ \sqrt{z/\mathrm{cm}}$ [164], which gives 1.8 mm at long drift.

7.6 TPC alignment

All of the preceding adjustments and corrections apply to the coordinate system *within* the individual TPCs. Although each of these corrections are important, it is equally important to be able to transform from the coordinate system of the TPC to the SLD global coordinate system. To do this, we must know the positions and orientations of each of the 40 TPCs.

Unfortunately, no mechanical survey of the TPCs was done when they were installed, as time pressures in the assembly of the SLD were too great. The midplane mounting pins (see Fig. 4.10) were surveyed before the CRID vessel was moved into the SLC collider hall, but this occurred before the vessel was loaded with TPCs and liquid radiators, so the midplane may well have shifted since then. In addition, one might expect the whole CRID structure to sag somewhat with the extra weight. Furthermore, a clearance problem was discovered with the installation of the north-side TPCs, and many of the mounting blocks had to be moved and re-glued *in situ*. Thus, one cannot rely on any engineering specifications of the positions of the TPCs; they must be determined empirically.

This alignment is done by comparing the positions of tracks extrapolated from the CDC with ionization deposits in the CRID. Because of the saturation of the CRID amplifiers by minimum ionizing particles (MIPs), this is somewhat problematic. For saturating hits, the CRID pulsefinding algorithm reports the first bucket above threshold (in the deconvolved space) as the position of the hit. We assume that this is the time at which the first photoelectrons arrive at the detector plane. If the track comes from the IP, then the region of ionization outermost in radius (TPC-y) will be the region that generates those first photoelectrons.

However, this comparison is complicated by the diffusion of the electrons as they drift towards the CRID detectors, which is different for the collection of ~ 1000 electrons deposited by MIPs than for single photoelectrons. Therefore, we do not try to extract an alignment in z from the track-MIP comparisons. Instead, we use the centroid of the MIP cluster in TPC-x (SLD azimuth) to compare with the point at which the track crosses the center of the TPC, and extract shifts in ϕ [166]. We can also extract rotations $\partial\phi/\partial z$ of individual TPCs by considering the azimuthal shifts in bins of drift distance z.

Combining the average shift and the rotation, we can present the alignment results as a set of azimuthal shifts of each end of each TPC (shown in Fig. 7.9). The shifts at the high-voltage end (CRID midplane) should be opposite for
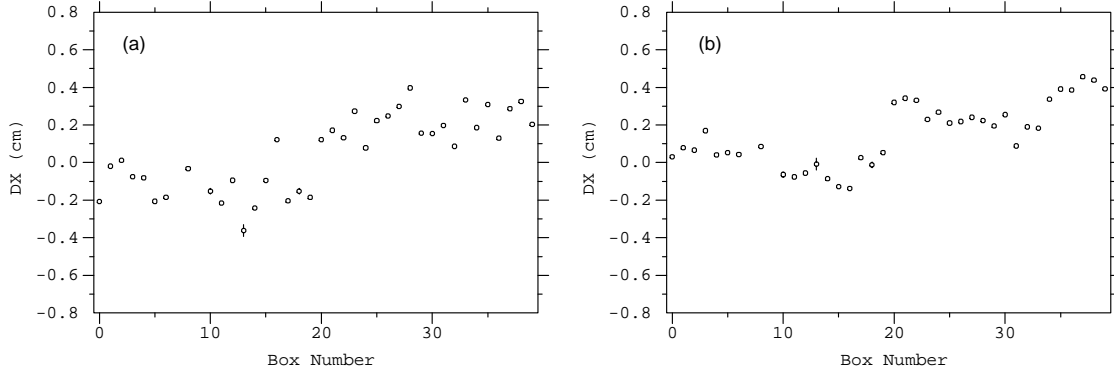
Figure 7.9: Measured shifts and rotations of each of the 40 Barrel CRID TPCs, presented as the shifts in each end of the TPCs. The shifts in TPC-*x* at the high-voltage end (*i.e.*, at the CRID midplane) are shown in (a), and the shifts at the detector end of the TPC are shown in (b). For a discussion of the misalignments implied by these data, see the text.

back-to-back TPCs, since they share a common mount pin. The global offset of ~ 2 mm between north and south TPCs indicates a relative misalignment in azimuth of the CRID with respect to the CDC. When this global rotation is added to the endplate positions in Fig. 7.9b, the south TPCs are uniformly ~ 2 mm away from zero, indicating a shift in the south end structure with respect to the midplane.

Finally, by comparing positive and negative tracks below 0.7 GeV/c (which have significant curvature), we can extract δr and $\partial r / \partial z$. Such measurements show a tendency for the TPCs to be tilted such that the detector end lies at a smaller radius. These radial measurements, however, have limited precision (~ 1 mm) with current statistics [166].

7.7 Liquid Radiator Gaps

After the procedure of the previous section to fix the positions of the TPCs, the remaining degrees of freedom for liquid rings are the positions and orientations of the liquid radiator trays. Since the trays are nominally homogeneous
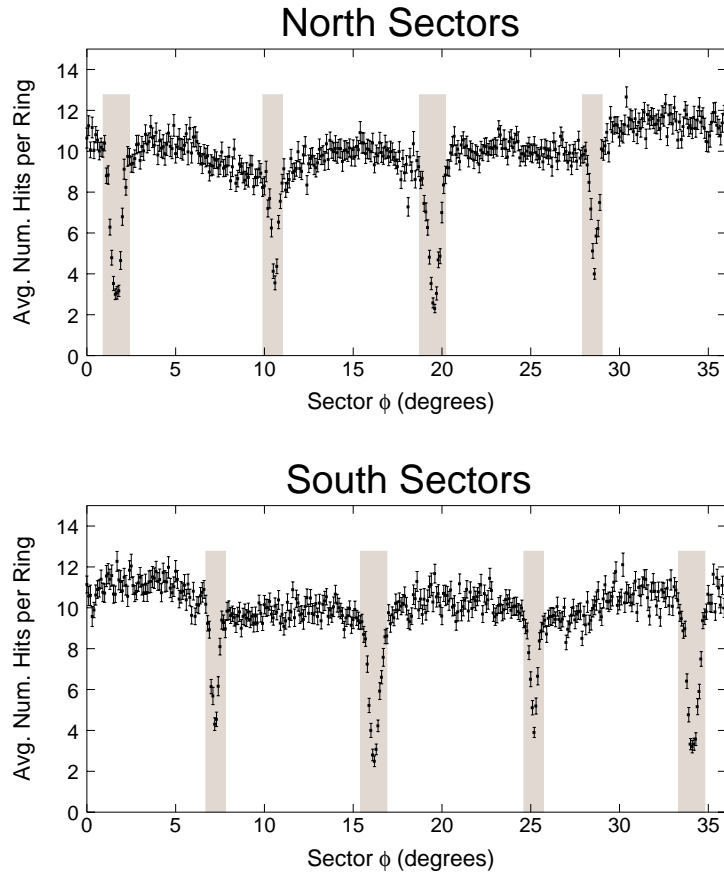
Figure 7.10: Average number of hits per liquid ring for $p > 3\,\mathrm{GeV}/c$ tracks as a function of the azimuthal position of the incident track modulo the CRID sector width of $36°$. The four dips that are present correspond to the two gaps between the liquid trays and to the G-10 support rib in the center of each tray. The fiducial cut described in the text is shown by the shaded bands.

planes, only the radial positions of the trays and the location of their edges are important. That is, we need to be able to identify tracks which miss the liquid trays and would not, therefore, be expected to produce a liquid ring.

These edges can be searched for in the data, by considering the average number of liquid ring hits for $β = 1$ ($p > 3\,\mathrm{GeV}/c$) tracks as a function of track azimuthal position and z position. The azimuthal part of this is shown in Fig. 7.10. One can clearly see dips between the trays (at $16°$ and $34°$ on the

south, and $2°$ and $20°$ on the north). One can also see dips at the middle of the trays, where there is a supporting rib of G-10. From this study, we can select a fiducial region of the trays that ensures no degradation of N_0 from tray edge effects. This region corresponds to a cut of 1.0 cm within the tray and away from the central rib, as demonstrated in Fig. 7.10.

7.8   Liquid Radiator Tilts

The other important piece of aligning the liquid radiator trays is knowing their radial positions. Since the reconstructed Cherenkov angle is proportional to the relative separation of the TPC and liquid tray (see section 6.2), it is important to know the relative position in radius of all points on the tray with respect to the TPC. Because of the engineering constraints of the mounting of the trays, we expect the tilt in $\partial r/\partial \phi$ to be less significant than tilts in $\partial r/\partial z$. The design of the CRID has tilts in each tray such that any bubbles in the C_6F_{14} will rise to the endplate edge of the tray, where the outlet pipes are located. Additional tilts can arise from misalignments of the CRID endplates with the midplane, such as those seen in the TPC alignment (section 7.6). The survey of the liquid radiator mounting pins suggests that welding misalignments in the end structure generally shrunk the endplate in the radial direction [167], and this is consistent with the TPC $\partial r/\partial z$ alignment.

The technique used to measure the radial positions and tilts of the trays is to consider the radius of liquid rings as a function of track dip angle or of the TPC-z position of the Cherenkov photon hits.* As in the t_0 analysis (section 7.2), we split up liquid ring hits into quadrants in ϕ_c along z, forward, backward, and sideward (see Fig. 7.4). The situation before alignment (using the surveyed positions of the liquid tray mounting pins) is shown in Fig. 7.11, where we see a large spread among the trays.

---

*The track dip angle, the z of the hit, and the Cherenkov azimuthal angle ϕ_c are all related (see section 6.2). If we specify two of these variables, we effectively determine the third.
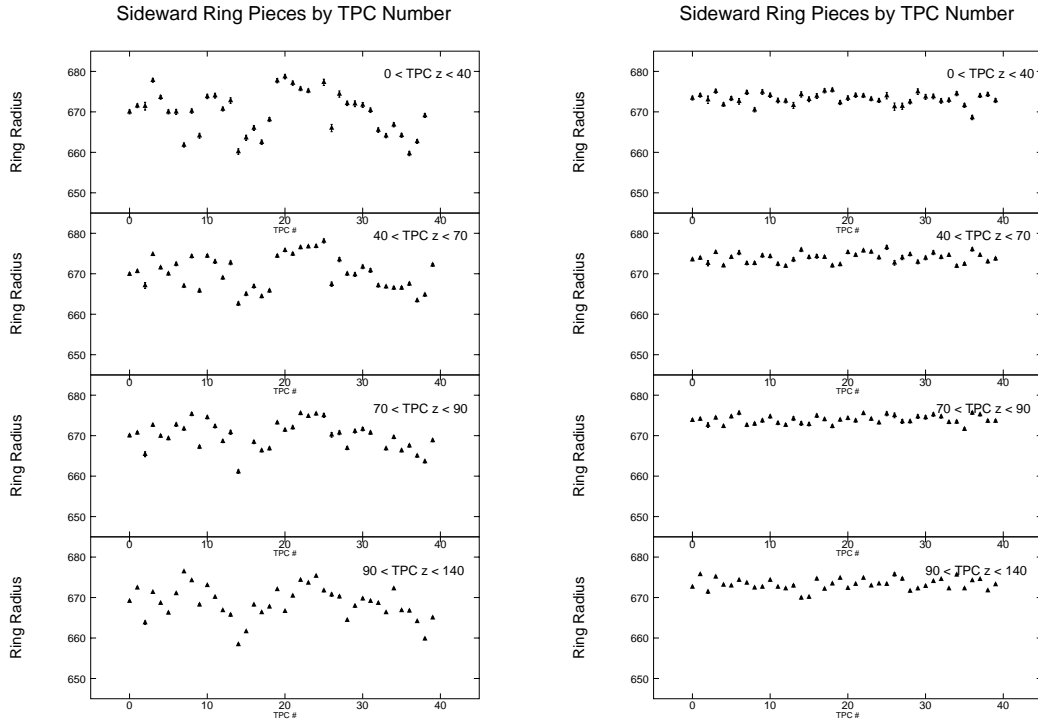
Figure 7.11: Average $\beta \simeq 1$ Cherenkov angle in the liquid for hadronic events by TPC number for four slices in TPC-z. The plots at left are prior to the alignment of individual trays, and the plots on the right are post-alignment, using the same dataset.

The procedure for measuring tilts is demonstrated in Fig. 7.12b. We compare the average liquid Cherenkov angle of $p > 3$ GeV/c tracks from hadronic events as a function of the TPC-z position of the hit. By shifting the ends of the liquid trays (typically $\lesssim 1$ mm), we are able to remove the variation of Cherenkov angle with the position of the hit in the TPC. The overall radial position of each tray is adjusted so as to equalize the average Cherenkov angle over all the trays at a value of 672 mrad. We input into the CRID reconstruction the corresponding liquid index, adjusted for the difference between the momenta of the tracks used and that of a $\beta = 1$ sample. This liquid index differs from the expected index (675 mrad *v.* 668 mrad); however, the particle identification performance is unaffected by this.
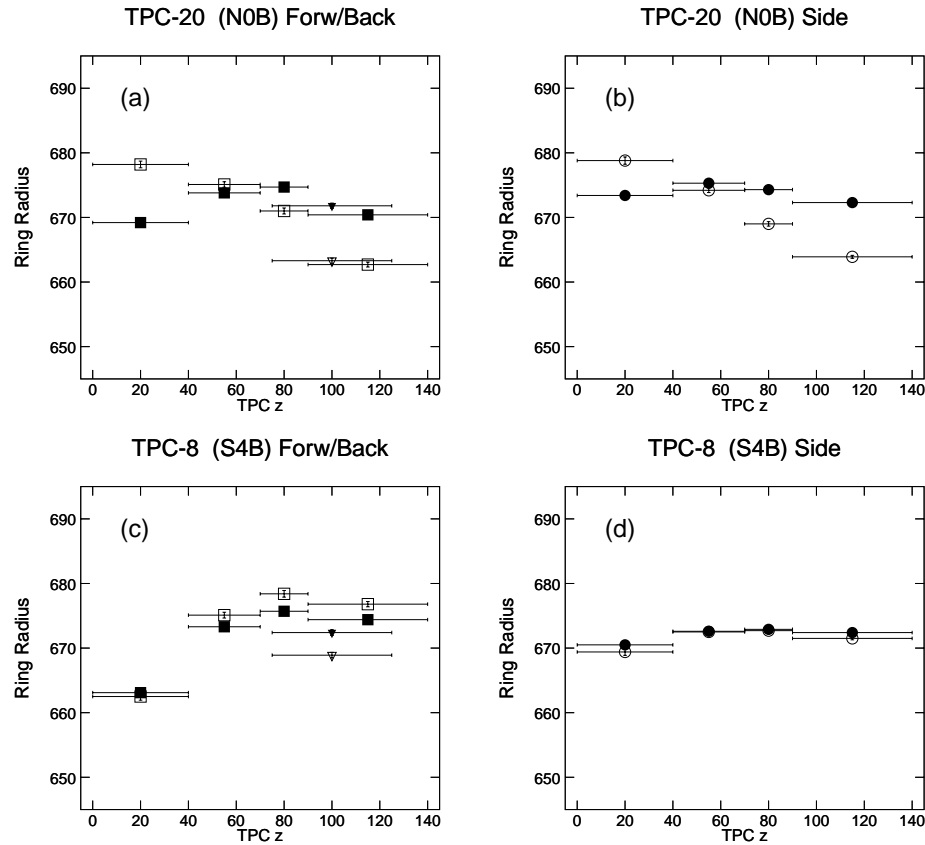
Figure 7.12: An example of liquid radiator tilt correction is shown for TPC N0B in (a) and (b). The open points are the average liquid Cherenkov angles before the correction, and the solid points are after correction, which show a flat dependence on TPC-z (within ± 3 mrad). A similar example for z-shifts of the TPCs is shown in (c) and (d) for TPC S4B. The triangles are the forward quadrant angles and the squares are the backward quadrant angles. In the open points (before correction), there is a 8 mrad spread between forward and backward angles, which is removed after the z-shift.

7.9   TPC z-shifts

The technique for determining shifts in z of each TPC is the same as that for determining the liquid radiator tilts above. After flattening the dependence of the Cherenkov angle as a function of TPC-z for the sideward liquid ring pieces (tilts in the liquid trays), we consider the forward and backward quadrants of the liquid rings. As in the t_0 analysis (section 7.2), these pieces are sensitive to shifts of the TPCs along z. We introduce a shift for each TPC and vary this shift until the forward and backward quadrants have the same Cherenkov angle (see Fig. 7.12c).

The result of both of the TPC z-shifts and the liquid radiator tilts is shown in Fig. 7.11. We see that the variation of average Cherenkov angle among the TPCs and within the TPCs is now quite small. In addition, the average angle of all of the forward, backward, and sideward pieces are in good agreement, indicating that our model for these alignments is sufficient up to the current precision.

7.10   Mirror Alignment

For the gas rings, rather than aligning radiator trays, we need to align the 400 spherical UV-mirrors which sit at the outer radius of the CRID. This is done by fitting rings for a sample of isolated $p > 4.5$ GeV/c tracks from all available hadronic and leptonic Z^0 decays [166]. In the fits, the Cherenkov radius, θ_c, as well as the position of the center of the ring, (x_c, y_c), in Cherenkov angle space is allowed to vary. Only rings with 5 or more hits and with low background are used in the fits, which corresponds to about 50% of tracks or roughly 100–200 rings per mirror, with a large variation. A subset of the fit results is shown in Fig. 7.13. One can see that prior to alignment, the spread of ring centers was a dominant contribution to gas ring resolution. The alignment reduced the RMS spread of the fitted ring centers from 6.0 mrad to 4.0 mrad. This remains slightly larger than the Monte Carlo expectation of 3.5 mrad (by 2.0 mrad in
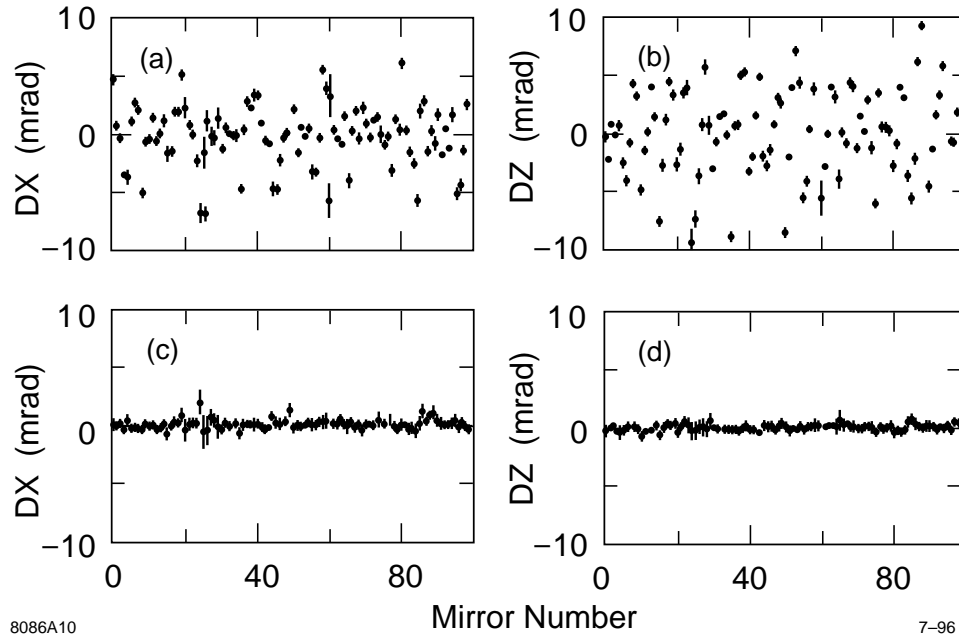
Figure 7.13: The average shifts of ring centers in TPC-*x* (a) and *z* (b) from ring fits for a quarter of the Barrel CRID mirrors. The results of the fits after mirror alignment are shown in (c) and (d). Note that the data samples are identical, so (c) and (d) serve only as a check that the ring-fit results were correctly translated into geometry constants.

quadrature), indicating the presence of some sort of correlated smearing of the gas rings. As discussed in section 7.15, we include a correlated smearing in our Monte Carlo simulation.

7.11   Gas Index of Refraction

One difficulty affecting the gas resolution is the time-dependence of the CRID gas radiator mix. Because the CRID is operated with a mixture of C_5F_{12} and N_2 (see section 4.3.1), the index of refraction is dependent on the exact mixture. Unfortunately, this mixture has not been entirely stable over time. The mixture is controlled by a feedback circuit that adjusts the mix in order to maintain a target sound velocity in an ultrasonic flow meter. Instabilities
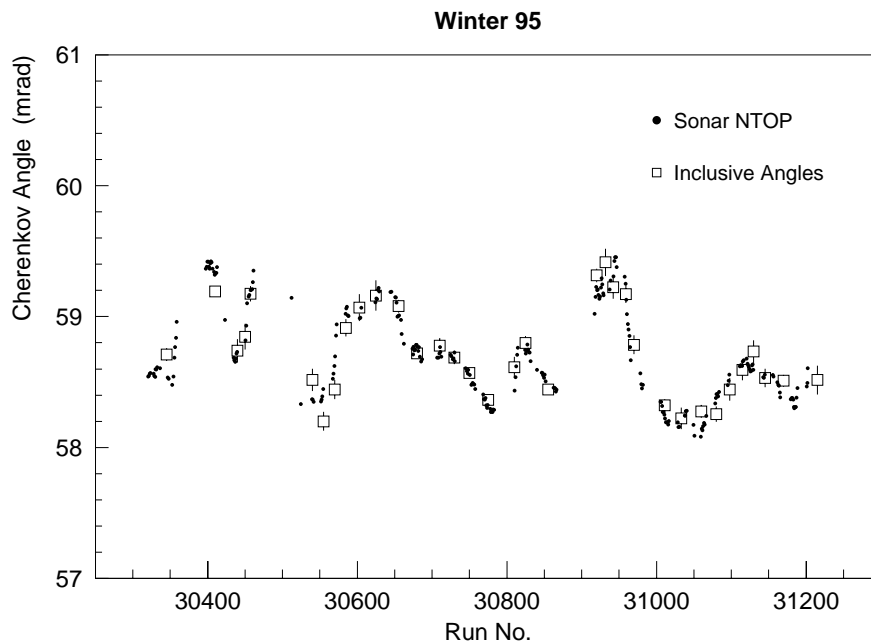
Figure 7.14: The $\beta \simeq 1$ Cherenkov angle measured from ring reconstruction (squares), compared with the value expected from the gas index measured by sound velocity in the CRID vessel and corrected for atmospheric pressure (dots). These points are for a selected range of time in the winter of 1995, which corresponds to a period of relatively unstable mixture.

in the analog sonar readout introduced variations in mixture of as much as 2–3%. There were also deliberate increases in the C_5F_{12} concentration of the gas radiator of 1–5%, which occurred infrequently, but must also be accounted for in the reconstruction. Fortunately, the readout of the CRID vessel sonar monitors is not subject to the same drifts, and these values are recorded to tape regularly. Figure 7.14 shows the excellent correspondence between the average Cherenkov angle for $\beta \simeq 1$ tracks from the inclusive angle distributions and the angle expected from the sonar velocity measurements, corrected for pressure variation. This sonar data is used to establish an empirical relation for the gas refraction index, n_g, as a function of time, which is then used as input to the reconstruction.

7.12 Cherenkov Angle Resolution

The effects of all of the preceding corrections and alignments can be summarized by the Cherenkov angle resolutions seen in hadronic data. These are shown in Fig. 7.15 for gas rings and Fig. 7.16 for liquid. In Fig. 7.15c, we see the residuals of the gas Cherenkov angle hits after fitting for both the center and radius of the ring in $e^+e^- \rightarrow \mu^+\mu^-$ events. The width of this distribution implies a "local resolution" or ideal performance of the CRID of 3.6 mrad. The distribution in Fig. 7.15b is similar, but shows the distance of each hit with respect to the fitted ring center (*i.e.*, it does not include variation in the radius of the ring). The width of this peak is 4.0 mrad; however, the time-dependence of the gas radiator index n_g (see section 7.11), which should account for ~ 1.0 mrad of this extra smearing, has not yet been removed from Fig. 7.15b. The remainder of the 1.7 mrad difference between (b) and (c) is believed to be due to variations in the radius of curvature of the CRID mirrors. Figure 7.15a shows the inclusive gas Cherenkov angle width, which is the "global resolution" seen
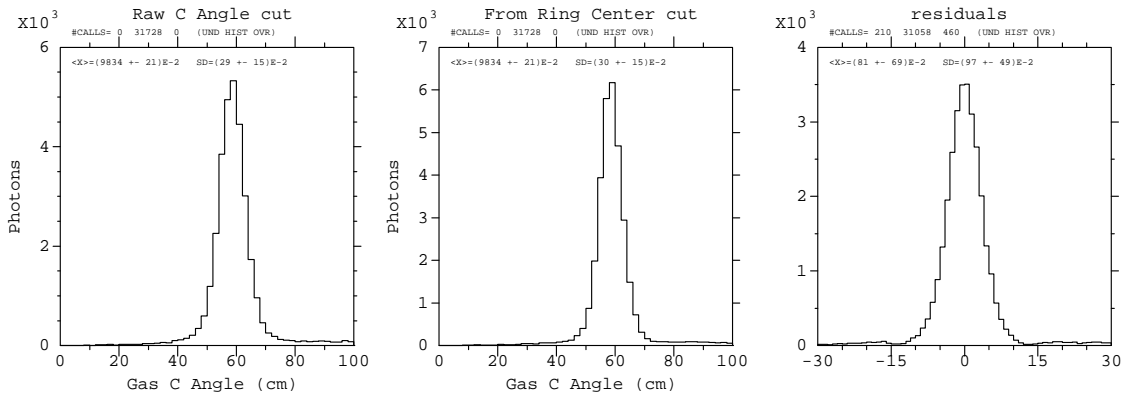
Figure 7.15: Gas Cherenkov angles for $e^+e^- \rightarrow \mu^+\mu^-$ events from inclusive reconstruction (a) and for ring fits (b) and (c). The distribution in (c) are the residuals from the fitted circle and represents the true "local resolution" (3.6 mrad) of the CRID. The distribution in (b) is the distance from the fitted center, and therefore includes variation in the ring radius. The width of the distribution in (a) represents the overall gas angle resolution (4.5 mrad).

in the data (4.5 mrad). This extra width is accounted for by the smearing of the ring centers of 2.0 mrad described in section 7.10. We parametrize the total difference between the global resolution and that expected from local resolution and time variation of n_g as an additional Gaussian error of 1.5 mrad (`CRDRECP%(GSYSERR)`).

Unlike the situation in the gas rings, where we do not expect the Cherenkov angle resolution to vary much over the acceptance of the CRID, the liquid Cherenkov angle resolution is strongly dependent on geometrical factors (*e.g.* what angle the incident track makes with the liquid radiator). Therefore, we present it as a function of track angle (Fig. 7.16a and b). The resolution also varies with the azimuthal angle of the Cherenkov photon (ϕ_c), as shown in Fig. 7.16c and d. We derive the resolution points shown in Fig. 7.16 by averaging over the available ϕ_c range for each track angle with equal weighting. Note, however, that the maximum likelihood analysis of section 6.4 uses the expected σ_θ to weight individual hits.

The inclusive liquid angle resolution for $\beta \simeq 1$ tracks is shown in Fig. 7.16a for hadronic events and for $Z^0 \to \mu^+\mu^-$ and $Z^0 \to e^+e^-$ events. Because the background shape under the Cherenkov ring also varies strongly with track dip angle (due to total internal reflection and other phase-space effects), we expect some systematic variation in the Gaussian fits with dip angle. The dimuon sample, however, is largely free of background, so the dimuon points should better parametrize the true resolution.

We compare the observed (data) resolution curve with a similar curve derived from Monte Carlo with no extra smearing of hits in Fig. 7.16b. Because much of the intrinsic liquid angle resolution is dominated by chromatic dispersion and the thickness of the liquid radiator, and because we have confidence in the photoelectron point resolutions from the gas-ring results, it is reasonable to believe that the Monte Carlo resolution represents the "ideal" resolution achievable in the liquid. The difference between the data and ideal Monte Carlo curves in Fig. 7.16b is parametrized as an extra error of 10 mrad added in quadrature (`CRDRECP%(LSYSERR)`). The Monte Carlo hits are smeared by
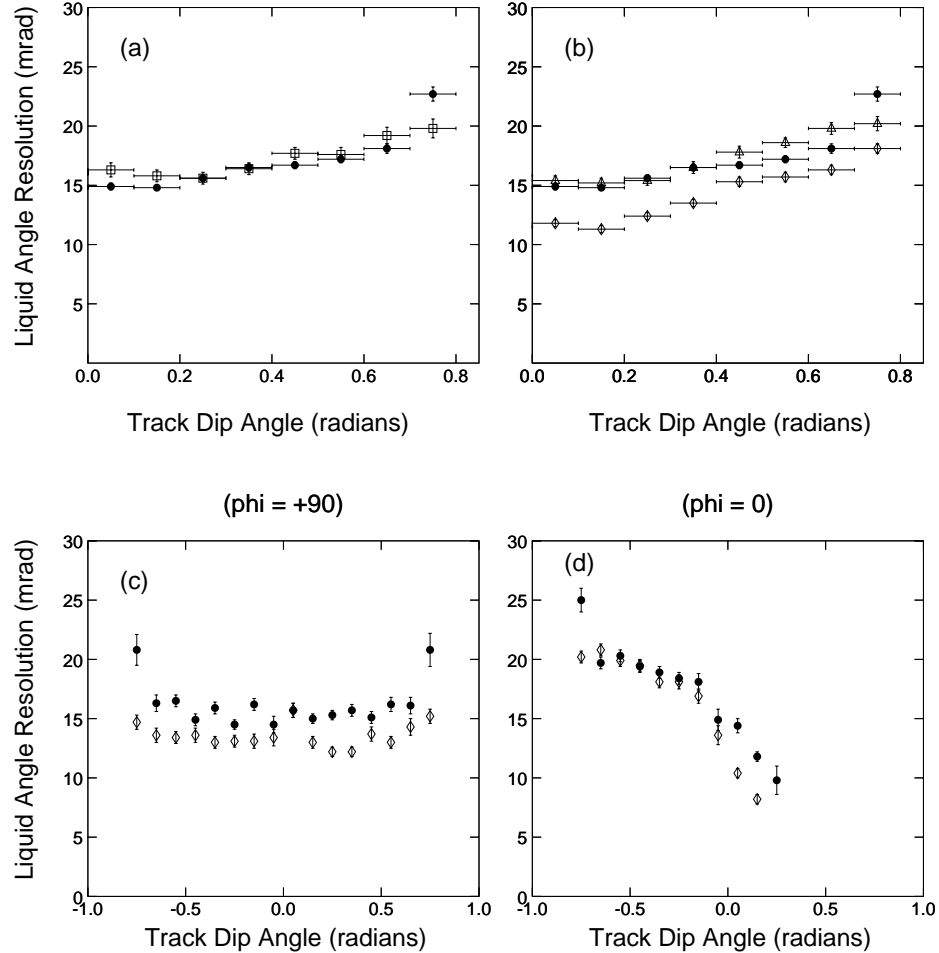
Figure 7.16: Liquid Cherenkov angle resolution seen in the 1994 data (a). The squares are results from hadronic events, while the dots are from $e^+e^- \rightarrow \mu^+\mu^-$ and $e^+e^- \rightarrow e^+e^-$ events, which are a cleaner test (see text). The dimuon resolution is compared with Monte Carlo simulation in (b). The diamonds are the resolution from our standard simulation, which are consistently lower than the data. The triangles are the same simulation with an extra 10 mrad smearing (see section 7.15), which matches the data reasonably well. The variation of resolution around the ring with ϕ_c is demonstrated in plots (c) and (d), which show the dip angle dependence of resolution for two different quadrants in ϕ_c.

this amount, as discussed below in section 7.15. This smearing is presumed to be due to remaining misalignments, $\partial r/\partial \phi$ tilts of the liquid radiator trays, bowing of the windows in the liquid trays or in the TPCs, or similar effects.

7.13   Number of Hits

Besides Cherenkov angle resolution, the other primary figure of merit for ring imaging Cherenkov devices is the N_0 parameter, which is related to the number of photons observed per ring by Eq. (4.4). The N_0 is an inclusive figure that accounts for all efficiencies in photon detection and for all losses of photons due to imperfect transparency, mirror reflectance, or any analysis cuts applied in reconstruction.

One method of determining N_0 is from the inclusive Cherenkov angle distributions, Fig. 7.15a. We can find the total number of photoelectrons in the sample by fitting for the number of hits above background in the inclusive angle distribution. Before dividing by the number of tracks in the sample, however, we must correct for the path length of radiator traversed by each

Data sample	N_0 (cm^{-1})	Hits per full ring
Liquid dimuons (std. cuts)	41.6	16.1
Liquid hadronic (std. cuts)	25.0	11.2
Liquid hadronic (tight cuts)	29.7	12.8
Gas dimuons (std. cuts)	63.9	10.0
Gas hadronic (std. cuts)	53.7	8.4
Gas hadronic (isolated)	58.8	9.2

Table 7.1: SLD CRID N_0 and number of hits per ring for various data sets, and for liquid and gas radiators. The numbers for the hadronic dataset are shown for both "standard cuts," which corresponds to a check on the `BADID` bit described in section 8.3, as well as for "tight cuts," which corresponds to the full complement of cuts described in section 8.3.
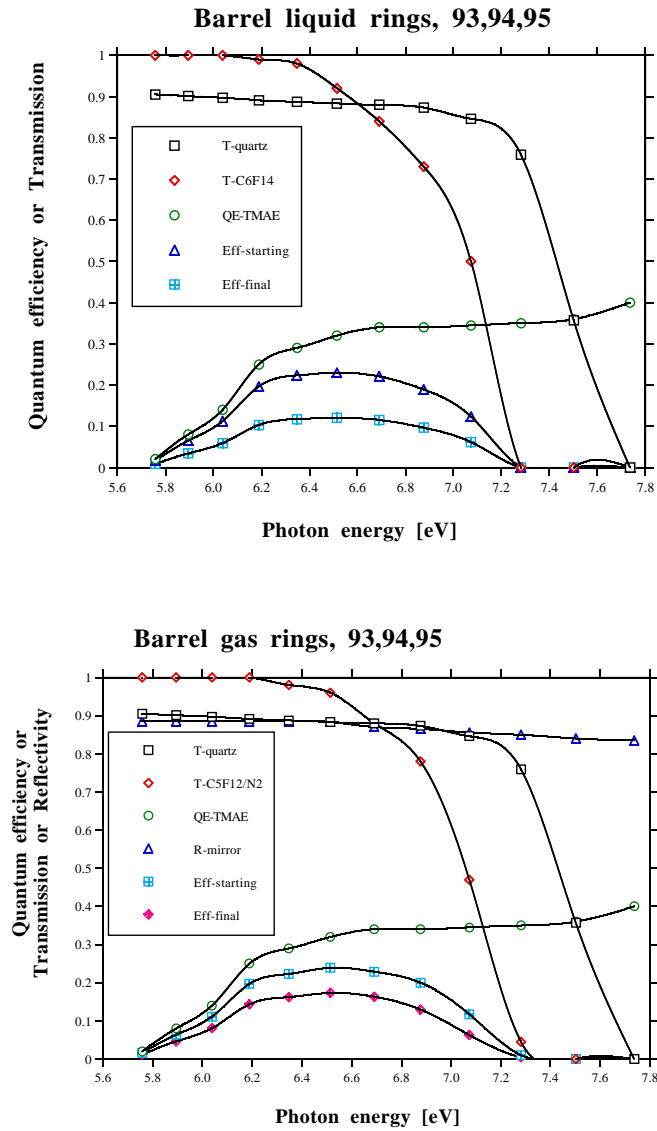
Figure 7.17: Cherenkov radiator and quartz window transmission, mirror reflectivity, and TMAE quantum efficiency are shown as a function of photon energy. The product of these curves gives the one labelled "Eff-starting" and represents the maximum possible number of hits with perfect photoelectron detection. When finite electron lifetime, photoelectron detection efficiency, thickness of the TPCs, and fiducial coverage of the TPCs are included, we obtain the curves labelled "Eff-final," which represent expected N_0 values of 45 cm^{-1} for liquid and 64 cm^{-1} for gas when integrated [168].
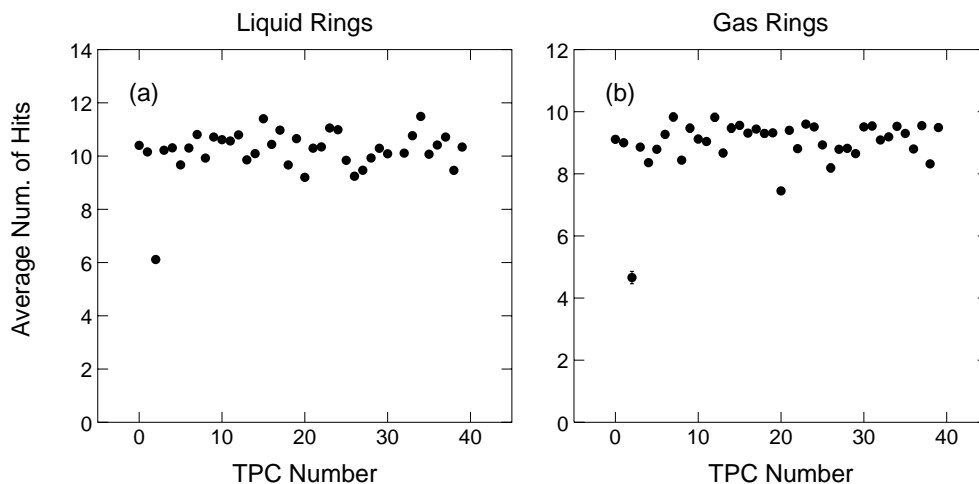
Figure 7.18: The average number of hits per ring as a function of TPC number for liquid rings (a) and gas rings (b). The spread of these measurements is introduced into our Monte Carlo simulation via a set of *ad hoc* factors.

track. In the liquid, we also correct for the effects of total internal reflection, which when averaged over all track angles, reduces the available ring arc to an average of 0.56 of 2π. Thus, the liquid N_0 we report is representative of a track at normal incidence to the liquid radiator trays. The resulting N_0 values and the equivalent number of hits per ring are shown in Table 7.1. These numbers may be compared to expectations based on radiator transmission, mirror reflectance, TMAE quantum efficiency, and electron detection efficiency [168]. The expected N_0's do not include the hit-quality cuts described in section 6.1. Therefore, we expect only the dimuon values in Table 7.1 to agree well with the N_0 expectation of Fig. 7.17, which they do.

In further analysis, it was discovered that the data possess more variation in number of hits than our Monte Carlo simulation predicts. Possible contributions to this effect include variations in the photon detection efficiency among the TPCs and MWPC detectors, in the transmission of TPC quartz windows, in the reflectivity of the mirrors, and in the transmission of the C_6F_{14} liquid

or its quartz windows. The first two factors would affect liquid and gas rings similarly for a given TPC, while the latter two would be independent for liquid and gas. Therefore, we repeat the N_0 analysis for both liquid and gas rings contained in each of the TPCs. Since we only require a relative efficiency and not an absolute number of hits, it is simpler to average the number of hits with signal weight above background in the maximum likelihood analysis (`PHCRID%(GAS,NHFND)` and `PHCRID%(LIQ,NHFND)`) for each track, rather than fit the inclusive Cherenkov angle distribution and subtract a background. The results of this study are shown in Fig. 7.18 and indicate a substantial variation of the number of hits among the 40 TPCs. There is general agreement between gas and liquid, but not perfect agreement, indicating that the effect is likely to be caused by a combination of the factors listed above. This effective efficiency is now modelled in the Monte Carlo simulation, improving the agreement on the width of the number of hits found per ring.

Another source of variation in number of hits is changes in detector gain over the run period. There is a short period of the 1994 run (about 10% of the dataset) in which the gain was reduced on all of the south detectors. This resulted in a $\sim 15\%$ decrease in the N_0 for those TPCs in that period.

An analysis of variation of number of hits with azimuthal angle and track dip angle is shown in Fig. 7.19 for gas rings. One can see structure that is produced by path-length variation as the track traverses various mirrors. The rises around $0°$ and $20°$ in azimuth come from gaps between TPCs, which increase available path length from 45 cm to ~ 55 cm. For every TPC, there are two rows of five mirrors, one of which is 2 cm farther away from the TPC (we call the farther row the "outer mirrors"). This 5% difference in path length is modelled in our simulation, but as we see in Fig. 7.19a, the difference between inner and outer mirrors in the data is much larger than expected. The reason for this is not yet understood; instead, we introduce an empirical correction for it into the simulation.

One can also see the effect of path-length variation on the gas average number of hits in the orthogonal direction, *i.e.*, with track dip angle. This is
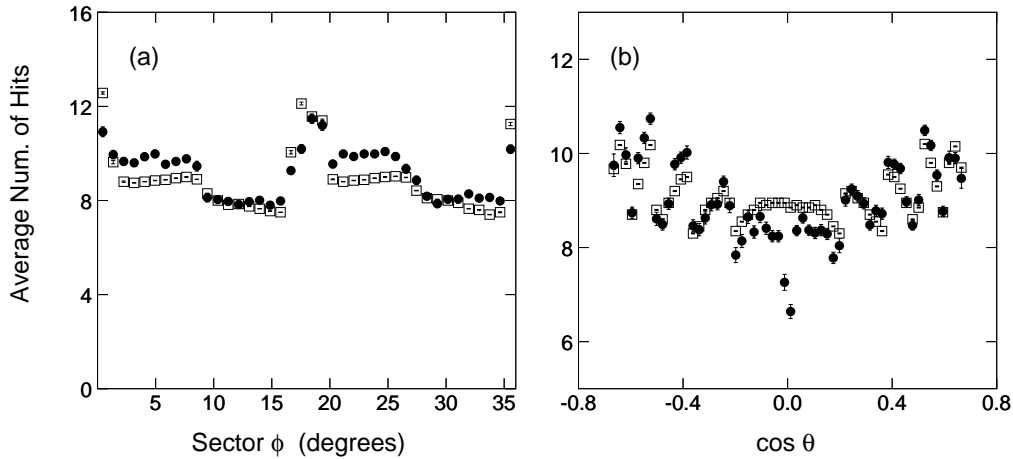
Figure 7.19: The average number of hits per gas ring is shown as a function of track dip angle (a) and of the track azimuthal angle within a sector (*i.e.*, modulo $36°$). The circles are numbers calculated from the 1994–95 data and the squares are the expectation from Monte Carlo simulation. Although the structure produced by the five mirrors on each side is reproduced fairly well in (b), it is clear that more hits are lost at long drift ($\cos\theta = 0$) in the data, which is attributed to losses due to finite electron lifetime in the drift gas (which was not included in the simulation depicted here).

shown in Fig. 7.19b. Here, one can see the shape induced by the five mirrors on each side of the CRID. In comparing with the Monte Carlo simulation, however, we see a depletion of hits at long drift (near a track angle of $\cos\theta = 0$). This is attributed to a finite electron lifetime of 200 μs (9 m) in the drift gas, where this value has been determined by tuning the simulation to match the data in Fig. 7.19b. This value is consistent with that measured in the online Electron Lifetime Monitor (see section 5.5.1).

7.14   Identification Efficiency

Although resolution and N_0 are the two basic factors which determine identification efficiency, we nevertheless require some direct tests of identification
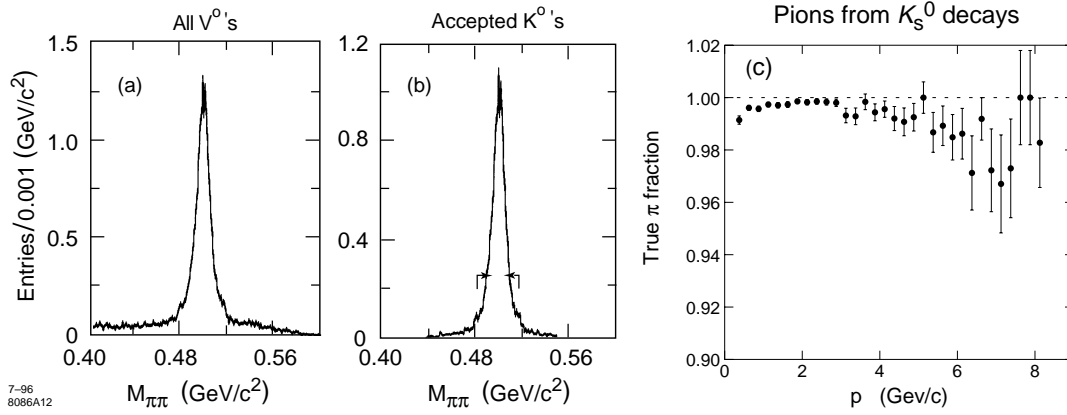
Figure 7.20: Mass peak for the decay $K_s^0 \to \pi^+\pi^-$ before (a) and after (b) cuts to remove $\Lambda^0 \to p\pi^-$ decays. Also shown (c) is the purity of $\pi^\pm$ in our selected sample of tracks (based on Monte Carlo simulation).

efficiency. One way to do this is to consider a sample of tracks with known particle identity. In all of the following test samples, the selection cuts of Chapter 8 are applied, and the particle identification criteria of section 8.3 are used. The most straightforward of such samples is pions from $K_s^0 \to \pi^+\pi^-$ decays. These can be found with good efficiency using displaced vertices, and contamination from $\Lambda^0 \to p\pi^-$ decays can be removed with a cut on helicity angle $|\cos\theta^*| < 0.8$. The resulting sample is very pure, as shown in Fig. 7.20. According to Monte Carlo simulation, some $> 97\%$ of the K_s^0 candidates within a $\pm 3\sigma$ mass window are true K_s^0, and $\sim 99.5\%$ of the candidate tracks selected from this procedure are actually pions (since a majority of tracks making up fake vertices are also pions), as shown in Fig. 7.20c. This sample provides an effective test for π identification in the liquid, and also for the lower momentum range of the gas (up to 8 GeV/c or so).

The identification efficiency rates extracted from K_s^0 pions are shown in Fig. 7.21 for the liquid and gas. We see that the correct-flavor ID is above 80% for the peak momentum range in both cases, and that the misidentification rates are below 5% in the liquid and 12% in the gas (for $p < 8$ GeV/c).
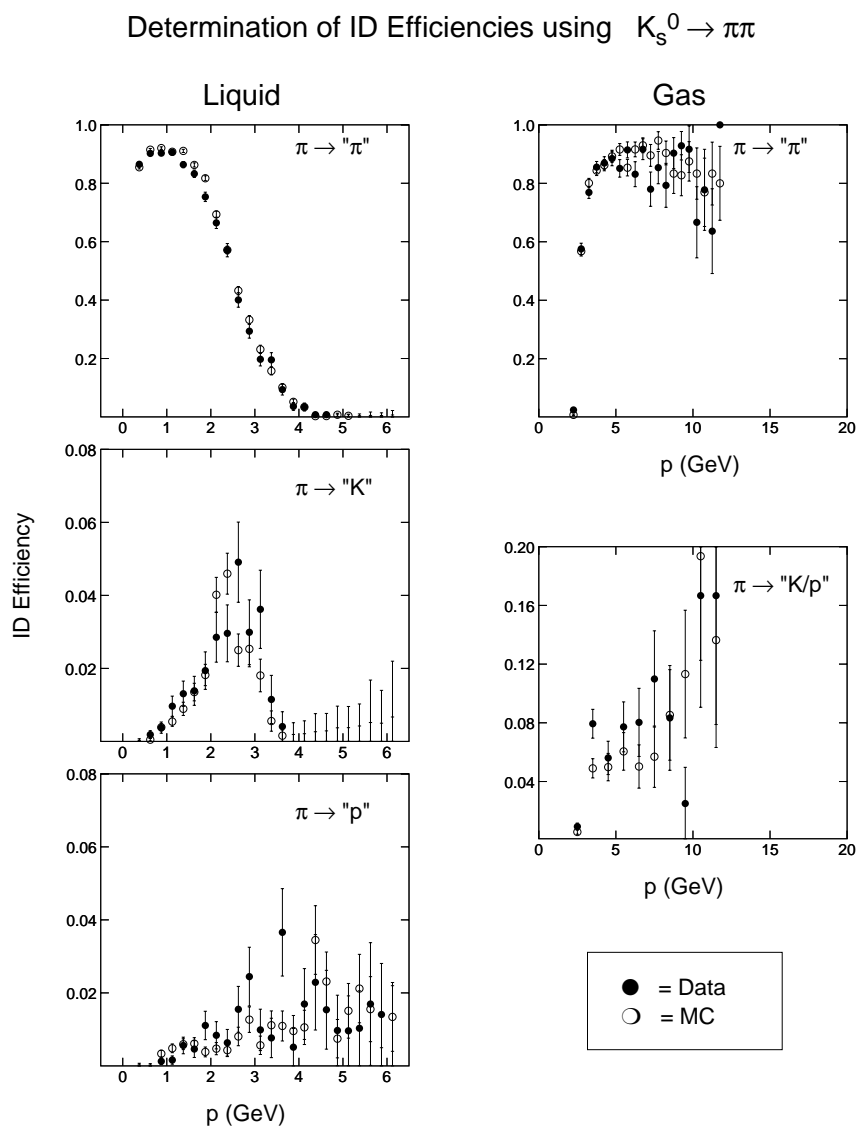
Figure 7.21: The particle identification efficiency in the liquid (left) and gas (right) obtained from a sample of $K_s^0 \to \pi^+\pi^-$ decays. The data points are shown as dots, while the results of a similar analysis applied to Monte Carlo are shown as open circles.
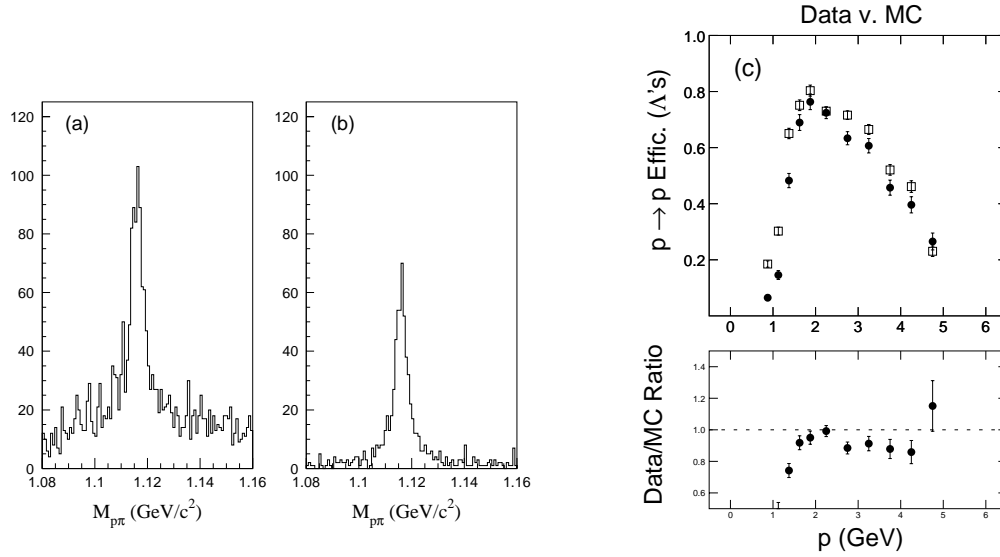
Figure 7.22: Mass peaks for $\Lambda^0 \to p\pi$ decays for a sample where the p track passes the CRID selection cuts of Chapter 8. The plot (a) has no selection on log-likelihoods applied, while the plot (b) requires the standard $L_p - L_\pi > 5$ and $L_p - L_K > 5$ criteria. The proton identification efficiency extracted by comparing the areas of the background-subtracted peaks in (a) and (b) is shown in (c) for data (dots) and Monte Carlo (squares).

Also shown is the results of a similar analysis performed on the simulation described in section 7.15. Agreement with the simulation is generally good, but not perfect, with some 3–5% discrepancies in the pion ID.

Another sample of known particle type is protons from $\Lambda^0 \to p\pi^-$ decays (and the charge conjugate). This sample is smaller than the K_s^0 pion sample by a factor of 6, due to the lower production rate and to there being only one track per V^0 vertex that is a proton. In addition, the purity is not as good, only 70% as estimated by Monte Carlo. Thus, the proton sample is not as stringent a test of identification efficiency as the pion sample. Nevertheless, we can extract a constraint on the p ID efficiency via the technique depicted in Fig. 7.22. An identical Λ^0 selection analysis is performed for tracks tagged as protons with a log-likelihood cut of 5 (Fig. 7.22b) as for all tracks passing the CRID selection
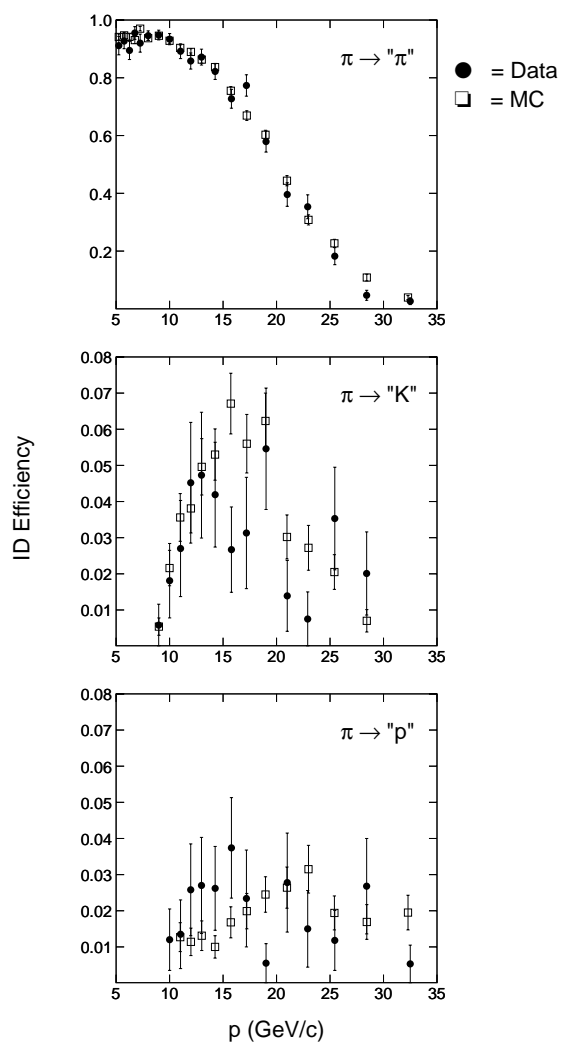
Figure 7.23: The particle identification efficiency in the gas obtained from a sample of $\tau \to e/\mu/\pi$ decays. Note that the leptons are indistinguishable from pions in the CRID at these momenta.

cuts (Fig. 7.22a). The resulting efficiency is shown in Fig. 7.22c for data and Monte Carlo. The agreement between data and Monte Carlo is within 10% except for the points just above the proton threshold, where we expect our simulation to be less reliable.

Finally, we can use $e^+e^- \to \tau^+\tau^-$ events to test pion identification in the high momentum range of the gas, as shown in Fig. 7.23. This is predicated on the small $\tau \to K$ branching ratio, which is reasonably well-measured, giving us a kaon fraction in τ decays of (1.8 ± 0.3)% [2]. The agreement of data and Monte Carlo in this regime is found to be excellent. All of the above samples of known particle type will serve as calibration samples for determining identification efficiency directly from the data, as described in section 9.2.2.

7.15   Monte Carlo Tuning

The final step of understanding the identification performance of the CRID is to be able to reproduce the observed identification efficiency distributions with our Monte Carlo simulation. Because of the residual misalignments discussed earlier, we need to add some *ad hoc* smearing of Cherenkov angles to the simulation (see section 7.12).

Since liquid rings cover a large area of several TPCs and are generated at a localized region of the liquid radiator, we expect the possibility that misalignments smear the Cherenkov angles in a correlated fashion. Other problems, however, may not be correlated with the track direction or the z axis. Therefore, we consider two classes of smearing. Figure 7.24 shows the effect of smearing Cherenkov angle in these ways for the liquid radiator. We see that the "uncorrelated smearing" (each Cherenkov hit is smeared in θ_c independently) does a good job of reproducing the K_s^0 identification efficiency at the high momentum end, but is too high in the region around 2 GeV/c. The "correlated smearing" curve (entire ring smeared along TPC-z or $\phi_c = 0$) is better in the 1.5–2.5 GeV/c region, but is too high above 3 GeV/c. The "mixed smearing" case, which consists of even parts of both of the previous two types of smearing, seems to do a
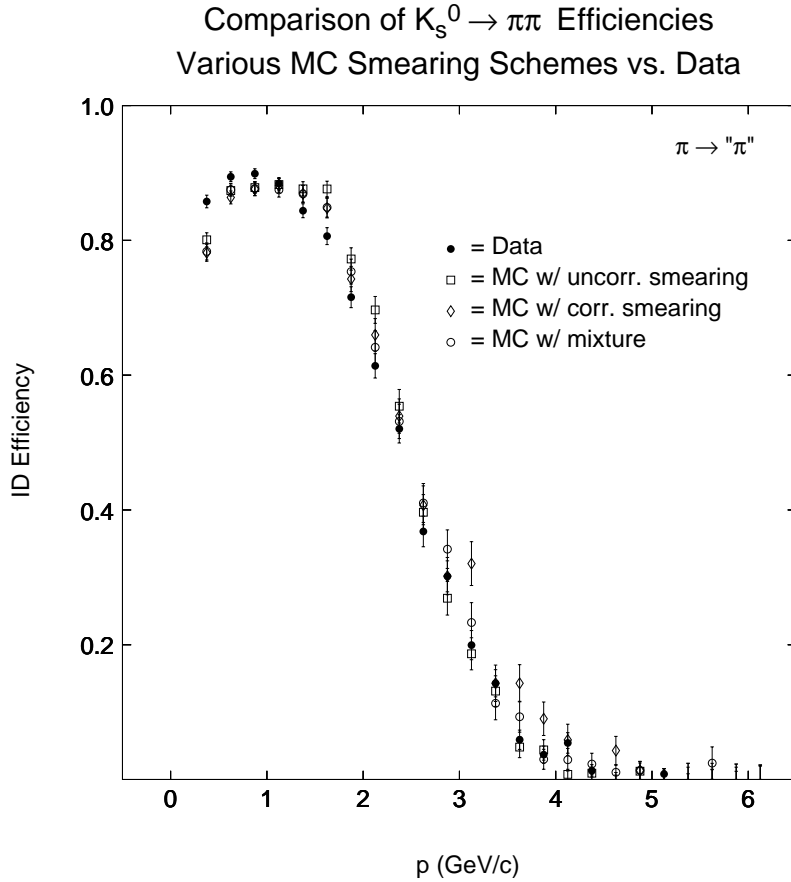
Comparison of $K_s^0 \to \pi\pi$ Efficiencies
Various MC Smearing Schemes vs. Data

$\pi \to "\pi"$

- • = Data
- □ = MC w/ uncorr. smearing
- ◇ = MC w/ corr. smearing
- ○ = MC w/ mixture

ID Efficiency

p (GeV/c)

Figure 7.24: The pion identification efficiency in the liquid for $K_s^0 \to \pi^+\pi^-$ decays in data and from Monte Carlo samples with various Cherenkov angle smearing (see text).

good job of reproducing the K_s^0 data. It also does an excellent job of reproducing the $\pi \to K$ misidentification rate seen in the data (see Fig. 7.21). Therefore, we employ this smearing model in our simulation of the liquid.

In the gas, the ring fits done for the mirror alignment show correlated shifts in the ring positions, as described in section 7.10. This type of correlated smearing can arise, for example, if the dominant error in Cherenkov angle comes from uncertainty on the dip angle of the track. Therefore, we add "correlated
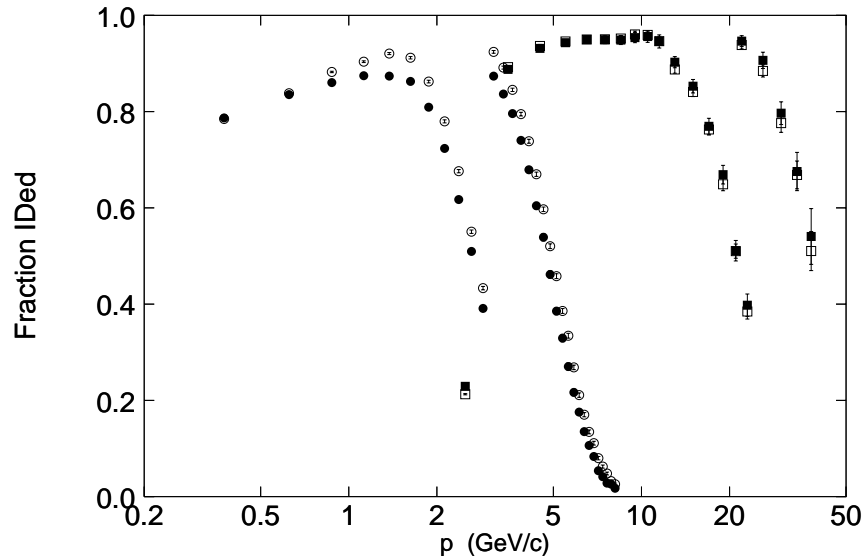
Figure 7.25: The fraction of unambiguously identified tracks is shown as a function of momentum when either two or three hadronic hypothesis are considered. The solid points represent the 1994–95 data, and the open symbols represent the Monte Carlo simulation. The circles represent the liquid radiator region, and the squares are for the gas radiator region. Different momentum ranges represent different analyses depending on whether π/K or K/p hypotheses are indistinguishable in the CRID over those ranges.

smearing" to the gas simulation, and the resulting Monte Carlo adequately reproduces the Cherenkov angle resolution seen in data. The correlated smearing also gives a generally good representation of the data (see Fig. 7.23). As a result, no uncorrelated smearing was considered.

As discussed in section 7.13, there was considerable variation in number of Cherenkov hits found with TPC number and with inner/outer mirrors. Therefore, a number of *ad hoc* photon efficiency parameters are introduced into the simulation. The technique is to generate an excessive number of Cherenkov photons at the early stages of the simulation, and then to discard some fraction of them at the later simulation stages, where this fraction may depend on the various *ad hoc* parameters. This technique allows for easy tuning of

the parameters without regenerating the entire simulation. The result of this process is excellent agreement of the variation of number of hits with TPC number, track dip angle, and azimuthal angle.

A final test of the Monte Carlo simulation is to consider the rate of tracks that are unambiguously identified as any of the available hadronic hypotheses ($\pi/K/p$). This is the complement of the fraction of tracks identified as ambiguous by the CRID. This test is not as stringent as those of section 7.14 because we might have offsetting errors that give the same total rate; but on the other hand, it is a high-statistics test which we can perform on the full hadronic data sample. The result is shown in Fig. 7.25 for the hadronic data and for the Monte Carlo simulation. There is excellent agreement in the gas region, and there is good agreement (discrepancies of 3–5%) in the liquid region. This adds confidence that our simulation is a reasonably close representation of the identification performance seen in the data.

7.16   Backgrounds

One of the larger concerns in the CRID simulation is the modelling of background hits. As discussed in section 6.4, the background model (uniform density) used in the maximum likelihood analysis is only a rough approximation to the true shape. Therefore, the identification algorithm is likely not to be immune to the characteristics of the background observed, and it is important for the Monte Carlo simulation to have comparable background characteristics.

To this end, we overlay hits from Random triggers onto our simulated events. This is found to produce roughly the right data volume, but does not quite match the characteristics of background in true hadronic events. In particular, the number of background hits in the vicinity of tracks is lower in the Monte Carlo than in data (see Fig. 7.26). It should not be too surprising that a significant source of background be correlated with the presence of tracks.* Although

---

*Of course, we do exclude the signal Cherenkov hits from other tracks in this discussion of background hits correlated with the presence of tracks. What is suggested by the data is that
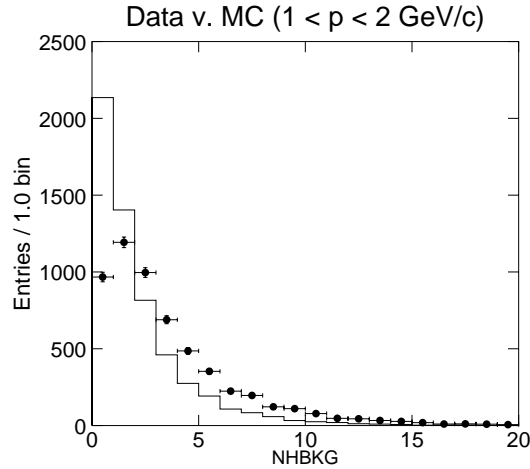
Figure 7.26: The number of hits in the vicinity of the expected liquid Cherenkov angles whose signal weight is below the background level for $1 < p < 2$ GeV/c tracks in the liquid is shown. Hits which have significant weight for a Cherenkov ring for some other track in the event are not included in this number. The points represent the 1994–95 data and the histogram represents the result from the Monte Carlo simulation. Clear differences are apparent, despite attempts to model backgrounds and overlay hits from random triggers.

δ-rays in the TPC volume and TPC windows are simulated, there could be other similar processes that are not properly simulated. One potential weakness in our simulation is the non-linear response of the CRID amplifiers to MIPs and the pulses induced by cross talk on other wires. We remove most of these spurious hits with the cuts described in section 6.1, but any remaining hits are likely not to be simulated properly. This area is one of the remaining major problems for investigation in the understanding of CRID performance.

---

some process (other than Cherenkov radiation in the liquid radiator or quartz windows) that is correlated with the presence of tracks might be responsible for the background.

Chapter 8

Event and Track Selection

An important part of any analysis is to specify precisely what events are included in the data sample. In this chapter, we describe criteria for selecting hadronic Z^0 decays and removing non-hadronic backgrounds, for the tagging of initial quark flavor, and for reliable determination of particle identification information. All of these criteria will be employed in the analysis of Chapter 9. In each of these tasks, the overriding concern is to ensure that the selected data are well-modelled by our Monte Carlo simulation. For hadronic event selection, we restrict events to a fiducial region in the central part of the detector where our tracking efficiency is high, and we make cuts to remove background from leptonic decays of the Z^0, from two-photon interactions, and from interactions of the beam with detector material or accelerator structures. In the flavor-tagging selection, we make cuts to ensure that our tagging efficiencies and purities are well-modelled. Finally, selection criteria for particle identification are made to ensure reliable operation of the CRID and to improve our ability to model the identification efficiency. Since there are plenty of hadronic Z^0 decays in our data sample, we can afford reduced statistics on tracks in order to improve our systematic uncertainties in the identification efficiency.

8.1   Selecting Hadronic Events

The first part of event selection takes place in the triggering of the detector, for if an event is not read out it is not available for further analysis! This task is relatively straightforward in e^+e^- annihilation at the Z^0 since the event rates are low enough that only a loose trigger is required. The trigger criteria are outlined in section 3.2.7, and more detailed discussions are available in [81, 169]. The combined efficiency of the three hadronic triggers (Energy, Track, and Hadron) is estimated to be $\geqslant 96\%$ for accepting hadronic Z^0 decays [170].

During part of the 1993 run (approximately $\frac{2}{5}$ of the 1993 dataset), a trigger veto condition on drift chamber occupancy was improperly configured, resulting in a bias against high-multiplicity events. This is described in more detail in [81], and it is simulated in the SLD Monte Carlo. In this analysis, however, we simply ignore events from this run period. For the remainder of the run periods, the fraction of hadronic Z^0 decays rejected by this drift chamber veto is estimated to be $< 1\%$.

The next step in the process of event selection is the SLD "PASS1" filter. Because true hadronic events comprise only 5% or less of all triggers written to tape, it is efficient to make a common, loose hadronic-event selection on the full data set. The output of this PASS1 filter is fed to the "PASS2" process, which reconstructs the PASS1 events and performs further selection of various samples. All of the PASS1 events are retained and comprise the sample of events which are (readily) available for data analysis. For our purposes, the PASS1 selection consists of the EIT1 filter described in [171], which is based on calorimetry information and requires a minimum total energy and cluster multiplicity. The efficiency of the trigger plus filter is estimated to be $\geqslant 92\%$ [170].

We treat the events coming from the trigger plus filtering process as a starting point and apply selection criteria designed to accept hadronic events in the barrel region and reject non-hadronic backgrounds. These criteria are essentially the same as in [81, 85, 172], where they are described in more detail.

The selection is based on charged tracks, which are necessary for particle identification. Therefore, we begin with the following track selection criteria:

- The momentum transverse to the beam axis must exceed $p_t > 0.2$ GeV/c. This reduces backgrounds from material interactions, which are generally soft, as well as ensuring that the track reaches the CRID without spiraling back on itself.

- The total momentum $|\vec{p}| < 50$ GeV/c. Tracks above the beam momentum are poorly measured, often because they contain hits belonging to other tracks. There are, however, very few of these tracks ($< 0.05\%$ of all tracks).

- The track polar angle must be within $|\cos\theta| < 0.8$. This is the effective limit of the CDC acceptance, corresponding to the requirement that 7 of 10 superlayers contain hits.

- The point of closest approach to the IP in xy must be within 1 cm of the IP, and within 5 cm in rz. This serves to remove tracks coming from interactions in the detector material.

- The χ^2 per degree of freedom of the CDC track fit must be $\chi^2_{\mathrm{CDC}}/DOF < 5$. This excludes poorly found or spurious tracks. Note that the CDC fit is done by layers, so a typical number of DOF is 15 and not 70, as one might have from fitting individual hits.

- The number of CDC hits on the track must be above 40, $N_{\mathrm{hits}} > 40$. This requirement ensures there are enough points to get a good momentum measurement and that we are not measuring part of a track which scattered or decayed in flight.

Collectively, these cuts ensure that tracks are well-measured and consistent with an origin at the IP, as opposed to an interaction of the beams with radiation masking, the beampipe wall, or other accelerator structures.

For each event, the above criteria define a set of tracks for the event. We then accept the event as a hadronic Z^0 decay if it meets three criteria:

- The angle of the thrust axis relative to the beam direction, θ_{th}, as determined from calorimetry clusters, satisfies $|\cos\theta_{th}| < 0.71$.

- The total visible energy, E_{vis}, calculated from the selected tracks assuming the $\pi^{\pm}$ mass for each track, satisfies $E_{vis} \geqslant 18$ GeV/c.

- The number of selected tracks, n_{ch}, in the event is at least 7, $n_{ch} \geqslant 7$.

The $\cos\theta_{th}$ cut is made to ensure that the event is well-contained in the barrel region of the detector. We use the thrust axis from calorimetry to avoid biasing the thrust axis near the edge of acceptance of the CDC (see the discussion in [81]). The E_{vis} cut is designed to remove events with a significant fraction of tracks going out of our acceptance, in addition to removing beam-wall interaction background and two-photon events. The n_{ch} cut is motivated primarily by a desire to remove contamination from $Z^0 \rightarrow \tau^+\tau^-$ decays. This cut is estimated to accept $< 1.2\%$ of τ decays and $> 98\%$ of hadronic decays with thrust axis $|\cos\theta_{th}| < 0.8$ [169]. The overall acceptance for hadronic Z^0 decays is $\sim 61\%$, with losses mainly due to the $\cos\theta_{th}$ cut. Events of different primary quark flavor were found to be equally likely to pass the selection within Monte Carlo statistical uncertainty [81]. The total number of events is 61129 for 1994–95 and 28127 for 1993, with residual contamination of non-hadronic events in the sample estimated to be $< 0.2\%$ [85].

8.2   Selection for Flavor Tagging

One of the important elements of this analysis is the separation of $e^+e^- \rightarrow q\bar{q}$ events according to the flavor of the primary quarks q, $\bar{q}$. We do this by making use of the excellent impact-parameter resolution of the SLD vertex detector (see section 3.2.1) and the relatively long decay lengths of charm and bottom hadrons. The technique is to use the impact parameter of tracks with respect to the IP in the xy plane. This has been employed in several other measurements at the SLD [85, 81, 169], so we do not describe it in detail here. Briefly,
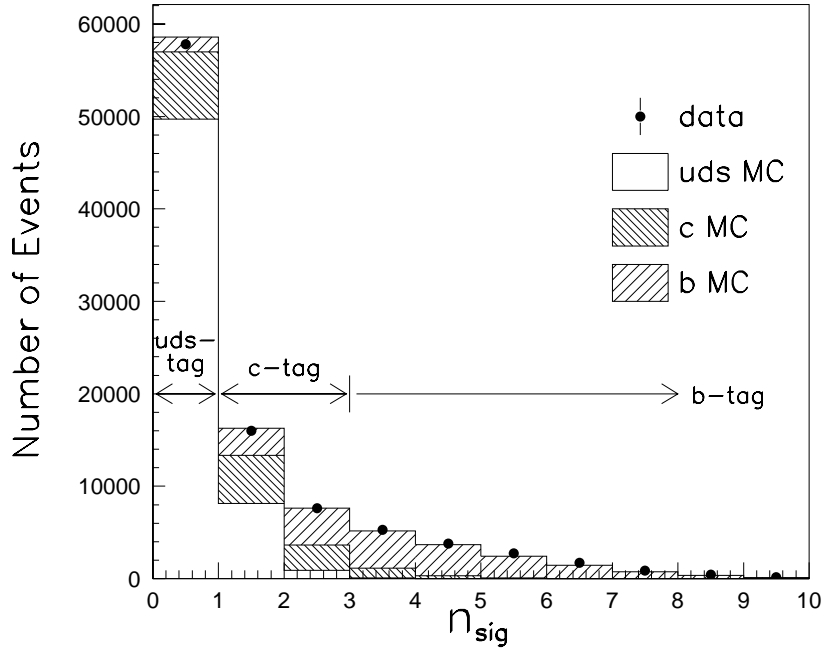
Figure 8.1: The number of "quality tracks" (see text), n_{sig}, whose two-dimensional impact parameter is inconsistent with the IP at $> 3\sigma$ is shown for the data sample (dots) and for Monte Carlo events (histograms). The Monte Carlo is split up by the flavor of the primary $q\bar{q}$, showing the purities of our tags ($n_{sig} = 0$, $n_{sig} = 1, 2$, and $n_{sig} \geqslant 3$).

it consists of counting the number of tracks whose two-dimensional impact parameters are inconsistent with the IP at the level of 3σ. This number of significantly displaced tracks, denoted n_{sig}, serves as the tagging variable for event flavor (see Fig. 8.1). A detailed discussion of this tag variable is available in [89].

To use the two-dimensional impact parameter tag, we need to make some additional event and track selection. These are discussed in [85, 89]. In order to be used for flavor tagging, an event must pass the following additional criteria:

- There must be a good IP position extracted from the primary vertex of tracks in the neighboring 30 hadronic events.

- There must be 3 or more tracks in the event which are linked to 2 or more VXD hits. This is to ensure proper readout of the VXD.

Furthermore, we need to ensure that the tracks used for the impact parameter tagging are very well measured and properly linked to VXD hits. Therefore, we require some additional criteria for "quality tracks," which are the tracks eligible for counting in n_{sig}:

- The track must link to one or more hits in the VXD.

- The momentum transverse to the beam axis must be above $p_t > 0.4\,\mathrm{GeV}/c$. We remove tracks with $0.2 < p_t < 0.4\,\mathrm{GeV}/c$ because the impact parameter distribution of low-momentum tracks has larger non-Gaussian tails, and these tracks are less likely to carry tagging information from b and c decays.

- The xy impact parameter, b, must be within $b < 3$ mm.

- The error on the impact parameter, σ_b, must be less than $250\ \mu$m (this would implicitly cut tracks below $p < 300$ MeV/c because of the uncertainty due to multiple scattering).

- The position of closest approach to the IP must be within 1.5 cm in rz.

- The χ^2 per degree of freedom of the combined CDC-VXD track fit must satisfy $\chi^2_{CDC+VXD}/DOF < 5$.

- The track must be inconsistent with coming from $K^0_s \to \pi^+\pi^-$ or $\Lambda^0 \to p\pi^-$ decays, or $\gamma \to e^+e^-$ conversions. The detailed criteria for identifying these decays are described in [89].

The distribution of the tagging variable n_{sig} is shown in Fig. 8.1 and motivates our assignment of the tagging samples. Events with $n_{sig} = 0$ are defined to be the *uds*-tagged sample (*i.e.*, $\mathrm{Z}^0 \to u\bar{u}$, $d\bar{d}$, or $s\bar{s}$). Events with $n_{sig} \geqslant 3$ make up the b-tagged sample ($\mathrm{Z}^0 \to b\bar{b}$). The remaining events, $n_{sig} = 1$ or 2, are denoted the c-tagged sample (although the c purity is not very high). The fraction of

	uds-tag	c-tag	b-tag
uds-efficiency	0.851	0.147	0.002
c-efficiency	0.441	0.477	0.082
b-efficiency	0.072	0.334	0.594
Purity	0.850	0.335	0.894

Table 8.1: Efficiencies and purities for the flavor tags. The efficiencies are relative to events passing the selection cuts listed in the text. These numbers come from Monte Carlo simulation and are assigned a systematic uncertainty of ± 0.02.

selected events of each primary quark flavor that are tagged in each of the three samples is listed in Table 8.1, along with the purity of each tag, based on the SLD Monte Carlo simulation. These are essentially the same as in [81], but with a revised SLD tracking reconstruction. These efficiencies are subject to uncertainties at the $< 3\%$ level from modelling of the b and c decays and from detector simulation [81]. Our analysis is relatively insensitive to the exact values of the efficiencies, so we assign a conservative error of ± 0.02.

8.3   Selection for Particle Identification

Because the use of the CRID for particle identification is central to our measurement, we need to add additional selection criteria to ensure that the CRID was functioning properly and that we can obtain good-quality particle identification information. These are composed of criteria for events and separate criteria for tracks in the liquid- and gas-radiator regimes of the CRID.

8.3.1   Event Selection

For event selection, we add these criteria:

- Barrel CRID high voltage on, as determined by a combination of event-by-event ADCs (1994–95 only), slow-monitor logging, and event size. The

ADCs provide high voltage monitoring for each triggered event, but there are only two channels, each sampling one detector voltage (S5A and N5A), and this signal was not present before the 1994–95 run. The slow-monitor information, on the other hand, samples all of the CRID voltages, but it is not available for each event. The nearest slow-monitor record in time is used to determine the high voltage status of any particular event. In 1993, the slow-monitor records were written every 20 minutes (changed to every 1–2 minutes in 1994–95), leaving a potentially large gap between an event and the nearest record. Therefore, we also remove events whose CRID datasize is less than 0.8 times the drift chamber datasize. This cut is based on an empirical analysis of the relative CRID and DC datasizes.

- No truncations in any of the CRID WSMs. Occasional noisy events push the CRID data volume over its buffer limit of 512 kB. Although we could just remove those TPCs whose readout was truncated, these occurrences are sufficiently infrequent that it was judged better to cut all events with truncations.

- Good CRID drift velocity calibration (1993 only). There are some periods which have no valid v_d splines (see section 7.1), generally due to hardware problems with the Xe flashlamps. In 1994–95, drift velocities for most of these times can be inferred from atmospheric pressure (except when there are no valid measurements sufficiently close in time), but the events from such periods in 1993 data are removed.

The losses from these cuts are shown in Table 8.2.

8.3.2   Track Selection

Finally, we turn to extra track selection cuts that are made in order to ensure an excellent understanding of the particle identification performance and to decrease the likelihood that a track is misidentified because it came from a secondary interaction in the detector or because it was mistracked. These cuts

	1993		1994–95	
Event Cut	events	percentage	events	percentage
Starting sample	16538	-	61129	-
CRID HV off	3161	19.1 %	3015	4.9 %
WSM Truncation	504	3.0 %	2778	4.5 %
Bad v_d calibration	3546	21.4 %	583	1.0 %
Total events rejected	5083	30.7 %	5062	8.3 %
Total events passed	11455	69.3 %	56067	91.7 %

Table 8.2: Event losses due to extra CRID event selection criteria described in the text. All of the cut losses are calculated by applying each cut independently.

reduce our sensitivity to the details of detector material in the Monte Carlo simulation and to the simulation of tracking performance. Common criteria for both the liquid and gas momentum regions are:

- Track polar angle $|\cos\theta| \leqslant 0.68$. We tighten the barrel fiducial region. The value of 0.68 is motivated by the acceptance of the gas radiator and mirrors, but it is also useful in the liquid. As track polar angle decreases, total internal reflection in the liquid radiator cuts off a larger portion of the Cherenkov ring, and decreases the identification capability (see Fig. 8.2a). Having a common fiducial cut also simplifies some elements of the analysis.

- CDC last hit $r_{last} \geqslant 90$ cm. Because the CRID is dependent on a reliable extrapolation of the particle trajectory, it is important to select the highest quality tracks. Clearly, having a hit from the last CDC layer ($r \simeq 95$ cm) minimizes the lever arm for extrapolation. Furthermore, because losses from two-track overlap are minimal at the outer layer, a track that is missing hits from the last layer is potentially a particle that scattered or decayed in flight, and therefore unlikely to be identified properly. Finally,
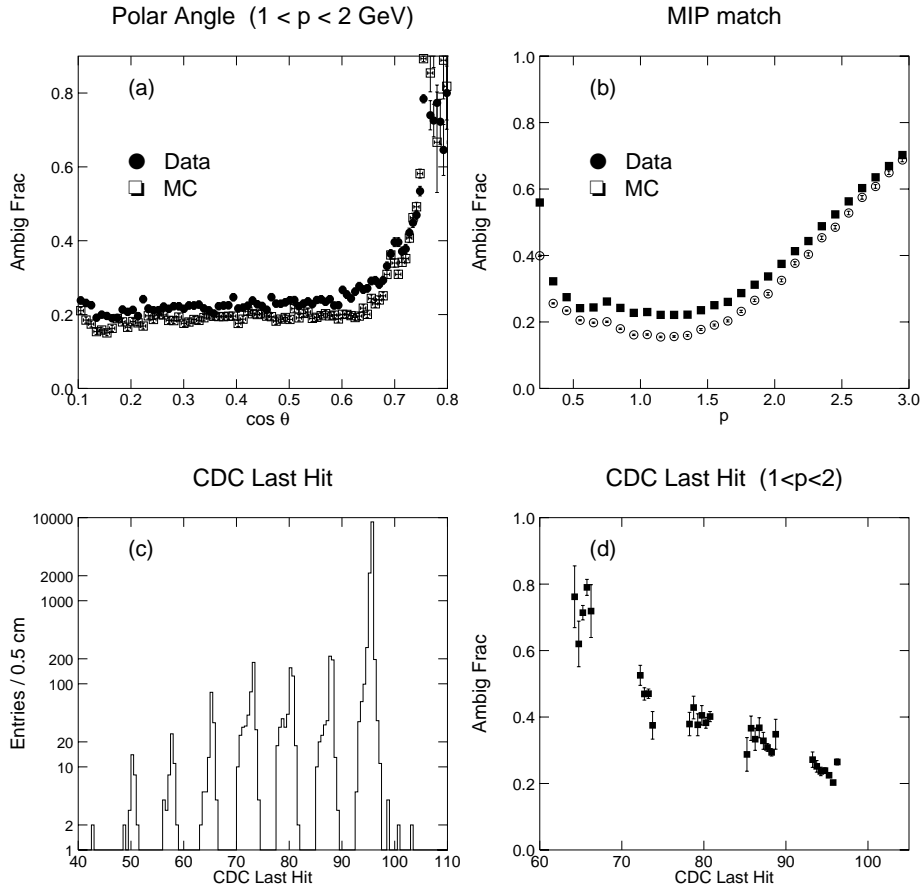
Figure 8.2: The effect of cuts on various quantities is shown on the liquid-radiator ambiguous fraction, the portion of tracks for which the CRID does not give a definite particle identification (log-likelihood cut of 5). The lower the ambiguous fraction, the better the identification performance. In (a) the dependence on the track polar angle θ is shown for 1994–95 data (dots) and Monte Carlo (squares). A cut is placed at $|\cos\theta| \leqslant 0.68$ (see text). The ambiguous fraction is plotted against track momentum in (b), for all tracks in the data (squares) and for the subset of tracks passing the MIP association cut (circles). In the momentum region of the best identification ($0.5 < p < 1.5$ GeV/c), an improvement of 6% is apparent. The distribution of the radius of the last CDC hit on the track is plotted for 1994–95 data in (c), and the CRID ambiguous fraction as a function of this r_{last} is plotted in (d). The identification performance clearly worsens with decreasing r_{last}, which motivates us to cut on $r_{last} \geqslant 90$ cm.

the losses from such a cut on the last CDC layer are minimal: 96% of all tracks pass the cut. The effect of this cut is shown in Fig. 8.2d.

- Rejection of $\gamma \to e^+ e^-$ candidates. Ultimately, our goal is to measure the fractions of hadronic particles in hadronic Z^0 decays. Therefore, removing contamination from photon conversions in the detector material is a useful cut to make early. We use the identification procedure of [89], which cuts on $m_{ee} < 30$ MeV/c^2, separation in xy of $DOCA_{xy} < 0.3$ cm, and an opening angle $\theta_{12} < 200$ mrad. We estimate from Monte Carlo that 83% of these candidates are true γ-conversions. The mistagged tracks (those which are not γ conversions) are generally unbiased among $\pi/K/p$ species, but we correct for this from the Monte Carlo expectation in our analysis.

Liquid Region

For the liquid region of CRID particle identification, we make the following additional selection criteria on tracks, based on the standard CRID reconstruction flags set in the `PHCRID` banks:

BADID This basic flag is set if there is no valid liquid identification information available. We start with the standard CRID log-likelihood information and require that the `BADID` flag not be set. This subsumes the requirements that tracks pass through the liquid radiator trays, that the TPC containing the majority of the expected liquid ring be active and functional, and that the track transverse momentum be above $p_t > 0.150$ GeV/c.

TPCBAD or TPCSICK Although the `BADID` cut removes tracks for which the primary TPC (the one containing the majority of the expected liquid ring) has high voltage off or electronics readout problems, we make a further cut requiring the two TPCs containing most of the expected liquid ring to be functional. Furthermore, we cut TPC S1B, which was found to have a much lower photon detection efficiency (see Fig. 7.18).

MAYMSLR We restrict the fiducial region of the liquid radiator trays to 1.0 cm within the walls and away from the central rib. As discussed in section 7.7, this ensures that there are no losses from the edges or the opaque central rib of the liquid radiator trays.

NOMIP Because of a concern about tracks which scatter between the CDC and the CRID or are otherwise mistracked, and because we have no tracking chamber outside the radius of the CRID, we impose the requirement that an ionization deposit (saturated hits) be present in a CRID TPC within a loose region of 3 cm from the extrapolated position of the track. This cut has low efficiency because the TPCs cover only $\sim 80\%$ of the solid angle in the Barrel CRID. Nevertheless, it is quite effective at increasing particle identification efficiency (see Fig. 8.2b).

The number of tracks affected by each of these cuts is shown in Table 8.3. In the liquid region of the CRID we use an identification cut of 5 in log-likelihood.

	1993		1994–95	
Liquid Track Cut	tracks	percentage	tracks	percentage
Starting sample	196779	-	973754	-
$\|\cos\theta\| > 0.68$	15836	8.0 %	76958	7.9 %
$r_{last} < 90$	7619	4.2 %	28823	3.2 %
$\gamma \to e^+e^-$ rejection	8735	5.0 %	43951	5.1 %
BADID	33293	20.2 %	100140	12.2 %
TPCBAD/TPCSICK	16643	12.7 %	62100	8.6 %
MAYMSLR	15463	13.5 %	87624	13.2 %
NOMIP	25533	25.7 %	140758	24.5 %
Total tracks rejected	123122	62.6 %	540354	55.5 %
Total tracks accepted	73657	37.4 %	433400	44.5 %

Table 8.3: Losses due to extra CRID track selection criteria in the liquid radiator regime. All of the cuts are applied sequentially, with the percentages referring to the fraction of tracks remaining after the preceding cuts are applied.

Region	π ID	K ID	p ID
Liquid Ring **0.75–3.0 GeV**/c	$\log L_\pi - \log L_K > 5$ *and* $\log L_\pi - \log L_p > 5$	$\log L_K - \log L_\pi > 5$ *and* $\log L_K - \log L_p > 5$	$\log L_p - \log L_\pi > 5$ *and* $\log L_p - \log L_K > 5$
Liquid High Mom. **3.0–5.0 GeV**/c	—	—	$\log L_p - \log L_\pi > 5$ *and* $\log L_p - \log L_K > 5$
Gas Threshold **2.5–10.0 GeV**/c	$\log L_\pi - \log L_K > 3$ *and* $\log L_\pi - \log L_p > 3$	—	—
Gas Ring **10.0–23.0 GeV**/c	$\log L_\pi - \log L_K > 3$ *and* $\log L_\pi - \log L_p > 3$	$\log L_K - \log L_\pi > 3$ *and* $\log L_K - \log L_p > 3$	$\log L_p - \log L_\pi > 3$ *and* $\log L_p - \log L_K > 3$
Gas High Mom. **23.0–36.0 GeV**/c	—	—	$\log L_p - \log L_\pi > 3$ *and* $\log L_p - \log L_K > 3$

Table 8.4: The criteria used for identifying samples of hadronic particle type are listed for various momentum regimes.

Thus, to identify a track as a pion, we require $\log L_\pi - \log L_K > 5$ *and* $\log L_\pi - \log L_p > 5$. Similarly, we require $\log L_K - \log L_\pi > 5$ and $\log L_K - \log L_p > 5$ to identify a track as a kaon, and $\log L_p - \log L_\pi > 5$ and $\log L_p - \log L_K > 5$ to identify a track as a proton. In the region $3 < p < 5$ GeV/c, we only identify protons and do not attempt to distinguish between π and K hypotheses. The identification criteria are listed in Table 8.4 for reference.

Gas Region

A similar set of criteria are applied to tracks in the gas radiator region of the CRID particle identification. These are outlined as follows:

BADID We, again, start with the standard CRID log-likelihood information and require that the status indicate viable identification information. This subsumes the requirements that the TPC onto which the ring image is reflected be active and functional, that the image not reflect from any known bad mirrors, that the track curvature be less than the cutoff of $p_t > 0.150$ GeV/c, and that the GASMESS criterion (described in section 6.3) of MIP hits overlapping more than half of the gas ring not be satisfied.

TPCSICK As in the liquid case, we cut tracks whose rings go to TPC S1B, because of the reduced detection efficiency observed in that TPC (see Fig. 7.18).

NOMIP and NOLIQR In the gas, we have an additional handle on tracks which scatter or are mistracked. Because the gas momentum regime is above that of the liquid, all gas candidate tracks are above threshold in the liquid and should have rings detected. Therefore, we can look for the presence of 4 or more hits with signal weight above background weight for the liquid Cherenkov angle. In practice, we combine the liquid-ring cut with the MIP-match cut described above and obtain a more-efficient selection criterion to help ensure that tracks measured in the CDC were, in fact, present in the CRID.

GASXISO In order to ensure a good understanding of the identification effi-
ciency, we make a further cut on the isolation of gas rings from regions of
ionization in the TPCs. The ordinary cut (subsumed in BADID above) al-
lows some overlap of MIP hits with the gas ring. We impose the additional
criterion that no MIP hits occur within 5 cm of the gas ring center. This
cut does not bias the track sample significantly because the CRID mir-
rors generally focus gas rings away from the ionization of the originating
track. The effect of this isolation cut is shown in Fig. 8.3 as a function
of the angle ψ between a track and the thrust axis of the event. There is
4.6% more loss in the core of jets than elsewhere, which would produce at
most a bias of 0.046 in the hadronic fractions analysis of Chapter 9, if all
of these tracks were only one hadronic species. Since we do not expect a
large variation in species composition, we ignore this as a potential source
of bias.
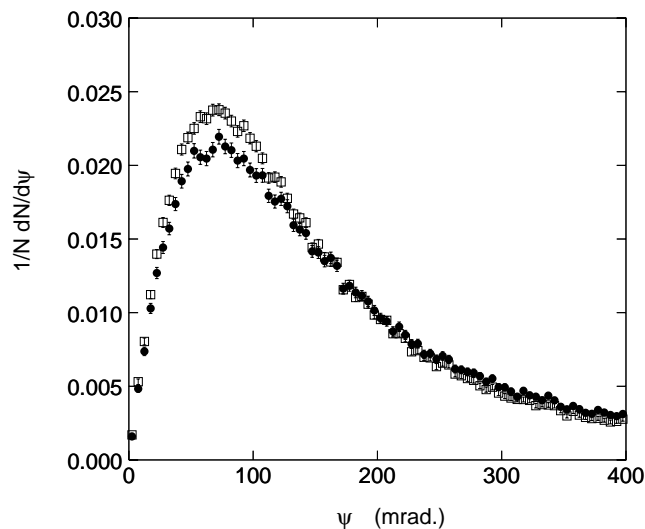
Figure 8.3: The effect of the GASXISO isolation cut is seen in the 1994–95 data as a
function of the angle ψ between a track and the thrust axis of the event. The sample
without the isolation cut is shown as squares, and the sample with the cut are the dots.
Both samples are normalized to the number of tracks in each, thus showing the bias
of the gas ring isolation cut on the angle ψ.

Gas Track Cut	1993		1994–95	
	tracks	percentage	tracks	percentage
Starting sample ($p > 2\,\text{GeV}/c$)	76337	-	378847	-
$\lvert\cos\theta\rvert > 0.68$	5813	7.6 %	26778	7.3 %
$r_{last} < 90$	3025	4.1 %	11634	3.3 %
$\gamma \to e^+e^-$ rejection	1709	2.5 %	8779	2.6 %
BADID	16539	25.1 %	56687	17.1 %
TPCSICK	1530	3.1 %	7789	2.8 %
NOMIP and NOLIQR	2411	5.1 %	9819	3.7 %
GASXISO	17742	39.2 %	103307	40.1 %
Total tracks rejected	48769	63.9 %	224793	59.3 %
Total tracks accepted	27568	36.1 %	154054	40.7 %

Table 8.5: Losses due to extra CRID track selection criteria in the gas radiator regime. All of the cuts are applied sequentially, with the percentages referring to the fraction of tracks remaining after the preceding cuts are applied.

The number of tracks affected by each of these cuts is shown in Table 8.5. The requirements for particle identification are similar to those in the liquid, except that a cut of 3 in log-likelihood is used. They are also summarized in Table 8.4. Furthermore, the gas contains a significant regime where both K and p hypotheses are below threshold and there can be no K-p discrimination. In this region only pions are identified.

With all of these selection criteria for reliable CRID identification, we achieve the agreement of data and Monte Carlo identification efficiencies presented in the previous chapter (Figs. 7.21, 7.23, and 7.25). The agreement is not perfect, but is within 5% and is close enough for the calibration of identification efficiencies described in the next chapter. All of the selection criteria presented in this chapter will be used in the analysis presented in Chapter 9.

Chapter 9

Measurement of Hadronic Spectra

In this chapter, we present first a measurement of hadronic particle fractions in e^+e^- annihilation at the Z^0 resonance. After describing the analysis technique and formalism, we focus on the heart of that measurement: determining the identification efficiencies achieved with the SLD CRID. After this, a simple unfolding procedure is used to extract the true hadronic fractions in Z^0 decays. Next, we proceed to unfold the hadronic spectra for different initial quark flavors. Finally, we extend the analysis to look at the differences in particle production between quark and antiquark jets and describe the observation of the leading particle effect.

9.1   Analysis Technique

The basic particle fractions measurement is conceptually very straightforward. We bin all observed charged tracks in momentum. For each momentum bin, we count the number of tracks identified as π, K, or p by the CRID. Call this number of observed tracks n_i, with $i = \pi/K/p$. We can relate this number to the

true fraction f_j produced at that momentum by

$$\begin{pmatrix} n_\pi \\ n_K \\ n_p \end{pmatrix} = \begin{bmatrix} \varepsilon_{\pi\pi} & \varepsilon_{\pi K} & \varepsilon_{\pi p} \\ \varepsilon_{K\pi} & \varepsilon_{KK} & \varepsilon_{Kp} \\ \varepsilon_{p\pi} & \varepsilon_{pK} & \varepsilon_{pp} \end{bmatrix} n_{ch} \begin{pmatrix} f_\pi \\ f_K \\ f_p \end{pmatrix}, \tag{9.1}$$

where n_{ch} is the total number of charged tracks observed, and the ε_{ij} represent the efficiency for identifying a particle of type j as type i. The measurement of the fractions f_j, then, follows trivially from the n_i if we know the matrix $\boldsymbol{\varepsilon}$:

$$\begin{pmatrix} f_\pi^0 \\ f_K^0 \\ f_p^0 \end{pmatrix} = \frac{1}{n_{ch}} \begin{bmatrix} & & \\ & \boldsymbol{\varepsilon} & \\ & & \end{bmatrix}^{-1} \begin{pmatrix} n_\pi \\ n_K \\ n_p \end{pmatrix}. \tag{9.2}$$

One important point to note is that the matrix $\boldsymbol{\varepsilon}$ is normalized to the number of tracks in the input sample (those passing all of the selection cuts described in Chapter 8). It does not contain the constraint that the hadronic particle fractions sum to unity (*i.e.*, $f_\pi + f_K + f_p = 1$). Instead, we can use this sum as a cross-check of our method. Although it is not a sufficient condition, the sum of the fractions being close to one is a necessary condition for having confidence in our $\boldsymbol{\varepsilon}$ matrix.

However, the fractions of selected tracks, denoted here by f_i^0, are not quite what we wish to measure, which are the fractions of hadrons produced from fragmentation or from the decays of short-lived ($\tau < 3 \times 10^{-10}$ second) fragmentation particles. Although most observed tracks are of this "fragmentation hadron" category, there are also tracks from leptons, from photon conversion and other interactions in the detector material, and from background tracks not associated with the Z^0 decay, for all of which we must apply corrections.

The largest of these corrections is the one for leptonic tracks in our sample. In the CRID, electrons and muons are only distinguishable from pions at the lower end of the momentum regime of each radiator. Hence, we do not attempt to distinguish e and μ hypotheses from the π hypothesis in the CRID, and
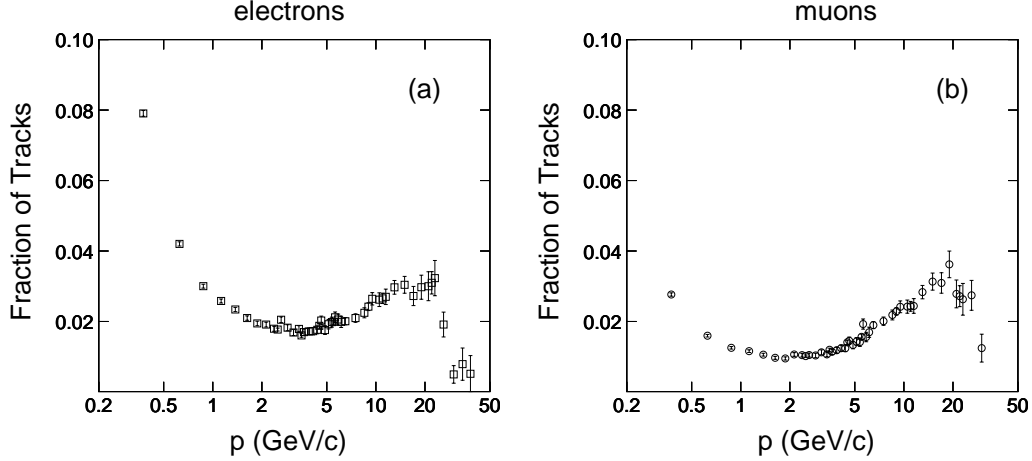
Figure 9.1: The fraction of electrons (a) and muons (b) in the selected track sample, based on the SLD-tuned JETSET 7.4 simulation. The track selection criteria (section 8.3) include cuts to remove $\gamma \rightarrow e^+ e^-$ conversions.

rather lump all these together into one category. We then correct for the lepton production using Monte Carlo. Fortunately, the overall rates of leptons in hadronic Z^0 decays are relatively small (see Fig. 9.1), and they are dominated by b and c semileptonic decays, which are reasonably well-constrained [169]. Let f_e and f_μ be the fraction of all charged tracks in a momentum bin that are electrons and muons. We then modify Eq. (9.2) to get

$$
\begin{pmatrix} f_\pi^c \\ f_K^c \\ f_P^c \end{pmatrix} = \frac{1}{1 - f_e - f_\mu} \begin{pmatrix} f_\pi^0 - f_e - f_\mu \\ f_K^0 \\ f_P^0 \end{pmatrix}
\tag{9.3}
$$

Similarly, we also need to correct for tracks in our sample that come from beam-wall background, from $\gamma \rightarrow e^+ e^-$ conversions, or from other interactions in the detector material. As described in section 8.3, we reject tracks from our sample that are consistent with coming from photon conversions, which reduces the correction we need to apply. The other tracks coming from detector-material interactions are predominantly $\pi^\pm$ and p (not $\bar{p}$). To reduce our

dependence on the simulation of detector material, we analyze only negatively-charged tracks below 2 GeV/c. This removes the protons produced in interactions, but still leaves us with the π^- tracks to correct for. We use the Monte Carlo to derive the corrections $f_j^{(i)}$, and modify Eq. (9.3) to read

$$\begin{pmatrix} f_\pi^c \\ f_K^c \\ f_p^c \end{pmatrix} = \frac{1}{1 - f_e - f_\mu} \frac{1}{1 - n_{int}/n_{ch}} \begin{pmatrix} f_\pi^0 - f_e - f_\mu - f_\pi^{(i)} \\ f_K^0 - f_K^{(i)} \\ f_p^0 - f_p^{(i)} \end{pmatrix}, \qquad \text{for } p > 2\text{GeV}/c$$

(9.4)

$$\begin{pmatrix} f_\pi^c \\ f_K^c \\ f_p^c \end{pmatrix} = \frac{1}{1 - f_{e^-} - f_{\mu^-}} \frac{2}{1 - n_{int}/n_{ch}} \begin{pmatrix} f_{\pi^-}^0 - f_{e^-} - f_{\mu^-} - f_{\pi^-}^{(i)} \\ f_{K^-}^0 - f_{K^-}^{(i)} \\ f_{\bar{p}}^0 - f_{\bar{p}}^{(i)} \end{pmatrix}, \qquad \text{for } p < 2\text{GeV}/c,$$

(9.5)

where n_{int}/n_{ch} is the total fraction of tracks coming from detector-material interactions in our selected sample ($< 2\%$).

Finally, we need to correct for the particles in our "stable hadron" category ($\tau > 3 \times 10^{-10}$ second) which nevertheless decay before we observe them. We can parametrize this correction as a decay matrix D_{ij} that relates our observed fractions f_i^c to the true hadronic fractions f_j^t

$$\begin{pmatrix} f_\pi^c \\ f_K^c \\ f_p^c \end{pmatrix} = \begin{bmatrix} D_{\pi\pi} & D_{\pi K} & D_{\pi p} \\ D_{K\pi} & D_{KK} & D_{Kp} \\ D_{p\pi} & D_{pK} & D_{pp} \end{bmatrix} \begin{pmatrix} f_\pi^t \\ f_K^t \\ f_p^t \end{pmatrix}.$$

(9.6)

Here, D_{ij} is the fraction of particles of type j at the fragmentation level that decay to type i by the time they can be observed in our detector. Because we do

not separate the leptons from pions, this matrix is of the form

$$
\begin{bmatrix} & & \\ & \mathbf{D} & \\ & & \end{bmatrix} = \begin{bmatrix} 1 & d & 0 \\ 0 & 1-d & 0 \\ 0 & 0 & 1 \end{bmatrix} \tag{9.7}
$$

where d is 0.055 at $p = 0.5$ GeV/c and decreases to < 0.01 above $p > 2$ GeV/c, as determined from Monte Carlo simulation.

9.2 Particle Identification Efficiencies

The central part of our measurement lies in understanding the particle identification efficiency achieved by the CRID. Of course, this efficiency depends on how we select the input sample and what criteria we use to define identification. The selection criteria are presented in Chapter 8, and the identification requirements are summarized in Table 8.4. They are chosen so as to maximize the reliability of our simulation of identification performance and to increase our confidence in understanding the identification performance.

9.2.1 Monte Carlo Efficiencies

Our starting point is the identification efficiency matrix shown in Fig. 9.2, which is taken directly from the CRID simulation and includes all of the tuning discussed in section 7.15. If one had perfect confidence in the simulation, we could simply stop here and use this ε matrix to unfold the data. In the real world, however, we know that simulations are never perfect. Although the data/Monte Carlo comparisons in section 7.14 show that agreement is generally good, we are not able to produce perfect agreement despite our best efforts to tune the simulation (see Fig. 7.21, for example). Ultimately, we desire to make a more accurate measurement than these $\sim 5\%$ discrepancies would permit.

However, our simulation is reasonably close to the data, and we believe that it adequately represents the characteristics of the CRID identification
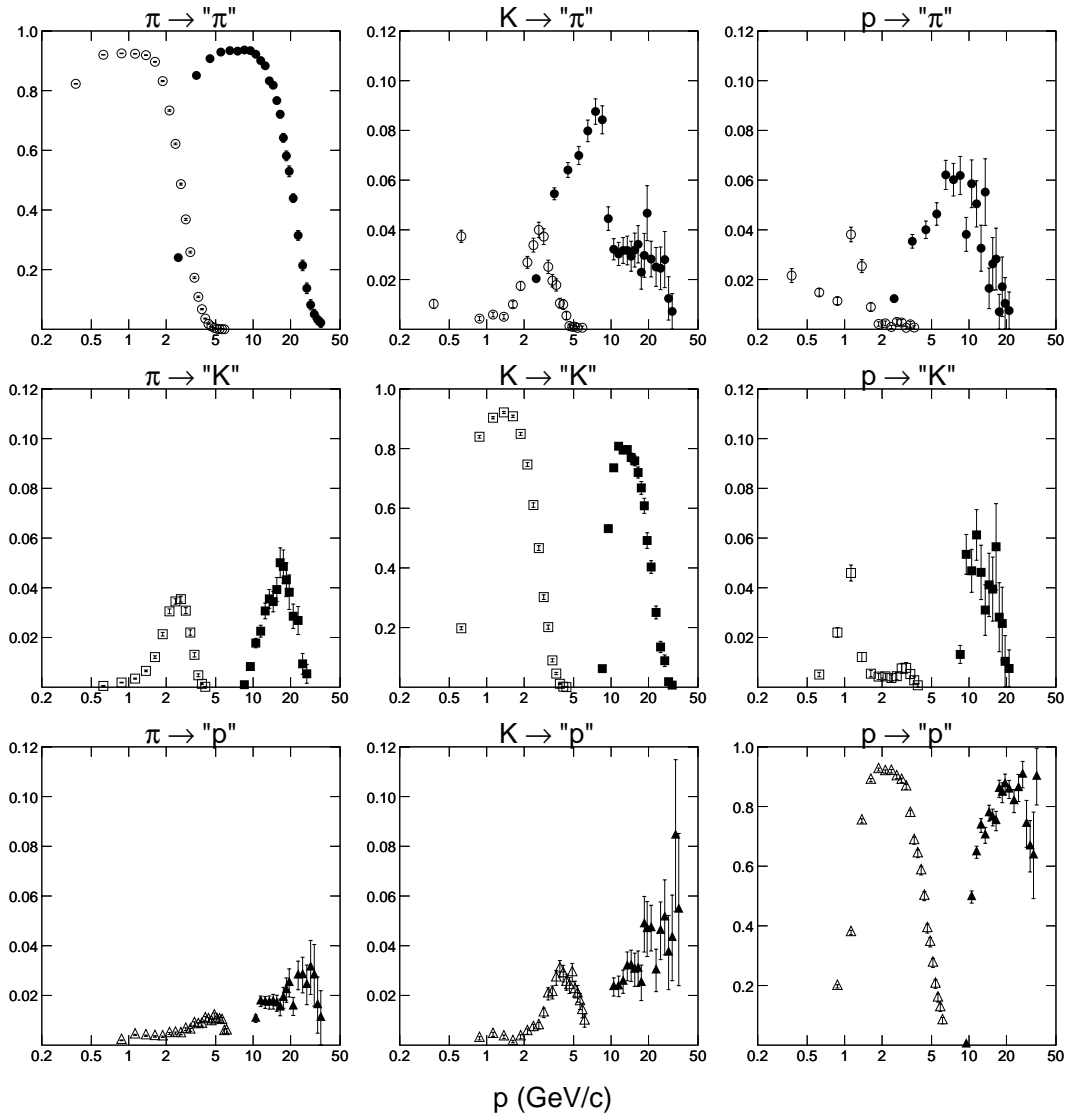
Figure 9.2: The matrix of hadronic particle identification efficiencies, as predicted from our simulation of the CRID, is shown as a function of momentum. The open points are those coming from the liquid radiator, and the solid points are those from the gas radiator.

efficiency and the shape of its momentum dependence. Therefore, we *calibrate* our identification efficiency from the known-particle-type data samples described in section 7.14, and we use our simulation to make small corrections and to extract the identification efficiency terms that we cannot measure directly.

The primary calibration samples for this are pions from K_s^0 decays, and pions (or leptons) from τ decays. Protons from Λ decays have marginal statistical power, so we use them primarily as a cross-check. The general procedure is to use the identification efficiency measured in the data sample, modified by the difference between the result of a similar (calibration-sample) analysis performed on Monte Carlo and the expected Monte Carlo efficiency for the full hadronic sample (as in Fig. 9.2). This difference corrects for effects such as the impurity of the calibration sample and any systematic differences in track quality between the calibration sample and the inclusive track sample.

The first step in this procedure is to fit the Monte Carlo efficiencies with a functional form. This not only smooths out fluctuations from Monte Carlo statistics but also give us a convenient representation with a small number of parameters. The functional form used has no deep significance. It is not expected that the true identification efficiencies follow such a simple form, since the number of factors going into the efficiency calculation is large (which, after all, is why we use Monte Carlo simulation to calculate the identification efficiency). However, all that is required is that the functional form be a good representation of both the data and the simulation. A study of various functional forms is shown in Fig. 9.3, where it is clear that the "flat + Gaussian" form is a good representation of the Monte Carlo pion efficiency in the liquid. Any of the three forms is adequate to describe the K_s^0 data, which do not have enough statistical power to distinguish among the three. A similar study of the gas threshold region shows that a "threshold" function $A(1 - e^{-\lambda(p-p_0)})$ is a good parametrization. Therefore, we use a piecewise-continuous functional form, a threshold function, then a flat plateau, then a Gaussian falloff, to fit all of our identification efficiencies.
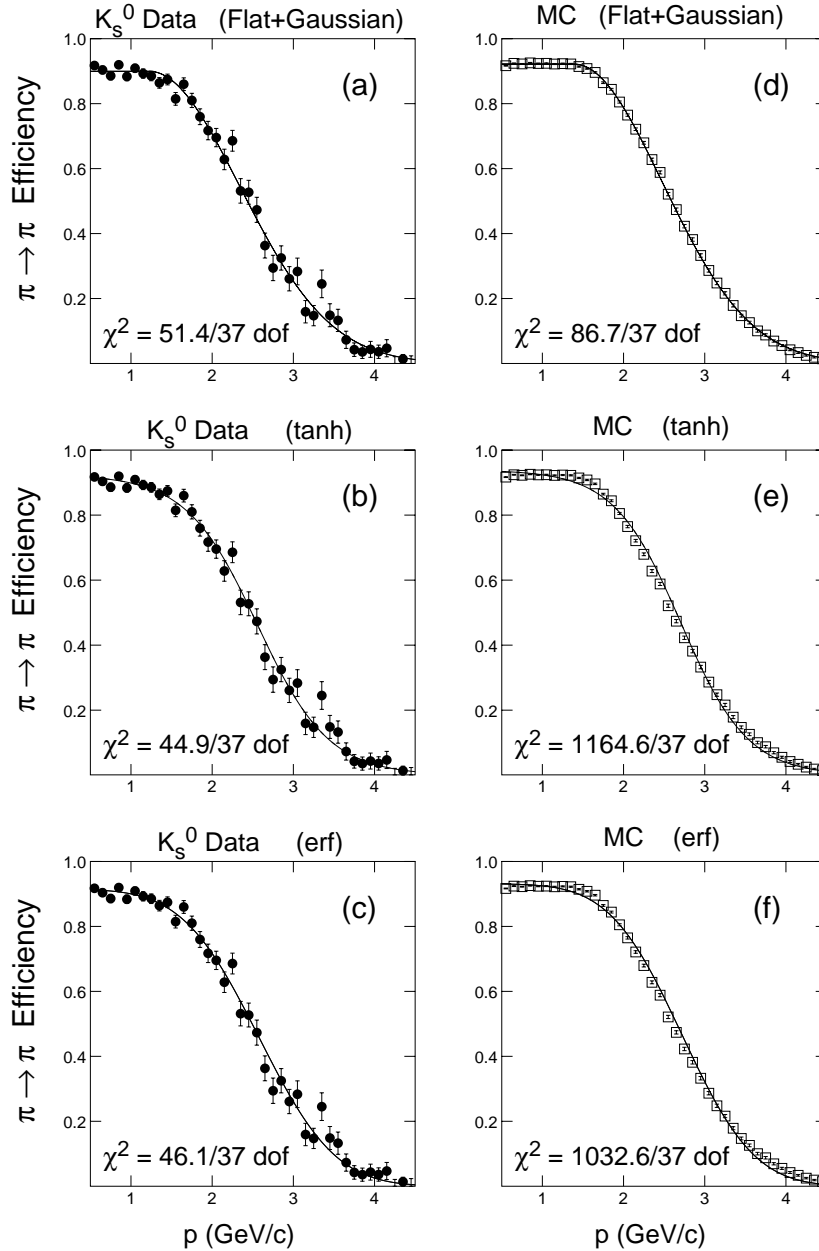
Figure 9.3: The pion identification efficiency in the liquid for pions from $K_s^0 \to \pi^+\pi^-$ decays (a–c) and for true pions in the Monte Carlo simulation that pass analysis cuts (d–f) are shown with a variety of fitting functions. Although the K_s^0 pions are insufficient to distinguish among the functions, the Monte Carlo points are best fit by a flat plateau with Gaussian falloff.

An advantage of this parametrization is that it has relatively few parameters, and these parameters control the shapes in mostly orthogonal ways. For example, the position of the start of the Gaussian falloff in momentum is related to the angular resolution σ_θ in the CRID. This region in momentum is where the Cherenkov angles of two particle hypotheses start to become close to one another. The poorer the resolution on θ_c is, the sooner two hypotheses become indistinguishable in the CRID. Similarly, the height of the flat plateau is related the photon yield. To a good approximation, we can consider these parameters to be independent.

9.2.2 Measured Data Efficiencies

We turn now to the extraction of identification efficiencies from the data. This is done by fitting the functional form described above to the observed efficiencies. For each element of the efficiency matrix ε, we have three data samples to consider: the calibration sample from data, the results of a similar calibration-sample analysis on Monte Carlo, and the full Monte Carlo identification efficiency (from Fig. 9.2). We start with the fit parameters from the data sample, and modify them by the difference between similar parameters derived from the expected Monte Carlo efficiency and those from the Monte Carlo calibration sample. Generally, these differences are manifested as a shift of the edge in momentum or a shift of the plateau height (*i.e.*, normalization). We parametrize the identification efficiency separately in three different momentum regimes.

Liquid ring region

The procedure is demonstrated in Fig. 9.4 for the liquid $\pi \to \pi$ efficiency. The discrepancy between the Monte Carlo efficiency and the efficiency observed in the data can be seen in Fig. 9.4a. This difference corresponds well to our two orthogonal parameters, a shift in momentum of the Gaussian falloff due to resolution and a shift of the plateau height due to photon yield. Because the identification efficiency of pions from K_s^0 decays may not be identical to the
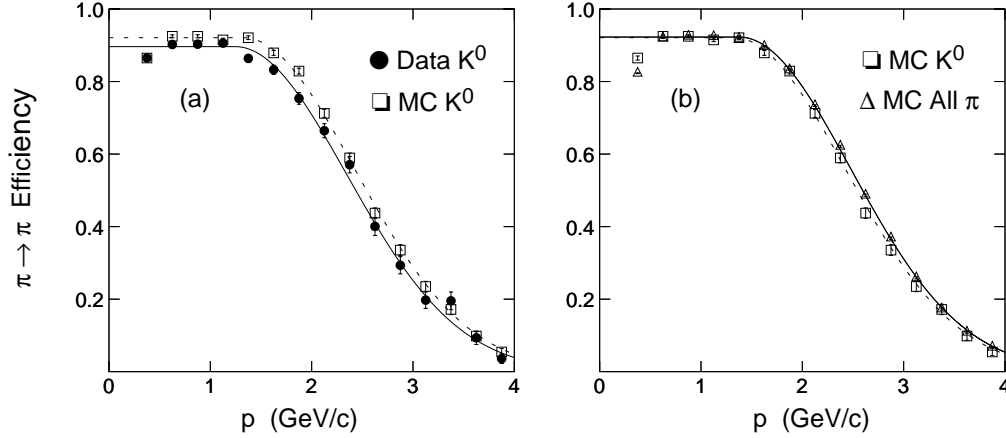
Figure 9.4: The identification efficiencies predicted from Monte Carlo simulation and observed in the data for a sample of pions from K_s^0 decays are shown in (a). Also shown are the parametrizations of efficiency that we fit to this data. In order to correct for any potential biases of the K_s^0 calibration sample, we adjust the measured efficiency of the data in (a) by the difference of the curves in (b), which are the Monte Carlo efficiency derived from $K_s^0 \to \pi^+\pi^-$ and from true pions in the Monte Carlo.

efficiency of an inclusive pion sample, however, we correct the data curve of Fig. 9.4a by the difference between the Monte Carlo K_s^0 pion and inclusive pion efficiencies in Fig. 9.4b. The correction turns out to be negligible in normalization, but corresponds to a small shift in the edge, as might be expected if Cherenkov angle resolution on these tracks were worse than on those from the IP.

A similar procedure for the liquid $p \to p$ efficiency at high momentum is used. We employ the same pion sample for the calibration by making use of an empirical relation that the Gaussian falloff in efficiency is nearly identical for complementary samples. Consider the case where we try to distinguish between only two hypotheses, proton and pion. In the momentum range of this Gaussian falloff, the particle identification comes purely from measuring the observed ring radius and deciding whether it is within $n\sigma$ of one hypothesis and not within $n\sigma$ of the other. In this symmetric, two-hypothesis case, the fraction
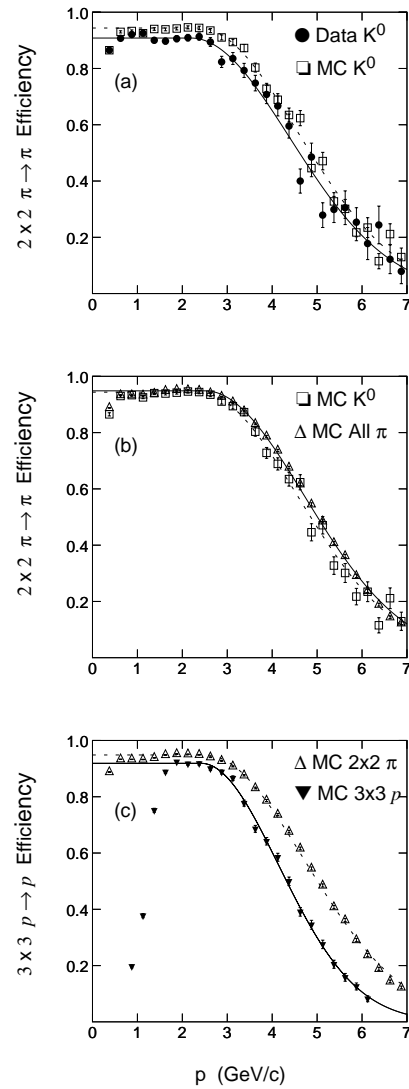
Figure 9.5: As described in the text, we use the $\pi \to \pi$ efficiency in a 2×2 π/p analysis to estimate the $p \to p$ efficiency. The Monte Carlo and data identification efficiencies for a sample of pions from K_s^0 decays is shown in (a). The small bias in efficiency of the K_s^0 sample is shown in (b). The Monte Carlo pion efficiency in the 2×2 analysis and the proton efficiency in the full 3×3 analysis are shown in (c).

of protons close enough to the proton radius and far enough away from the pion radius to be identified is the same fraction as the fraction of pions identified. Thus, we can perform a 2×2 pion *v.* proton analysis on the K_s^0 pion sample, and use that shape to derive the $p \rightarrow p$ efficiency in the full 3×3 analysis.

This is demonstrated in Fig. 9.5. The corresponding plots to Fig. 9.4 are shown in parts (a) and (b). Again, the difference between the Monte Carlo K_s^0 pions and inclusive pions in (b) is very small. Figure 9.5c shows the correction from the 2×2 pion *v.* proton efficiency to the full 3×3 $p \rightarrow p$ efficiency. Above 3 GeV/c, this correction is due to the additional requirement of discrimination between the K and p hypotheses, and it is somewhat larger than the previous corrections. Since our simulation does a good job of modelling the shape of the $\pi \rightarrow \pi$ efficiency, we are confident that it can be used to relate the π/p (and π/K) separation to the p/K separation in this momentum region.

Below 1.75 GeV/c, the $p \rightarrow p$ efficiency is determined by the threshold behavior of the protons, and therefore the K_s^0 pion sample provides no test of the proton identification. In order to measure these points, and also to cross-check our pion-based calibration procedure, we employ the $\Lambda^0 \rightarrow p\pi^-$ sample of section 7.14. Figure 9.6 shows the $p \rightarrow p$ efficiency curves extracted from both methods. The agreement is excellent within the precision of the Λ^0 points. We use the Λ^0 points for determining the $p \rightarrow p$ efficiency below 1.75 GeV/c.

Having established this "complementarity principle" on the $p \rightarrow p$ identification, we may now apply it to the $K \rightarrow K$ efficiency. Unfortunately, the $\pi \rightarrow \pi$ and $K \rightarrow K$ efficiencies are not quite complementary because the kaon hypothesis lies between the pion and proton ring radii (the kaons get squeezed from both sides). However, we can derive a correction factor for this difference between the $\pi \rightarrow \pi$ and $K \rightarrow K$ efficiencies from the Monte Carlo. This is shown in Fig. 9.7. We see that the $\pi \rightarrow \pi$ and $K \rightarrow K$ efficiencies are identical up to 2.5 GeV/c. Therefore, we use the $\pi \rightarrow \pi$ parametrization for the range 1.0–2.5 GeV/c, and we divide the (data-derived) $\pi \rightarrow \pi$ efficiency by the ratio of the Monte Carlo $\pi \rightarrow \pi$ and $K \rightarrow K$ shown in Fig. 9.7 above 2.5 GeV/c. For the points below 1.25 GeV/c, we use the Monte Carlo values and assign an uncertainty based on
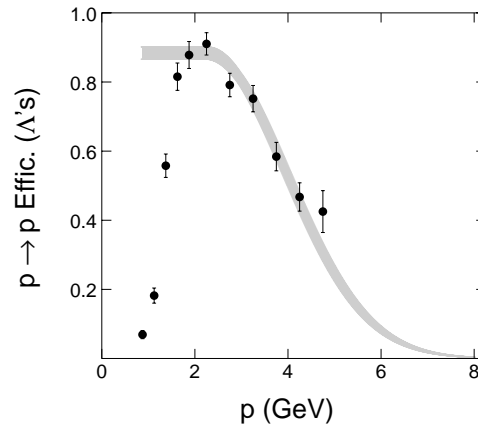
Figure 9.6: The $p \to p$ identification efficiency extracted from the $\Lambda^0 \to p\pi^-$ sample of section 7.14 (dots) is compared to the efficiency from the analysis of Fig. 9.5 (shaded region). The points below 1.75 GeV/c cannot be extracted from the pion-based analysis and must be determined from the Λ^0 sample.
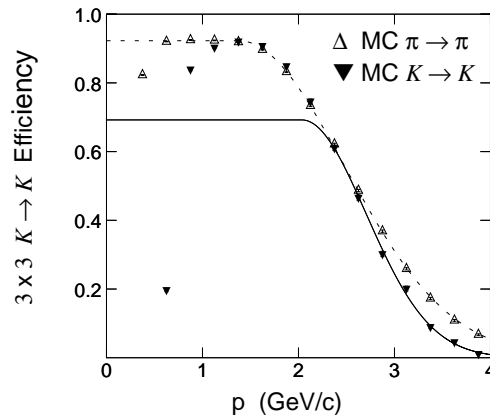
Figure 9.7: The $K \to K$ identification efficiency from simulation is shown in the solid triangles, compared to the $\pi \to \pi$ efficiency shown in the open triangles. As described in the text, the kaon efficiency is expected to be similar to the pion efficiency, except in the high-momentum region where the expected Cherenkov angle of the p hypothesis approaches that of the K hypothesis. The correction for this region is modelled by the ratio of the solid to dashed curves.
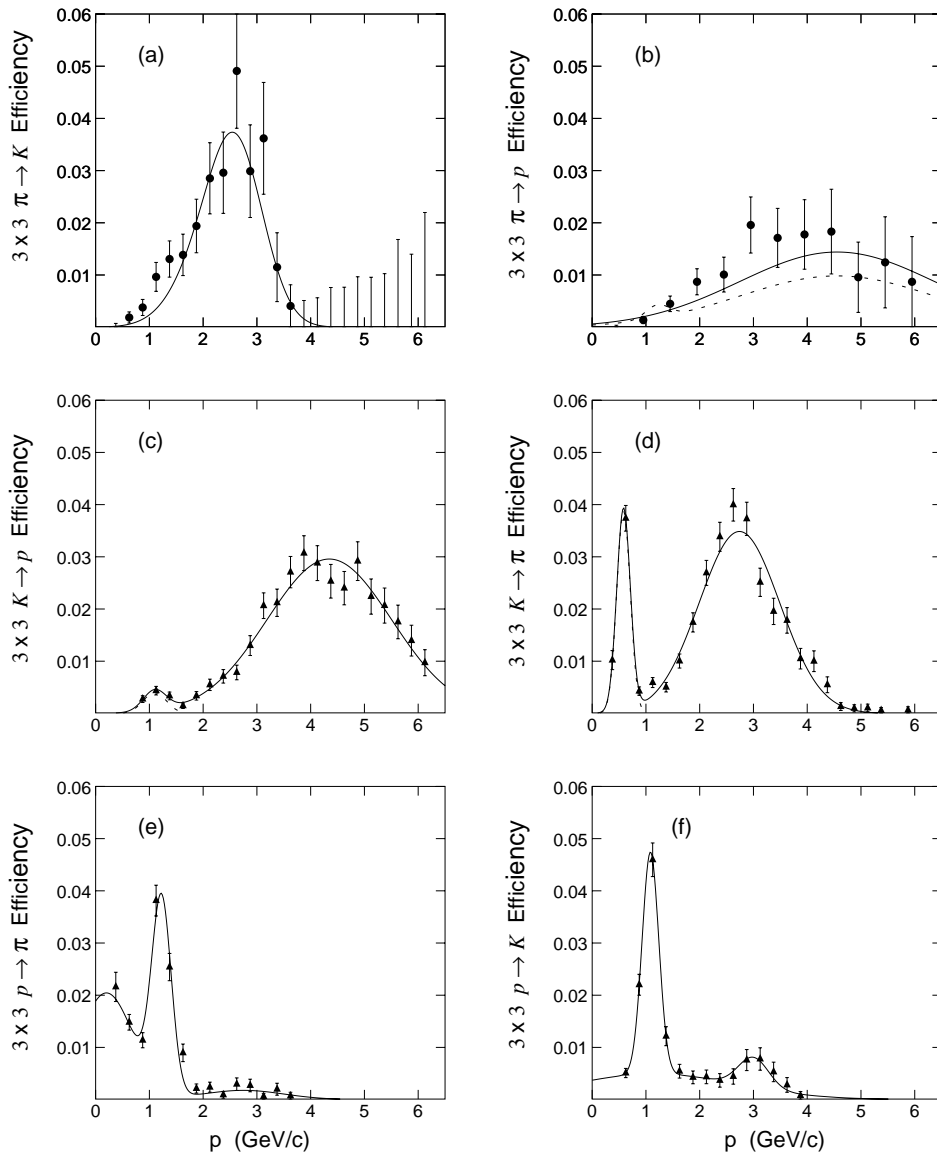
Figure 9.8: The off-diagonal elements of the efficiency matrix $\boldsymbol{\varepsilon}$ for the liquid are shown ($\varepsilon_{\pi K}$ in (a), $\varepsilon_{\pi p}$ in (b), ε_{Kp} in (c), $\varepsilon_{K\pi}$ in (d), $\varepsilon_{p\pi}$ in (e), and ε_{pK} in (f)). The dots are data from $K_s^0 \to \pi^+\pi^-$ decays, and the triangles are Monte Carlo simulation. Also shown are fits to the data or the Monte Carlo where no data are available. In (b), the dashed curve is the fit to the Monte Carlo for $\varepsilon_{\pi p}$.

the uncertainty of the comparable points in the $p \to p$ efficiency (derived from the Λ^0 sample).

That completes the diagonal terms in $\boldsymbol{\varepsilon}$ for the liquid-radiator regime, but leaves us with the off-diagonal misidentification rates. These are conceptually a bit simpler. Since the rates are so small, the statistical precision of our K_s^0 data set cannot discern any difference from the Monte Carlo misidentification rate. Therefore we fit a shape to the Monte Carlo distribution and assign an uncertainty somewhat larger than the statistical error on the data sample to allow for some variation of the shape. The Monte Carlo shape is generally modelled well by a sum of up to three Gaussians. These parametrizations are shown in Fig. 9.8.

A common feature of the upper off-diagonal elements ($\varepsilon_{ij} = \varepsilon_{K\pi}, \varepsilon_{p\pi}, \varepsilon_{pK}$) is a large bump just below the threshold of particle type i. This is caused by the transition from threshold-based identification for particle i to ring-based identification. Below threshold, the identification effectively consists of counting the number of hits within $n\sigma$ of the expected ring for hypothesis j and deciding if this number of hits is consistent with background expectation. As the expected radius of the ring for hypothesis i increases, the possibility for background fluctuations to produce 4 or 5 hits consistent with the ring increases. Above threshold, the identification switches effectively to a comparison of the number of hits within $n\sigma$ of each expected ring radius, thus decreasing the probability of misidentification. Unfortunately, we have no direct measurements to constrain these upper off-diagonal ε_{ij} terms. Therefore, we assign a conservative systematic uncertainty of 25% of the ε_{ij} value for these below-threshold peaks.

Gas ring region

We can now repeat this whole process in the gas high-momentum region. There, the calibration data sample is τ decays (see section 7.14), but the procedure is essentially the same. One concern is potential differences in identification performance between low-multiplicity tau events and the hadronic events. We correct for this with the difference in efficiency between a τ-pair Monte
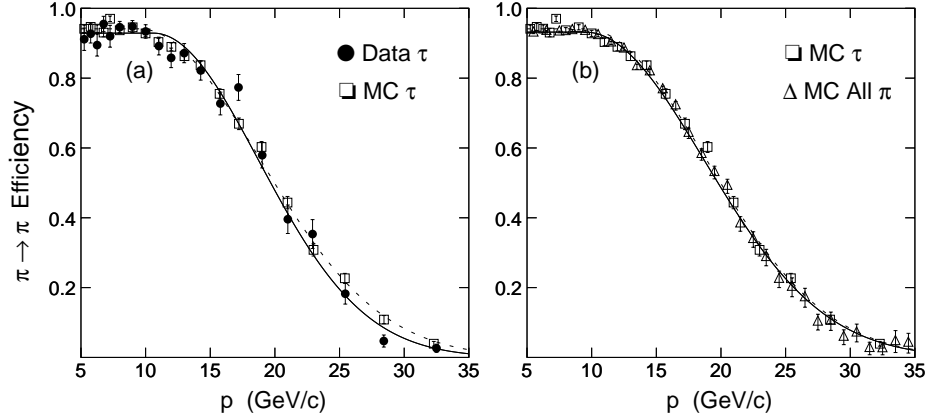
Figure 9.9: The identification efficiency measured in the data for a sample of $\tau \to \pi/e/\mu$ decays is shown as dots in (a). Also shown is the efficiency predicted from our τ Monte Carlo simulation (squares). The pion identification efficiency in the τ sample and in the full hadronic events, based on our simulations, are shown in (b). Here, the τ efficiencies are the squares and the hadronic efficiency is shown as the triangles.

Carlo and the inclusive pion efficiency from hadronic Monte Carlo, similar to the technique used with the K_s^0 sample in the liquid. It turns out that this correction is very small (see for example Fig. 9.9b), presumably due to the gas ring isolation cut and the generally low background levels in gas rings.

The gas $K \to K$ efficiency follows the procedure of the liquid $K \to K$ efficiency. We use the same efficiency as the $\pi \to \pi$ parametrization from 15–19 GeV/c, and correct the $\pi \to \pi$ parametrization by the ratio of the solid to dashed curves in Fig. 9.10 for momenta above 19 GeV/c. For momenta below 15 GeV/c, we correct the $\pi \to \pi$ parametrization by the ratio of the pion and kaon points in Fig. 9.10.

For the gas $p \to p$ efficiency, we employ the same "complementarity method" as in the liquid. This is shown in Fig. 9.11. For the very high momentum protons ($p > 25$ GeV/c), we have low statistics in our Monte Carlo sample. The Monte Carlo 3×3 $p \to p$ efficiency points are consistent with the 2×2 pion points of Fig. 9.11b, so we apply no correction and assign an uncertainty based on the proton Monte Carlo statistics. Most of the gas ring identification region, however, is below 25 GeV/c. For this range ($10 < p < 25$ GeV/c), the $p \to p$
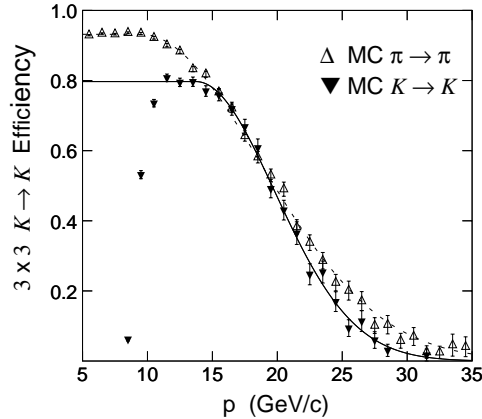
Figure 9.10: The $K \rightarrow K$ identification efficiency from simulation is shown in the solid triangles, compared to the $\pi \rightarrow \pi$ efficiency shown in the open triangles. As described in the text, the kaon efficiency is expected to be similar to the pion efficiency, except in the high-momentum region where the expected Cherenkov angle of the p hypothesis approaches that of the K hypothesis and in the low-momentum region where the kaons are just above threshold. The correction for this region is modelled by the ratio of the solid to dashed curves.

efficiency follows a threshold function, as shown in Fig. 9.11c. We assign an uncertainty based on a cross-check with a sample of protons from Λ^0 decays.

Finally, the misidentification terms for the gas ring region are shown in Fig. 9.12. These have the same characteristics as the misidentification elements in the liquid ring region. We fit these with Gaussians, or with a threshold function for the $\varepsilon_{\pi p}$ and $\varepsilon_{K p}$ cases.

Gas threshold region

In the gas threshold region ($p < 10$ GeV/c), we again follow a similar procedure, but there are some differences. For one, there are only four $\boldsymbol{\varepsilon}$ terms to parametrize, since there is no K-p separation in this momentum regime. Second, the shapes are simpler, with a threshold function serving as a good model for the identification efficiencies, and the misidentification rates being
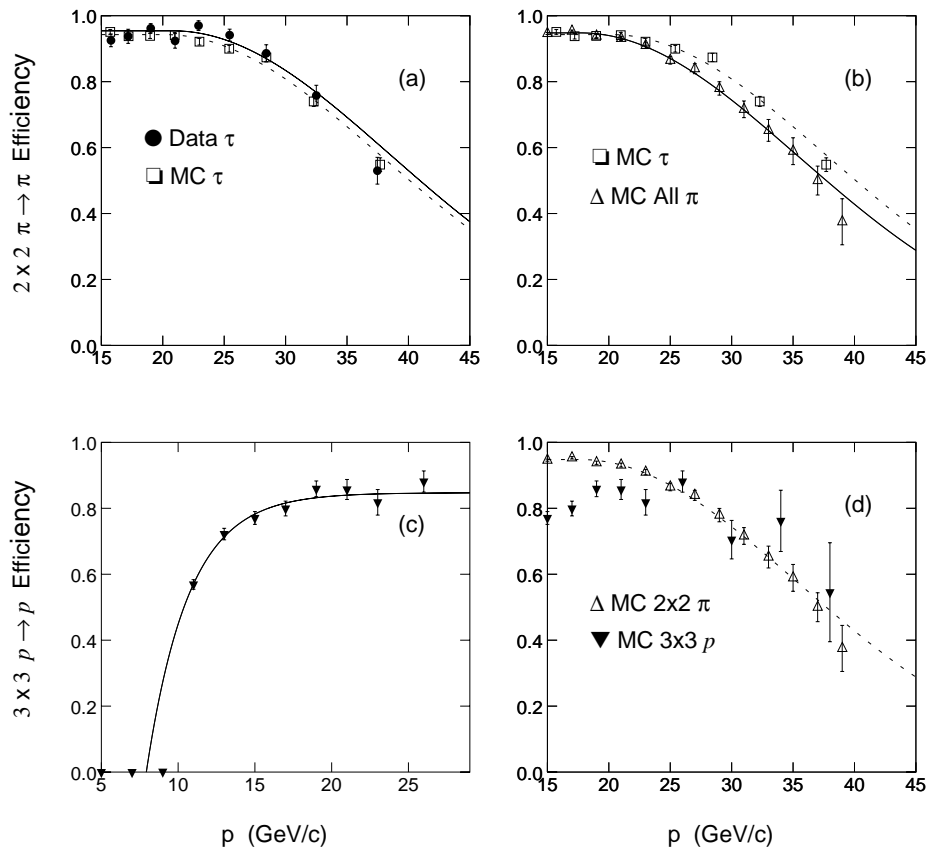
Figure 9.11: The Monte Carlo and data identification efficiencies for a sample of pions from τ decays when analyzed against the proton hypothesis are shown in (a). The bias of the τ sample compared to Monte Carlo true pion in hadronic events (triangles) is shown in (b). A fit to the Monte Carlo $3 \times 3 \; p \to p$ efficiency in the lower momentum region ($10 < p < 25$ GeV/c) is shown in (c). For momenta above 25 GeV/c, as shown in (d), the protons are consistent with the shape of the Monte Carlo pion curve from (b).
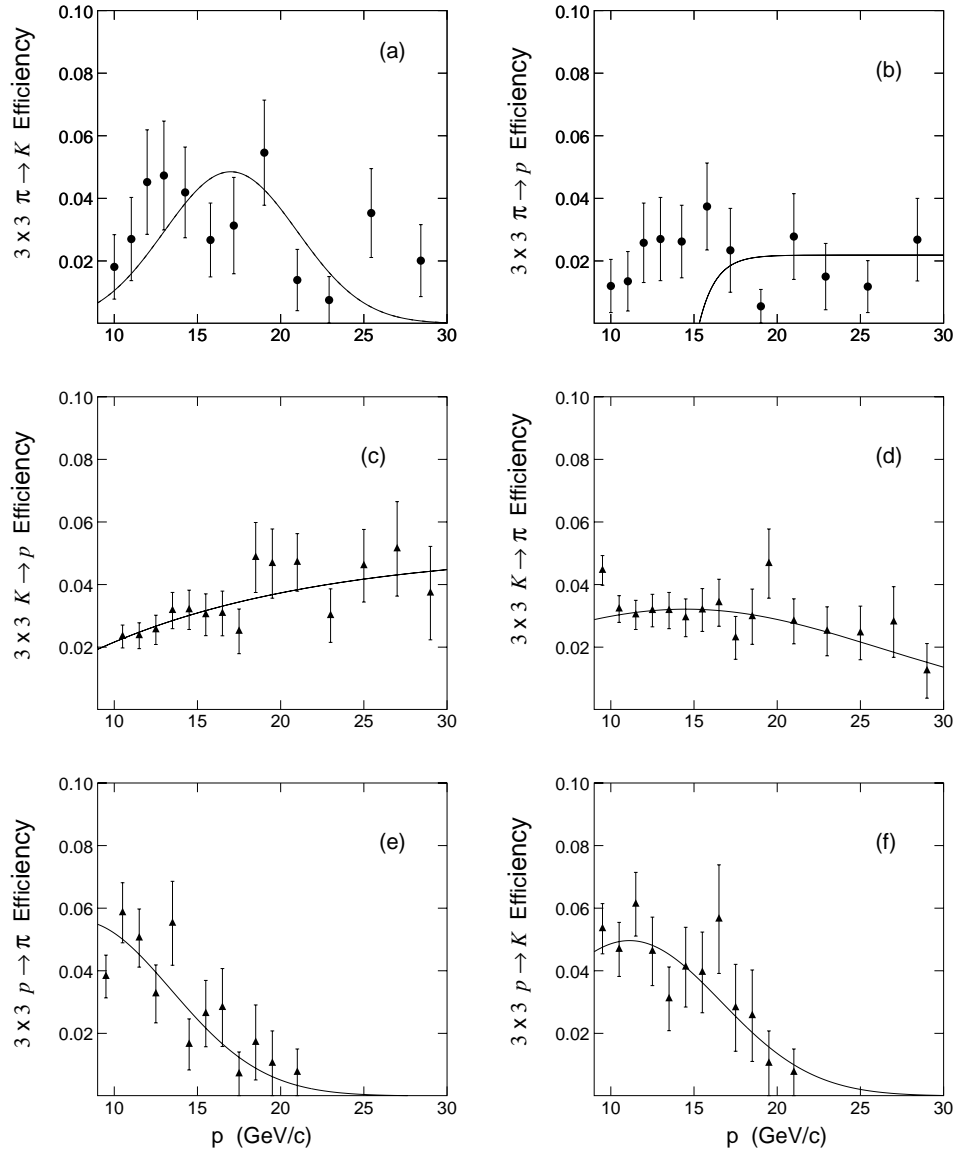
Figure 9.12: **The off-diagonal elements of the efficiency matrix $\boldsymbol{\varepsilon}$ for the gas ring region** ($10 < p < 35$ GeV/c) are shown ($\varepsilon_{\pi K}$ in (a), $\varepsilon_{\pi p}$ in (b), ε_{Kp} in (c), $\varepsilon_{K\pi}$ in (d), $\varepsilon_{p\pi}$ in (e), and ε_{pK} in (f)). The dots are data from τ decays, and the triangles are Monte Carlo simulation. Also shown are fits to the Monte Carlo. These fits are consistent with the data in (a) and (b).
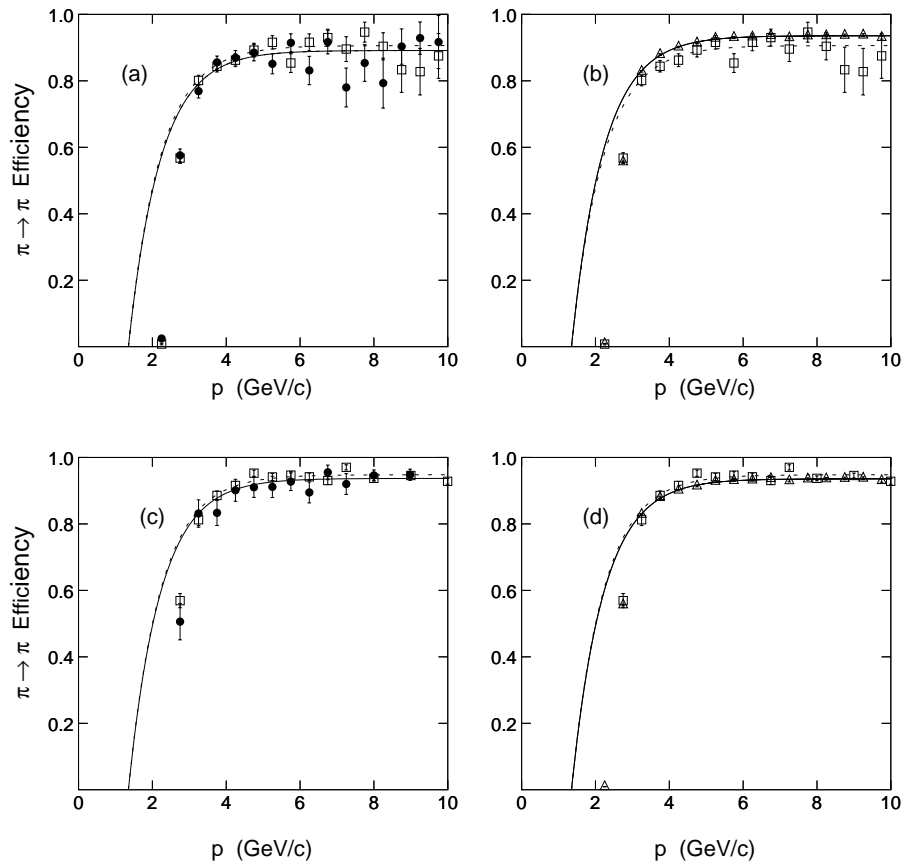
Figure 9.13: The $\pi \to \pi$ efficiency in the gas threshold region is summarized. The efficiency extracted from the K_s^0 pion sample in the data (dots) and Monte Carlo (squares) are shown in (a), while the Monte Carlo K_s^0 sample is compared to the hadronic pion efficiency (triangles) in (b). A similar pair of plots for the τ decay sample are shown in (c) and (d). The dots are the data τ sample, the squares are the Monte Carlo τ sample, and the triangles are the same Monte Carlo pion efficiency as in (b).
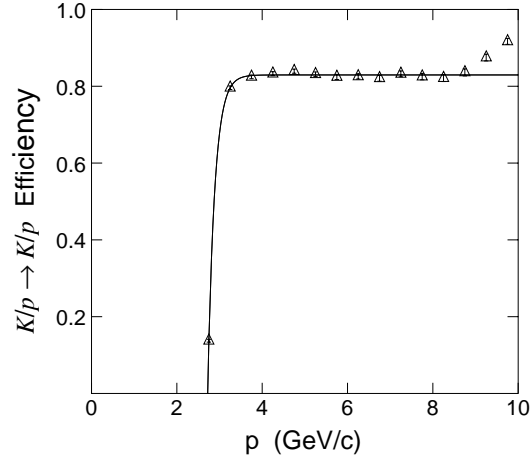
Figure 9.14: The efficiency for the non-pion hypothesis ($K/p \rightarrow K/p$) in the gas threshold region. The momentum dependence is essentially flat. The curve is a fit to the Monte Carlo efficiency, which has been cross-checked against a sample of protons from Λ^0 decays.

essentially flat. Finally, we have the advantage of being able to employ both the K_s^0 and τ decay samples.

The $\pi \rightarrow \pi$ efficiency analysis is shown in Fig. 9.13 for both samples. As in the other elements, we use the measured data sample efficiencies of (a) and (c), and correct for the small difference between the identification efficiency in the calibration sample and that of inclusive pions in hadronic events (b) and (d). The efficiency points below 3 GeV/c cannot be parametrized with the same curve as the rest of the distribution, so we treat them individually. The results of the two samples (K_s^0 and τ decays) show good agreement.

The $K/p \rightarrow K/p$ efficiency is shown in Fig. 9.14. The momentum dependence is essentially flat over this region. We cross-check the height of the plateau with a sample of protons from Λ^0 decays, and find good agreement. Therefore, we use the Monte Carlo parametrization and assign a normalization uncertainty of 0.02 based on the Λ^0 statistics.
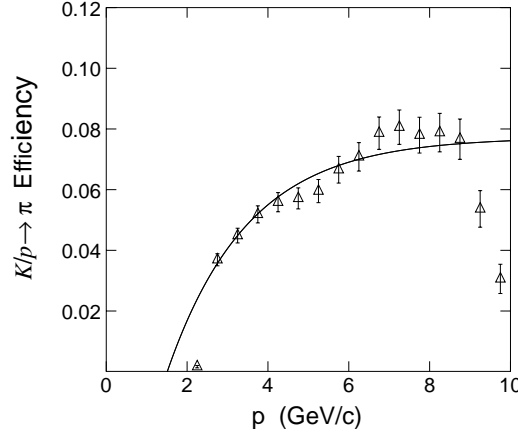
Figure 9.15: The misidentification rate for the non-pion hypothesis to be identified as a pion ($K/p \to \pi$) in the gas threshold region from the Monte Carlo simulation is shown. Also shown is a parametrization of this efficiency with a threshold function for the range $3 < p < 9$ GeV/c.

The misidentification terms for the gas threshold region are shown in Figs. 9.15 and 9.16. For the $K/p \to \pi$ term, we parametrize the Monte Carlo points with a threshold function as shown in Fig. 9.15. For the $\pi \to K/p$ term, we have pions from both the K_s^0 and τ calibration samples. Figure 9.16b indicates that there might be a bias of 2% extra misidentification in the K_s^0 sample at these momenta, but such a bias is absent in the τ sample (see Fig. 9.16c). The agreement between Monte Carlo and data for the two calibration samples (in Fig. 9.16a and c) is good. Therefore, we use the parametrization to the full Monte Carlo $\pi \to p/K$ term and assign an uncertainty based on the τ statistics.

Combined identification efficiency

Combining these parametrizations of the various identification regimes, we arrive at the "final" particle identification efficiency matrix shown in Fig. 9.17. All errors in the plot now represent our best knowledge of the identification uncertainty, based on our calibration samples. For the diagonal elements, the
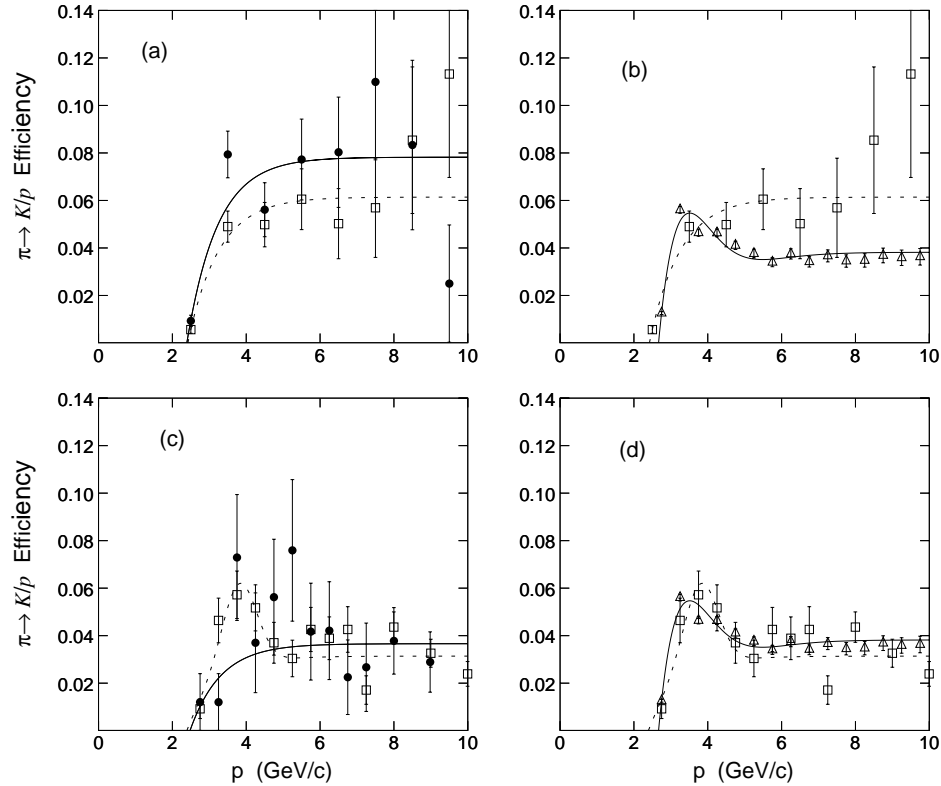
Figure 9.16: The pion to non-pion misidentification rate in the gas threshold region is analyzed with pions from both K_s^0 decays (a) and (b) and from τ decays (c) and (d). In (a) and (c), the pion sample from the data (dots) is compared to a similar calibration sample from Monte Carlo (squares). The solid curve is a fit to the data, and the dashed curve is a fit to the Monte Carlo points. In (b) and (d), the Monte Carlo calibration samples are compared to the full hadronic Monte Carlo (triangles). In (d), we see that the τ decays do not have much bias on the misidentification rate, but we see in (b) that the K_s^0 sample has an extra 2% misidentification, presumably from a contamination of non-pions in the calibration sample at momenta above 5 GeV/c.
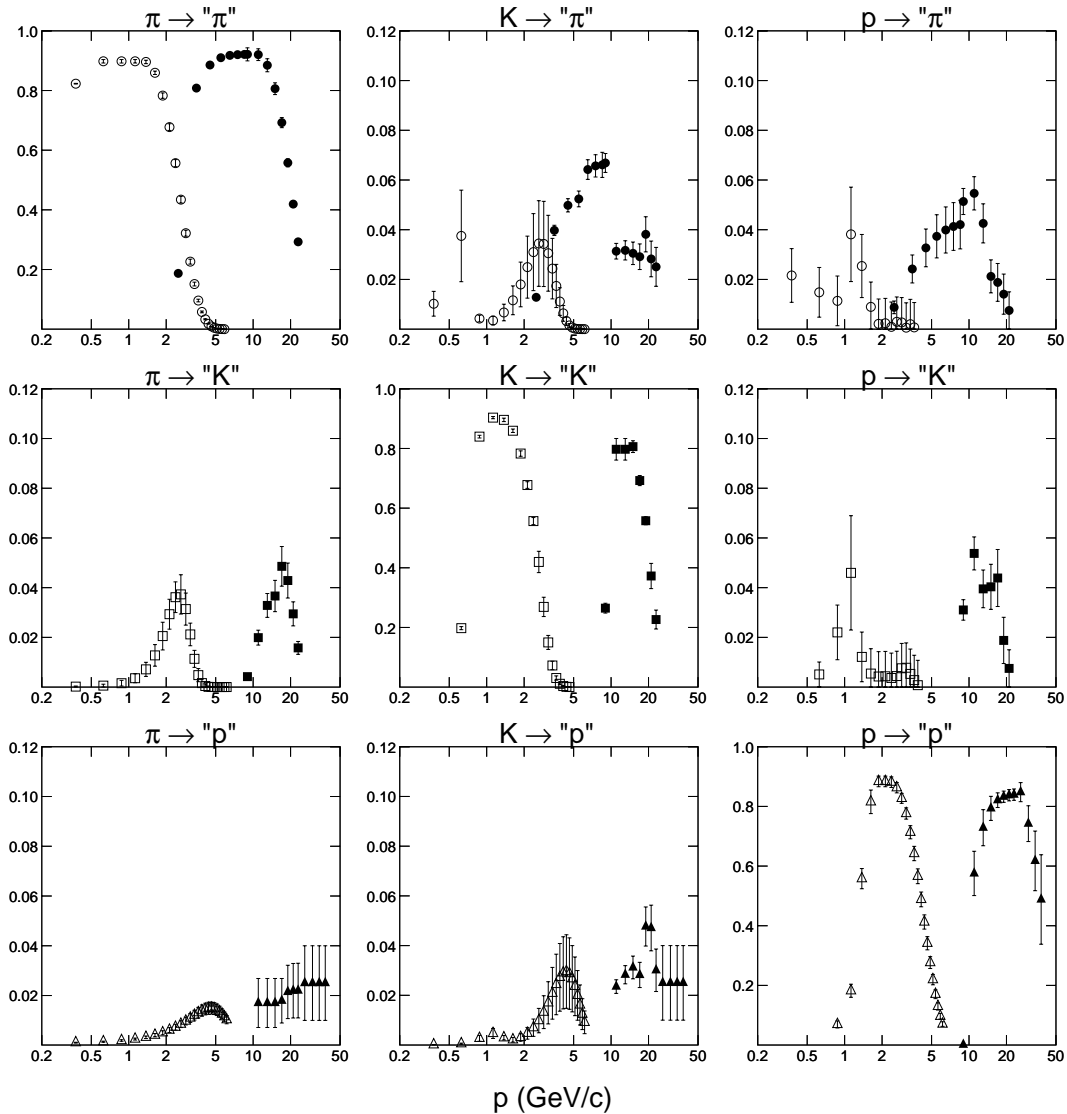
Figure 9.17: The matrix of hadronic particle identification efficiencies, as determined from calibrated data samples of known identity. The error bars reflect the systematic uncertainties, primarily coming from the statistical precision of our calibration samples. The open points are the ones from the liquid radiator, and the solid points are from the gas radiator.

assigned uncertainties derive from the errors on the fitted parameters and corrections. These are dominated by the statistical precision of our K_s^0 and τ calibration samples. It is harder to constrain the shape of the off-diagonal elements of the $\boldsymbol{\varepsilon}$ matrix, because the statistical errors on our calibration samples are larger relative to their values. Therefore we use the shape from the Monte Carlo and apply a conservative prescription of assigning as the uncertainty the largest one of: the uncertainty from our fit to the data, a 0.01 absolute error, or a relative error of 0.25 of the value. These errors are meant to include our uncertainty about the exact shapes of the misidentification terms.

9.3   Measured Particle Fractions

Armed with the selection criteria of Chapter 8 and the efficiency matrix of Fig. 9.17, it is now straightforward to determine the measured numbers of identified particles (n_i) and unfold the efficiency matrix $\boldsymbol{\varepsilon}$ using Eq. (9.6) to get the hadronic particle fractions. The raw, measured identified fractions are shown in Fig. 9.18, and the unfolded fractions are shown in Fig. 9.19. We see from Fig. 9.18 that statistical errors in the measured fractions are very small for all but the high momentum ($p > 15$ GeV/c) kaon and proton points. With the exception of those high-momentum points in the gas radiator, the errors in Fig. 9.19 are dominated by systematic uncertainties in our determination of the $\boldsymbol{\varepsilon}$ matrix. These systematics are likely to be strongly correlated from point to point.

In the unfolded fractions, we only include momentum points when the corresponding diagonal $\boldsymbol{\varepsilon}$ element is above 20%, as the relative uncertainty on the unfolding would blow up beyond that point. This limits the liquid π and K points to $p < 3$ GeV/c, the liquid proton points to $p < 5$ GeV/c, and the gas π and K points to $p < 24$ GeV/c.

Internally, our data show good consistency. The liquid and gas momentum ranges overlap slightly for the pion fractions. These points show good agreement. In addition, we have the consistency check of the sum of the three
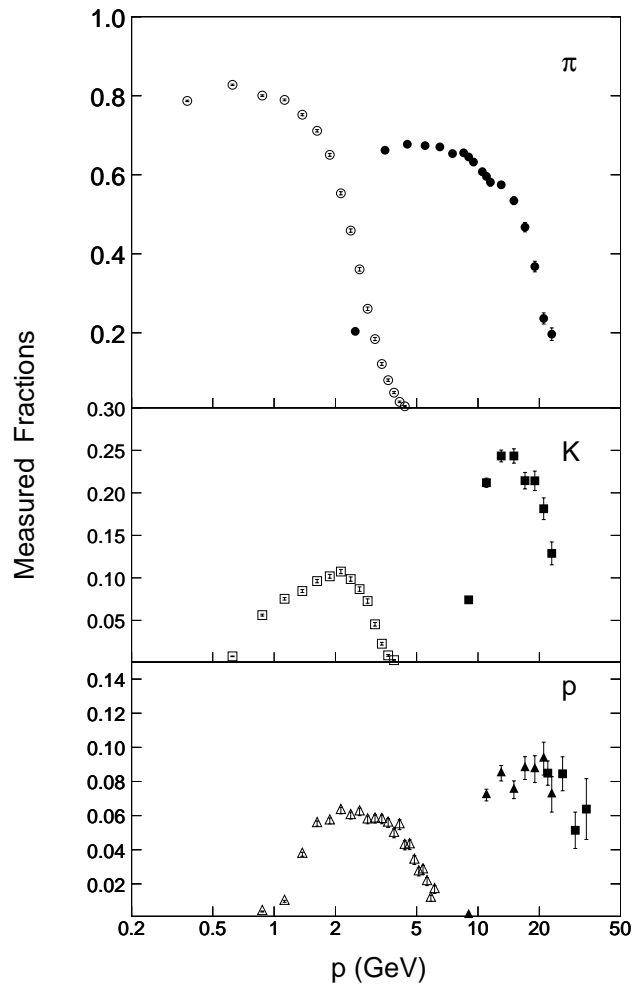
Figure 9.18: The fractions of selected tracks that are identified as π, K, and p in the CRID for the 1994–95 dataset. The errors are statistical only.
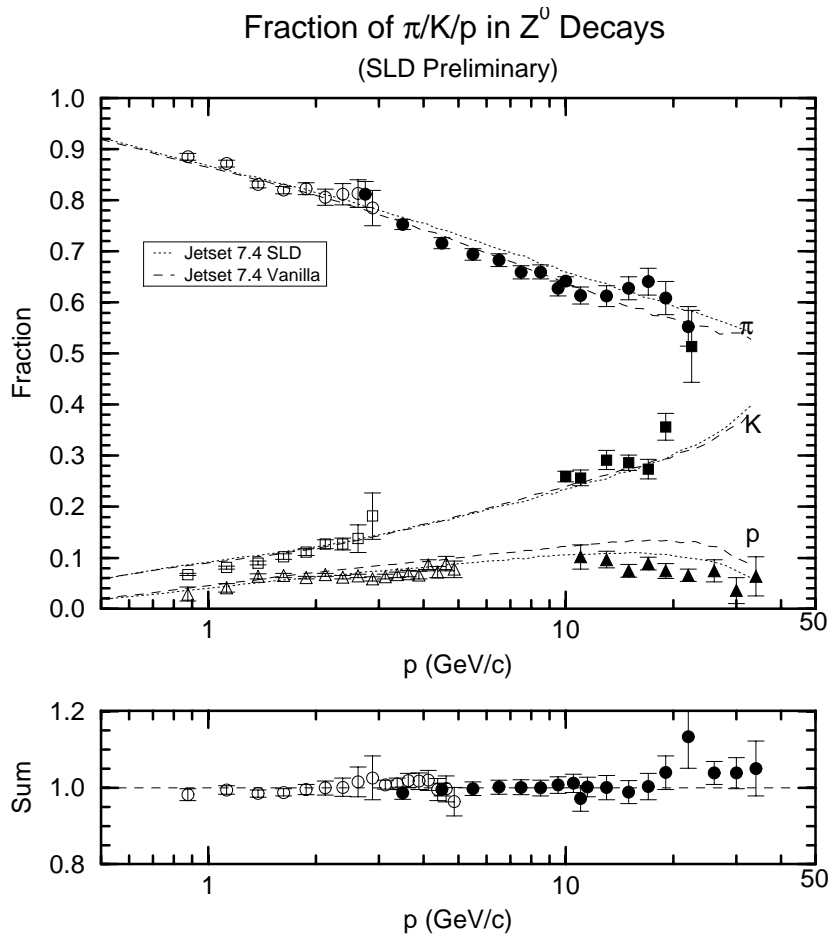
Figure 9.19: Hadronic particle fractions for $\pi^{\pm}$ (circles), $K^{\pm}$ (squares), and $p/\bar{p}$ (triangles). The open (solid) symbols correspond to fractions extracted using liquid (gas) radiator information in the CRID. Also shown are the predictions of the JETSET 7.4 model, both with default parameters (dashed curve) and with the SLD-tuned parameters (dotted curve). The sum of the particle fractions, shown in the bottom plot, serves as a cross-check of the identification efficiency matrix used for unfolding (see section 9.1).

hadronic fractions, as discussed in section 9.1. This is shown at the bottom of Fig. 9.19 and indicates consistency with unity at the level of 1–2% for most points. All of these checks give us additional confidence in our parametrization of the CRID identification performance, ε.

The features of the hadronic fractions are generally what we might expect. At low momenta, pions dominate the hadronic spectra. This is the region where the masses of the kaon and proton would make a large impact on the available phase space for production of these particles. As particle momentum increases, the kaon fraction rises and the pion fraction decreases. Our data do not cover high enough in momentum to determine if the π and K fractions become equal as the particle momentum approaches the beam energy. The proton fraction also increases somewhat with momentum, but never exceeds 10%. At high momentum, in fact, it decreases and may even approach zero for momentum equal to the beam energy.

Our data are consistent with other measurements of hadronic fractions at the Z^0. The liquid-ring K and p measurements fill in the gap in coverage of the ionization energy loss measurements of OPAL [173] and ALEPH [174]. Our data are in good agreement with the Cherenkov ring imaging data of DELPHI [175] and cover a slightly larger momentum range.

The predictions of JETSET 7.4 with both the default parameters and with the SLD-tuned parameters are shown in Fig. 9.19. The default parameters were tuned to similar data at PEP and PETRA energies. The general agreement of the default JETSET with our data indicates that the JETSET parameters are relatively independent of energy. The SLD parameters were tuned to measurements including ones from LEP and show better agreement with the high-momentum protons in our data.

We can also express our hadronic fractions as normalized particle production rates $F^h(x_p)$ in scaled momentum $x_p = 2p/\sqrt{s}$. To do this, we need only to multiply by the total charged-hadron cross section $1/N \, dn^{ch}/dx_p$. This cross section, however, requires a good understanding of tracking efficiency in the SLD. That work is still in progress, so we found it more expedient to use the
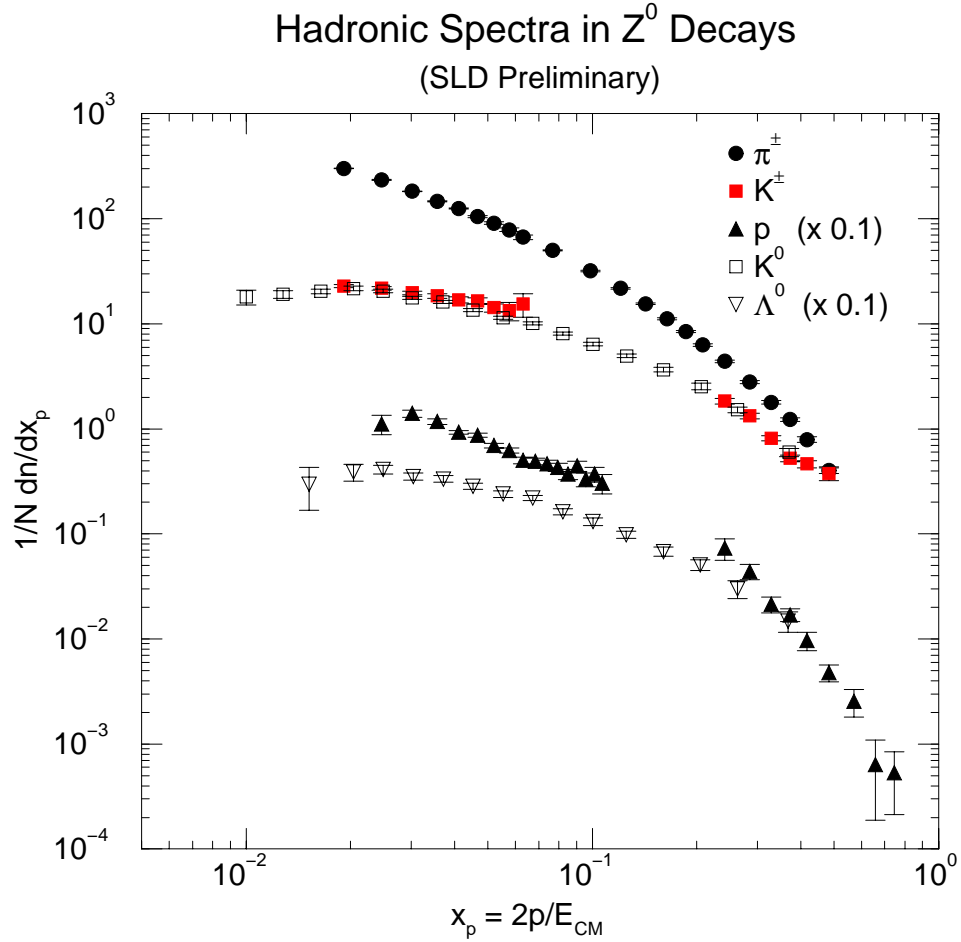
Figure 9.20: Normalized production rates $F^h(x_p)$ for various hadron species are shown as a function of scaled momentum $x_p = 2p/\sqrt{s}$. The $\pi^\pm$ (dots), $K^\pm$ (solid squares), and $p/\bar{p}$ (solid triangles) points are obtained from the hadronic fractions of Fig. 9.19 by multiplying by the total charged hadron cross section as described in the text. The K^0_s (open squares) and Λ^0 (open triangles) points come from [172]. The p and Λ^0 points have been scaled by 0.1 for clarity in presentation.

measurement of [176], which is well-reproduced by the SLD-tuned JETSET 7.4 model. The resulting hadronic spectra are shown in Fig. 9.20, along with the SLD measurements of K^0 and Λ^0 spectra from [172]. These spectra show excellent agreement between the charged and neutral kaons, as expected from isospin symmetry. There is also an interesting similarity in the relative behavior of the π and K spectra and the p and Λ spectra. In the simple IF models, for example, the ratios of these two pairs of spectra should be related purely to the strange suppression parameter γ_s.

9.4   Flavor Unfolding

For the reasons discussed in Chapter 2, we wish to push beyond the particle spectra of Fig. 9.20 and measure the spectra in events of different quark flavor. The tagging procedure is discussed in section 8.2. We use events with $n_{sig} = 0$ as our *uds* sample ($Z^0 \to u\bar{u}$, $d\bar{d}$, or $s\bar{s}$), events with $n_{sig} = 1$ or 2 as our *c* sample ($Z^0 \to c\bar{c}$), and events with $n_{sig} \geqslant 3$ as our *b* sample ($Z^0 \to b\bar{b}$). The tags have imperfect purities, as shown in Table 8.1. In order to arrive at the true particle spectra, we must unfold these purities. In addition, we must consider biases on the momentum spectra from the tagging process.

The unfolding procedure is nearly identical to that in [172] for the K_s^0 and Λ^0 measurements. The expected number of particles of type h per i-tagged event n_i^h ($i = 1, 2, 3$ for $n_{sig} = 0$, 1–2, $\geqslant 3$, respectively), can be related to the true number per j-flavor event $\bar{n}_j^h$ ($j = uds$, c, b) by

$$n_i^h(x_p) = \sum_j \frac{R_j E_{ij} b_{ij}(x_p)}{\sum_k R_k E_{ik}} \bar{n}_j^h(x_p),\tag{9.8}$$

where R_j is the Standard Model fraction of hadronic Z^0 decays into quark type j

$$R_j = \frac{N_{Z^0 \to j\bar{j}}}{N_{Z^0 \to hadrons}},\tag{9.9}$$

E_{ij} is the event-tagging efficiency matrix given in Table 8.1

$$E_{ij} = \frac{N_{j \to i}}{N_j},\tag{9.10}$$

with $N_{j \to i}$ the number of selected j-flavor events that are in the i-tagged sample and N_j the total number of selected j-flavor events. The b_{ij} is a bias term

$$b_{ij}(x_p) = \frac{n^h_{j \to i}(x_p)}{E_{ij}\bar{n}^h_j(x_p)}.\tag{9.11}$$

Here, $n^h_{j \to i}(x_p)$ is the number of reconstructed particles of species h from quark flavor j that are found in the i-tagged sample.

Note that the conventional definition of tag purity (P_{ij}) is related to the above matrices by

$$P_{ij} = \frac{R_j E_{ij}}{\sum_k R_k E_{ik}} = \frac{N_{j \to i}}{\sum_k N_{k \to i}}.\tag{9.12}$$

In the absence of tagging bias ($b_{ij} = 1$), the fraction of the particles of a given species in the i-tagged sample that comes from j-flavor events would be the same as the event purities, and Eq. (9.8) would be a simple relationship based solely upon the purities of the tag.

The sources of the biases are nearly identical to those in [172]. Since the tags require certain numbers of tracks with impact parameter separation $> 3\sigma$ from the IP, it follows that events with higher track multiplicity will be more likely to be tagged as b or c events. By conservation of energy, however, events with higher multiplicity will also tend to have a lower average track momentum/energy and fewer tracks at high x_p. In addition, pions and protons from K^0_s and Λ^0 decays, and from interactions, will tend to have larger impact parameters (if they survive the track quality cuts). Due to the excellent vertexing, these biases turn out to be generally small. Also, the biases are generally similar for π, K, and p species, indicating a correction mostly on the total multiplicities and a smaller effect on the fractions.
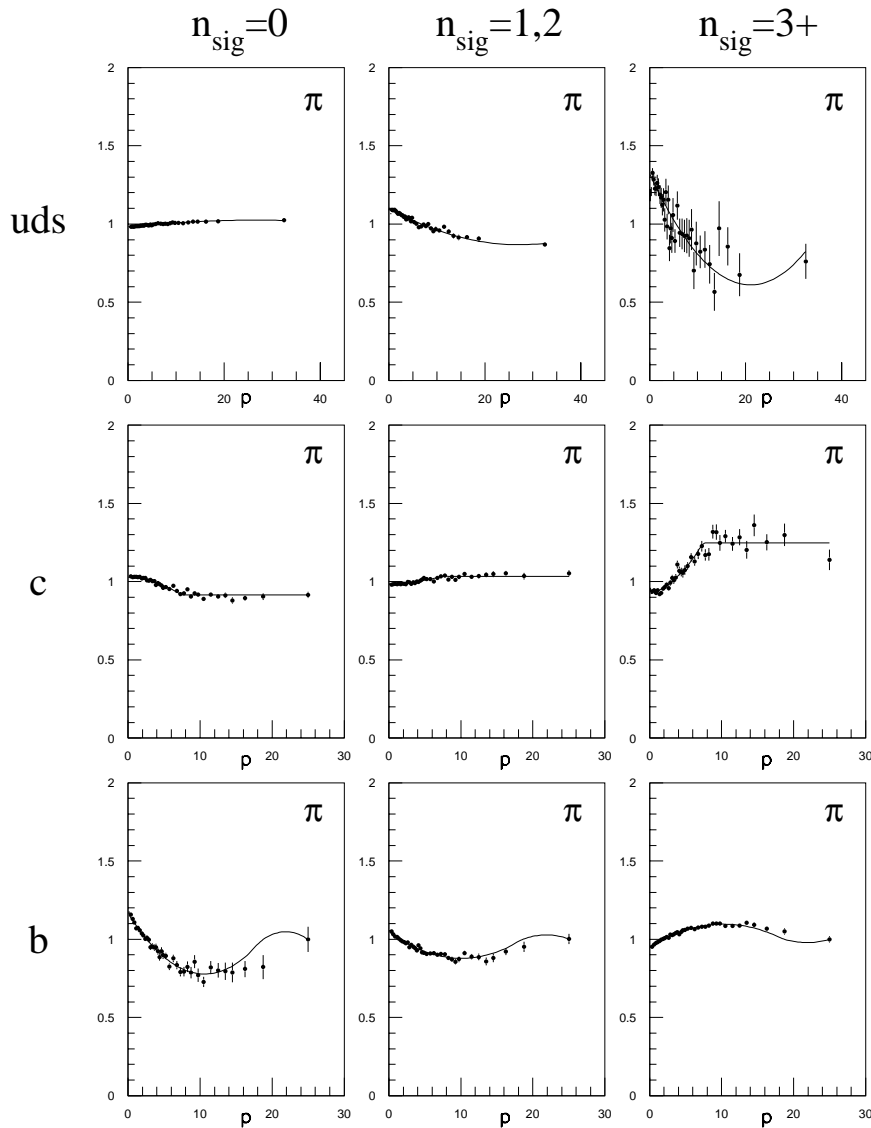
Figure 9.21: The bias induced in the pion momentum spectra as a result of the two-dimensional impact parameter tag for event flavor. The points are from the SLD-tuned JETSET 7.4 simulation, and the curves are parametrizations of the Monte Carlo points. A relative uncertainty of 20% of deviation from unity is assigned as a conservative upper bound, following the analysis of [172].
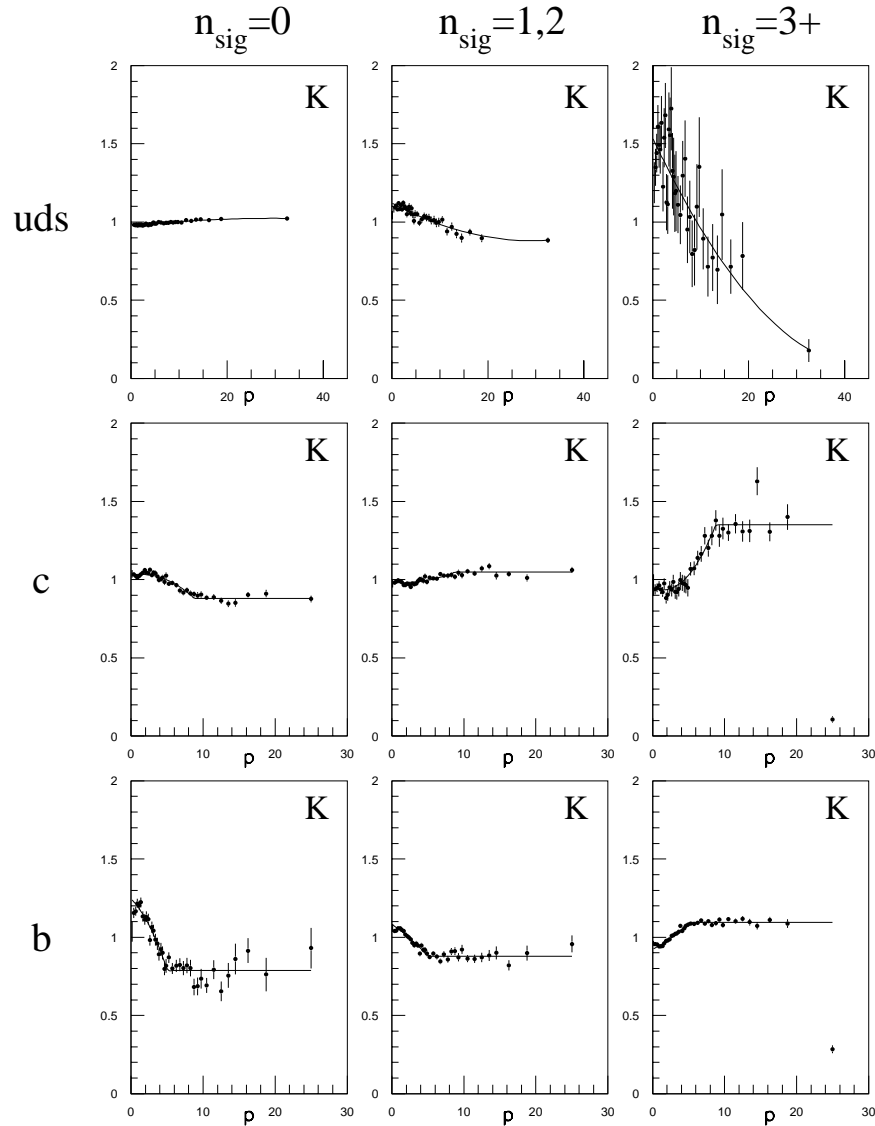
Figure 9.22: The bias induced in the kaon momentum spectra as a result of the two-dimensional impact parameter tag for event flavor. The points are from the SLD-tuned JETSET 7.4 simulation, and the curves are parametrizations of the Monte Carlo points. A relative uncertainty of 20% of deviation from unity is assigned as a conservative upper bound, following the analysis of [172].
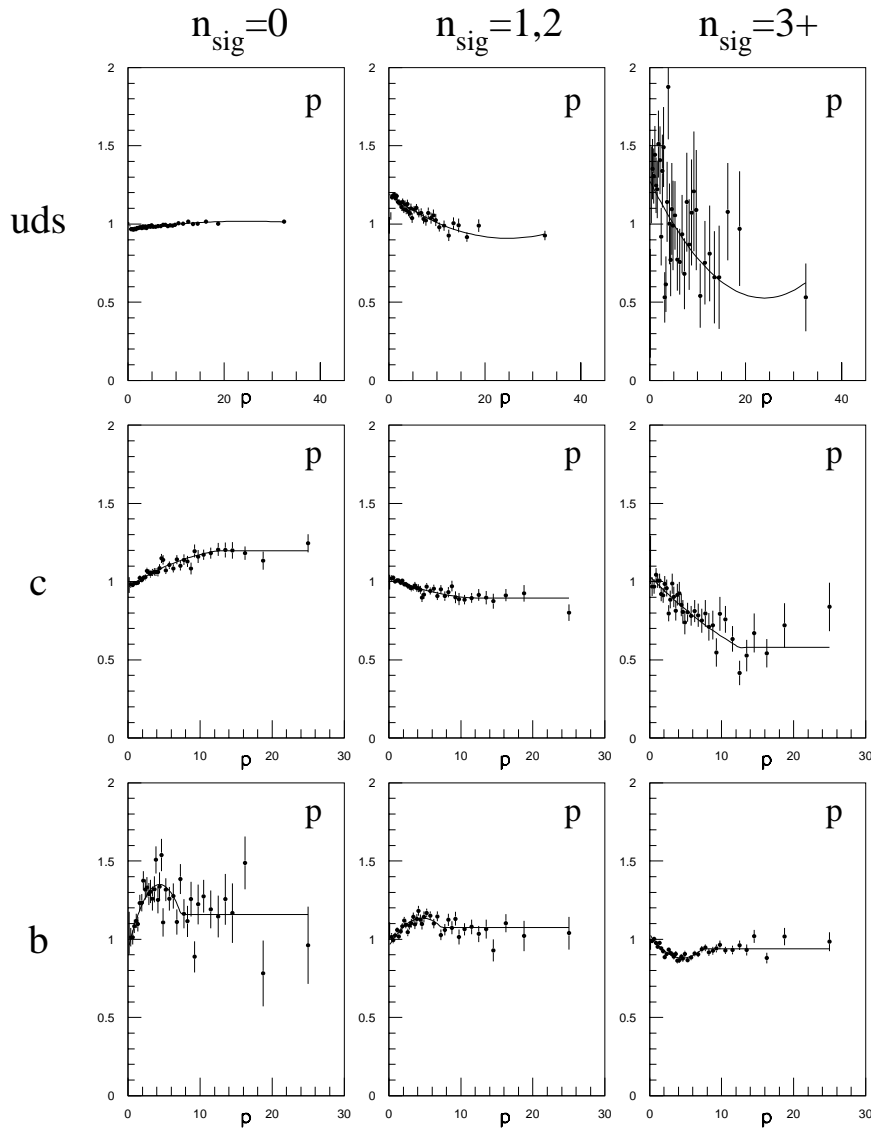
Figure 9.23: The bias induced in the proton momentum spectra as a result of the two-dimensional impact parameter tag for event flavor. The points are from the SLD-tuned JETSET 7.4 simulation, and the curves are parametrizations of the Monte Carlo points. A relative uncertainty of 20% of deviation from unity is assigned as a conservative upper bound, following the analysis of [172].

We use the SLD-tuned Monte Carlo to obtain the 3×3 bias matrices b_{ij} as functions of momentum. These are shown in Figs. 9.21, 9.22, and 9.23. The diagonal terms for the bias elements are reasonably close to 1, with the bias generally under 10% in all important terms. The elements that show the most variation from unit value are the terms that have the lowest contributing populations (*i.e.*, the product $E_{ij}b_{ij}$ is small). Simple parameterizations of the shapes were performed with the constraint that $\sum_i E_{ij}b_{ij}(x_p) = 1$. These parameterizations are used for the unfolding, rather than the individual points, so as to reduce fluctuations due to finite Monte Carlo statistics. We vary the parametrizations by 20% of their difference from unity in order to estimate the uncertainty in our unfolding due to these bias terms.

By inverting Eq. (9.8), we can derive the $\bar{n}_j^h$ from the n_i^h measured in our three flavor-tagged samples. What we are primarily interested in are the $\bar{n}_{uds}^h$, which are shown in Fig. 9.24. These spectra show the same features as those in Fig. 9.20; however, they are now free from the effects of heavy quark decays and the hard heavy quark fragmentation functions. This measurement of hadronic spectra in light-quark fragmentation is unique in e^+e^- annihilation and should be very useful to test or to tune fragmentation models, such as those discussed in section 2.4.2.

Another result we can extract from the flavor unfolding is the ratio of particle production in b and uds events. This is shown in Fig. 9.25. Although there is much structure apparent in these ratios, the physics behind it is that of B meson decays, along with the fragmentation function of the b-quark, and not really the physics of hadronization in QCD.

These features can be understood from the hard b fragmentation and the high decay multiplicity of B-meson (and other b hadrons). Splitting the momentum of the B among several particles tends to depopulate the region at high x_p, compared to light-quark jets. Since the overall multiplicity is higher in b jets, this must then lead to a relative increase of particles at the lower momenta. Figure 9.25 shows that this increase occurs for $x_p \lesssim 0.1$ in the pions and for $0.02 \lesssim x_p \lesssim 0.2$ in the kaons, but does not occur for the protons. This
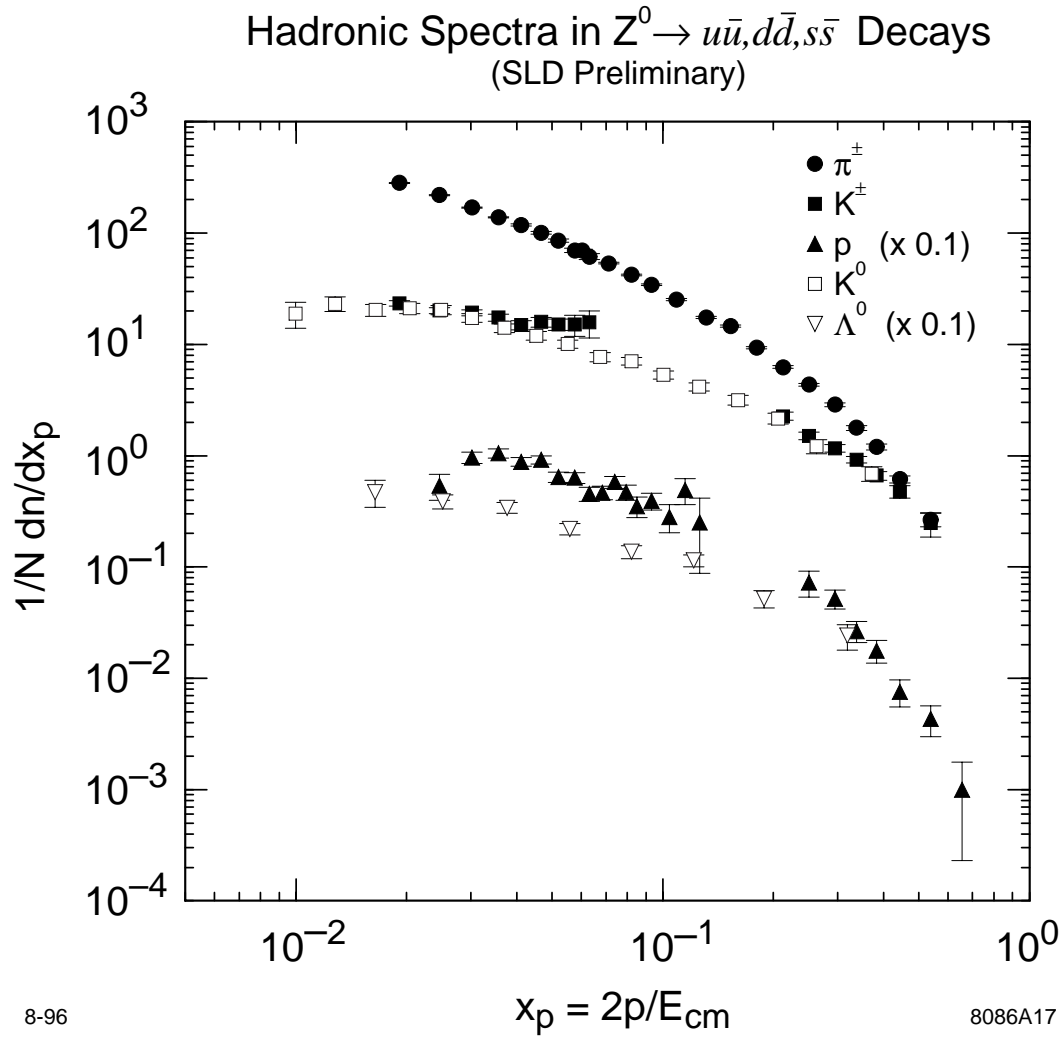
Figure 9.24: Normalized particle production rates $F^h(x_p)$ for various hadron species in $e^+e^- \to u\bar{u}, d\bar{d}, s\bar{s}$ events are shown as a function of scaled momentum $x_p = 2p/\sqrt{s}$.
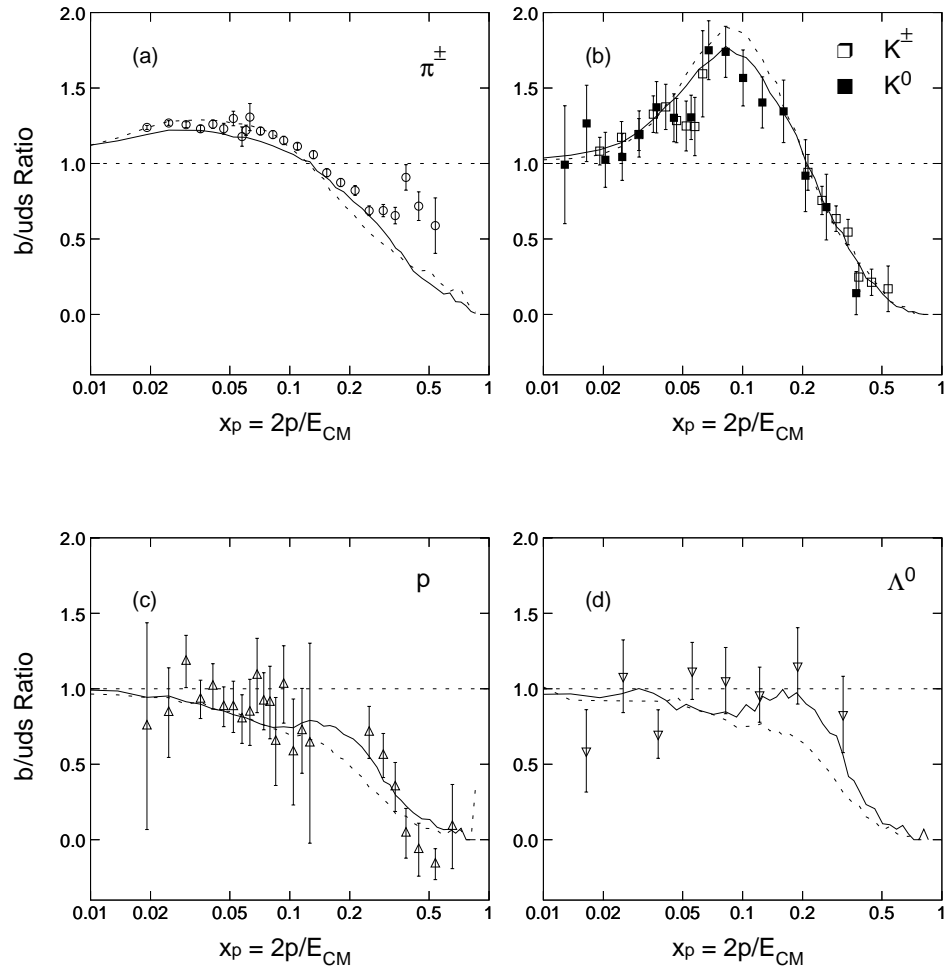
Figure 9.25: The Ratio of particle production rates between *b* and *uds* events are shown as the points. Also shown are the predictions of the JETSET 7.4 model, both with default parameters (dashed curve) and with the SLD-tuned parameters (solid curve).

is contrary to the DELPHI result of [177], which shows an increase of proton multiplicity in $b\bar{b}$ events. These features are well-reproduced by the SLD-tuned JETSET 7.4 simulation, indicating that the data are consistent with current understanding of b hadron decays.

9.5   Leading Particle Effect

As discussed in Chapter 1, the incident electron polarization and the electroweak asymmetries of the quarks allow us to measure the differences in hadron production between quark and antiquark jets. Because we expect most of the hadronization process to produce hadrons and their antiparticles with equal probability, we attribute any differences between quark and antiquark jets to the hadronization of the primary quark (or antiquark). Our prejudice is that such hadrons produced from the primary quark might be found at high momentum fraction x_p, but this is something to be tested experimentally.

9.5.1   Tagging Procedure

The forward-backward asymmetry (Eq. (2.17)) implies that the distribution of q jets in $\cos\theta$ for left- and right-handed electron beams looks like that in Fig. 9.26. The quark jet prefers to follow the electron (positron) direction for left- (right-)handed incident electrons.

    We can make use of this asymmetry to separate quark and antiquark jets. We start with our light-quark (uds) sample, so as to remove the heavy hadron decays from our analysis. We approximate the quark direction with the thrust axis of the event, and separate the event into two hemispheres using the plane perpendicular to the thrust axis. Let $|\theta_{th}|$ be the polar angle of the thrust axis with the electron direction.* Because the quark asymmetry vanishes in the central region of the detector, we require $|\cos\theta_{th}| > 0.2$ so as to improve

---

*we do not sign the thrust axis in this analysis, so the sign of θ_{th} is undetermined
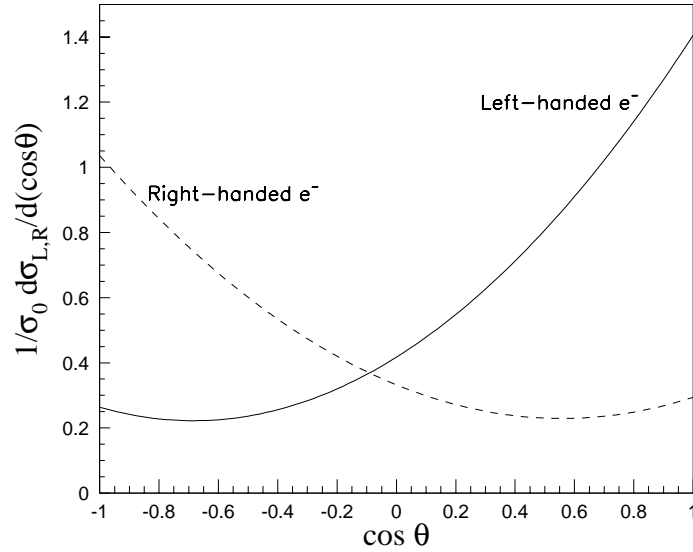
Figure 9.26: The Standard Model prediction for the asymmetry in polar angle with respect to the electron direction $\cos\theta$ for left-handed (solid) and right-handed (dashed) electron beams in the process $e^+e^- \rightarrow Z^0 \rightarrow q\bar{q}$. An electron polarization of 73% is assumed, and we average over the three possible light-quark flavors, using their Standard Model branching ratios.

our analyzing power (see [172] for an analysis of this cut value). Each hemisphere is associated with either the quark or antiquark direction. For each event, we have the sign of electron polarization recorded. If the polarization is left-handed (negative), we assign the hemisphere in the forward (negative-z) direction* as the "quark hemisphere," and if the polarization is right-handed (positive), we assign the hemisphere in the backward (positive-z) direction as the "quark hemisphere." In both cases, the opposite hemisphere is assigned as the "antiquark hemisphere." This tag has a purity of $\sim 73\%$, if one assumes the Standard Model quark couplings and quark flavor production rates, and uses the luminosity-weighted average polarizations of $72.8 \pm 0.5\%$ for the 1993 and 1994–95 datasets [172].

---

*The SLD-z axis is defined along the incident positron direction.

9.5.2 Results

Given the tag of quark and antiquark hemispheres, it is now straightforward to repeat the particle fractions analysis on those two samples and extract separately the production rates of π^-, K^-, and p in quark and antiquark hemispheres. Because the identification efficiency is the same for positive and negative tracks in the CRID, the systematic uncertainty associated with the correct knowledge of the efficiencies cancels when we compare particles and antiparticles. To increase statistics, we assume CP invariance and include the charge-conjugate particles with the opposite quark/antiquark sample. We can also perform the same quark/antiquark separation on the sample of Λ^0 and $\bar{\Lambda}^0$ measured at SLD [172]. This gives a second baryon species with which to check our results.

The tagged hemispheres still contain some residual heavy-quark jets which could induce production differences between the samples. Therefore, we correct for the heavy-quark contamination by subtracting the signal expected from Monte Carlo. This correction is rather small, however, due to the high purity of our *uds* tag (85%). We then unfold for the 73% purity of the quark/antiquark hemisphere tag.

We present the comparison of quark/antiquark production rates of particle species h in terms of the normalized difference $D_h(x) = (F_q^h(x) - F_{\bar{q}}^h(x))/(F_q^h(x) + F_{\bar{q}}^h(x))$ of the quark and antiquark production rates. This variable has value 0 if the production is the same in quark and antiquark jets, and it goes to 1 if there is no production of h in antiquark jets at momentum fraction x.

The normalized differences for production of π^-, K^-, p, and Λ^0 are shown in Fig. 9.27. One can see a clear signal for differences of fragmentation in quark and antiquark jets. The normalized difference in the baryons is zero at low momentum, but approaches 1 at high x. Because baryons may contain primary quarks but not primary antiquarks, this excess of baryons in quark jets is direct evidence for the leading particle effect in e^+e^- jets (*i.e.*, that faster particles are more likely to contain the primary quark of the jet).
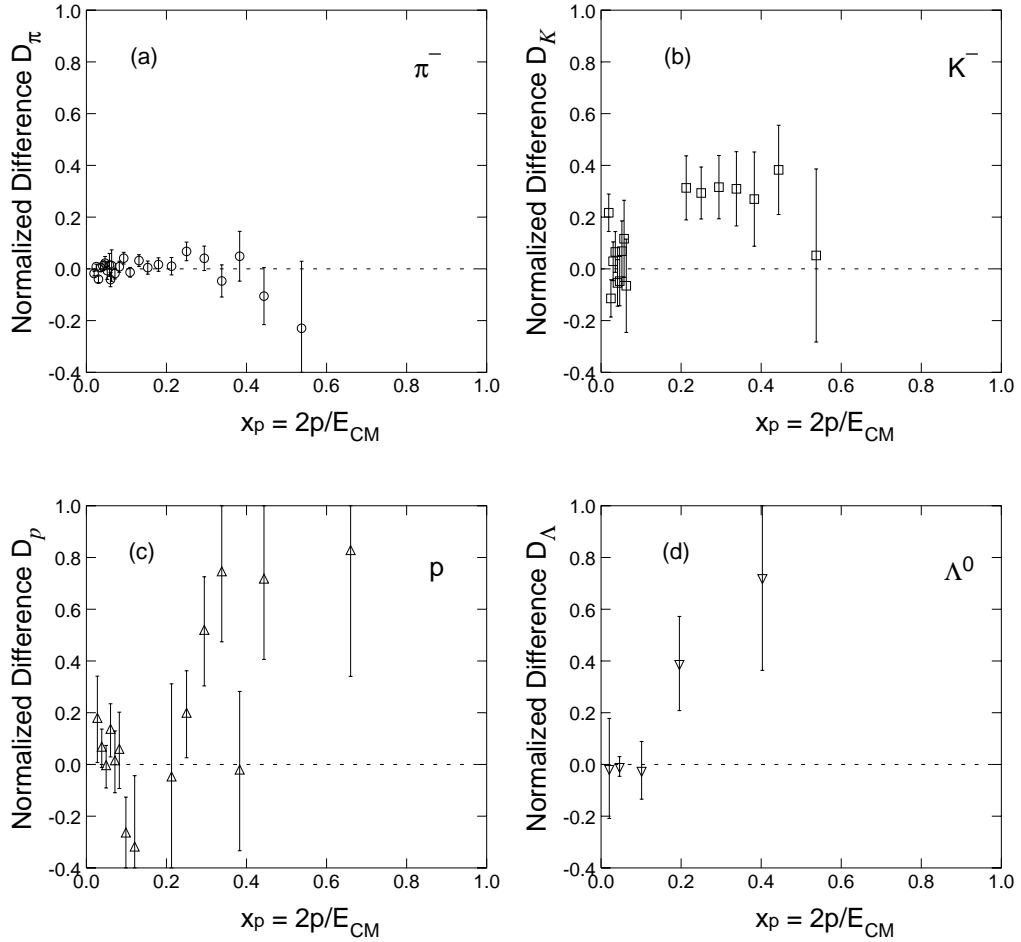
Figure 9.27: The normalized difference $D_h(x) = (F_q^h(x) - F_{\bar{q}}^h(x))/(F_q^h(x) + F_{\bar{q}}^h(x))$ in production rates between quark and anti-quark jets are shown for $h = \pi^-$ (a), K^- (b), p (c), and Λ^0 (d). Evidence for differences in quark and antiquark fragmentation is clear. This difference is interpreted as evidence for the leading particle effect in e^+e^- annihilation.

The kaons have similar features, but the normalized difference is only as high as 0.3 or so. This is consistent with the leading particle effect and the additional assumption that creation of $s\bar{s}$ quarks from the vacuum is suppressed relative to the creation of $u\bar{u}$. If the production of K^- were equal in s and $\bar{u}$ jets, one would expect a signal of 0.13 from the difference in Z^0 couplings to the u and s quarks. In the pions, we would also expect a signal of at most 0.13. Our data show no deviation from zero in the pions, within our precision, indicating that pions are not predominantly leading at $x_p < 0.4$. We also interpret this as a reassuring cross-check that we are not somehow imposing a bias from the analysis procedure.

Chapter 10

Summary

In order to probe the hadronization process, we measure the spectra of $\pi^\pm$, $K^\pm$, and $p/\bar{p}$ in e^+e^- annihilation at the Z^0 resonance. We accomplish this by making use of the SLD CRID, one of a first generation of devices that have been developed over the past 20 years for efficient particle identification over a wide momentum range.

As with many first-generation devices, a great deal of work has been required to achieve successful particle identification results. This includes many years of design, prototyping, and engineering effort, but it also includes a large effort in calibration, tuning, and understanding the identification performance characteristics. The result of such labor is that the SLD CRID now achieves excellent particle identification performance.

As described in Chapter 7, the local point resolutions within the CRID TPCs have achieved their design values. The global resolutions on Cherenkov angle are slightly degraded from design, but this has a relatively small effect on identification efficiency. The degradation is believed to be due to remaining misalignments of the CRID components (TPCs, mirrors, and liquid radiator trays), and work is still progressing to resolve such misalignments. The number of Cherenkov photons observed per ring (N_0) is also slightly degraded from the original design due to constraints of operating parameters (*e.g.* mixture

of C_5F_{12}/N_2), but has otherwise been quite good. This is a testament to the efficacy of the CRID gas and liquid systems at maintaining purity and good UV transmission. A simulation has been developed that models the known features and problems of the CRID, and this simulation reproduces the overall identification performance of the CRID to within a few percent.

The successful operation of the SLD CRID for particle identification allows us to extract the inclusive hadronic fractions in Z^0 decays. These results are shown in Fig. 9.19, and are in good agreement with other measurements at the Z^0 [173, 174, 175]. They represent a complementary technique to that of [173, 174], and also fill in gaps in the coverage of those measurements. Our measurement is similar to the ring-imaging measurement of [175] but covers a larger momentum range. Along with the measurements of [173, 174], our data indicate a drop in proton production at high scaled momentum x_p which is qualitatively different from the behavior of $K^{\pm}$ production there.

In order to probe the hadronization process further, we repeat the measurement of hadronic spectra for samples of events tagged with different initial quark flavor. We separate $Z^0 \rightarrow b\bar{b}$ and $Z^0 \rightarrow c\bar{c}$ events from the remaining light-quark events ($Z^0 \rightarrow u\bar{u}$, $d\bar{d}$, $s\bar{s}$) in order to remove the effects of the harder heavy-quark fragmentation and of the decays of b and c hadrons. This process results in the spectra shown in Fig. 9.24, which represent the first measurement of particle production in light-quark jets at the Z^0. We also measure the difference in particle spectra in b and uds jets directly (Fig. 9.25). We find these results to be well reproduced by the SLD-tuned JETSET Monte Carlo, indicating that our results are consistent with conventional understanding of heavy-flavor physics.

Finally, we add the information from incident electron polarization and employ the quark forward-backward asymmetries to separate light-quark jets from light-antiquark jets. This lets us study the difference in production between particles in quark jets and antiquark jets. We would expect the production of hadrons and their antiparticles to be equally likely in the fragmentation process *except* for hadrons associated with the initial quark of the jet.

We observe a significant excess in the production of fast p and Λ^0 in quark jets as compared to antiquark jets. Baryons are an unambiguous probe, since a primary quark may form a baryon but not an antibaryon. The signal we observe is peaked towards high momentum fraction x_p, suggesting a leading particle effect in e^+e^- jets, like the effect seen in hadron-hadron collisions where production of the same particle type as the incident particle is enhanced at large x_p [8]. Here, it suggests that particles containing the primary quark are more likely to populate the high-x_p region than are other hadrons. Such an effect is not unexpected, and is a feature of many fragmentation models (although cluster-fragmentation models, for example, generally have difficulty describing leading particles). this measurement, together with the observation by ALEPH of nonzero Λ^0 polarization [178], represent the first clear and quantitative demonstrations of the leading particle effect in e^+e^- jets. Furthermore, our quantitative measurement is potentially useful to other experiments that wish to use high-x_p particles as a tag for primary quark flavor.

As with most measurements in science, this one raises many more questions for further study than it answers. There are a number of ways to improve on the basic measurements presented here. The most straightforward is increased running. Future runs of the SLC and SLD are expected to triple the current statistics. This would be very helpful for improving the measured points at high momentum. It would also improve our systematic uncertainties across the whole range, since they are currently dominated by the statistical precision of our calibration samples of K_s^0, Λ^0, and τ decays.

There is still room for improved CRID performance, presumably in removing the remaining misalignments of components, and also in understanding the characteristics of background hits seen in the data (see section 7.16). Such improvements in performance would not only extend our momentum coverage somewhat, but would likely improve our understanding of identification efficiencies considerably.

There are also extensions to the basic analysis that could be made with the current dataset. One such area is to measure correlations among particle

species, either in baryon number or in strangeness. This is an area where efficient particle identification is tremendously helpful, as the measurement of correlations depends on the square of the identification efficiency. Correlations between baryons or strange particles at short range probe the locality of baryon number or strangeness conservation in the hadronization process. Correlations at long range probe the fragmentation of leading quarks and production of leading particles.

One of the difficulties with the measurement of hadronic particle spectra as a probe of the hadronization process is that the majority of measured particles come from the decays of other, short-lived resonances and not directly from the fragmentation process. For those particles, we expect the mass of the primary resonance to be the mass scale involved in the dynamics of hadronization, rather than the mass of the pion, kaon, or proton. The only solution to this would be a program of measuring the spectra of all accessible meson and baryon resonances and then subtracting the feed-down components in order to get a coherent picture of the production of particles at the hadronization stage (before decays of resonances). The highly efficient particle identification of the CRID is also necessary for this effort. Such a program, of course, is a large undertaking. However, the measurement of the stable hadrons is a solid first step in that program.

Appendix A

The SLD Collaboration

K. Abe,[29] I. Abt,[14] C.J. Ahn,[26] T. Akagi,[27] N.J. Allen,[4] W.W. Ash,[27]†
D. Aston,[27] K.G. Baird,[24] C. Baltay,[33] H.R. Band,[32] M.B. Barakat,[33]
G. Baranko,[10] O. Bardon,[16] T. Barklow,[27] A.O. Bazarko,[11]
R. Ben-David,[33] A.C. Benvenuti,[2] G.M. Bilei,[22] D. Bisello,[21]
G. Blaylock,[7] J.R. Bogart,[27] T. Bolton,[11] G.R. Bower,[27] J.E. Brau,[20]
M. Breidenbach,[27] W.M. Bugg,[28] D. Burke,[27] T.H. Burnett,[31]
P.N. Burrows,[16] W. Busza,[16] A. Calcaterra,[13] D.O. Caldwell,[6]
D. Calloway,[27] B. Camanzi,[12] M. Carpinelli,[23] R. Cassell,[27]
R. Castaldi,[23](a) A. Castro,[21] M. Cavalli-Sforza,[7] A. Chou,[27] E. Church,[31]
H.O. Cohn,[28] J.A. Coller,[3] V. Cook,[31] R. Cotton,[4] R.F. Cowan,[16]
D.G. Coyne,[7] G. Crawford,[27] A. D'Oliveira,[8] C.J.S. Damerell,[25]
M. Daoudi,[27] R. De Sangro,[13] P. De Simone,[13] R. Dell'Orso,[23] M. Dima,[9]
P.Y.C. Du,[28] R. Dubois,[27] B.I. Eisenstein,[14] R. Elia,[27] E. Etzion,[4]
D. Falciai,[22] C. Fan,[10] M.J. Fero,[16] R. Frey,[20] K. Furuno,[20] T. Gillman,[25]
G. Gladding,[14] S. Gonzalez,[16] G.D. Hallewell,[27] E.L. Hart,[28] A. Hasan,[4]
Y. Hasegawa,[29] K. Hasuko,[29] S. Hedges,[3] S.S. Hertzbach,[17]
M.D. Hildreth,[27] J. Huber,[20] M.E. Huffer,[27] E.W. Hughes,[27] H. Hwang,[20]
Y. Iwasaki,[29] D.J. Jackson,[25] P. Jacques,[24] J. Jaros,[27] A.S. Johnson,[3]
J.R. Johnson,[32] R.A. Johnson,[8] T. Junk,[27] R. Kajikawa,[19] M. Kalelkar,[24]
H. J. Kang,[26] I. Karliner,[14] H. Kawahara,[27] H.W. Kendall,[16] Y. Kim,[26]

233

M.E. King,[27] R. King,[27] R.R. Kofler,[17] N.M. Krishna,[10] R.S. Kroeger,[18]
J.F. Labs,[27] M. Langston,[20] A. Lath,[16] J.A. Lauber,[10] D.W.G.S. Leith,[27]
M.X. Liu,[33] X. Liu,[7] M. Loreti,[21] A. Lu,[6] H.L. Lynch,[27] J. Ma,[31]
G. Mancinelli,[22] S. Manly,[33] G. Mantovani,[22] T.W. Markiewicz,[27]
T. Maruyama,[27] R. Massetti,[22] H. Masuda,[27] E. Mazzucato,[12]
A.K. McKemey,[4] B.T. Meadows,[8] R. Messner,[27] P.M. Mockett,[31]
K.C. Moffeit,[27] B. Mours,[27] D. Muller,[27] T. Nagamine,[27] S. Narita,[29]
U. Nauenberg,[10] H. Neal,[27] M. Nussbaum,[8] Y. Ohnishi,[19]
L.S. Osborne,[16] R.S. Panvini,[30] H. Park,[20] T.J. Pavel,[27] I. Peruzzi,[13](b)
M. Piccolo,[13] L. Piemontese,[12] E. Pieroni,[23] K.T. Pitts,[20] R.J. Plano,[24]
R. Prepost,[32] C.Y. Prescott,[27] G.D. Punkar,[27] J. Quigley,[16]
B.N. Ratcliff,[27] T.W. Reeves,[30] J. Reidy,[18] P.E. Rensing,[27]
L.S. Rochester,[27] P.C. Rowson,[11] J.J. Russell,[27] O.H. Saxton,[27]
S.F. Schaffner,[27] T. Schalk,[7] R.H. Schindler,[27] B.A. Schumm,[15]
A. Seiden,[7] S. Sen,[33] V.V. Serbo,[32] M.H. Shaevitz,[11] J.T. Shank,[3]
G. Shapiro,[15] S.L. Shapiro,[27] D.J. Sherden,[27] K.D. Shmakov,[28]
C. Simopoulos,[27] N.B. Sinev,[20] S.R. Smith,[27] J.A. Snyder,[33] P. Stamer,[24]
H. Steiner,[15] R. Steiner,[1] M.G. Strauss,[17] D. Su,[27] F. Suekane,[29]
A. Sugiyama,[19] S. Suzuki,[19] M. Swartz,[27] A. Szumilo,[31] T. Takahashi,[27]
F.E. Taylor,[16] E. Torrence,[16] A.I. Trandafir,[17] J.D. Turk,[33] T. Usher,[27]
J. Va'vra,[27] C. Vannini,[23] E. Vella,[27] J.P. Venuti,[30] R. Verdier,[16]
P.G. Verdini,[23] S.R. Wagner,[27] A.P. Waite,[27] S.J. Watts,[4]
A.W. Weidemann,[28] E.R. Weiss,[31] J.S. Whitaker,[3] S.L. White,[28]
F.J. Wickens,[25] D.A. Williams,[7] D.C. Williams,[16] S.H. Williams,[27]
S. Willocq,[33] R.J. Wilson,[9] W.J. Wisniewski,[27] M. Woods,[27] G.B. Word,[24]
J. Wyss,[21] R.K. Yamamoto,[16] J.M. Yamartino,[16] X. Yang,[20] S.J. Yellin,[6]
C.C. Young,[27] H. Yuta,[29] G. Zapalac,[32] R.W. Zdarko,[27] C. Zeitlin,[20]
Z. Zhang,[16] and J. Zhou,[20]

235

$^{(1)}$*Adelphi University, Garden City, New York 11530*

$^{(2)}$*INFN Sezione di Bologna, I-40126 Bologna, Italy*

$^{(3)}$*Boston University, Boston, Massachusetts 02215*

$^{(4)}$*Brunel University, Uxbridge, Middlesex UB8 3PH, United Kingdom*

$^{(5)}$*California Institute of Technology, Pasadena, California 91125*

$^{(6)}$*University of California at Santa Barbara, Santa Barbara, California 93106*

$^{(7)}$*University of California at Santa Cruz, Santa Cruz, California 95064*

$^{(8)}$*University of Cincinnati, Cincinnati, Ohio 45221*

$^{(9)}$*Colorado State University, Fort Collins, Colorado 80523*

$^{(10)}$*University of Colorado, Boulder, Colorado 80309*

$^{(11)}$*Columbia University, New York, New York 10027*

$^{(12)}$*INFN Sezione di Ferrara and Università di Ferrara, I-44100 Ferrara, Italy*

$^{(13)}$*INFN Lab. Nazionali di Frascati, I-00044 Frascati, Italy*

$^{(14)}$*University of Illinois, Urbana, Illinois 61801*

$^{(15)}$*Lawrence Berkeley Laboratory, University of California, Berkeley, California 94720*

$^{(16)}$*Massachusetts Institute of Technology, Cambridge, Massachusetts 02139*

$^{(17)}$*University of Massachusetts, Amherst, Massachusetts 01003*

$^{(18)}$*University of Mississippi, University, Mississippi 38677*

$^{(19)}$*Nagoya University, Chikusa-ku, Nagoya 464 Japan*

$^{(20)}$*University of Oregon, Eugene, Oregon 97403*

$^{(21)}$*INFN Sezione di Padova and Università di Padova, I-35100 Padova, Italy*

$^{(22)}$*INFN Sezione di Perugia and Università di Perugia, I-06100 Perugia, Italy*

$^{(23)}$*INFN Sezione di Pisa and Università di Pisa, I-56100 Pisa, Italy*

$^{(24)}$*Rutgers University, Piscataway, New Jersey 08855*

$^{(25)}$*Rutherford Appleton Laboratory, Chilton, Didcot, Oxon OX11 0QX United Kingdom*

$^{(26)}$*Sogang University, Seoul, Korea*

$^{(27)}$*Stanford Linear Accelerator Center, Stanford University, Stanford, California 94309*

[28] *University of Tennessee, Knoxville, Tennessee 37996*

[29] *Tohoku University, Sendai 980 Japan*

[30] *Vanderbilt University, Nashville, Tennessee 37235*

[31] *University of Washington, Seattle, Washington 98195*

[32] *University of Wisconsin, Madison, Wisconsin 53706*

[33] *Yale University, New Haven, Connecticut 06511*

[†] *Deceased*

[a] *Also at the Università di Genova*

[b] *Also at the Università di Perugia*

Bibliography

[1] A. Komar, "Observables, Correspondence, and Quantized Gravity," p. 325 in *Magic Without Magic: John Archibald Wheeler*, ed. John P. Klauder, Freeman, San Francisco (1972).

[2] Particle Data Group, Phys. Rev. **D50** (1994) 1173.

[3] S. L. Glashow, Nucl. Phys. **22** (1961) 579.

[4] A. Salam and J. C. Ward, Phys. Lett. **13** (1964) 168.

[5] S. Weinberg, Phys. Rev. Lett. **19** (1967) 1264.

[6] D. J. Gross and F. Wilczek, Phys. Rev. Lett. **30** (1973) 1343.

[7] D. H. Politzer, Phys. Rev. Lett. **30** (1973) 1346.

[8] M. Basile *et al.*, Il Nuovo Cimento **A66** (1981) 129.

[9] M. Gell-Mann, Phys. Lett. **8** (1964) 214.

[10] G. Zweig, CERN-TH-8182 and CERN-TH-8419 (1964).

[11] M. Y. Han and Y. Nambu, Phys. Rev. **139** (1965) 1806.

[12] M. Breidenbach *et al.*, Phys. Rev. Lett. **23**, (1969) 935; also summarized in J. I. Friedman and H. W. Kendall, Ann. Rev. Nucl. Sci. **22** (1972) 203.

[13] J. D. Bjorken, Phys. Rev. **179** (1969) 1547.

[14] R. P. Feynman, *Photon-Hadron Interactions*, Benjamin, New York (1972).

[15] C. N. Yang and R. L. Mills, Phys. Rev. **96** (1954) 191.

[16] G. 't Hooft, Nucl. Phys. **B254** (1985) 11.

[17] G. 't Hooft, Nucl. Phys. **B33** (1971) 173; **B35** (1971) 167.

[18] A. Zee, Phys. Rev. **D7** (1973) 3630.

[19] S. Coleman and D. J. Gross, Phys. Rev. Lett. **31** (1973) 851.

[20] G. Hanson *et al.*, Phys. Rev. Lett. **35** (1975) 1609.

[21] R. Brandelik *et al.* (TASSO Collab.), Phys. Lett. **B86** (1979) 243;
D. P. Barber *et al.* (MARK J Collab.), Phys. Rev. Lett. **43** (1979) 830;
Ch. Berger *et al.* (PLUTO Collab.), Phys. Lett. **B86** (1979) 418;
W. Bartel *et al.* (JADE Collab.), Phys. Lett. **B91** (1980) 142.

[22] M. Creutz, *Quarks, Gluons and Lattices*, Cambridge Univ. Press (1983);
see also, A. S. Kronfeld and P. B. Mackenzie, Ann. Rev. Nucl. Part. Sci. **43** (1993) 793.

[23] G. 't Hooft and M. Veltman, Nucl. Phys. **B44** (1972) 189;
G. 't Hooft, Nucl. Phys. **B61** (1973) 455.

[24] W. A. Bardeen *et al.*, Phys. Rev. **D18** (1978) 3998.

[25] W. Celmaster and R. J. Gonsalves, Phys. Rev. **D20** (1979) 1420.

[26] S. J. Brodsky, G. P. Lepage, and P. B. Mackenzie, Phys. Rev. **D28** (1983) 228.

[27] P. M. Stevenson, Phys. Rev. **D23** (1981) 2916.

[28] G. Grunberg, Phys. Rev. **D29** (1984) 2822.

[29] D. W. Duke and R. G. Roberts, Phys. Rep. **120** (1985) 275.

[30] E. C. G. Stückelberg and A. Peterman, Helv. Phys. Acta **26** (1953) 999;
M. Gell-Mann and F. E. Low, Phys. Rev. **95** (1954) 1300;
K. Symanzik, Commun. Math. Phys. **18** (1970) 227.

[31] S. G. Gorishny, A. L. Kataev, and S. A. Larin, Phys. Lett. **B259**
(1991) 144;
L. R. Surgalach and M. A. Samuel, Phys. Rev. Lett. **66** (1991) 560;
erratum, **66** (1991) 2461.

[32] J. Ellis, M. K. Gaillard, and G. G. Ross, Nucl. Phys. **B111** (1976) 253;
erratum **B130** (1977) 516.

[33] A. Ali *et al.*, Nucl. Phys. **B167** (1980) 454;
K. J. F. Gaemers, J. A. M. Vermaseren, Z. Phys. **C7** (1981) 421;
R. K. Ellis, D. A. Ross, and A. E. Terrano, Nucl. Phys. **B178** (1981) 421;
D. Danckaert *et al.*, Phys. Lett. **B114** (1982) 203.

[34] K. Fabricius, G. Kramer, G. Schierholz, and I. Schmitt, Phys. Lett. **B97**
(1980) 431; Z. Phys. **C11** (1982) 315.

[35] F. Gutbrod, G. Kramer, and G. Schierholz, Z. Phys. **C21** (1984) 235.

[36] R. K. Ellis, D. A. Ross, and A. E. Terrano, Nucl. Phys. **B178** (1981) 421.

[37] G. Kramer and B. Lampe, Z. Phys. **C39** (1988) 101;
Fortschr. Phys. 37 (1989) 161.

[38] V. N. Gribov and L. N. Lipatov, Yad. Fiz. **15** (1972) 781, 1218 [Sov. J.
Nucl. Phys. **15** (1972) 438, 675].

[39] Yu. L. Dokshitzer, Zh. Eksp. Teor. Fiz. **73** (1977) 1216 [Sov. Phys. JETP,
46 (1977) 641].

[40] G. Altarelli and G. Parisi, Nucl. Phys. **B126** (1977) 298.

[41] K. Kato and T. Munehisa, Mod. Phys. Lett. **A1** (1986) 345;
K. Kato and T. Munehisa, Phys. Lett. **B214** (1988) 286.

[42] Yu. L. Dokshitzer, V. A. Khoze, A. H. Mueller, and S. I. Troyan, *Basics of Perturbative QCD*, Editions Frontières, Gif-sur-Yvette Cedex, France (1991).

[43] Yu. L. Dokshitzer, D. I. Dyakonov, and S. I. Troyan, Phys. Rep. **58C** (1980) 269;
A. Bassetto, M. Ciafaloni, and G. Marchesini, Phys. Rep. **100C** (1983) 201.

[44] C. P. Fong and B. R. Webber, Phys. Lett. **B229** (1989) 289.

[45] P. F. Smith, Ann. Rev. Nucl. Part. Sci., **39** (1989) 73;
L. Lyons, Phys. Rep. **129** (1985) 225.

[46] P. Nason and B. R. Webber, CERN-TH.7018/93 (1993).

[47] D. Buskulic *et al.* (ALEPH collab.), Phys. Lett. **B357** (1995) 699.

[48] T. Sjöstrand *et al.*, "Z Physics at LEP 1," CERN Yellow Book 89-08, vol. 3, p. 143.

[49] R. D. Field and R. P. Feynman, Nucl. Phys. **B136** (1978) 1.

[50] T. Meyer, Z. Phys. **C12** (1982) 77.

[51] P. D. Acton *et al.* (OPAL collab.), Z. Phys. **C56** (1992) 521.

[52] B. Andersson, G. Gustafson, and T. Sjöstrand, Physica Scripta **32** (1985) 574.

[53] P. Mazzanti and R. Odorico, Phys. Lett. **B95** (1980) 133;
Z. Phys. **C7** (1980) 61.

[54] X. Artru and G. Mennessier, Nucl. Phys. **B70** (1974) 93;
X. Artru, Phys. Rep. **97** (1983) 147.

[55] B. Andersson, G. Gustafson, and T. Sjöstrand, Z. Phys. **C6** (1980) 235.

[56] T. Sjöstrand, Comput. Phys. Commun. **39** (1986) 347.

[57] M. Begtsson and T. Sjöstrand, Nucl. Phys. **B289** (1987) 810.

[58] D. Buskulic *et al.* (ALEPH collab.), Z. Phys. **C55** (1992) 209;
B. Adeva *et al.* (L3 collab.), Z. Phys. **C55** (1992) 39;
R. Akers *et al.* (OPAL collab.), Z. Phys. **C63** (1994) 181.

[59] W. Bartel *et al.* (JADE collab.), Phys. Lett. **B101** (1981) 129;
H. Aihara *et al.* (TPC collab.), Z. Phys. **C28** (1985) 31;
M. Althoff *et al.* (TASSO collab.), Z. Phys. **C29** (1985) 29.

[60] M. Z. Akrawy *et al.* (OPAL collab.), Phys. Lett. **B261** (1991) 334.

[61] A. H. Mueller, Phys. Lett. **B104** (1981) 161;
B. I. Ermolaev and V. S. Fadin, Pisma Zh. Eksp. Teor. Fiz. **33** (1981) 285
[Soviet JETP Lett. **33** (1981) 269];
L. A. Gribov, E. M. Levin, and M. G. Ryskin, Phys. Rep. **100** (1983) 1;
A. Bassetto, M. Ciafaloni, and G. Marchesini, Phys. Rep. **100** (1983) 201.

[62] C. D. Buchanan and S. B. Chun, Phys. Rev. Lett. **59** (1987) 1997.

[63] C. D. Buchanan and S. B. Chun, UCLA-HEP-95-02 (1995).

[64] G. Gustafson, Nucl. Phys. **B175** (1986) 453;
G. Gustafson and U. Pettersson, Nucl. Phys. **B306** (1988) 746.

[65] L. Lonnblad, Comput. Phys. Commun. **71** (1992) 15.

[66] G. C. Fox and S. Wolfram, Nucl. Phys. **B168** (1980) 285.

[67] G. Marchesini *et al.*, Comput. Phys. Commun. **67** (1992) 465.

[68] T. D. Gottschalk, Nucl. Phys. **B214** (1983) 201.

[69] B. R. Webber, HERWIG 5.7 release notes.

[70] Ya. I. Azimov, Yu. L. Dokshitzer, V. A. Khoze, and S. I. Troyan, Z. Phys. **C27** (1985) 65.

[71] N. C. Brümmer, Z. Phys. **C66** (1995) 367.

[72] Ya. I. Azimov, Yu. L. Dokshitzer, V. A. Khoze, and S. I. Troyan, Z. Phys. **C31** (1986) 213.

[73] Yu. L. Dokshitzer, V. A. Khoze, and S. I. Troyan, J. Phys. **G17** (1991) 1602.

[74] Yu. L. Dokshitzer, V. A. Khoze, and S. I. Troyan, Z. Phys. **C55** (1992) 107.

[75] SLC Design Report, SLAC-R-229 (1980).

[76] SLD Design Report, SLAC-R-273, UC-43D (1984), and revisions.

[77] K. Abe *et al.* (SLD collab.), Phys. Rev. Lett. **70** (1993) 2515.

[78] K. Abe *et al.* (SLD collab.), Phys. Rev. Lett. **73** (1994) 25.

[79] M. Swartz, 1994 preliminary A_{LR} result, `http://www-sld.slac.stanford.edu/sldwww/physics/alr/` `1995_preliminary.html`.

[80] J. Kent *et al.*, SLAC-PUB-4922 (1989).

[81] M. D. Hildreth, Ph. D. dissertation, Stanford University, Stanford, CA (1995); also SLAC-R-95-458.

[82] D. L. Burke *et al.*, "First Results from the Final Focus Test Beam," in *Proceedings of the 1994 European Particle Accelerator Conference (EPAC 94)*, London (1994); also SLAC-PUB-6609.

[83] S. Hedges *et al.*, SLAC-PUB-95-6950, contributed to the 1995 International Europhysics Conference on High Energy Physics, Brussels, Belgium, Jul. 28–Aug. 2, 1995.

[84] R. Cotton, Ph. D. dissertation, Brunel University, Uxbridge, Middlesex, UK (1993).

[85] K. Abe *et al.* (SLD collab.), Phys. Rev. **D53** (1996) 1023.

[86] S. C. Berridge *et al.*, IEEE Trans. Nucl. Sci. **NS-39** (1992) 1242 .

[87] K. T. Pitts, Ph. D. dissertation, University of Oregon, Eugene, OR (1994); also SLAC-R-446.

[88] Leon Rochester and Bill Atwood, private communication.

[89] H. Neil, Ph. D. dissertation, Stanford University, Stanford, CA (1995); also SLAC-R-473.

[90] J. P. Venuti and G. B. Chadwick, IEEE Trans. Nucl. Sci. **NS-36** (1989) 595.

[91] D. C. Williams, Ph. D. dissertation, Massachusetts Institute of Technology, Cambridge, MA (1994); also SLAC-R-445.

[92] M. D. Hildreth *et al.*, IEEE Trans. Nucl. Sci. **NS-42** (1995) 451; M. J. Fero *et al.*, Nucl. Instrum. Methods **A367** (1995) 111.

[93] D. Axen *et al.*, Nucl. Instrum. Methods **A328** (1993) 472.

[94] S. Gonzalez, Ph. D. dissertation, Massachusetts Institute of Technology, Cambridge, MA (1994); also SLAC-R-439.

[95] A. C. Benvenuti *et al.*, Nucl. Instrum. Methods **A276** (1989) 94.

[96] E. Iarocci, Nucl. Instrum. Methods, **A217** (1983) 30.

[97] J. T. Walker *et al.*, IEEE Trans. Nucl. Sci. **NS-32** (1985) 616.

[98] A. Marchioro *et al.*, IEEE Trans.Nucl. Sci. **NS-34** (1987) 133.

[99] R. Brun *et al.*, *GEANT3*, CERN-DD/EE/84-1 (1987);
Cern Application Software Group, *GEANT 3.21 Program*, CERN
Program Library (1994).

[100] G. Grindhammer *et al.*, Nucl. Instrum. Methods **A290** (1990) 469.

[101] H. C. Fesefeldt, *Simulation of Hadronic Showers, Physics, and
Applications*, Technical Report PITHA 85-02, III Physikalisches
Institut, Aachen, Germany (1985).

[102] P. N. Burrows and H. Masuda, SLD Internal Physics Note 36, (1994).

[103] T. Ypsilantis and J. Séguinot, Nucl. Instrum. Methods **A343**, (1994) 30.

[104] J. Séguinot and T. Ypsilantis, Nucl. Instrum. Methods **A343** (1994) 1.

[105] B. M. Bolotowsky and Yu. N. Vavilov, Physics Today **48** (Dec. 1995) 11.

[106] V. P. Zrelov, *Cherenkov Radiation in High-Energy Physics*, Israel
Program for Scientific Translation, Jerusalem (1970).

[107] P. A. Cherenkov, Dok. Akad. Nauk SSSR **2** (1934) 451; **3** (1936) 413;
14 (1937) 101; **14** (1937) 105; **20** (1938) 651; **21** (1938) 116;
see also Phys. Rev. **52** (1937) 378 an early English summary.

[108] S. I. Vavilov, Dok. Akad. Nauk SSSR **2** (1934) 457.

[109] L. Mallet, C. R. Acad. Sci. **183** (1926) 274; **187** (1928) 222;
188 (1929) 445.

[110] I. E. Tamm and I. M. Frank, Dok. Akad. Nauk SSSR **14** (1937) 109.

[111] V. L. Ginzburg, Zh. Eksp. Teor. Fiz. **10** (1940) 589, 608.

[112] J. Litt and R. Meunier, Ann. Rev. Nucl. Sci. **23** (1973) 1.

[113] A. Roberts, Nucl. Instrum. Methods **9** (1960) 55.

[114] R. A. Holyroyd, J. M. Presses, C. L. Woody and R. A. Johnson, Nucl. Instrum. Methods **A261** (1987) 440.

[115] J. Séguinot and T. Ypsilantis, Nucl. Instrum. Methods **142** (1977) 377.

[116] G. Charpak, S. Majewski, G. Melchart, F. Sauli, and T. Ypsilantis, Nucl. Instrum. Methods **164** (1979) 419.

[117] D. F. Anderson, Nucl. Instrum. Methods **178** (1980) 125.

[118] E. Barrelet, T. Ekelof, B. Lund-Jensen, J. Séguinot, J. Tocqueville, M. Urban, and T. Ypsilantis, Nucl. Instrum. Methods **200** (1982) 219.

[119] R. J. Apsimon *et al.*, IEEE Trans. Nucl. Sci. **NS-33** (1986) 122.

[120] DELPHI 82-1/CERN-LEPC 82-8 and LEPC-16 (1982); see also DELPHI Technical Proposal, LEPC 83-3, pp. 83-86, and DELPHI Progress Report, LEPC 84-16.

[121] N. Fujiwara, N. Iido, and S. Naguchi, Nucl. Instrum. Methods **A263** (1988) 381.

[122] H. A. Bethe in *Handbuch der Physik*, 24/1, Springer, Berlin (1933) 491.

[123] M. Hauschild *et al.*, Nucl. Instrum. Methods **A314** (1992) 74.

[124] SLD Letter of Intent, SLC-LI-9 (1982).

[125] K. Abe *et al.*, IEEE Trans. Nucl. Sci. **NS-42** (1995) 518.

[126] A. Bean *et al.*, Nucl. Instrum. Methods **A300** (1991) 501.

[127] H. Kawahara and J. Va'vra, SLD CRID Internal Note 78 (1993).

[128] K. Abe *et al.*, p. 221 in *Novosibirsk Instrumentation Workshop*, World Scientific (1990).

[129] J. Vavra *et al.*, IEEE Trans. Nucl. Sci. **NS-35** (1988) 487.

[130] J. Va'vra, SLD CRID Internal Note 50 (1988).

[131] P. E. Rensing, Ph. D. dissertation, Stanford University, Stanford, CA (1993); also SLAC-R-421.

[132] Y. Iwasaki and F. Suekane, SLD CRID Internal Note 82 (1993).

[133] J. Va'vra *et al.*, Nucl. Instrum. Methods **A343** (1994) 74.

[134] H. D. Morgan and J. E. Mentall, J. Chem. Phys. **60** (1974) 4734.

[135] J. Va'vra, IEEE Trans. Nucl. Sci. **NS-34** (1987) 486.

[136] T. Bienz, Ph. D. dissertation, Stanford University, Stanford, CA (1990); also SLAC-R-369.

[137] P. Antilogus *et al.*, IEEE Trans. Nucl. Sci. **NS-38** (1991) 408.

[138] S. MacKenzie *et al.*, IEEE Trans. Nucl. Sci. **NS-34** (1987) 250.

[139] J. Va'vra, Nucl. Instrum. Methods **A371** (1996) 33.

[140] R. McCarthy *et al.*, Nucl. Instrum. Methods **A248** (1986) 69;
H. Glas *et al.*, IEEE Trans. Nucl. Sci., **NS-30**, (1983) 30.

[141] H.-W. Siebert *et al.*, Nucl. Instrum. Methods **A343** (1994) 60.

[142] O. Botner *et al.*, Nucl. Instrum. Methods **A257** (1987) 580.

[143] E. G. Anassontzis *et al.*, Nucl. Instrum. Methods **A323** (1992) 351;
see also P. Baillon *et al.*, p. 1867 in *26th International Conference on High Energy Physics (ICHEP 92)*, American Inst. Phys., (1993).

[144] P. Antilogus *et al.*, SLAC-PUB-5365, presented at the 1990 IEEE Nuclear Science Symp., Arlington, VA, Oct. 23–26, 1990.

[145] P. Coyle *et al.*, Nucl. Instrum. Methods **A343** (1994) 292.

[146] J. Séguinot *et al.*, Nucl. Instrum. Methods **A350** (1994) 430.

[147] K. Abe *et al.*, IEEE Trans. Nucl. Sci. **NS-40** (1993) 593.

[148] P. Antilogus *et al.*, Nucl. Instrum. Methods **A293** (1990) 136.

[149] J. Va'vra *et al.*, "The First Results from the CRID Detector at SLD," p. 1664 in *26th International Conference on High Energy Physics (ICHEP 92)*, American Inst. Phys., (1993).

[150] M. Cavalli-Sforza *et al.*, IEEE Trans. Nucl. Sci. **NS-37** (1990) 1132.

[151] G. D. Hallewell *et al.*, Nucl. Instrum. Methods **A264** (1988) 219.

[152] P. A. Coyle and T. Weber, SLD CRID Internal Note 34 (1987).

[153] G. Hallewell *et al.*, SLD CRID Internal Note 53 (1988).

[154] M. Cavalli-Sforza, SLD CRID Internal Note 15 (1986).

[155] J. Va'vra, SLD CRID Internal Note 77 (1993).

[156] Y. Iwasaki, SLD CRID Internal Note 81 (1993).

[157] S. J. Yellin, SLD CRID Internal Note 49 (1988).

[158] K. Abe *et al.*, Nucl. Instrum. Methods **A371** (1996) 195.

[159] U. Müller *et al.*, Nucl. Instrum. Methods **A343** (1994) 279.

[160] W. Adam *et al.*, Nucl. Instrum. Methods **A371** (1996) 240.

[161] K. Abe *et al.*, IEEE Trans. Nucl. Sci. **NS-40** (1993) 589.

[162] C. Simopoulos, SLD CRID Internal Note 55 (1995).

[163] J. Va'vra, Nucl. Instrum. Methods **A367** (1995) 353.

[164] H. Kawahara, D. Muller, and S. Narita, SLD CRID Internal Note 83 (1996).

[165] J. Va'vra, private communication.

[166] D. Muller, SLD CRID Internal Note 88, in preparation.

[167] Bill Dunwoodie, private communication.

[168] J. Va'vra, SLD CRID Internal Note 89, in preparation.

[169] T. Junk, Ph. D. dissertation, Stanford University, Stanford, CA (1995); also SLAC-R-95-476.

[170] P. N. Burrows, H. Park, K. T. Pitts, and J. M. Yamartino, SLD Internal Note 229, (1993).

[171] J. M. Yamartino, SLD Internal Physics Note 14, (1992).

[172] K. G. Baird, Ph. D. dissertation, Rutgers University (1996); also SLAC-R-483.

[173] R. Akers *et al.* (OPAL collab.), Z. Phys. **C63** (1994) 181.

[174] D. Buskilic *et al.* (ALEPH collab.), Z. Phys. **C66** (1995) 355.

[175] P. Abreau *et al.* (DELPHI collab.), Nucl. Phys. **B444** (1995) 3.

[176] D. Buskilic *et al.* (ALEPH collab.), Z. Phys. **C55** (1992) 209.

[177] P. Abreau *et al.* (DELPHI collab.), Phys. Lett. **B347** (1995) 447.

[178] D. Buskilic *et al.* (ALEPH collab.), Phys. Lett. **B374** (1996) 319.

Index